Rutile-TiO_2 based materials for lithium ion batteries

Thesis submitted for the Degree of Doctor of Philosophy

Nouf Hezam Alotaibi

DEPARTMENT OF MATERIAL SCIENCE AND ENGINEERING

UNIVERSITY OF SHEFFIELD

UNITED KINGDOM

JULY 2015

Dedication

To my late father,
who unfortunately didn't stay in this world long enough
to see his daughter in what he aspires to

Acknowledgments

"In the name of Allah, the Most Gracious, the Most Merciful"

First of all I express my humble thanks to God and then to my Parents without whose blessings I am unable to do anything.

It has been a great honour and privilege for me to have worked under the supervision of Professor A. R. West; I am truly blessed to have such an inspirational, motivating and caring guide like him. His words of encouragement and desire for excellence have been my driving force.

Special thanks are due to Mr. Andrew Mould for his consistent help and valuable advice during carrying out the experiments.

All colleagues in working groups “Li- ion Battery” and “Electro- ceramics” in Materials Science and Engineering department are gratefully acknowledged for their support and help during this work. Special thanks to Dr. Sobri, Adil and Fayaz.

The financial support by the Royal Embassy of Saudi Arabia Cultural Bureau in London and King Saud University in Riyadh is gratefully acknowledged.

My sincere thanks and heartfelt regards are due towards my friends: Prof. Fatima Ahmad, Dr. Salma Altamimi and Zeenat Alkhayat.

Last but not the least, I wish to thank my siblings; Bader, Amal, Dr. Dalal, Amjad, Abdullah and Mohammed, for their love and support.

Special thanks to my Nephews and my niece: Mohammed, Omar, Majed and Nouf, whom I missed a lot during these years.

My deepest appreciation for my sister, Delo who has been with me throughout my Ph.D jounery for her care, support and encourgement.

Thanks to Allah almighty

Sheffield

Abstract

Although widely used, the most promising Li-based energy storage systems still suffer from a lack of suitable electrodes. There is therefore a need to seek new materials to satisfy the increasing demands for energy storage worldwide. TiO_2 is a very promising anode material for lithium rechargeable batteries. It has a low insertion voltage of Li and high theoretical specific capacity. However, Li insertion into bulk rutile is negligible at room temperature due to the dense close packing of the rutile structure; also it suffers from a poor electronic conductivity. The electrochemical performance of pure rutile reveals that only 0.11 mol of Li can be inserted into rutile structure with a specific capacity of ~26 mAh/ g. The main objective of this thesis has been to seek ways to improve the performance and charge storage capacity of rutile by compositional modification

Improvement of the electronic conductivity of rutile by quenching oxygen-deficient samples and its influence on electrochemical performance have been studied and compared with that of fully oxidized rutile. An improvement in charge-discharge capacity was achieved; 0.21 Li per mol of TiO_2 corresponding to 49 mAh/ g in the first cycle, but for subsequent cycles, both became similar which indicates that increasing the electronic conductivity by quenching did not give a long term improvement and suggests that lattice dimensions rather than electronic conductivity may be the reason for the poor perfomance of rutile anode.

Substitution of Ti^{4+} with metal ions of either similar or different valence to increase the lattice dimensions and/or to increase the electronic conductivity is an option to improve the electrochemical performance of rutile TiO_2. In this study, the effect of doping with large Sn^{4+} and co-doping with Cu-M (M= Nb, Ta) on the electrical and electrochemical performance is presented. The objective was first, to increase the unit cell dimensions of rutile by doping. This is based on the hypothesis that insertion of Li into TiO_2 rutile would be easier with an expanded unit cell.

Solid solutions have been prepared via solid state reaction where Ti^{4+} is partially replaced by either Sn^{4+} or a combination of divalent (Cu^{2+}) and pentavalent ions (Nb^{5+}, Ta^{5+}). Single-phase solid solutions of the doped systems have been characterised by XRD and indexed on a tetragonal rutile structure; lattice parameter refinement confirms the expansion in the unit cell dimensions.

Lithium test cells were fabricated using the rutile solid soultions as anodes. The first discharge step reveals that up to one mole of Li ion can intercalate into co-doped Cu-Nb or Cu-Ta at room temperature with a discharge capacity up to 78 mAh/g while a specific capacity of 154 mAh/ g was delivered by Sn-doped rutile. These examples of lattice expanded doped rutile show a much higher electro-activity towards Li insertion than undoped rutile with excellent retention of capacity during cycling. Ex-situ XRD indicates excellent structural stability during cycling with no evidence of major changes in the rutile crystal structure. However, a major drawback in their electrochemical behaviour was a significant loss of capacity on cycling.

The variation in the electrical properties of doped systems with the nature and composition of metal electrode and atmosphere was studied for Cu-Nb and Cu-Ta co-doped rutile. The formation of a potential barrier, due to the presence of residual phase at the grain boundary, was indicated by impedance spectroscopy (IS) in co-doped system, the data showing a Schottky-like nature. The $Sn_xTi_{1-x}O_2$ system exhibits resistive behaviour, with high activation energy for all compositions.

The effect of rutile TiO_2 as starting material on the electrochemical performance of $Li_4Ti_5O_{12}$ (LTO) was examined and compared with that of anatase TiO_2. High purity LTO was obtained using rutile starting material but the specific capacity was slightly higher for LTO prepared using anatase than rutile.

Table of Contents

List of Figures

List of Tables

1. INTRODUCTION AND LITERATURE REVIEW

1.1 Introduction

Rechargeable lithium ion battery (LIB) systems are currently employed as power sources in portable electronics and automotive applications such as electric vehicles (EVs) and hybrid electric vehicles (HEVs) due to their high voltage, high energy density, and long cycle life. The rechargeable LIB is considered the most promising energy storage system for renewable energy systems.

The history of lithium ion battery development and commercialisation can be summarised as follows. The concept of the rechargeable lithium ion battery originated in the early 1970's when Whittingham from Exxon showed a working Li metal/TiS_2 cell in 1970. By the end of the decade (1979) Goodenough published the possibility of using $LiCoO_2$ as an intercalation cathode. Lithium ion battery technology underwent a revolution with the graphite anode concept discovered by Rachid Yazami in 1980. In 1991, Sony Corporation released the first commercial lithium ion battery with a carbon anode. Nowadays, many devices use rechargeable lithium ion batteries and several cathode chemistries have been developed. The market is growing rapidly from portables to automotive and grid with light, high energy dense systems and a great cycling efficiency.

1.1.1 Electrochemical principles of LIB operation

Lithium ion batteries are electrochemical devices that store electrical energy by directly converting it to a chemical form. A Li -ion battery is composed of an anode (negative electrode) and a cathode (positive electrode) that are electrically insulated by a porous polypropylene membrane separator in a non-aqueous, organic electrolyte containing lithium salt. Separating the positive and negative electrodes is necessary to prevent a short circuit. During charging, Li^+ is extracted from the cathode intercalation host, diffuses towards the anode through the electrolyte and a porous separator, and subsequently intercalates into the anode, while the electrons pass around the external circuit. The reverse process occurs during discharging, is shown schematically in **Figure 1-1** (1).

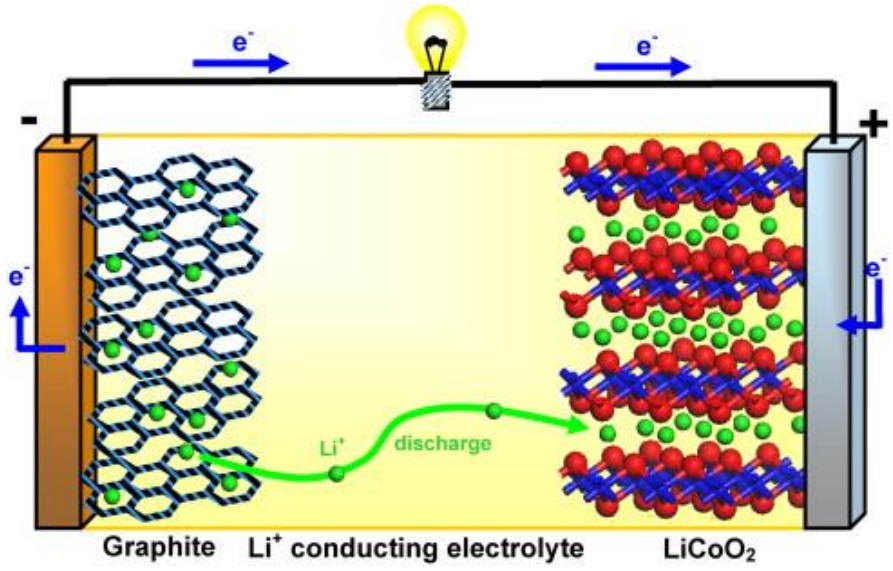

Figure 1-1: Schematic illustrating the lithium ion battery operation showing the Li ion movement and the electron transport during discharge process, adapted from Solid State Ionics, 179/21-26, Bruce PG. Energy storage beyond the horizon: Rechargeable lithium batteries, 752–60, Copyright (2008), with permission from Elsevier (1).

The electrodes have different potential and this provides the driving force for battery performance. The open circuit voltage (OCV) between the anode and cathode of Li batteries is typically ~ 2.7 – 3.4V, depending on the materials of the anode and cathode.

The current Li -ion battery employs insertion/de-insertion of lithium ions between the positive $LiCoO_2$ electrode (cathode) and the negative graphite/carbon electrode (anode). During the charging process, the lithium ions are extracted from the $LiCoO_2$ electrode by oxidation of cobalt and this is accompanied by lithium ion insertion (intercalation) between the layers of the graphite/carbon electrode. At the same time, the electrons flow through the external circuit from the cathode to the anode. In the discharge process, the lithium ions insert into the $LiCoO_2$ electrode and this is accompanied by a reduction of cobalt. At same time, the electricity is produced.

Reversible oxidation- reduction reactions at cathode and anode can be expressed as:

- Cathode

$$LiCoO_2 \underset{\text{discharge}}{\overset{\text{charge}}{\rightleftharpoons}} Li_{1-x}CoO_2 + (x)\, Li^+ + (x)\, e^- \qquad (1)$$

- Anode

$$C + (x)\, Li^+ + (x)\, e^- \underset{\text{discharge}}{\overset{\text{charge}}{\rightleftharpoons}} Li_xC \qquad (2)$$

- Overall

$$LiCoO_2 + C \underset{\text{discharge}}{\overset{\text{charge}}{\rightleftharpoons}} Li_{1-x}CoO_2 + Li_xC \qquad (3)$$

1.1.2 Reactions at the electrodes

The reactions at the electrodes involve the insertion and extraction of lithium ions into/ from the electrode. These insertion and extraction processes require a stable host structure to permit mobility of lithium ions. Ideally, the insertion and extraction processes should avoid any structural change to the host. Structural change can induce mechanical stresses, affect the electronic conductivities of the electrode material and decrease energy outputs of lithium batteries (2).

1.1.2.1 Intercalation reaction

Intercalation and de-intercalation reactions are specific terms used to describe the insertion and extraction of lithium ions into/ from an electrode with a 3D open framework containing interconnected channels and tunnels, a 2D layered and a 1D

ribbon type structure. It requires the insertion of an ion or molecule (guest species) into the solid host structure without structural modification to the the host (3).

The intercalation reaction is known as a topotactic reaction or a solid solution reaction (4) (5). In a topotactic reaction, the chemical composition changes without any changes in the crystal structure of the host. Actually, a slight modification is required for accommodating the guest species, with an extra positive charge in the host structure while maintaining electro-neutrality in the crystal structure.

Lithium intercalation into the host structure can be carried out either chemically or electrochemically.

Chemical lithium intercalation mainly involves the reaction of the host lattice with n-butyl lithium (C_4H_9Li) in hexane as a solvent.

In the electrochemical method, lithium can be intercalated or deintercalated into/from the host structure by reduction or oxidation in non aqueous electrolyte using lithium metal as a counter electrode. A host structure such as layered TiS_2 was used as a cathode in the first rechargeable lithium batteries by Exxon in 1970 (6).

For electrochemical intercalation, the parent structure should have either a 2D or 3D framework with cages or tunnels allowing a reversible intercalation of lithium without any severe modifications to the structure. The structural changes in the host structure that occur during the de-intercalation of lithium ions will lead to the formation of metastable materials or a new phase (5). The host structure selected for the electrochemical intercalation should have reducible species. Thus, transition metal oxides are good hosts for the intercalation reactions because of their possibility for multiple oxidation states (3) where the variation in oxidation state has no effect on the crystal structure.

Intercalation reactions limit the capacity to one, or a maximum of two, lithium atoms per transition metal host ($M^{+(x+1)} \leftrightarrow M^{+x}$), as the addition/removal of Li^+ expands / contracts the lattice of the crystal structure of the host material. The reversibility of the intercalation process affects the cyclability and cycle life of batteries. Depending on how drastic the structural changes are, any changes in the host structure may lead to disturbing the pathway of diffusion and hence affect the mobility of lithium ions and the diffusion rate (5).

1.1.2.2 Conversion reaction

The conversion reaction is a reversible electrochemical reaction of lithium with transition metal oxides (7), and can be represented as:

$$M_aX_b + (b \cdot n)\ Li \leftrightarrow aM + bLi_nX \qquad (4)$$

where M = transition metal, X = anion, and n = formal oxidation state of X.

There are usually two steps:

$$\text{Oxide} \rightarrow \text{metal} \leftrightarrow \text{Li metal alloy}$$

Tin oxide (SnO or SnO_2) is a good example for conversion reaction as will be discussed later in more detail.

There is a correlation between the oxidation state of the metal and the amount of lithium that can be reacted per mole of metal as the metal in M_aX_b is reduced from $M^{e+}x$ to M^0, unlike the intercalation reaction in which usually only one oxidation step is available (e.g. Co^{4+}/Co^{3+} in $LiCoO_2$).

Many transition metal compounds that do not have any vacant sites in their structure cannot intercalate lithium but can deliver stable gravimetric capacities as much as three times that of carbon.

Conversion reactions have already been reported for some oxides and sulphides (8–11) also, the reversible conversion reactions in binary M–X compounds with X = O, N, F, S, or P have been reported. These were found to be electrochemically reversible for hundreds of cycles (12–14). The reversibility of the conversion reaction seems to be explained by the formation of nanoparticles of the metal upon reduction which are maintained even after several reduction-oxidation cycles (15), however, the first part of the conversion reaction is usually irreversible.

1.2 Battery components (basic construction)

Batteries consist of three main components: a cathode (positive electrode), an anode (negative electrode) and an electrolyte.

1.2.1 Cathode materials

The cathode is an insertion material that represents the positive electrode. The main criteria required for cathode materials can be summarized as follows (16):

- The discharge reaction should have a high discharge voltage to maximize the cell voltage.
- The host structure must have a low molar mass and the ability to intercalate large amounts of lithium, giving high storage energy capacity.
- The intercalation -de-intercalation process should be highly reversible.
- The host structure must have a high lithium chemical diffusion coefficient to ensure fast redox reactions.
- The host structure must have a good electronic conductivity (σ_e) and lithium ion conductivity (σ_{Li}) to minimize additives needed and polarization losses.
- There must be minimal volume change, and structural modification, during intercalation and de-intercalation giving a long cycle life.
- It must be low cost, have low toxicity and be environmentally friendly

Cathode materials can be classified into two groups: The first comprises layered compounds with an anion close-packed lattice. The alternate layers between the anion sheets are occupied by redox-active transition metal cations, and lithium ions are intercalated into remaining empty layers. The materials in this kind of electrode include $LiCoO_2$, $LiNi_{1-x}Co_xO_2$, $LiMnO_2$ and $LiNiO_2$.

The second class of cathode materials have a more open structure, such as vanadium oxides (V_2O_5), the tunnel compounds of manganese oxides (MnO_2) and transition metal phosphates such as olivine $LiFePO_4$(17,18).

Layered Li_xCoO_2 (17,19,20), Li_xNiO_2 (18,21,22) and Li_xMnO_2 (23–25), spinel $Li_xMn_2O_4$ (26–28) and olivine Li_xFePO_4 (29) are the most studied positive electrode materials in the last two decades (17). Therefore, the next paragraphs focus on these kinds of cathode materials.

1.2.1.1 Layered oxides

$LiCoO_2$

Lithium cobalt oxide, $LiCoO_2$, has been widely used as cathode in commercial Li-ion batteries since it was released by Sony Corporation in 1991. It crystallises in a layered structure which is isomorphic with α-$NaFeO_2$ (R-3m space group) and can be described as a rock salt structure with oxygen in a cubic close packed arrangement and parallel planes containing Li^+ and Co^{3+} ordered in alternating (111) planes of octahedral sites.

The electrochemical properties of $LiCoO_2$ in terms of high energy density were first reported in 1980 by Goodenough et al. (17). It has a flat operating voltage of 3.6 V vs. Li^+/Li and a theoretical capacity of 248 mAh/g; however, only 120-180 mAh/g can be delivered in practise. Layered Li_xCoO_2 is stable upon lithium intercalation or de-intercalation despite several phase transformations at specific lithium contents.

Although the $LiCoO_2$ cathode has been successfully commercialised, it has several drawbacks, including environmental issues due to its toxicity and the high price of cobalt. Furthermore, Co^{4+} is thermally unstable and its reactivity with the electrolyte leads to increased safety concerns about the battery. The large concentration of Co^{4+} may result in destruction of the cathode crystalline structure and hence loss of cell reversibility (19). To avoid this, delithiation is restricted to ~ 0.5 Li and hence the theoretical capacity is not reached.

The above drawbacks were the main motivation for exploring new materials similar to $LiCoO_2$ in structure, such as $LiNiO_2$ and $LiMnO_2$ but substituting different metals for some or all of the Co, Ni and Mn.

$Li(Ni,Mn)O_2$

$LiNiO_2$ and $LiMnO_2$ are isostructural with $LiCoO_2$ and adapt the α- $NaFeO_2$ crystal structure (30). However, it is difficult to attain $LiNiO_2$ as a pure crystalline phase due to lithium volatilization as reported by Kanno (31). The discharge capacity of $LiNiO_2$ was reported by Guo to be 195- 210 mAh/g (32), however the losses are rapid, which lead to poor cyclability (33). To overcome this, considerable work has been dedicated to improving the structural stability and, hence the capacity and

cyclability by coating it with a metal oxide or by partial substitution of the Ni with other metals, such as Al, Mg, or Co.

$LiMnO_2$ is a promising candidate for a cathode due to its low cost, nontoxic nature and high theoretical capacity. Despite all these advantages, it is thermodynamically unstable at elevated temperature. Various synthesis approaches are used to obtain pure $LiMnO_2$ including: an ion exchange reaction from α-$NaMnO_2$ (23), hydrothermal reaction (34) and high-temperature firing in an air atmosphere (35).

The capacity of $LiMnO_2$ was reported by Bruce et al. to be 230 mAh/g on the first cycle and to drop to 130 mAh/g in subsequent cycles (23).

1.2.1.2 $LiMn_2O_4$ Spinel

$LiMn_2O_4$ has a theoretical capacity of 148 mA h/ g with a flat operating voltage of 3.95 - 4.1 V, as well as high thermal stability, low cost and low toxicity. $LiMn_2O_4$ presents a 3D spinel framework structure that allows reversible intercalation-deintercalation of lithium ions without structural changes. However, the reversible capacity is lower than that of $LiCoO_2$. The high lithium ion flow is due to the interconnection between the empty 16c octahedral sites and empty tetrahedral sites which form a 3D diffusion pathway for lithium. On the other hand, the capacity fading, during cycling, limits the electrochemical performance of $LiCoO_2$ (28).

1.2.1.3 $LiFePO_4$ Olivine

A new class of intercalation compounds, phosphates rather than oxides was discovered and identified as cathode materials for lithium -ion batteries by the Goodenough team in 1997 (29). Lithium metal phosphates with olivine-structure (phospho-olivines) have a general formula $LiMPO_4$ (M = Fe, Mn, Co, or Ni).

For many different reasons, including low toxicity, low cost, availability, environmental benignity, resistance to overcharge and high thermal stability, $LiFePO_4$ could have a major impact on electrochemical energy storage. It has a theoretical specific capacity of 170 mAh/g combined with a flat oxidation-reduction voltage plateau at discharge voltage of 3.40 V vs. Li^+/Li, which leads to a very high

energy density. Moreover, it is stable during discharge/recharge and thus has excellent cycling performance with no obvious capacity fading observed even after a hundred cycles (29).

$LiFePO_4$, however, has a low conductivity at room temperature (less than 10^{-9} S/cm)(36), and requires additional treatment to achieve a reasonable capacity, either by coating or mixing with a conductive additive such as carbon or by reduction of the grain size to improve the lithium ion diffusion (37). Doping $LiFePO_4$ with metals supervalent to Li^+ may increase the electronic conductivity (36).

The crystal structures of the three main classes of cathode materials are shown in Figure 2, the structure and electrochemical characteristic are sammarised in Table 1-1. Lithium ion diffusion during insertion/de-insertion reactions and Li-ion transportation within the electrode materials is in 1D, 2D and 3D for olivine, layered and spinel structure respectively (38).

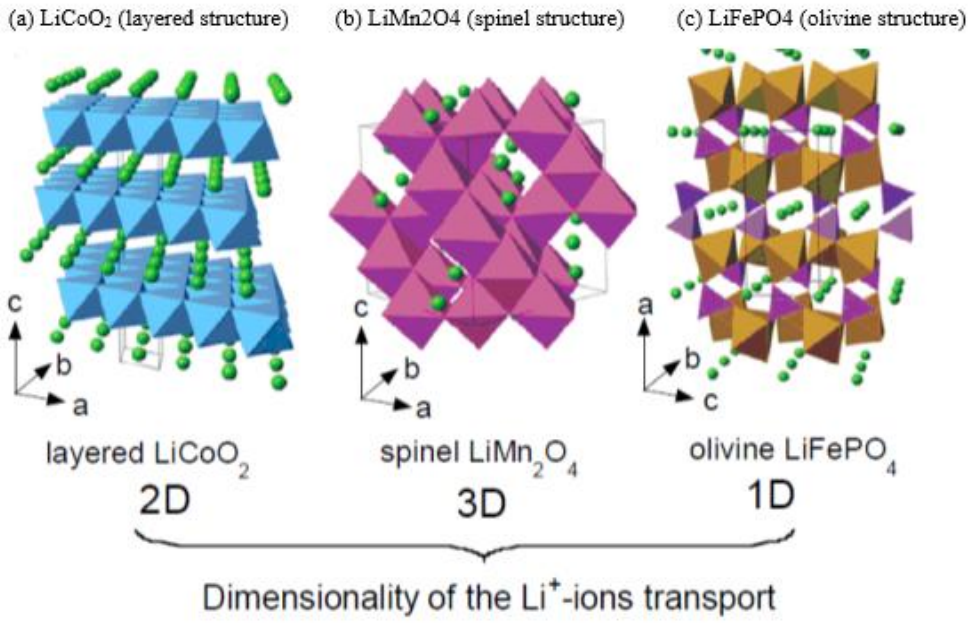

Figure 1-2: Schematic illustrations of the crystal structures of (a) layered rock salt structure, (b) spinel structure, and (c) olivine structure in which the Li^+ ions are mobile through the 2-D (layered), 3-D (spinel) and 1-D (olivine) frameworks, from Ref. (39)

Table 1-1: Main characteristics of the three classes of the most common insertion compounds(39)(40).

characteristics	$LiCoO_2$	$LiNiO_2$	$LiMn_2O_4$	$LiFePO_4$
Framework	Layered rock salt	Layered rock salt	Spinel	Olivine
Redox couple	Co^{4+}/Co^{3+}	Ni^{4+}/Ni^{3+}	Mn^{4+}/Mn^{3+}	Fe^{3+}/Fe^{2+}
Average potential (V vs. Li/Li+)	4.2	4.0	4.1	3.45
*Specific capacity (mAh/ g)	272	274	148	170
**Discharge capacity (mAh/ g)	140	160	120	160
Safety	Fair	Poor	Good	Good
Environmental	Poor	Fair	Good	Good
Cost	High	Fair	Low	Low

* Theoretical ** Practical

1.2.2 Electrolyte

The electrolyte provides the medium for the transfer of mobile ions but not electrons between the electrodes. The electrolyte must have specific criteria such as (30,41):

- Good ionic conductivity ($\sigma_i > 10^{-3}$ S/cm) to minimize internal resistance.
- Negligible electronic conductivity (Zero σ_e).
- High chemical stability at necessary potentials and temperatures.
- Compatibility with anode/cathode.
- Minimal side reactions with electrodes, as much battery failure is caused by electrolyte side reactions.

Electrolytes are divided into three categories: liquid electrolytes, polymer electrolytes and solid electrolytes. *Liquid electrolytes* are obtained by dissolving lithium salts in organic solvents. A variety of lithium salts have been used over the years. $LiClO_4$ has a high ionic conductivity, a wide electrochemical stability up to 5.1V (42) and a low interfacial resistance (43). However, $LiClO_4$ is not safe, because the perchlorate anion is a strong oxidant which can react with organic

solvents under extreme conditions such as high temperature or high current charge (44). $LiBF_4$ is safer but has poor Li cycling efficiency and only a moderate ionic conductivity (45) $LiPF_6$ is the most commonly used, exhibits high conductivity (10^{-3} S/cm) and high lithium ion transference number (~ 0.35); also, its safety is acceptable (46). However, $LiPF_6$ is known to be thermally unstable and decomposes to LiF and PF_5 (47,48). Recently, lithium bis(oxalate)borate (LiBOB) (49,50) has been reported as a new lithium salt in liquid electrolyte. It has suitable properties such as high conductivity, low cost and stability to hydrolysis (51). The most common salts used in liquid electrolytes for LIBs are listed in Table 1-2.

Table 1-2: Common lithium salts and their properties taken from Ref. (48).

Conducting salt	E_{ox}, V vs. Li/Li^+	Advantages	Disadvantages
$LiPF_6$	6.8	standard conducting salt, most balanced properties	thermally unstable, forms highly toxic HF with moisture
$LiClO_4$	6.1	economical, high anodic stability	explosive, impractical for industry purpose
$LiBF_4$	6.6	less toxic, good electrochemical properties	hydrolysis, moderate ion conductivity, thermally unstable

Liquid electrolytes are a solution of lithium salt and organic solvent. The organic solvent should have properties such as, high dielectric constant and low viscosity, be inert to the other cell components, have a low melting point, a high boiling point, low vapour pressure and finally, be low cost and of assured safety. Many organic solvents have these properties such as; ethylene carbonate (EC), propylene carbonate (PC), dimethylcarbonate (DMC) and diethylene carbonate (DEC). All have advantages and disadvantages and to overcome their individual drawbacks a mixture of solvents can be used.

Despite their advantages, liquid electrolytes are mechanically unstable and there is a possibility of flammability. Therefore, interest in the development of lithium ion conducting polymer or solid electrolytes has increased, to improve electrochemical properties.

Polymer electrolytes can be classified into five different types of homogeneous electrolytes:

Type I. Classical liquid electrolytes;

Type II. Gel electrolytes;

Type III. Dry polymer electrolytes;

Type IV. Dry single-ion-conducting polymer electrolytes; and

Type V. Solvated single-ion- conducting polymer electrolytes. (52).

The key advantages of these electrolytes are flexibility, design flexibility, reduced flammability and low cost.

Solid electrolytes are inorganic solid materials that conduct lithium ions at room temperature. Solid electrolytes can replace organic liquid electrolytes, which are flammable and toxic; thus the safety of the batteries improves which allows the use of lithium metal as the anode. They are classified into two major categories: crystalline electrolytes and glass-based electrolytes (53).

Crystalline electrolytes include:

LISICON, a lithium superionic conductor with the general formula $Li_{16-2x}D_x(TO_4)_4$ where D is a divalent cation and T is a tetravalent cation. When D= Zn^{2+} and T= Ge^{4+} , $Li_{14}ZnGe_4O_{16}$, has a conductivity at room temperature of 1.0×10^{-7} S/cm (54).

Garnet-type $Li_7La_3Zr_2O_{12}$ with a room temperature conductivity of 2.1×10^{-4} S/cm (55).

NASICON-type, a Na superionic conductors with a general formula $A_xM_2(XO_4)_3$, and $Li_{1+x}Al_xTi_{2-x}(PO_4)_3$ (x = 0.3) and a room temperature conductivity of 7×10^{-4} S/cm (56).

The glass-based electrolytes, include glassy: $50Li_2S$-$17P_2S5$−33LiBH (57) and glass-ceramic systems made of oxides and sulphides: $70Li_2S{\cdot}30P2S5$ (58).

There are two crucial issues regarding the use of solid electrolytes, the impedance of the solid–solid interface between electrode and electrolyte and the relatively low ionic conductivity at room temperature. Both are still huge challenges to achieving high-performance solid electrolytes.

1.2.3 Anode materials

The anode materials represent the negative electrodes in lithium ion batteries. They are classified into three main groups:

- Insertion-type materials such as carbon materials, $Li_4Ti_5O_{12}$, TiO_2,
- Alloying-type materials such as Sn, Si and SnO_2 ,
- Conversion-type materials such as cobalt oxides and iron oxides.

Anode materials have the following requirements:

- Operating voltage close to metallic lithium, ≤ 1V vs. Li^+/Li.
- High energy density.
- No structural change of the host during charge and discharge processes.
- No Li electroplating under fast charge rate.
- Good capacity retention upon cycling.
- Abundant (readily available).
- Environmentally friendly.
- Low cost.
- Non-toxic.

1.2.3.1 Lithium metal

Li metal has been used as an anode in primary (i.e. not rechargeable) and secondary (rechargeable) lithium batteries (59). Lithium has three important main features, a high specific capacity (3.86 Ah/g, 7.23 $Ahcm^{-3}$), the lowest standard reduction potential vs. the standard hydrogen electrode (E_0 = - 3.04 V vs. SHE) and it is the lightest metal (M = 6.94 g mol^{-1}, corresponding to 3860 Ah/kg). These features plus others such as a wide operating temperature range, flat voltage discharge characteristics, superior shelf life and stability in non aqueous solvents due to the formation of a passivation film on the Li surface (46), make Li metal the

optimal anode for a lithium ion battery. However, plating the Li metal during the charge process leads to a dendritic structure formation on the Li anode, which results in a significant energy density loss (60) and can generate a short circuit when dendrites penetrate the separator/electrolyte contacting the cathode, which can lead to flaming of the battery or a battery explosion (61). Hazard related to short-circuiting has been a critical problem that has hindered the use of Li metal and such high risks have been a major barrier to the development of batteries which use Li metal as an anode.

1.2.3.2 Carbon-based materials

Two kinds of carbon-based materials are used as anodes in LIBs: 1) soft carbon (graphite carbons) with crystallites lined up in the same direction, and 2) hard carbon (non-graphite carbons) in which crystallites have a disordered orientation. This classification depends on the degree of crystallinity and how carbon atoms are arranged (62–64).

Graphite

Almost all commercial rechargeable lithium batteries use graphite/carbon based materials as the active anode material. Various types of graphite are commercially available, the most popular being: mesocarbon microbead (MCMB), mesophase-pitchbased carbon fibre (MCF), vapour grown carbon fibre (VGCF) and massive artificial graphite (MAG).

Graphite has a planar layered structure of carbon atoms with a hexagonal or rhombohedral form; see Fig. 3 (a). Hexagonal graphite was reported by Hull in 1917 and the stacking sequence of graphite sheets repeats after two layers, while the stacking in the rhombohedral form has a repetition after three layers. Rhombohedral graphite is thermally less stable than hexagonal graphite as the layers shift to adopt the two layer sequence (65).

Graphite anodes have many desirable properties, such as high capacity and low (less than 0.1 V vs. Li+/Li) and flat operational voltage for lithium intercalation. Also, they can insert lithium reversibly at an initial capacity of 372 mAh/g, nominally to give LiC_6 when charged. On the other hand, it has several drawbacks that open the window for alternative materials. The major problems related to carbon electrodes include: 1) crucial safety concerns attributed to their low operating

potential; 2) solid electrolyte interface (SEI) film formation during the initial cycle which leads to a large, irreversible capacity loss; 3) limited stability due to their fragile structure: the change of volume is about 10% which subsequently decreases the cycle stability (59,66).

Recently, Bao et al. (67) reported a new synthetic approach to prepare 3D porous graphitic carbon from conjugated polymer molecular framework by a simple one-step synthesis using low cost raw materials. They demonstrated that the resulting, highly graphitic carbon offers a 3D hierarchically porous graphitic (HPG) carbon framework with ultrahigh surface area along with large pore volume and interconnected graphene-like network structures. HPG electrode meets all of the critical requirements for high-performance electrodes; it provides a good mechanical flexibility and high conductivity. These properties lead to excellent electrochemical activity and high stability, with unique performances in both super-capacitors and Li−sulfur batteries.

Graphene

Graphene is fundamentally a single layer of graphite, a layer of sp^2 hybridized carbon atoms bonded into two dimensional sheets with nanometer thickness arranged in a hexagonal lattice, see Figure 1-3 (b) (68). It has attracted much attention because of its electrochemical properties which make it a suitable electrode material for LIBs. These properties include: good electrical conductivity, good mechanical strength, high charge mobility and high surface area (69,70). However, the lithium storage mechanism and thus the capacity of graphene are still in debate. The capacity of graphene depends on the form of interaction between lithium and the graphene, either absorption of Li ions on both faces of graphene (<372 mAh/g), or trapped Li ions at the benzene ring in a covalent bond (~780 to 1116 mAh/g).

Many studies have attempted to understand the relationship between the graphene structure and capacity value. Pan et al. prepared disordered graphene sheets by various methods and reported that the graphene sheets achieve high capacity in the range 790-1050 mAh/g due to the presence of additional active sites for lithium. However, the drawback of the disordered structure is poor electronic conductivity (71). Lian et al. reported that graphene sheets exhibit high capacity close to 1200 mAh/g during the initial cycles and attain values around 848

mAh/g at the 40th cycle by using high quality graphene with few graphite layers and high surface area (72).

Recently, research has focused on improving graphene structure and this includes: synthesis of doped hierarchically porous graphene (DHPG) electrodes by Wang et al. (73), synthesis of nano-ribbons from MWCNTs (74) and the use of hybrid systems such as: graphene/metals or semiconductors, graphene/metal oxides/phosphides (75–77) and nanorod/graphene (78).

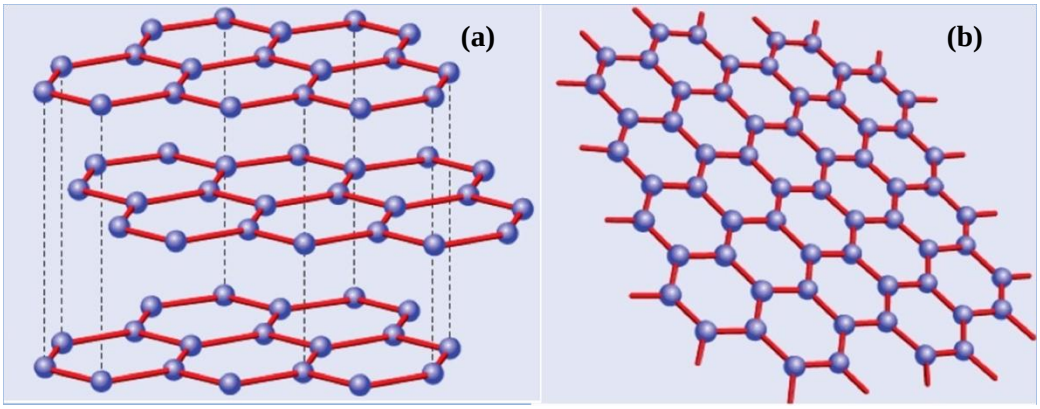

Figure 1-3: Graphite as a stack of graphene layers and (b) Graphene as a single layer of hexagonal lattice of carbon atoms, adapted with permission from IOP Publishing from ref. (68).

1.2.3.3 Li- metal alloys and intermetallic alloys

Lithium- metal alloys have attracted a lot of attention as alternatives to carbon electrodes in lithium ion batteries. Li-Al alloy has been used to solve the dendrite problem (79) but the first commercial cell introduced by Matsushita in the 1980s was based on Wood's metal (a low-melting alloy of Bi, Pb, Sn and Cd) (59).

Li alloy electrodes have high gravimetric capacity, for example: $Li_{4.4}Sn$ (993 mAh/g) which is double the capacity of graphite (372 mAh/g) and $Li_{4.4}Si$ (4200 mAh/g) (80). However, they suffer from cyclability issues due to extreme changes in volume (up to 200%) during operation. This causes a loss of electrical contact between particles and hence deteriorating cycling performance with increased depth of discharge (59). To overcome this issue several strategies have been adapted including: a reduction in alloy particle size to nano-dimensions (81,82), which reduces cracking within the electrode and thus improved cycling behaviour, but is not able to reduce the volume expansion (80,83). The second strategy to

overcome the problem of volume change is using composite negative electrodes by mixing two alloys that react at different potentials and the electrochemically active phase is imbedded in a non-electrochemically active matrix (59) for example; 3D porous silicon, tin-carbon (Sn-C) or Co-Sn-C (Sony Nexelion battery (84,85).

To address the problems of alloy expansion, a new approach based on displacement reactions was proposed by Thackeray et al.,(86) consisting of a metal alloy with a binary intermetallic AB phase. Intermetallic alloys Li_xM such as Cu_6Sn_5, InSb, and Cu_2Sb show a strong structural relationship with their lithiated products (80). The lithiation and delithiation of these displacement reaction negative electrodes leads to a small expansion resulting in total electrode volume change of up to 46%. However, this expansion is small compared to the expansion of binary systems such as Li-Al alloys which can change by 200-300%. Despite the intermetallic electrodes having a smaller expansion than alloys, they still suffer from poor cycling life, particularly upon the initial cycle (59).

1.2.3.4 Tin-based compounds

Materials based on tin oxides are potential alternative anodes with many advantages including: being abundant, low-cost and nontoxic and having a considerable theoretical specific capacity with respect to lithium and a very high lithium diffusion coefficient (~10^{-8} cm^2/s) (87).

The first anode materials based on tin oxides announced in 1997 by Fujifilm were tin-based composite oxides (TCO) with the general formula SnM_xO_y (where M = B, P or, Al) (88). They are based on Li–Sn alloying and dealloying reactions which result in $Li_{4.4}Sn$ formation with a theoretical capacity of 993 mAh/ g, but the initial capacity loss is 300-600 mAh/g. However, they suffer from large volume changes (about 259%) during cycling and thus have poor capacity retention. Problems related to the large volume expansion/contraction of metallic tin could be avoided by using tin oxides. In its first cycle of use, tin oxide (SnO or SnO_2) is irreversibly converted to metallic tin according to eqn. (5), below (89). Tin oxide reacts with lithium and this leads to the formation of metallic tin together with lithium oxide which forms an amorphous matrix acting as a stabilizer for the tin particles and preventing structural collapse. In subsequent cycles, the tin phase could store and

released Li ions through the Li–Sn alloying and de-alloying reactions as expressed in eqn. (6) below (89):

$$SnO_2 + 4Li+ + 4e^- \rightarrow Sn + 2Li_2O \quad (5)$$

$$Sn + xLi+ + xe^- \rightarrow Li_xSn\ (0 \leq x \geq 4.4) \quad (6)$$

An improvement in stability of negative electrodes based on tin oxides is achieved by: the doping of tin dioxide with molybdenum (90) , the application of mesotubes of tin dioxide (91), using composites of tin oxides with other materials such as carbon nanotubes (92) silicon oxides (93) and cobalt oxide (94), control of the particle size (95) the using of thin film materials (96) and restricting the working potential range.

1.2.3.5 Transition metal oxides

The first application of transition metal oxides as anode materials in LIBs was reported in 2000 for nano-phase transition metal oxides such as MO, where M= Co, Cu, Ni, Fe, MnO_2, Co_3O_4 or Fe_2O_3 (7,97). The electrochemical reaction mechanism involves the reduction/oxidation of the transition metal along with the formation/deformation of lithium oxide as shown below:

$$CoO + 2Li^+ + 2e^- \leftrightarrow Li_2O + Co \quad (7)$$

Lithium reversibly interacts with the reduced metal without formation of an alloy. In this case, the source of irreversible capacity loss which characterises the materials based on tin oxides disappears; however, the irreversible capacity loss related to reduction of electrolyte and formation of SEI still exists (98,99). Excellent improvement in their electrochemical properties when used as anode materials in LIBs was demonstrated with a reversible capacity of 600–700 mAh/g (7,12,97). A number of different forms of transition metal oxides have been studied. Porous nanostructures, nanosheets, nanocubes, nanowires and nanotubes have been prepared by various synthetic routes (100).

Cobalt oxide materials CoO and Co_3O_4 are used as anodes for LIBs for their theoretical capacities of 715 and 890 mAh/g respectively (101,102) and excellent capacity retention. However, the anodic process occurs at ~2 V which is a considerably high potential (100).

Iron oxides, Fe_2O_3 and Fe_3O_4, have low cost, non-toxicity and high abundance with a theoretical capacity of 900-1000 mAh/g (102). However, iron oxides suffer from high volume expansion and iron aggregation during cycling, low electrical conductivity and low diffusion of Li-ions which lead to poor cycling performance.

Therefore, to overcome these limitations, researchers have focused on modifying iron-oxide size, shape and porosity as the studies indicate that both size and morphology strongly affect the rate and lithium storage capability of iron oxides.

Carbon coating or carbon based composites of Fe_2O_3 and Fe_3O_4 (103–105) show stabilized iron oxide structures, improve the electrochemical kinetics and power capability and also exhibit a stable capacity of around 900 mAh/g. These results indicate that low cost iron based oxides with highly conductive carbon composites can be a valid alternative to graphite anodes. Several types of transition metal sulphides (MS_x), nitrides (MN_x) and phosphides (MP_x) with M= iron, molybdenum, tin, antimony, nickel, cobalt and tungsten have been investigated as potential anodes due to their high lithium storage capability and structural advantages during the charge-discharge process (100).

1.2.3.6 Anodic materials based on titanium oxides

Anodic materials based on titanium oxides (TiO_2 and spinel $Li_4Ti_5O_{12}$) are promising candidates as alternative materials to carbonaceous anodes. They are low-voltage intercalation hosts for Li, have low toxicity and good chemical and thermal stability. Moreover, high theoretical specific capacity to intercalate lithium (335 mAh/g) and small volume change during charge/discharge processes (about 3%) make TiO_2 an attractive anode material (106,107). Titanium oxide anodes offer superior safety compared to carbon electrodes, since they intercalate lithium at a potential of around 1.5 V vs. Li^+/Li, and hence both the reduction of the electrolyte and the formation of the SEI layer on the anode can be avoided (108–112). Anodic materials based on titanium dioxides are discussed in detail later.

1.3 The future of lithium-ion batteries

Worldwide battery demand, driven mainly by consumer electronics and electric power tools, is expected to generate revenue in excess of $33 billion by 2019, with

a compound annual growth rate (CAGR) of 14.4 percent over seven years, according to Research and Markets (113).

Current research into lithium-ion batteries for various applications focuses on increasing energy density and power density and improving safety. The future of rechargeable lithium batteries depends on new approaches, new materials and new understanding. Research activities related to the development of electrodes for construction of high-performance Li-ion batteries (LIBs) and investigations that consider multivalent cations that offer more than one electron per redox event are desirable. In addition, a new generation of batteries that can perform beyond the limits of the current lithium-ion based battery such as lithium-air, lithium-sulfur, and organic batteries have attracted considerable attention due to their high energy density and rapid response (114,115). A significant step towards a battery that could outperform the current lithium-ion technology is associated with developing: 1) novel anode materials and 2) new technologies for batteries that move lithium-ion electrochemistry to higher potentials. Next generation anode materials include; silicon-based (near future) and nanomaterials (technical challenges).

1.3.1 Si-based anode

Some researchers have used silicon in place of graphite for the new electrodes. In contrast to graphite, silicon as the anode material in Li-ion batteries has a greater energy storage capacity, almost ten times that of graphite, a longer battery life and also allows for smaller battery size.

At the carbon anode: $6C + Li^+ + e^- \leftrightarrow LiC_6 \Rightarrow 372\ mAh/g$ (8)

At the silicon anode: $4Si + 15Li^+ + 15e^- \leftrightarrow Li_{15}Si_4 \Rightarrow 3580\ mAh/g$ (9)

However, problems of poor cycle life attributed to the volume expansion issue (400%) hinder the commercial application of Si-based anodes. Recently, Nexeon has patented a new way of structuring silicon; as a composite of Si pillared nanoparticle arrays on micro particle cores by metal assisted etching, that overcome the previous problems. Nexeon's patented Si significantly increases the capacity (in the range 600–1,200 mA·h/g) and delivers extended cycle life without degradation of capacity (116). Silicon anodes will most likely dominate the market in the future as their popularity increases (117).

1.3.2 Metal-air batteries

Metal-air batteries are a new technology in which the graphite and other metals are replaced with the oxygen in the air, providing a cathode that can simply be replaced with fresh air.

This saves weight and leads to a higher energy density, which means a longer life. Currently, there are problems of degradation due to blockages and internal corrosion, being difficult to recharge, having poor recharging life and stability, all of which have hampered commercialisation of metal-air battery technology. However, this technology could be in electric vehicles in the near future.

While an electric Citroen C1 was driven 1,800 km on a single charge using Al-air technology, Tesla has a patented system for incorporating metal-air batteries into its electric cars (118). Within the next five years, there will be more opportunities for the development of new products, including lithium-air (117).

1.3.3 Lithium-sulfur battery

Sulfur-based batteries are an excellent alternative to the currently used lithium-ion batteries owing to their higher energy density, longer battery life (at least twice the battery life) and lower production cost. The technology has been in development for over 20 years, and at least one company is aiming to have lithium-sulfur batteries as a power source for electric cars by 2016.

Lithium-sulfur batteries deliver up to five times the capacity of current lithium-ion batteries. However, the cyclability problems associated with both the sulfur cathode and the lithium metal anode hinder the commercial application of lithium–sulfur batteries.

A new approach has been adapted to develop a lithium–sulfur battery showing cycle performance similar to that of lithium-ion batteries by using a reversible dual-type solid sulfur cathode and a nanosphere lithiated Si/SiO_x as anode. This lithium–sulfur exhibits superior battery performance in terms of high specific capacity of ~750 mAh/ g over 500 cycles with excellent charge/discharge efficiency (85% of the initial capacity) and remarkable cycle life (119).

Although Li−sulfur batteries offer a promising technology they have a serious drawback: lithium polysulfide molecules, a product of lithium and sulfur reaction,

can leak from the electrode into the electrolyte and result in the battery failure. A 3D hierarchically porous graphitic (HPG) carbon framework has been demonstrated lately by Bao et al. (67) as a sulfur host for Li−sulfur batteries which can prevent the leakage of the polysulfides (67). HPG with very small pores can allow lithium ions to diffuse through the carbon but trap the polysulfides from leaching out, leading to improved battery performance.

However, currently, lithium- ion batteries are expected to remain the main source for power systems, and thus further improvements in both electrode chemistry and architecture are needed (120,121). In addition, there are fire dangers associated with the LIBs anode that must be resolved.

1.4 Titanium based oxides

Titanium dioxide has been widely studied in the literature because of its good properties, such as low cost, low toxicity and physical and chemical stability (122,123). Because of these excellent properties, TiO_2 has become one of the most commonly used materials in several applications including, UV protection by reflecting and/or scattering most of the UV-rays (124), photocatalysts in the photodegradation of pollutants in both: water and air (125–127), sensors for various gases and humidity by exploiting electrical or optical properties that change upon adsorption and as a negative electrode for lithium ion batteries (128) as well as uses in the medical field, for example: bone and joint replacement (129).

1.4.1 TiO_2 based oxides in LIBs

Titanium based oxides attract attention as possible negative electrodes for lithium ion batteries, owing to their low volume change (2-3%) on both lithium insertion/de-insertion and an excellent cycling life (130,131). Moreover, this kind of anodic material shows only minor safety concerns along with other important features such as low cost and low toxicity. However, it also shows low electronic conductivity and low theoretical capacity, in the range of 175-330 mAh/g (47).

Lithium is reversibly intercalated into titanium dioxide polymorphs forming a variable composition phase:

$$x\mathrm{Li}^+ + \mathrm{TiO_2} + x\mathrm{e} \leftrightarrow \mathrm{Li}_x\mathrm{TiO_2}. \qquad (10)$$

From Eq. (10), TiO_2 can offer a specific capacity up to 335 mAh/g corresponding to the intercalation of one mole of Li^+ per one mole of TiO_2 (132). This redox reaction typically occurs at 1.5–1.8 V vs. Li^+/Li. The relatively high working potentials, compared to graphite ~ 0.1V, prevent reactions at the electrode/electrolyte interface and hence make TiO_2- based electrodes safer than the graphite anode. At the same time, this can cause a decrease in the voltage of batteries, particularly with conventional cathodes.

A variety of work has been devoted to using titanium dioxides with several structural modifications, such as: rutile, anatase and TiO_2 (B) structure as negative electrodes (133–135). It has been found that the electrochemical performance and capacity of the lithium insertion/removal into/from titanium based oxides depend on their structure, morphology and size.

1.4.2 Spinel $Li_4Ti_5O_{12}$

The spinel lithium titanium oxide ($Li_4Ti_5O_{12}$, LTO) has received attention in battery research due to its excellent safety characteristics, its high voltage, perfect cycling performance and long lifetime (136–140). LTO anodes operate at a potential above 1.55 V vs. Li/Li^+ (141) which is significantly above the reduction potential of most organic electrolytes, 0.8 V. In this case, the reduction of the electrolyte on the electrode surface and the formation of an SEI layer can be avoided (142). It has been demonstrated that spinel-LTO shows a good structural stability owing to its negligible volume change (only 0.2–0.3%) during the Li-ion insertion/extraction processes (136,137,139), with good reversibility (128,139).

Many experimental and theoretical investigations have shown that LTO has great potential to achieve better performance as a Li-ion battery anode. Compared to the conventional graphite anode, LTO shows better thermal stability performance between 60 °C (139) and 230 °C (143). This can offer a significant safety advantage and hence, LTO can be used to develop extremely safe Li-ion batteries for electric vehicle (EV) and hybrid vehicle (HEV) applications (144). LTO is known as a “zero-strain material” (136), meaning no volume change occurs during the charging/discharging process, unlike graphite which expands by up to 10% during charging (140).

The LTO anode can accommodate up to three lithium ions per formula unit in the spinel structure at a discharge voltage of 1.55 V (vs. Li/Li^+) with a theoretical

capacity of 175 mAh/g and excellent coulombic efficiency > 95% at 1 C (141). Ohzuku et al. (136) reported that the LTO anode exhibits a very flat charge–discharge plateau which is a typical characteristic of the phase transition between a Li- poor phase (spinel-LTO) and a Li-rich phase (rock-salt-LTO) (145).

Low electrical conductivity of LTO (10^{-13} S/cm) and diffusion coefficient of Li in spinel (ranging between 10^{-9} and 10^{-16} cm^2/s) influence the rate capability of the LTO and limit the capacity at high charge/discharge rates (146–148). To improve conductivity and the rate performance of LTO, various techniques were applied including; surface coating typically by conductive carbon, reducing the particle size of LTO to the nanoscale, and doping with metals (149–151).

LTO has practical applications in several areas of portable electronic devices, and automobile applications including; Hybrid Electric Vehicles (HEV), Plug-In Hybrid Electric Vehicles (PHEV), and Electric Vehicles (EV). Three examples of the use of LTO in large scale energy storage are:

1) A ‘‘Nanosafe’’ Li-ion battery developed by Altair Engineering Inc., which employs LTO as the anode and $LiMn_2O_4$ as the cathode. This improves the performance for grid applications in term of ultra-high energy conversion efficiency during the charge/discharge process of more than 91%.
2) A ‘‘SCiB’’ Li-ion battery developed by Toshiba Corporation and using LTO as the anode and $LiCoO_2$ as the cathode which has exhibited excellent cycling stability, low capacity loss (less than 10% after 3000 cycles) and significant rate capability.
3) A type of HEV developed by EnerDel and Think Nordic Corporation which is an example of using LTO as the anode in an electrically-powered system. (128).

The spinel structure of $Li_4Ti_5O_{12}$ and its electrochemical performance is discussed in depth in chapter 4.

1.4.3 TiO_2 structure

TiO_2 has many different polymorphs, the common ones are: rutile (tetragonal, space group $P4_2/mnm$), anatase (tetragonal, space group $I4_1/amd$) and TiO_2(B) (monoclinic, space group $C2/m$) (108,109,152). Anatase and rutile are crystalline polymorphs of TiO_2 found in nature and TiO_2(B) is a metastable polymorph which

was first synthesised and then found in nature. Under standard conditions, rutile is the most stable structure of TiO_2, and also the most available in natural form. The electrochemical behaviour of TiO_2 polymorphs is variable: anatase and TiO_2 (B) are the most active and can accommodate more Li ions than bulk rutile, which can be considered inert to lithium intercalation.

The electrochemical performance and the capacity of lithium insertion/de-insertion mainly depend on the TiO_2 structure. Generally the structures consist of TiO_6 octahedra sharing corners and/or edges. Three polymorphs differ in the way that octahedral are linked together. The TiO_2 unit structure is made of Ti^{+4} at the centre, octahedrally coordinated to six O ions that occupy the corners of octahedra. The different structures represented by TiO_6 octahedra are shown in Figure 1-4.

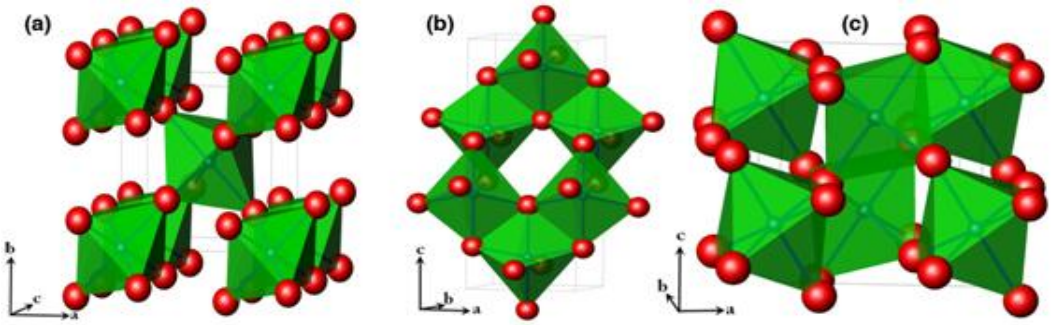

Figure 1-4: Crystal structures of (a) Rutile, (b) Anatase and (c) TiO_2-(B) phases, adapted from Ref.(152).

Rutile is comprised of distorted TiO_6 octahedra sharing edges in the *c*-direction and corners in the *ab* plane (153). Li^+ diffusion in rutile is fast along the *c*-axis, the diffusion coefficient (D_{Li}) was found to be ~10^{-6} cm^2/s, but slow in the *ab*-plane (D_{Li}) ~ 10^{-15} cm^2/s (154). The diffusion path for Li insertion is nearly 1D in rutile (155) (156) (153).

Anatase consists of strongly distorted TiO_6 octahedra sharing edges; these form a stacking of 1D zigzag chains. The absence of corner-shared oxygen leads to empty zigzag channels. The diffusion path for Li insertion is 3D in the anatase framework

and diffusion coefficient (D_{Li}) values range between 7×10^{-14} and 2×10^{-13} cm^2/s for insertion/extraction of the Li^+.

TiO_2-(B) consists of edge and corner sharing TiO_6 octahedra with a Perovskite-like layered structure which offers open channels perpendicular to (110) that lead to fast Li^+ diffusion (157).

The structural type, space group, and lattice parameters for the three phases are summarised in the table below (Table 1-3).

Table 1-3: Structural features of different polymorphs of TiO_2.

Properties	Rutile	Anatase	TiO_2-(B)
Crystal structure	Tetragonal	Tetragonal	Monoclinic
Lattice parameter (Å)	a=b= 4.59 c= 2.96	a=b= 3.79 c= 9.51	a=12.17, b=3.74, c=6.51
Density (g/cm^3)	4.25	3.89	3.76
Space group	$P4_2/mnm$	$I4_1/amd$	C2/m

1.4.4 Electrochemical behaviour of TiO_2 polymorphs

1.4.4.1 Anatase

Anatase is one of the most active TiO_2 polymorphs for lithium intercalation and can accommodate more Li ions than rutile.

Anatase can intercalate 0.5-1 Li^+ per Ti but the amount that can be intercalated varies with the crystallite size of the host. At room temperature, anatase accommodates up to 0.5 Li per formula unit without any major structural changes, reaching a theoretical capacity of 168 mAh/g (108,158).

Oxygen cubic close packed (ccp) structure in anatase offers vacant octahedral and tetrahedral interstitial sites where Li^+ can be accommodated. It has been reported that the first 0.5 of Li^+ are inserted in the favoured empty octahedral sites. Li-insertion is accompanied by a decrease in the anatase unit cell symmetry. When 0.5 Li^+ is intercalated, symmetry transforms from tetragonal $I4_1/amd$ for anatase TiO_2 into orthorhombic $Pmn2_1$ for $Li_{0.5}TiO_2$ (159). The change in symmetry results in 4% change in the unit cell volume (111). Insertion of the additional Li^+ can be achieved at elevated temperature (160) or at nanoscale.

Kavan et al. (161) and Wagemaker et al. (162) reported that one mole of Li^+ can be intercalated into nanosized anatase with a theoretical specific capacity of 335 mAh/ g and this leads to phase transformation from tetragonal to cubic. Wagemaker and his coworker have demonstrated that the Li^+ is inserted into the octahedral sites of the structure leading to an ordered rock salt type with an increase in volume of ~ 3.49% (162).

The Li can intercalate into anatase by a multi-step reaction including solid-solution formation with a potential drop of open-circuit potential to ~1.7 V vs. Li^+/Li, a two-phase reaction with a long flat plateau at 1.7 V, a bulk-intercalation, and interfacial storage gradually decreasing beyond ~1.7 V (152).

A distinct flat voltage plateau at the potential of ~ 1.7 V during the electrochemical insertion of lithium ions into bulk anatase demonstrates bi-phase equilibrium of a Li-poor (tetragonal) and a Li-rich (orthorhombic) phase (156).

Many drawbacks limit the development of anatase as anode, including a poor rate performance and reversibility, significant capacity loss in the first cycle, and higher Li^+ insertion potential than that of the other TiO_2 polymorphs. Carbon additives can be used to overcome the poor rate performance drawback either by adding anatase to a carbon matrix as a composite, but the initial capacity loss and the high operating potential remains. Nanocomposites of various carbon-based materials including graphene sheets (134,163), or graphite (164,165) provide an improvement of the electron transport and thus high charge–discharge rate of Li-ion storage. Also, nanocomposites of anatase and metallic nanoparticles such as Au, Ag (166) Sn (167), or oxides such RuO_2 (168), can be applied.

Anatase TiO_2 has been prepared as nanosized particles either mesoscopic (169) or nanotubes (170,171), to reduce the length of Li diffusion which improves the

high-rate Li- ion storage performance and improves its cycling life due to minimized strain during Li- ion insertion/extraction (172–174).

1.4.4.2 TiO_2-(B)

TiO_2-(B) has attracted remarkable attention for its use as an attractive host for Li^+ intercalation. It exhibits a higher specific capacity than other polymorphs of TiO_2 (107,175,176), and has many other features, such as a lower operating potential (~1.55 vs. Li^+/Li) compared to anatase (~1.75 vs. Li^+/Li), a high power capability and good reversibility (177).

TiO_2-(B) has a relatively open crystal structure (178) which is ideal for the facile insertion/extraction of Li^+ and thus there are no complications noted in the Li insertion reaction mechanism, which is important for its use as an anode in Li-ion batteries. This monoclinic structure exhibits a unique feature characterised by parallel channels running along [010]. Experimental (107,175,176) and theoretical studies (179)(180)(181)(182) demonstrate that the parallel channels running along the *b*-axis in the [010] orientation is the favourable pathway for Li diffusion. Moreover, Zokalova et al. (161) reported that Li^+ diffusion in TiO_2-(B) is a pseudocapacitive faradaic process, which is faster than solid-state diffusion in anatase or rutile.

Storage devices using nanoscale TiO_2-(B) as an anode are reported by Armstrong et al.(175) and Guo et al. (183). TiO_2-(B) coupled with the olivine $LiFePO_4$ as the cathode shows a significantly improved rate capability and energy density which is nearly identical to that of $LiCoO_2$/ TiO_2 anatase, along with superior safety and inherent overcharge protection compared to graphite. However, the aggregation tendency of TiO_2-(B) nanomaterials leads to an increase in interparticle contact resistance and hence affects the performance at high discharge/charge rates (184).

A novel type of TiO_2-(B)@carbon composite nanowire with a core/shell architecture was synthesised by Yang et al. (185). The composite nanowire exhibits a high reversible capacity of 705 mAh/g after 10 cycles and 560 mAh/g after 100 cycles as well as an excellent rate capability. Although the capacity of the composite is very promising, the coulombic efficiency is low and the capacity loss upon cycling is quite high.

One drawback of TiO_2-(B) when employed as a host for Li-ion intercalation is related to its limited rate capability due to the poor electron transport. Usually, conducting additives can overcome this problem and improve the rate performance, but in TiO_2-(B), a large amount is required which consequently reduces the volumetric energy density of the TiO_2-(B) electrode (186). To improve the rate performance of the TiO_2-(B) electrode, mesoporous microspheres have been synthesized by Brown et al. (187). These porous microspheres of TiO_2-(B) with 12 nm pore size, offer a capacity of ~120 mAh/ g at the high current rate of 60C.

1.4.4.3 Rutile

In contrast to anatase and TiO_2-(B), in which the maximum electrochemical insertion of Li is about 0.5 and 0.71 Li- ions per TiO_2 unit respectively , Li insertion into bulk rutile is usually reported to be negligible (<0.1 Li per TiO_2 unit) at room temperature (188,189). This changed after Macklin and Neat (190) demonstrated successful insertion and extraction of lithium ions into bulk rutile at high temperature (120°C) using polymer electrolyte instead of liquid electrolyte. On the first discharge cycle, Li insertion up to 1.0 Li per TiO_2 rutile was achieved at 120°C. Also, a similar result has been reported with the very low current density of C/300 (i.e., one lithium ion per formula unit in 300 h) during the discharge process at room temperature, resulting in very low capacity (191). These results suggest that the insertion of Li^+ into rutile is thermodynamically favourable, and the difficulty of Li intercalation at room temperature is due to kinetic restrictions (191–193). The kinetic difficulty is linked to the solid-state diffusion of Li in intercalation electrodes. For the rutile phase, the tetragonal structure forms narrow channels along the [001] direction, as shown in Figure 1-5, owing to the edge-sharing connection along the *c* direction and corner-sharing connection in the *ab*- plane. Li ions prefer to occupy the oxygen octahedral vacancy (155); this involves the migration of Li ions through the tetrahedral site in the *ab*- plane (194). As a result of this special arrangement, Li^+ diffusion in rutile is highly limited by the *c*-channels and highly anisotropic, proceeding via fast diffusion along the *c* direction channels (approximately 10^{-6} cm^2s^{-1}), while in the *ab* planes Li diffusion is very slow (approximately 10^{-15} cm^2s^{-1}). The Li ion inserted in the *ab*- plane blocks the channels along the *c* direction by trapped Li ion pairs in the ab-plane along with the strong repulsive Li–Li interactions, hindering further insertion (158,195).

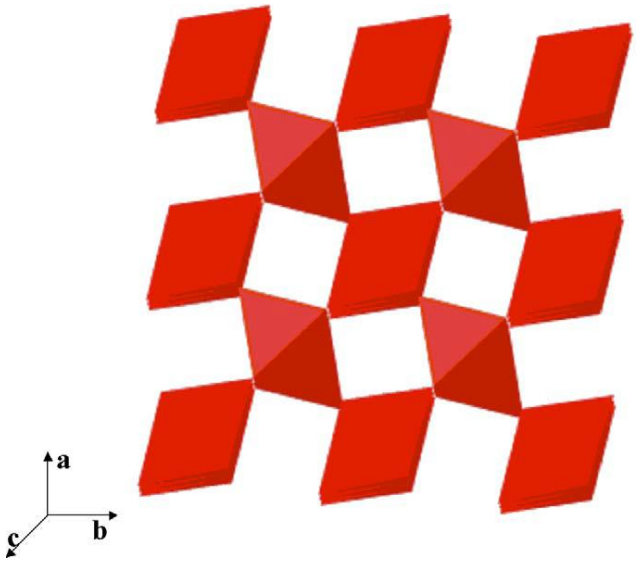

Figure 1-5: The crystal structure of rutile-TiO_2 along [001] direction, Adapted from Electrochemistry Communications, 8 /8, Reddy MA, Kishore MS, Pralong V, Caignaert V, Varadaraju U V., Raveau B., Room temperature synthesis and Li insertion into nanocrystalline rutile TiO_2, 1299–303, Copyright (2006), with permission from Elsevier (133).

One drawback however, is that rutile, as with all TiO_2 polymorphs, is known to suffer from poor lithium ionic and electronic conductivity in its bulk form which limits charge/discharge rates and hence the electrochemical performance of TiO_2 as an electrode material.

The main features of different Li insertion behaviour of TiO_2 polymorphs; rutile, anatase and TiO_2 (B) are summarized in Table 1-4.

Table 1-4: Electrochemical properties of various TiO_2 polymorphs.

Structure	Insertion Potential, V	Quantity of Li^+ intercalated, mole		Specific Capacity, mAh/g
		Bulk	Nano	
Rutile	1.5- 2.1	0.1	0.85	270
Anatase	1.7- 2.1	0.5	1.0	335
TiO_2-(B)	1.5- 2.0	0.71	1.0	305

1.4.5 Strategies to improve the electrochemical performance of rutile TiO_2

Rutile TiO_2 exhibits negligible lattice changes upon Li^+ intercalation and de-intercalation and this enhances the structural stability. However, drawbacks include the poor lithium and electronic conductivity in the bulk state and low specific capacity. Several strategies are employed to increase the ionic and electronic conductivity and thus improve the electrochemical performance of rutile TiO_2 including decreasing the crystallite size from the micro to the nanoscale, using additives such as carbon-based materials, generating a mixed valence by oxygen non-stoichiometry and also metal ion doping.

1.4.5.1 Nanostructured rutile

The lithium intercalation/de-intercalation process in all TiO_2 polymorphs depends typically on their structure, particle size, morphology, and surface area (194,196,197). Therefore, use of nanostructured TiO_2 is one approach to increasing the rate performance and achieving better energy storage capacity and longer cycling life than that of bulk materials (198–200). Nanostructured TiO_2 materials provide a large surface area which results in high electrode-electrolyte contact area and hence distributes the current density and increases the charge/discharge rate. Additionally, the nanomaterial provides short transport path lengths for electrons

and Li^+ which permit the use of materials with low ionic conductivity in the battery and minimizes strain during the insertion/extraction of Li^+ (174,201,202).

Nanostructured forms of TiO_2 in 1D and various morphologies including nanowires (203), nanotubes (204,205), nanorods (169,206), hollow nanospheres (207,208), and nanoribbons (205) , composites with carbon (209,210), tin (167,211), silicon (92), and also thin films (212,213) have been reported to show a higher capacity and much improved capacity retention and rate capability in comparison to bulk materials.

The first synthesized TiO_2 nanotubes from amorphous TiO_2 were reported in 1998. Since then, a lot of effort has been spent in the development of anode materials based on nanostructured TiO_2 in various particle morphologies.

Regarding the rutile form of TiO_2, the low lithium diffusion in the *ab*- plane is a key factor in improving the charge/ion transport properties and improving electrochemical properties. It is necessary to address this issue by fabricating nanostructured rutile with a small diameter in the *ab*- plane (191). Nanosized rutile (133,191,214,215) has been reported to show much improved electrochemical properties by decreasing the crystallite size from the micro to the nanoscale. Up to 0.85 moles of Li^+ can be inserted into nanosized rutile at room temperature in comparison with only 0.1–0.25 mol of Li into microsized rutile (214).

The difference in the behaviour of Li^+ insertion between micro and nanosized rutile was shown by Hu et al. in 2006 (191). Nanosized rutile with a needle-like shape has a diameter of ~5 nm corresponding to the *ab*- plane. This nanotructured material exhibits a reversible insertion of ~0.5 mol Li^+ per mol TiO_2 at room temperature. This insertion/extraction of ~0.5 mol Li^+ using nanosized rutile was confirmed by Reddy et al. (133). Hu et al. also suggested that up to ~ 0.15 Li is stored at the surface (191). In contrast, Wagemaker et al. demonstrated that a fraction of ~0.15 actually enters the rutile host structure, accompanied by a slight change in the lattice parameters (216).

Tarascon *et al.* demonstrated that the rutile nanoparticles (10 nm x 200 nm in size) can accommodate ~0.85 moles of Li^+ during the first reduction and 0.5 mole of Li is reversibly cycled with a capacity of 150 mA h/g after 60 cycles. The charge-discharge profile in **Figure 1-6** (a), suggests that the Li insertion occurs through two solid solution domains followed by irreversible phase transformation of electro-

active $LiTiO_2$ (rock-salt type) (214). These results are supported by in situ TEM investigation of the structural transformation of rutile nanowire (NW) in which a single-crystal rutile TiO_2 nanowire underwent electrochemical lithiation (217). The transformation of the NW rutile to a monoclinic non-reversible intermediate structure was observed in Li_xTiO_2 upon lithium insertion while upon full lithiation (~ 0.85) the transformation resulted in a rock-salt structure (Fm-3m), **Figure 1-6** (b).

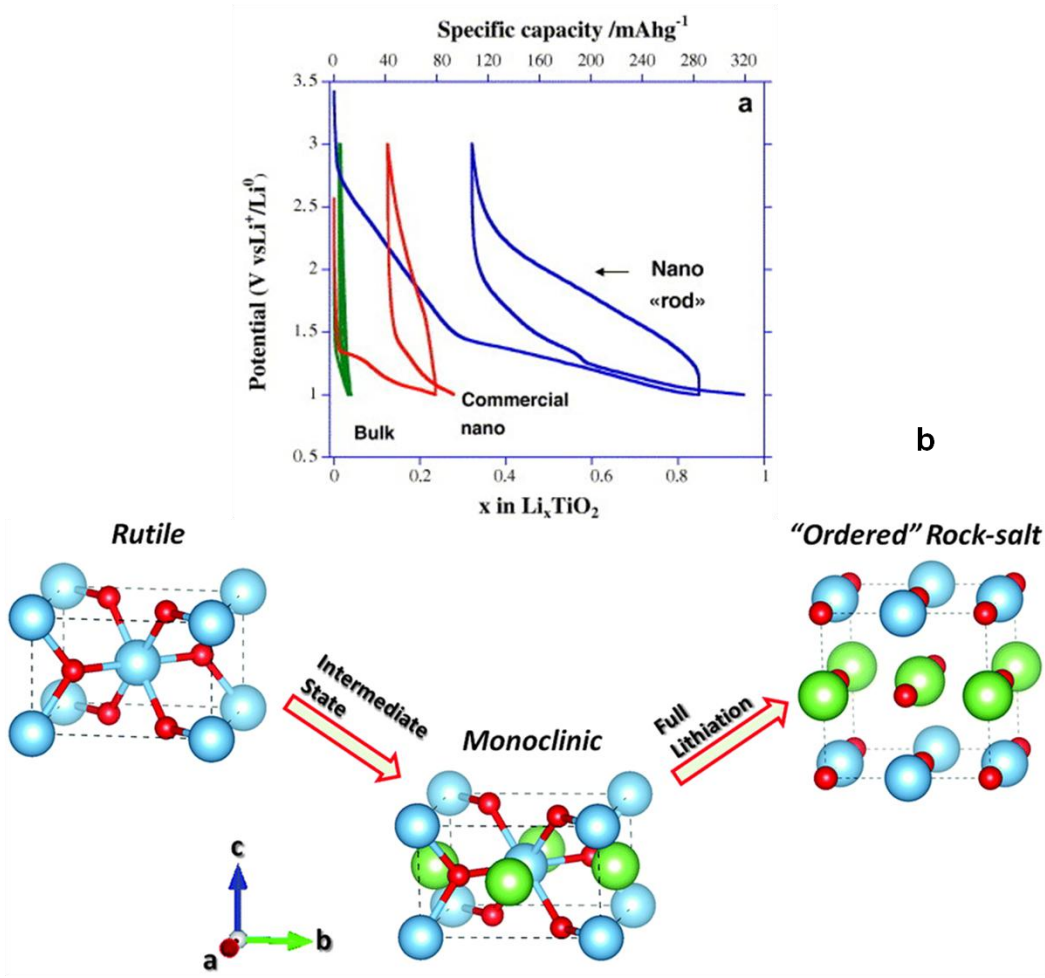

Figure 1-6: (a) Galvanostatic cycling curves of different rutile TiO_2 samples between 3 V and 1 V with rate 20 C, Adapted from Electrochemistry Communications, 9 /2, Baudrin E, Cassaignon S, Koelsch M, Jolivet JP, Dupont L, Tarascon JM., Structural evolution during the reaction of Li with nano-sized rutile type TiO_2 at room temperature, 337–42, Copyright (2007), with permission from Elsevier (214), (b) Schematics of structural transition of rutile Li_xTiO_2 from primitive tetragonal to a fully lithiated phase, adapted from (217) with permission of The Royal Society of Chemistry.

In contrast, Wagemaker et al. have argued that the fully lithiated form, Li_xTiO_2 (x=0.85), has a layered monoclinic structure similar to a hexagonal structure. This view is supported by structural investigation using neutron diffraction in which a needle-shaped nanocrystalline rutile (11 nm x 11 nm x 43 nm) was chemically lithiated, then the exact lithium position, maximum chemical intercalation fraction and phase transitions were determined (216). The results reveal that the Li^+ intercalation in the nanosized rutile occurs with two phase transitions, see Figure 1-7; with compositions up to x < 0.5, the phase transition is from the tetragonal rutile structure to the monoclinic P2/m space group. This intermediate phase is very similar to the tetragonal rutile structure, and is therefore referred to as P2/m(RUT). With a maximum composition of x = 0.85, and may be with the maximum theoretical composition x= 1.0, the phase transformation is from the monoclinic P2/m(RUT) structure to a layered monoclinic structure (P2/m space group). This layered structure is closely related to the hexagonal structure, hence it is referred to as P2/m(HEX) (216).

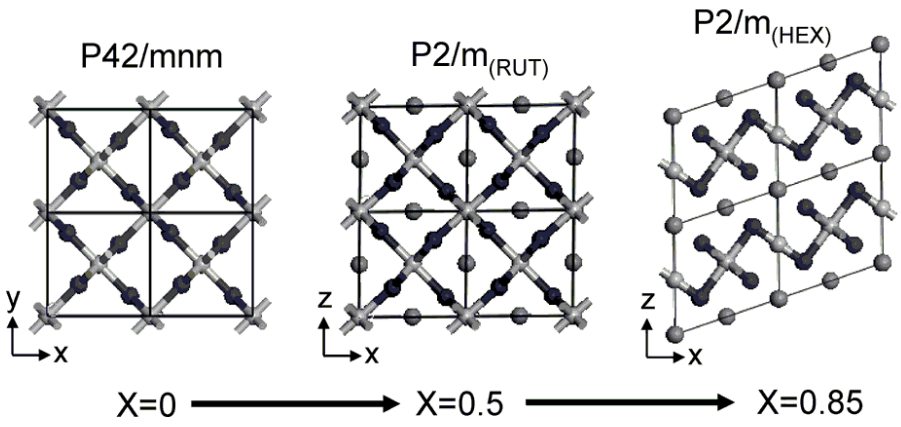

Figure 1-7: Structural evolution of nanoneedle rutile upon Li+ intercalation, where x indicates the composition (Li_xTiO_2). Adapted with permission from Chemistry of Materials, 20 /9, Borghols WJH, Wagemaker M, Lafont U, Kelder EM, Mulder FM, Impact of nanosizing on lithiated rutile TiO_2, 2949–55. Copyright (2008) American Chemical Society (216).

The dependence of Li insertion reactions on rutile particle size has been investigated by Zhou's team (171,215). Their results revealed progressively increasing Li capacity, and Li-ion solubility with decreasing particle size. By decreasing the particle size to 15 nm, a capacity of 378 mAh/ g was delivered at

first discharge and subsequent stable capacity of 200 mAh/ g corresponding to 0.6 Li per one molecule of rutile was observed over 20 cycles. However, with a particle size of 300 nm, a capacity of 110 mAh/ g was delivered at initial cycle then dropped to 50 mAh/ g at the 20^{th} cycle. These results suggest that the improvement in capacity and Li-ion intercalation are related to the nanosize characteristics. This finding was also confirmed by another group (202).

Wohlfahrt-Mehrens et al. reported on the electrochemical insertion of Li^+ in nanosized rutile prepared by sol–gel chemistry (154). Also, they demonstrated that extending the potential window of the rutile, which is typically 1-3 V, to potential windows of 0.5-3 V and 0.1-3 V results in an excellent reversible capacity of ~315 mAh/ g and a high rate capacity of ~196 mAh/ g at 5C. The cycling stability over 1000 cycles is excellent due to the good capacity retention (218).

Recently, Hassoun et al. (219) repeated the construction of a full-cell using nano rutile TiO_2 (~10 nm) as anode and the $LiFePO_4$ as cathode. It delivered a reversible capacity of ~150 mAh/ g with a potential window of 0.8- 3.8 V at room temperature with cyclability for 20 cycles.

Recently, the fabrication of rutile electrodes in the form of dandelion-like superstructures has been reported. Dandelion-like structures consist of numerous inter-aggregated single-crystalline nanorods of rutile; hence, this structure provides a larger specific surface area and the single-crystalline nanorod provides a stable structure and short path lengths for Li^+ diffusion and electronic transport, which improve the rate and cycle performances of the battery. Particularly, intensive research has been conducted to synthesise dandelion-like rutile superstructures. Dandelion-like rutile TiO_2 microspheres were synthesized for the first time by a hydrothermal method (220). Kim et al. reported the synthesis of dandelion-like rutile TiO_2 nanostructures through hydrolysis and demonstrated the best electrochemical performance (128 mAh/ g after 50 cycles) (221). Recently, Sun et al. synthesized novel dandelion-like rutile superstructures via a hydrolysis route (222) in which nanosized rutile rods (~6 nm) were grown along the *c*-axis, [001] direction, which facilitates the transport of lithium ions and electrons. The results from Sun et al. show that the synthesized rutile TiO_2 microspheres have a high reversible capacity of 242 mAh/g (~0.72 Li/Ti) and an excellent rate capability of 116mAh/ g at 20 C. Both groups reported that the dandelion-like rutile

superstructures exhibit good rate and cycle performances as anode materials of lithium ion batteries.

In general, the use of nanostructured materials as electrodes is more advantageous than bulk materials and nanostructuring is a well-recognized strategy for improving the capacity and cycling behaviour of TiO_2. However, the polarization increases by decreasing the crystallite size to the nanoscale. The large surface area of nanocrystalline materials increases the electrolyte-electrode contact area and leads to more side reactions with the electrolyte, resulting in a greater thickness of the solid electrolyte interface (SEI) layer than in the bulk TiO_2 and therefore hindering the transport of electrons and Li ions in and out of the rutile structure.

1.4.5.2 Nanosized rutile TiO_2 with additive carbon based materials

Nanosized TiO_2 with additives of graphene or reduced graphene oxides (RGO) seem to be the most promising tracks for improving the performance of LIBs.

A unique 3-D nano-structure of binder-free graphene–TiO_2 paper was achieved with nanosized TiO_2 intercalated between graphene layers (223). The flexible graphene/TiO_2 hybrid paper shows a significant increase in the rate of Li^+ insertion/extraction. At a current rate of 2 A/g, the specific capacity can reach 122 mAh/ g after 100 cycles and when the rates decrease to 200 mA/ g, the retained capacity of 175 mAh/ g is reached, which indicates an excellent stability.

TiO_2–RGO composites, of rutile TiO_2 nanoparticles on graphene nanosheets, could be promising candidate materials for high-power, low-cost and environmentally friendly anodes for lithium- ion batteries. The TiO_2-RGO nanocomposite prevents aggregation of TiO_2 nanoparticles and increases the electrical conductivity and mechanical stability of electrode materials in the presence of graphene nanosheets.

TiO_2–RGO composites are employed as anode materials for lithium-ion batteries, showing stable cyclic performance, large reversible capacity, and better rate capability, compared to pure TiO_2 and TiO_2-GO samples. These superior electrochemical performances can be attributed to the unique structure of TiO_2-RGO, in which the graphene network provides efficient pathways for electron transfer resulting in an increase in electrical conductivity. The TiO_2 nanoparticles

prevent the restacking of the graphene nanosheets resulting in an improvement in specific capacity (224).

Rutile TiO_2 nanobundles on reduced graphene oxides were synthesized through hydrothermal methods. The resulting RGO@TiO_2, as anode, shows an excellent stability with a reversible capacity of 300 mA h/ g at 0.6 C and 200 mA h/ g at 1.2 C after 500 cycles (225).

Rutile TiO_2 mesocrystals/reduced graphene oxide nanosheets (TGR) hybrids are fabricated via the in situ hydrothermal route. The cell made of TGR hybrids as anode material exhibits a large capacity over 150 mAh/ g at 20 C after 1000 cycles, and high rate capability up to 40 °C. These high performance characteristics may be attributed to the characteristics of TGR hybrids. Rutile TiO_2 mesocrystals with ultra-tiny rod-like nanoparticles and porous structure provide a short path for Li^+ transport which improves Li^+ intercalation into the rutile structure and also accommodates volume changes in the charge/discharge process. Both the rutile mesocrystals with pore structure and ultrathin RGO nanosheets provide a large surface area which increases the electrode/electrolyte contact area, leading to a higher charge/discharge rate. Reduced graphene oxide nanosheets also increase the electronic conductivity by enhancing the electron transport (226).

1.4.5.3 Generating a mixed valence by oxygen non-stoichiometry

This can be achieved either by doping with an anion such as N and/or F (227) or by quenching materials from high temperatures to produce $TiO_{2-\delta}$: δ =0.001 (228).

The Li-storage and electrochemical performance of (N,F)-co-doped-TiO_2 of composition, $TiO_{1.9}(N_{0.05}F_{0.15})$ has been reported (227). Compared to Li-cycling of rutile-TiO_2, nano-rutile-TiO_2 (N,F) exhibits an initial discharge capacity of 325 mAh/ g corresponding to ~1.0 mole of Li per mole of TiO_2(N,F)) with a reversible capacity of 210 mAh/ g (0.65 mole of Li) after the first cycle. However, slow capacity-fading is observed with a capacity-retention of 78% after 60 cycles. These results demonstrate that the electrochemical performance of TiO_2(N,F) is much better due to the presence of N^{3-} and F^- ions which are more electronegative than O^{2-} ions.

West et al. (228) demonstrated that the quenching of rutile from temperatures ≥ 1400°C leads to a significant improvement of the electrical conductivity of rutile

TiO_2. However, there are no reports on the electrochemical performance of Q-TiO_2, ($TiO_{2-\delta}$) in the literature.

1.4.5.4 Doping with aliovalent ions

One effective way to improve the conductivity and hence the electrochemical properties is by doping, as the presence of aliovalent ions affects electrical conductivity. Doping TiO_2 with transition metals has been reported to induce lattice expansion (229–231) and electrical conductivity.

There have been many studies of the electrochemical properties of TiO_2, both experimental and theoretical, especially if the TiO_2 is formed as a nanomaterial (134,158,191,214).

The substitutional doping of nano-sized TiO_2 with various cations (Nb, C) has been reported (209,232). In contrast, there are no experimental investigations of the effect of doping on the electrochemical performance of bulk rutile.

Boron-doped rutile submicrosphere TiO_2 (233) has been reported as an anode in lithium-ion batteries. It exhibits an excellent cycling performance and rate capability in comparison with undoped rutile with a stable capacity of ~190 mAh/ g for 500 cycles at 1C. Boron dopant with low concentration (<1.0 at %) could enhance the carrier mobility and electrical conductivity as demonstrated by the density functional theory (DFT) calculations.

Recently, Nb-doped rutile ($Ti_{1-x}Nb_xO_2$) was successfully synthesised by the sol−gel method with a particle size of 10−50 nm (234). Yoshioka et al. demonstrated that Nb-doped rutile is an attractive candidate as a Na-ion battery anode as well as a Li-ion battery anode. As the LIB anode, it shows an excellent rate capability with a capacity of 120 mAh/ g even at the high rate charge/discharge of 50C.

1.4.6 Challenges and outlook for TiO_2 polymorphs

Among the TiO_2 polymorphs, rutile, anatase, and TiO_2-(B) have been reported for lithium electrochemical reactivity. Even though anatase has been considered the most electro-active form, other polymorphs; rutile and TiO_2-(B), have also been widely investigated as insertion anodes (112,194,215).

For anatase, much effort has been spent on improving the electronic conductivity and various approaches for improvement of electron transport and high-rate performance were adapted, such as introducing a second conductive phase with carbon-based materials or as part of a composite with nanoparticle metals. However, apart from the academic interest, there is no scope for the development of anatase for practical applications, due to its poor rate performance and reversibility (only 0.5 mole of Li is reversible). By contrast, TiO_2- (B) exhibited more favourable electrochemical properties than anatase (152) and spinel LTO anodes (175,183). The excellent performance of TiO_2-(B) at high current rates make it a promising insertion host for high energy and high power Li-ion batteries used for zero emission transportation, such as EVs and HEVs. However, an important drawback hindering the usage of TiO_2-(B) is its capacity fading which must be addressed before achieving commercial applications. Low-temperature surface modification and composite preparation with carbonaceous materials have been used for enhancement of electronic conductivity. In addition, many studies focus on investigating the performance of TiO_2-(B) in 1D nanostructured components due to their exceptional performance, irrespective of the cathode or anode used. The exceptional performance of TiO_2-(B) makes it one of the most important and promising insertion hosts among the TiO_2 polymorphs in particular for the development of high power and high energy density Li-ion batteries.

Despite encouraging results (214,216,222), poor electrochemical activity of rutile leads to its elimination from possible practical applications as anode in LIBs. Further research is needed to improve the electrochemical activity of rutile.

Both TiO_2-(B) and rutile in their nanostructured forms are under extensive investigation as promising insertion anodes with varied morphological features and as composites with several carbon-based materials.

1.5 Aims and thesis layout

Carbon-based materials are used as standard anodes in commercial Li-ion batteries. At low potentials, Li plating on the carbon surface and growth of passivation layers restrict the full utilization of reversible insertion/de-insertion and limits the use of carbon-based materials in Li-ion batteries due to low discharge rate capability and safety considerations. There is therefore a need to seek new material concepts and suitable electrodes to satisfy the increasing demands for energy storage worldwide.

Rutile TiO_2, as described in section 1.4, is a very promising anode material because it has a low-voltage insertion of Li and high theoretical specific capacity. However, it suffers from a poor Li ionic and electronic conductivity. Li insertion into bulk rutile is negligible at room temperature due to the dense close packing of the structure of rutile and narrow pathway of Li ion diffusion.

The main objective of this PhD project is to investigate different ways to modify structure and properties of rutile. This falls in two groups: First, enhance electronic conductivity by quenching from high temperature and second, induce lattice expansion by doping; two groups of materials have been studied; Ti^{4+} is (i) partially replaced by Sn^{4+} and (ii) double-doped with a combination of divalent (Cu^{2+}) and pentavalent ions (Nb^{5+} and Ta^{5+}). The objective of increasing the unit cell dimensions of rutile by doping is based on the hypothesis that insertion of rutile Li into TiO_2 would be easier with an expanded unit cell. In addition, dopants may modify the electrical conductivity of rutile.

This PhD project aims at addressing specific areas:

1) Develop an anode material that is able to intercalate lithium reversibly with a high capacity and long life.
2) Investigate the electrochemical performance of reduced rutile-$TiO_{2-\delta}$;
3) Induce lattice expansion with doping; and
4) Investigate the doping influence on the electrochemical performance of rutile-TiO_2 and

5) Investigate the the electrical properties of doped-rutile.

In this work, compositional modification, in particular the substitution of Ti^{4+} by different valence metal ions was tested. Solid solutions were prepared where Ti^{4+} is (i) partially replaced by Sn^{4+} and (ii) double-doped with a combination of divalent (Cu^{2+}) and pentavalent ions (Nb^{5+} and Ta^{5+}). The doping effect on the electrical properties and electrochemical performance was investigated.

The work is presented in eight chapters.

Chapter one contains a comprehensive background on LIB science and literature review.

Chapter two describes the experimental procedures employed to synthesise and characterize the samples.

Chapter three reports on the electrochemical characterization of rutile TiO_2 before and after quenching.

Chapter four studies the effect of TiO_2 starting material on the electrochemical performance of LTO.

Chapters five and six deal with synthesis, electrochemical performance and electrical behaviour of $Cu_xM_{2x}Ti_{1-3x}O_2$; M=Nb^{5+}, Ta^{5+}.

Chapter seven introduces the electrical and electrochemical behaviour of Sn-doped rutile TiO_2.

Chapter eight presents the summary of this research work and the major conclusions; suggestions for further investigation are also presented.

2. EXPERIMENTAL PROCEDURE

The main experimental analysis techniques used in this thesis are described which include: solid solution (SS) methods of sample preparation; x-ray diffraction (XRD); scanning electron microscopy (SEM); cyclic voltammetry (CV); Galvanostatic cycling with potential limitation (GCPL) and impedance spectroscopy (IS). In addition to a review of relevant techniques, descriptions of specific methods developed for this work are included.

2.1 Materials synthesis

2.1.1 Sn-doped TiO_2

Sn-doped-rutile, TiO_2 with selected compositions given by the general formula $Sn_xTi_{1-x}O_2$ ($0 \leq x \leq 0.2$) and ($0.80 \geq x \leq 1.0$) were synthesised by conventional solid state reaction (SSR). The reagents were dried at specific temperature, Table 2-1. Reagents were weighed in the desired ratio, mixed and ground using an agate mortar and pestle in an acetone slurry, dried, pelleted, transferred to an alumina crucible and fired in a muffle furnace at 1200°C for 72 hours and then quenched by rapid cooling to avoid spinodal decomposition that can occur during slow cooling. The samples were quenched by removal from the furnace at 1200°C into air followed by cooling on a brass metal disc (235) and phase identification results monitored by XRD.

2.1.2 Cu-M doped TiO_2, M= Nb and Ta

Compositions of formula: $Cu_xTa_{2x}Ti_{1-3x}O_2$ with x=0.05, 0.10, 0.12 and 0.15 and $Cu_xNb_{2x}Ti_{1-3x}O_2$ with x=0.05, 0.10, 0.15 and 0.20; were synthesised. All the chemical reagents were obtained from Sigma-Aldrich and dried overnight at a specific temperature, Table 2-1. The desired amounts of the reagents were mixed and ground using an agate mortar and pestle in acetone media. The slurry was dried then calcined in Pt boats at 935°C (236) for 2-3 days with intermittent grinding; the results were monitored by XRD.

Table 2-1: Drying temperature and purity of reagents.

Reagent	Drying Temperature, °C	Purity, %
Rutile TiO_2	900	99.9
SnO_2	1100	99.9
CuO	700	99.0
Nb_2O_5	900	99.9
Ta_2O_5	900	99.8

2.2 Structural characterization

2.2.1 Powder X-ray diffraction

Powder X-Ray Diffraction (XRD) is one of the most versatile techniques available for phase determination structural characterization. The position (*d*- spacing) and intensities of reflections in the diffraction pattern provides a fingerprint for most crystalline solids (237). This technique is useful to identify new or unknown materials as each crystalline solid has a unique X-ray diffraction pattern. It is also used to analyse the phase purity of known materials. XRD can provide additional information about unit cell type, space group, lattice parameters, type and distribution of atom in the crystal structure, crystallite size and microstrain.

2.2.2 XRD Principle and Bragg's Law

In an XRD experiment, an X-ray beam is reflected from repeating lattice planes of atoms in a crystalline structure when the wavelengths of the scattered X-rays interfere constructively. Constructive interference is at a maximum when the differences in the travel path are equal to integral multiples of the wavelength. When this occurs, a diffracted beam of X-rays will leave the crystal at an angle equal to that of the incident beam and the intensity of the reflected beam is measured by a detector (237,238).

The reflection from two layers of a sample is shown schematically in Figure 2-1, where the path difference between the two reflected x-rays is $2d \sin \theta$. The position of the diffracted beam depends on the wavelengths of the incident X-rays and

spacing between the crystal lattice planes of atoms and the general relationship between them is known as Bragg's Law and expressed as:

$$n\lambda = 2d\sin\theta \qquad (1)$$

where n is any integer,

λ is the wavelength of the incident X-rays

d is the inter-planar spacing, and

θ is the diffraction angle

Peaks appear in the diffraction pattern at certain 2θ values from which *d*-spacings can be calculated. The *d*- spacings of the observed peaks are related to the size and shape of the unit cell while the intensities of the peaks are related to the atomic arrangement within the unit cell. Furthermore, the number of observed peaks is related to the symmetry of the unit cell. The sharpness of the peaks is a sign of the degree of ordering of the crystal structure while very broad peaks are a sign of disordered or less crystalline regions such as amorphous regions within the sample.

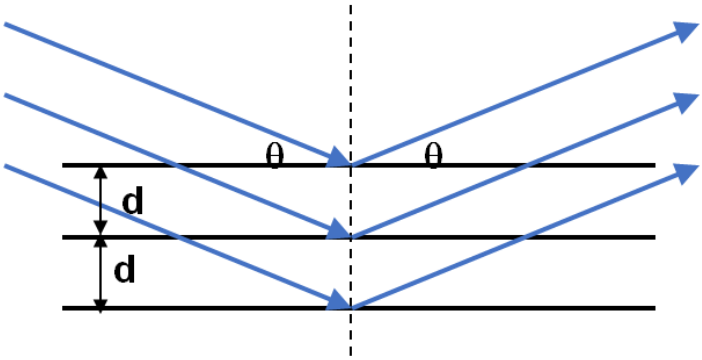

Figure 2-1: X-ray reflection from different parallel planes in the structure and derivation of Bragg's Law of diffraction.

2.2.3 Experimental

The XRD technique was used for phase analysis and lattice parameter measurements. The diffraction patterns were recorded using a STOE STADI P diffractometer (239) with position sensitive detector (PSD) and Mo Kα radiation (λ=0.7093 Å). The angular scan range was 5° ~ 40° 2θ with step size 0.1°. The sample holder was rotated to avoid preferred orientation effects. Accurate 2θ values were obtained by an angular correction using either external or internal silicon standard. The reasons for the use of Mo-$K_{\alpha 1}$ radiation over Cu radiation are

high intensity and less absorption in the case of titanium containing samples. A small amount of sample powder was ground and glued in between the centre of two circular acetate films, dried and placed in the circular holder. The sample holder was inserted in the rotation stage of the diffractometer system. In the case of the electrochemically treated samples, the powder was inserted between the two acetate films inside an argon-box and sealed temporarily and tightly to prevent any contact with atmospheric air and moisture before taking out.

Collected data were processed using the WinXPOW software package version 1.06 (239,240). Phase analysis was determined by comparing diffraction data against a database maintained by the International Centre for Diffraction Data (ICDD) and the lattice parameters were calculated.

2.2.4 Crystallite size

Different methods can be use to estimate the crystallite size and strain such as; Scherrer equation (average size, neglects strain) and integral breadth method (provide average values of size and strain)(238).

2.2.4.1 Scherrer equation

The particle size (D) can be estimated from the broadening of the X-ray diffraction peaks using the Scherrer equation (241):

$$D = \frac{K\lambda}{FWHM \cos\theta} \qquad (2)$$

where K = Scherrer constant,

FWHM = full width at half maximum of the reflection peak,

λ = wavelength of x-rays, and

θ = diffraction angle of x-rays

The Scherrer constant (K) depends on the shape of the particle and is generally taken to have the value 0.9 but K actually varies in the range 0.62 ~ 2.08 (242). The position of the highest intensity peak can be determined, along with the width of this peak at half maximum, and the d-spacing. The Scherrer equation gives a rough estimate of particle size and the size obtained yields the average particle-size for a material. The Scherrer equation may give an unreliable value of

crystallite size due to the fact that it does not take into account the effect of lattice strain and instrumental factors on peak broadening.

2.2.4.2 Integral breadth

The integrated intensity of diffraction peaks can be measured as the ratio of area under a peak to the maximum height of the peak.

In the Scherrer equation, FWHM of the diffraction peak is considered in the calculation while the microstrain, which can induce a greater broadening in the diffraction peak, is neglected. To overcome this limitation, the integral breadth was suggested to be used along with Scherrer equation to reduce large errors in crystallite size estimation.

In this work, crystallite size was determined from peak widths using the ‘Size/Strain' option in the WinXPOW software using the integral breadth as a measure of the peak width (240). The contribution of peak width from the instrument was corrected by using a standard material without peak broadening.

2.3 Microstructural characterization

Scanning Electron Microscopy (SEM) is an invaluable technique for revealing and analysing the microstructure, morphology and chemical composition of a solid sample. The object is viewed by scanning a beam of electrons across the surface and collecting the various signals that are produced, which are used to form the image and to analyse the composition. The images appear in shades of grey, are very clear and emphasise features of interest.

Samples were pelleted and sintered at a temperature 100°C higher than the calcining temperature. The pellet was ground on SiC paper with 400, 800 and 1200 grit and then polished using 6, 3 and 1 μm diamond polishing paste. The pellet after cleaning in acetone was thermally etched at a temperature 10% below its sintering temperature for 30 min. The pellet was mounted onto a conductive carbon tape and attached to a SEM pin stub. A conducting gold layer was sputtered onto the surface. The pellet was mounted on a specimen holder and the chamber evacuated to record images. The spot size was varied to obtain better images. The grain morphology, size, and secondary phases were examined for polished and

thermally etched surface microstructures by SEM using a Jeol, model 6400 (Tokyo, Japan) operating with an acceleration voltage of 20 kV and a varying spot size depending on the size of the features under investigation (243).

2.4 Electrochemical properties

A few points have to be explained as the electrochemical measurement involved electrode preparation and cell assembly in addition to the instrumentation and the measurement techniques.

2.4.1 Electrochemical cell

The electrochemical investigations were performed using two electrode electrochemical cells. Coin cells, standard CR2325, supplied by National Council Research of Canada (NRC) were used during this work. For ex-situ studies, a Swagelok- type cell was used.

Coin cells consist of several hardware parts: negative cup (bottom cap), separator, spacer, spring, plastic insulation ring and positive metal casing (top cap), Fig. 2.

Separators were used for isolating the working and counter electrodes and acted as a medium of ionic transport. A porous membrane of polypropylene (Celgard 3501, Celgard) was used in this work as a separator. Always, two pieces were used to avoid any short-circuit between anode and cathode in the cells.

2.4.2 Electrode preparation

The working electrode was prepared as a blend of active material (as-synthesized) with a carbon black conductive additive, to enhance the electronic conductivity, and polyvinylidene fluoride (PVdF) as a binder in the ratio 70:25:5 wt % respectively. The mixture was shapped into a 10 mm diameter pellet by pressing with 1 ton of pressure and then dried at 120°C for 12 h in a vacuum oven at 0.5 bars. The disks were transferred into a glove-box filled with argon (Ar) to avoid any adsorption of atmospheric moisture.

Metallic lithium (high purity lithium foil, 0.38 mm thick and 23 mm width, supplied by Aldrich) was used as the counter reference electrode. A circular piece of lithium about 12 mm diameter was cut from the ribbon and placed in the bottom cap of the coin cell.

The electrolyte solution used in this work was 1 M $LiPF_6$ in PC (Sigma- Aldrich). The electrolyte preparation was performed in a glove-box by dissolving the lithium salt in propylene carbonate (PC) and the mixture stirred over-night using a magnetic bar.

2.4.3 Cell construction

Coin cells were assembled inside the glove-box in the specific sequence as shown in Figure 2-2. The coin cells were sealed tightly (crimped) using pneumatic pressure of 150 psi of Ar gas and then used for the electrochemical studies. More precaution was required during coin cell construction to prevent any short-circuit between the cell parts.

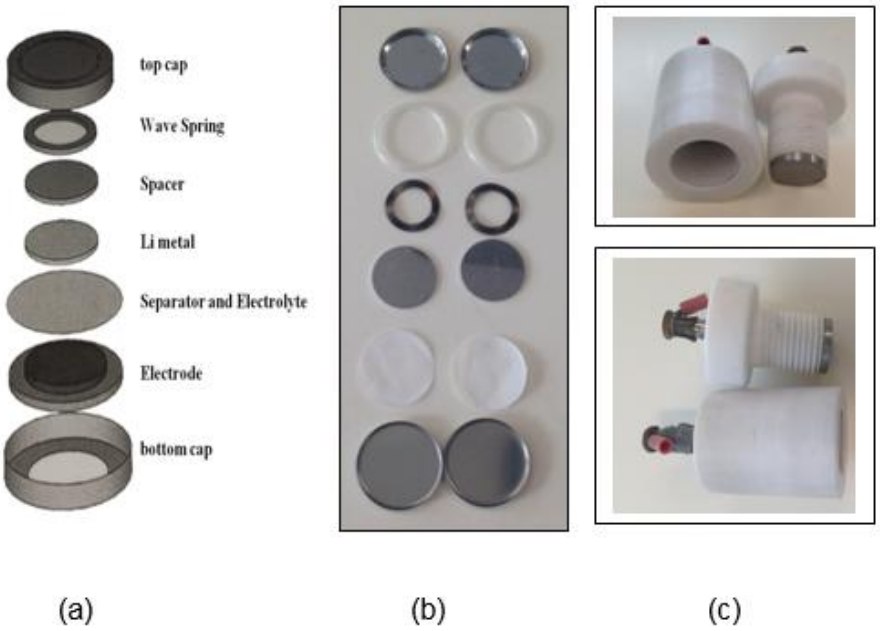

Figure 2-2: (a) Schematic representation of coin cell hardware, (b) Photograph of the parts of coin cell and (c) Photograph of the Swagelok-type cell

2.4.4 Instrumentation

The electrochemical performance was evaluated using a Variable Multichannel potentiostat VMP (Perkin Elmer Instruments, USA) which used the EC-Lab software. EC-Lab software is used to monitor a VMP and also used to process the resulting data (244).

2.4.5 Techniques of electrochemical measurements

2.4.5.1 Cyclic voltammetry (CV)

Cyclic voltammetry (CV) is used to determine the redox potentials of the electro active species in a material. It provides qualitative information about electrochemical reaction and also quantitative information about reaction kinetics and electron- transfer reactions (245). A cyclic voltammetry experiment is performed first using a wide voltage range to study the redox behaviour and obtain the electrochemical activity potential regions and then used as a potential limit for the GCPL cycling.

A typical cyclic voltammogram presents the current at the working electrode versus the applied voltage. It displays an oxidation peak/s during the anodic scan and reduction peak/s during the reversed scan in every cycle of the CV curves. The anodic and cathodic peaks are located at a specific potential relative to the electro-active species. The positions of the reduction and oxidation peaks are consistent with lithium ion insertion and extraction, respectively.

The shape of peaks provides information about the mechanism of lithium insertion and extraction in a material. A sharp peak at constant potential, independent of the C-rate indicates a mechanism involving phase transitions. When the peak shape and potential location depend on the C-rate, this may be due to a kinetic effect. Broad peaks can be usually attributed to irreversible processes of lithium extraction and insertion including solid-solution formation. Completely irreversible processes are accompanied by a shift of the peak potential with scan rate (245,246).

2.4.5.2 Galvanostatic cycling with potential limitation (GCPL)

Galvanostatic cycling with potential limitation (GCPL) tests were carried out at a constant current density and the variation in cell potential with time recorded within a selected potential window. The main advantage of the GCPL technique is that with constant current density, the electrode processes are investigated under real battery working conditions. GCPL is usually used to measure the charge-discharge capacity of a cell at a certain C-rate, where 1C is defined as the rate required for intercalating /de-intercalating one lithium ion in one hour.

2.4.6 Cell operation

After assembly, the coin cells were stored at room temperature for 10 hrs to ensure they reached equilibrium at open circuit voltage (OCV). Galvanostatic discharge-charge cycling was carried out at constant current at room temperature using the VMP electrochemical workstation with C/20 rate, i.e. 1 lithium ion de (intercalation) in 20 hours. For most of the experiments, the typical TiO_2 cut- off voltage, 1.0- 3.0 V was used. But in some cases the cells were operated at 0.5- 4.0 V. Cyclic voltammograms were recorded between 3.0 and 1.0 V with a scan rate of 0.01 mV/ s. All potentials in this study were measured vs. lithium.

2.4.7 Ex situ XRD studies of electrode

In order to investigate the XRD patterns and monitor any change in crystal structure of the electrodes during battery cycling, a Swagelok cell was used and run under the same conditions as coin cells; cut- off voltage, 1.0- 3.0 V at C/20 rate. After cycling, the cell was opened in the glove- box, the electrode was washed using anhydrous dimethyl carbonate (DMC), and then the powder was left to dry. A small amount of sample powder was loaded between two acetate films and sealed tightly to prevent any contact with air and moisture before taking out. The XRD patterns were recorded using a STOE STADI P diffractometer with PSD detector and Mo Kα radiation (λ=0.7093 Å). The data were collected between 5° and 40° 2θ with step size 0.1°.

2.5 Electrical property measurements

Impedance spectroscopy (IS) is a technique that is used to characterise the electrical properties and microstructure of electro-ceramics (247). It is useful to determine electrical inhomogeneities in ceramic materials in order to distinguish the different electrical regions: bulk, grain boundary and surface layer.

2.5.1 Sample Preparation

IS measurements were performed on samples in the form of pellets 5-8 mm in diameter and 1-2 mm in height. Pellets were pressed uniaxially at 2 tonnes for one minute, then a cold isostatic press (CIP) at 30,000 psi was applied for some materials; pellets were sintered at a specific temperature. Sintered pellets were polished on SiC paper with 800 and 1200 grit to remove the surface layers that

may contaminate or oxidize during the sintering process. The pellet diameter and thickness were measured using a micrometer screwgauge and the data used to calculate the geometric factor:

$$Gf = \frac{\mathrm{l}}{A} \qquad (3)$$

where, l is the thickness of the pellet in cm and *A* the pellet area in cm^2. The value of the geometric factor was used to correct the collected data for sample geometry. Therfore, all Z*,Z′, Z″ unites are Ωcm and all C values are Fcm^{-1}.

The pellet weight was measured to determine the material density by a geometric method using the equation:

$$\rho_{bulk} = \frac{m}{v} \qquad (4)$$

where, ρ_{bulk} is density of the sample, m is the mass of the pellet and *v* its volume.

The X-ray density (theoretical density) was calculated using standard relation:

$$\rho_{th} = \frac{MW * Z}{V * N_A} \qquad (5)$$

where, ρ_{th} is the theoretical density, *MW* is the formula weight, *Z* is the number of formula units in the unit cell, *V* is the unit cell volume in cm^3 and N_A is the Avogadro constant. The difference between the X-ray density and measured density gives the percentage density of the pellet, % ρ.

In this work, various types of electrodes were applied onto the pellets by different methods: sputtering and painting. Gold (Au) or platinum (Pt) were sputter-deposited as a thin film onto opposite sides of a pellet under vacuum with argon gas. For painted electrodes, opposite sides of pellets were coated with; Au, In-Ga or Pt. To decompose the organic solvent in the Au, Pt paste and stabilise the electrode contact, the coated pellets were gradually heated to 800°C for 2 hrs for Au and 900°C for 1 hour for Pt (248).

The pellet was attached to a ‘spaghetti’ measuring jig and placed inside a small tube furnace. For measurements in different atmospheres than air such as oxygen (O_2) or nitrogen (N_2), the jig was inserted inside a silica glass tube.

2.5.2 Instrumentation

Impedance spectroscopy was performed at low temperature, 10-320 K, by an Agilent E4980A with Intelligent Temperature Controller (ITC 503S). The pellet was placed between two sheets of gold in a cryocooler under a vacuum.

Impedance data at high temperature were collected using either an Agilent 4294A analyzer or a Hewlett Packard HP 4192A analyser over the frequency range 40 Hz to 1 MHz with an applied AC voltage amplitude of 100 mV and a DC bias of between 0 and 10 V at different temperatures. The exact temperature of the pellet was measured using a thermocouple. Data management and analysis was performed using the ZView software (Scribner Associates). Impedance data were corrected for overall pellet geometry but not for blank capacitance of the conductivity jig. Conductivity and capacitance data are reported in units of Scm^{-1} and Fcm^{-1}, respectively, that refer to correction for only the overall sample geometry.

2.5.3 Data Analysis

The frequency dependence of the electrical properties of a material can be expressed using four interrelated formalisms; impedance, Z*, admittance, Y*, electric modulus, M*, and permittivity, ε^* (249,250).

$$Y^* = (Z^*)^{-1} \quad (6)$$

$$Y^* = j\omega C_0 \varepsilon^* \quad (7)$$

$$M^* = j\omega C_0 Z^* \quad (8)$$

$$\varepsilon^* = (M^*)^{-1} \quad (9)$$

$j = \sqrt{-1}$, $\omega = 2\pi f$ is the angular frequency, $C_0 = \varepsilon_0 A l^{-1}$ in which C_0 is the vacuum capacitance of cell without sample, ε_0 is the permittivity of free space, 8.85×10^{-12} farad per meter (F/m), *A* and l are the area and thickness of the sample (251).

The impedance data can be analysed by an equivalent circuit consisting typically of two elements: resistance R and capacitance C, connected in parallel. The electrical response of each parallel RC gives rise to a semicircle in the complex plane.

For an RC element, the relaxation time or time constant (τ) and the complex impedance (Z*) are given by:

$$\tau = RC \quad (10)$$

$$Z^* = \frac{R}{1+(\omega RC)^2} R - jR\left[\frac{\omega RC}{1+(\omega RC)^2}\right] = Z' - jZ'' \quad (11)$$

R and C values can be extracted from the impedance complex plane as R is obtained from the intercept of the semicircular arc on the real axis (Z′) and C value from the maximum of semicircle $\omega_{max}RC = 1$ (247).

The impedance data can be presented in a variety plots which are constructed using the above formalisms and different information can be obtained (252). The impedance complex plane is commonly used as the impedance Z* can be separated into real and imaginary impedance and the imaginary Z″ (capacitive) plotted against the real Z′ (resistive component). Responses are ideally seen as semicircles.

Crystalline solids generally consist of grains separated by boundaries. The grain response is different from grain boundary response. The overall electrical responses can be expressed by an equivalent circuit consisting of two parallel RC elements connected in series. Frequently, a third element is necessary to model the impedance of the sample having electrode-interface. The impedance complex plane in this case contains two semicircles with different relaxation times giving rise to separate arcs. An ideal impedance complex plane plot is shown in Figure 2-3 in which the response of grain and the grain boundary are totally separated.

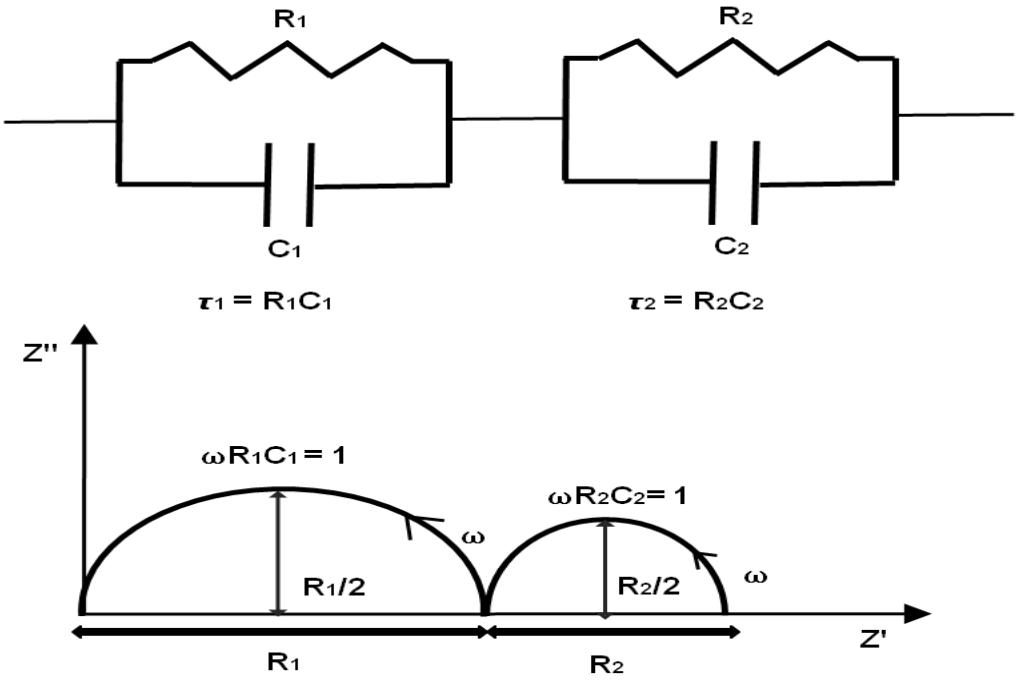

Figure 2-3: Impedance complex plane plot for an ideal electro-ceramic, in inset ideal equivalent circuit.

Different electrical region of a ceramics can be elucidated from the capacitance values.

This is useful for studying ceramics with overlapping responses such as grain boundaries, surface layers and non-ohmic electrode contacts.

Table 2-2: Regions responsible for observed capacitances based on BLM (247,253).

Capacitance/Fcm^{-1}	Phenomenon responsible
10^{-12}	Bulk
10^{-11}	Minor, second phase
10^{-11} – 10^{-8}	Grain boundary
10^{-9} – 10^{-7}	Surface layer
10^{-7} – 10^{-5}	Sample-electrode interactions
10^{-4}	Electrochemical reaction

The impedance measurement is carried out at different temperature. The conductivity usually increases as the temperature rises and so the temperature dependence of conductivity can be used to determine the activation energy. Activation energies were calculated from the gradient of an Arrhenius plot, in which the log of 1/R is plotted against 1000/T.

Arrhenius equation:

$$\sigma = A \exp(-E_a/KT) \qquad (12)$$

where, σ is the conductivity, A is the pre-exponential factor, E_a is the activation energy for conduction (eV), T is the temperature (K) and k is Boltzmann's constant (8.6173×10^{-5} eV K^{-1}).

3. ELECTROCHEMICAL CHARACTERISATION OF RUTILE TiO_2 AND OXYGEN-DEFICIENT $TiO_{2-\delta}$

3.1 Introduction

TiO_2 has four main polymorphs, rutile ($P4_2/mnm$), anatase ($I4_1/amd$), TiO_2 (B) ($C2/m$) and brookite ($Pbca$) (108,109). Under standard conditions, rutile is the most stable structure of TiO_2, and also the most available in natural form. The electrochemical behaviour of TiO_2 polymorphs as lithium battery anodes is variable: anatase and TiO_2 (B) are the most active and can accommodate more Li^+ ions compared to bulk rutile, which can be considered as inert towards lithium intercalation. Thus, in contrast to anatase, in which the maximum electrochemical insertion of Li^+ is about 0.5 Li ions per TiO_2 unit (132,158,254), Li insertion into rutile is usually reported to be negligible ($<$0.1 Li per TiO_2 unit) at room temperature (188–190,255). There are a few reports on increased electroactivity of rutile at high temperature (120°C) using polymer electrolyte instead of liquid electrolyte. On the first discharge, Li insertion up to 1.0 Li per TiO_2 rutile can be achieved at 120°C. Also, a similar result has been reported with a very low current density of C/300 (i.e. one lithium per formula unit in 300 h) during the discharge process at room temperature. This suggests that Li^+ insertion into rutile is thermodynamically favourable, and the difficulty of Li intercalation at room temperature is due to kinetic restrictions (190–193). The kinetic difficulty associated with intercalation and deintercalation processes is linked to the solid-state diffusion of Li.

Li insertion into/ extraction from rutile is highly anisotropic, proceeding via fast diffusion along the *c* direction channels (approximately 10^{-6} cm^2 s^{-1}), while in the *ab* planes, Li diffusion is very slow (approximately 10^{-15} cm^2 s^{-1}). The Li ion inserted in the *ab* plane at low concentration blocks the channels along the *c* direction, thus hindering further insertion (158,256). The crystal structure of tetragonal rutile, built up of TiO_6 octahedra, exhibits edge-sharing along the *c* direction and corner- sharing in the *ab* plane forming narrow channels along the [001] direction, as shown in Figure 3-1. Li^+ ions prefer to occupy the vacant octahedral sites; this involves the migration of Li ions through the tetrahedral site in the *ab* plane.

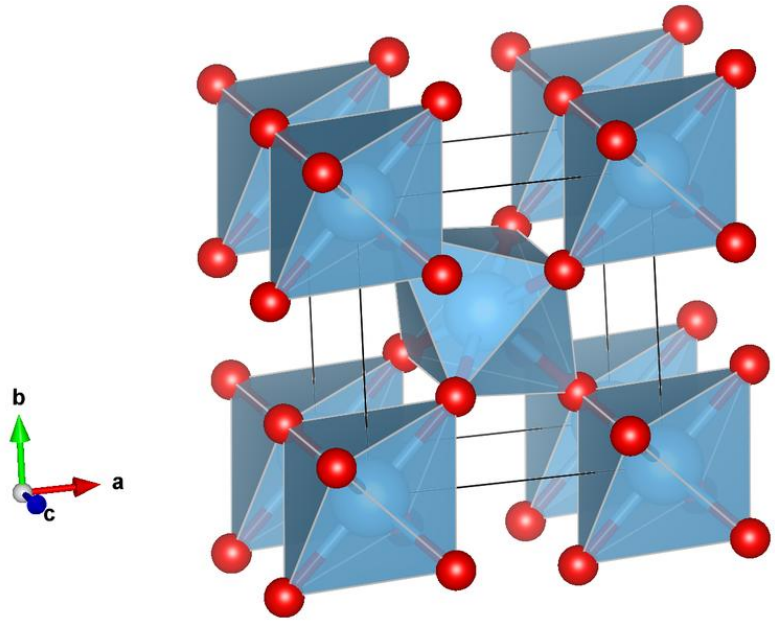

Figure 3-1: The crystal structure of rutile-TiO_2,from METADISE using VESTA from Ref. (257).

The electrochemical process of lithium insertion into/ extraction from TiO_2 rutile can be described by the following reversible electrochemical reaction:

$$TiO_2 + x\ Li^+ + x\ e^- \leftrightarrow Li_xTiO_2 \qquad (0 \leq x \leq 1) \qquad (1)$$

The redox reaction occurs at 1.5-1.8 V vs. Li/Li^+ which is above the reduction potential of electrolyte solvent; thus it could avoid the formation of SEI at the interface and makes TiO_2 a safer electrode than a graphite anode. On the other hand, it suffers from poor electronic conductivity which limits the electrochemical performance of TiO_2 electrode materials (132).

One effective way to overcome this issue and improve the conductivity and hence the electrochemical properties is doping, as the presence of aliovalent ions affects electrical conductivity (258). The introduction of ions with different valence state, than that of the titanium ion, changes the number of free charge carriers and thus the electronic properties (259). Introduction of ions in a lower valence state creates oxygen vacancies which may improve the oxide ion conductivity, while introducing ions with a higher valence state leads to mixed valence due to the reduction of an appropriate proportion of Ti^{4+} to Ti^{3+} (256,260). In this case, *n*-doped materials are created.

There have been many studies of the electrochemical properties of TiO_2, both experimental and theoretical, especially for nanosized TiO_2 (158,177,191,214). The substitutional doping of nano-sized TiO_2 with different cations (Nb, C) has been reported (209,232,261,262). In contrast, there are few experimental investigations of doping effects on the electrochemical performance of bulk rutile-TiO_2.

The effect on the electrochemical performance of rutile quenched from high temperatures so as to be oxygen-deficient was not studied before.

Therefore, in the present work, an experiment was designed to investigate the electrochemical performance of reduced rutile and compare it with that of fully oxidized bulk rutile.

3.2 Characterisation and structural properties of TiO_2

The XRD result, shown in Figure 3-2*,* indicates that the rutile TiO_2 powders are pure *single phase* and all observed reflections can be indexed on rutile-type crystal structure according to the JCPDS card no. 21.1276. The lattice parameters, a = b = 4.598 Å, and c = 2.962 Å and the unit cell volume V= 62.450 (Å) (158), for pure rutile TiO_2 are in good agreement with the reported values of a= 4.594 Å and c= 2.958 Å and V= 62.4 (Å) (158).

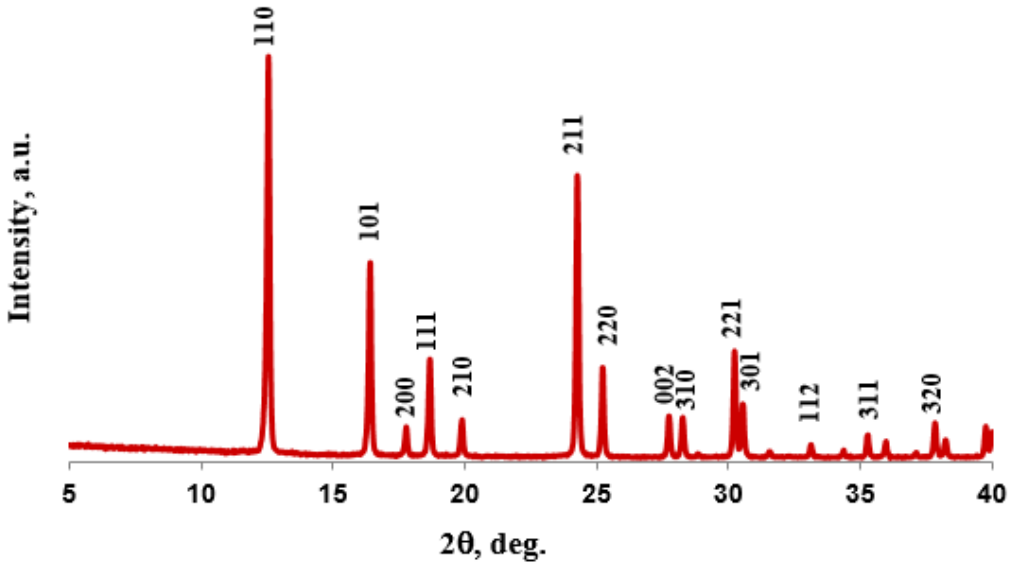

Figure 3-2: XRD pattern of rutile TiO_2; a.u. refers to arbitrary units of intensity.

3.3 Electrochemical characterisation of rutile-TiO_2

The electrochemical performance of rutile- TiO_2 was evaluated using a two-electrode coin cell. The cathode electrode was a composite of 70% TiO_2, 25% super P carbon black and 5% polyvinylidene fluoride (PVdF). Metallic lithium and 1M $LiPF_6$ solution in propylene carbonate were used as a counter electrode and electrolyte respectively. Cyclic voltammetric testing was carried out at room temperature with scan rate 0.01 mV/s between 1V and 3V. Galvanostatic discharge–charge cycling was carried out at constant temperature (25°C) and constant current and C/20 rate with cutoff voltage of 1.0- 3.0 V.

3.3.1 Cyclic voltammetry (CV)

To determine the electro-active ions in the material, cyclic voltammetry was performed between 1-3 V on rutile-TiO_2. The voltammograms are displayed in Figure 3-3, which clearly show the cathodic and anodic current peaks for a reversible reaction. The cathodic peak is centred at around 1.85 V while the anodic peak is located at potential 1.35 V. The positions of the reduction and oxidation

peaks are consistent with lithium ion insertion and extraction respectively which are reported to be 1.35 and 1.85 V for rutile-TiO_2 (255,263,264). The oxidation peak of TiO_2 is broad and not well defined indicating that reaction becomes more sluggish and is subject to kinetic control. The reduction peak, on the other hand, indicates a rapid reaction as it appears intense and sharp; however, its intensity decreases upon cycling.

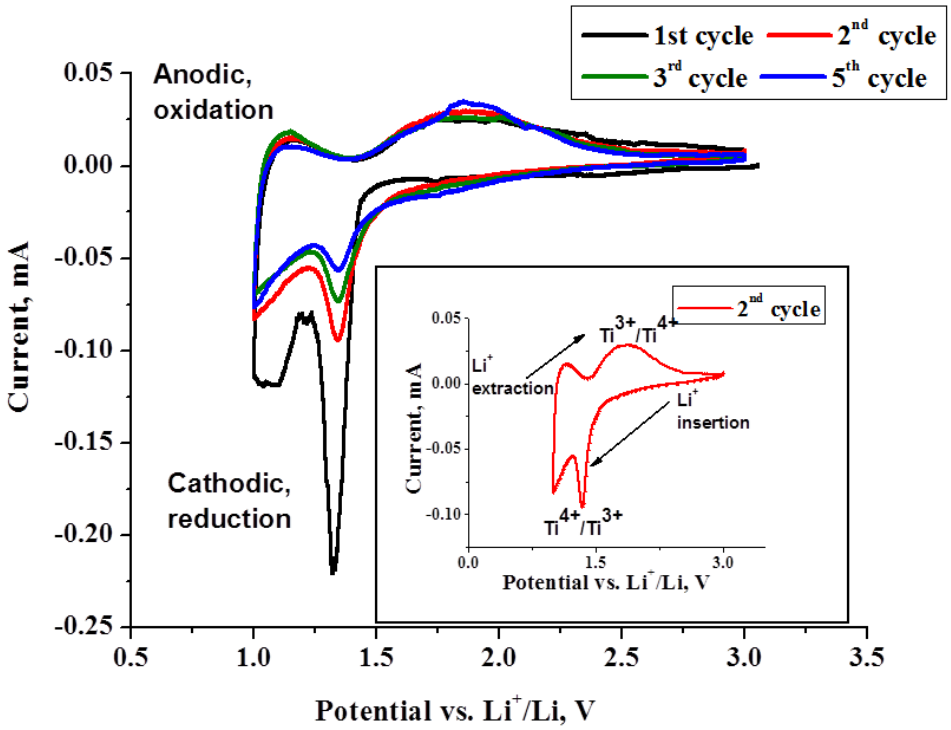

Figure 3-3: Cyclic voltammetric curves of rutile-TiO_2 electrodes in 1 M $LiPF_6$/PC electrolyte. Scan rate 0.01 mV/s at different cycles.

3.3.2 Galvanostatic cycling with potential limitation (GCPL)

The galvanostatic discharge-charge curves are presented in Figure 3-4. The discharge profile shows a flat plateau, (1) centred at ~ 1.4 V and then drops to ~ 1 V. Also, two solid solution domains, (2) and (3) are clearly visible during the first reduction which corresponds to formation of solid solution(133). After the first discharge, continuous sloping curves corresponding to an extraction of 0.06 lithium ions, Fig. 5 are clearly visible during the first charge.

Subsequent cycles exhibit a similar discharge-charge profile with a decrease in plateau extent as a consequence of a decrease in the Li^+ ion insertion in each cycle. However the shape of the curves are similar which indicates that the process is fairly reversible.

The first lithium insertion into undoped rutile leads to a capacity of about 26.5 mAh/g, corresponding to about 0.11 Li per mol of TiO_2, as shown in Figure 3-5, consistent with what was observed (216) and in agreement with previous studies that consider the rutile structure as inert towards lithium intercalation (≤ 0.1 Li per TiO_2 unit at room temperature) (188–190,255); the typical value of Li insertion into rutile is in the range 0.1-0.25mol (255).

Charge-discharge capacities up to 20 cycles, as seen in Figure 3-6, show ~ 35% capacity loss after the first cycle and capacity fading in the following 4 cycles. After 5 cycles, the capacity became constant.

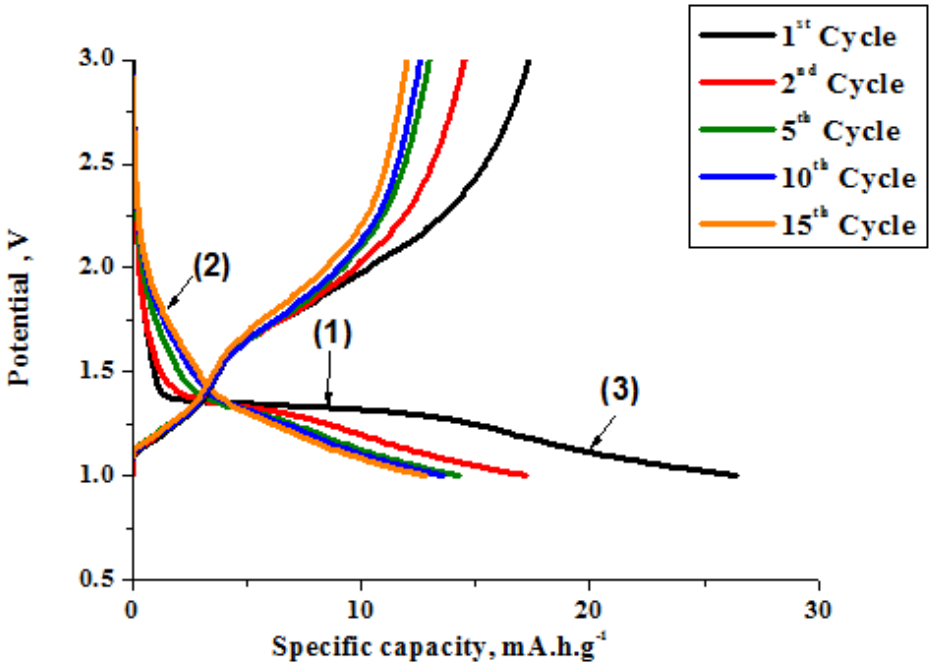

Figure 3-4: Charge-discharge profiles for TiO_2.

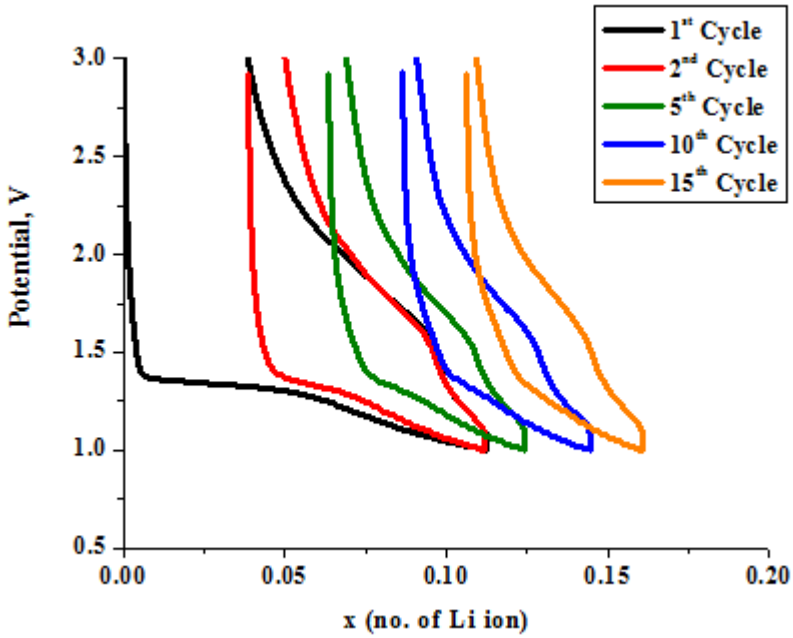

Figure 3-5: Li ion insertion–extraction profile for TiO_2 for 15 cycles.

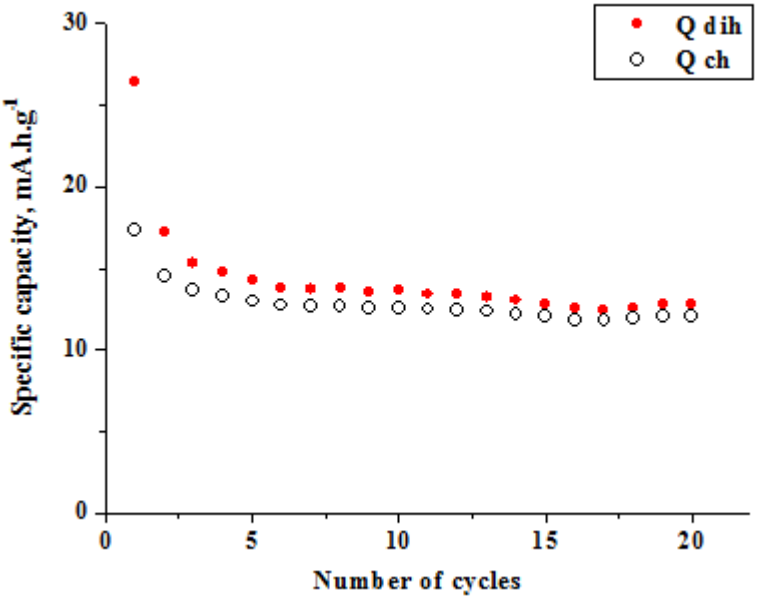

Figure 3-6: Charge-discharge capacities vs. number of cycles for TiO_2 for 20 cycles.

3.4 Electrochemical characterisation of reduced rutile-TiO_2

The reduction at high temperature associated with oxygen loss leads to change in the oxidation state of Ti^{4+} in TiO_2 and the formation of Ti^{3+} ions which are responsible for the electronic conductivity (232).

Reduction of TiO_2 can be achieved when a stoichiometric sample is quenched from high temperature. Pure rutile powder was heated for 1 h at 1400°C in air followed by rapid quenching in liquid N_2 results in highly conductive oxygen-deficient $TiO_{2-\delta}$ and δ was estimaed to be 0.001(228).

Charge-discharge profiles of TiO_2 quenched from 1400°C for 20 cycles are shown in Figure 3-7. The first discharge step has a noisy and rough plateau centred at ~ 1 V; the processes occurring during this first reduction step are similar to those in bulk rutile. There is a massive capacity loss (i.e. the difference on first discharge-charge capacity) in the first two cycles then became constant for subsequent discharge.

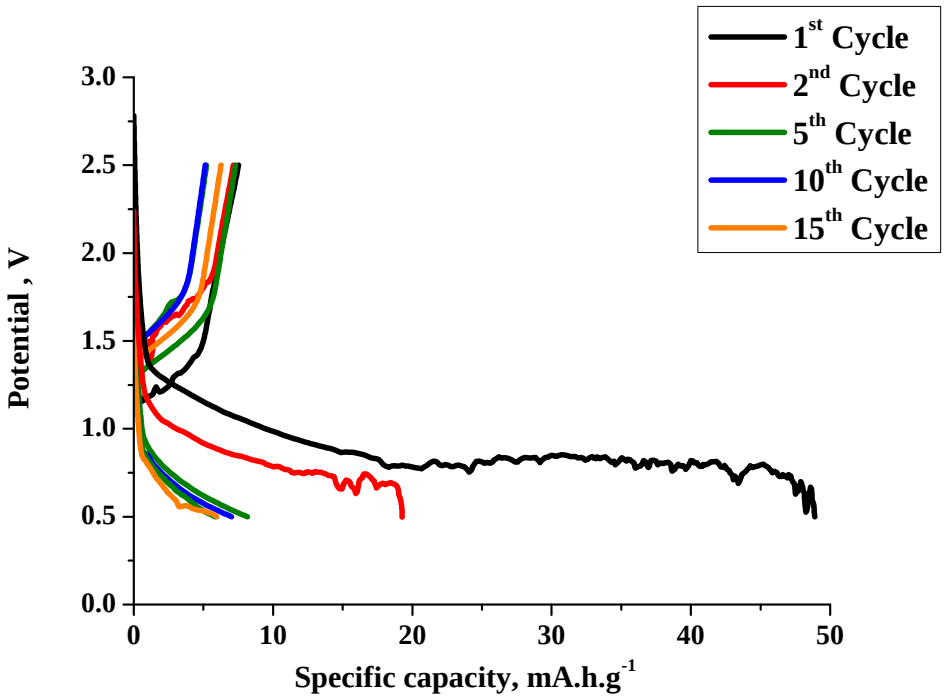

Figure 3-7: Charge-discharge profiles for TiO_2 quenched from 1400°C.

The profiles of Li ion insertion-extraction into/from quenched TiO_2 are given in Figure 3-8. By comparison with oxidized TiO_2, the reduced $TiO_{2-\delta}$ shows reasonable activity and is able to accommodate more Li ions, 0.21 Li per mol of TiO_2, corresponding to a capacity of 49 mA.h/g in the first cycle, after which it became inert towards Li insertion as was observed for bulk rutile.

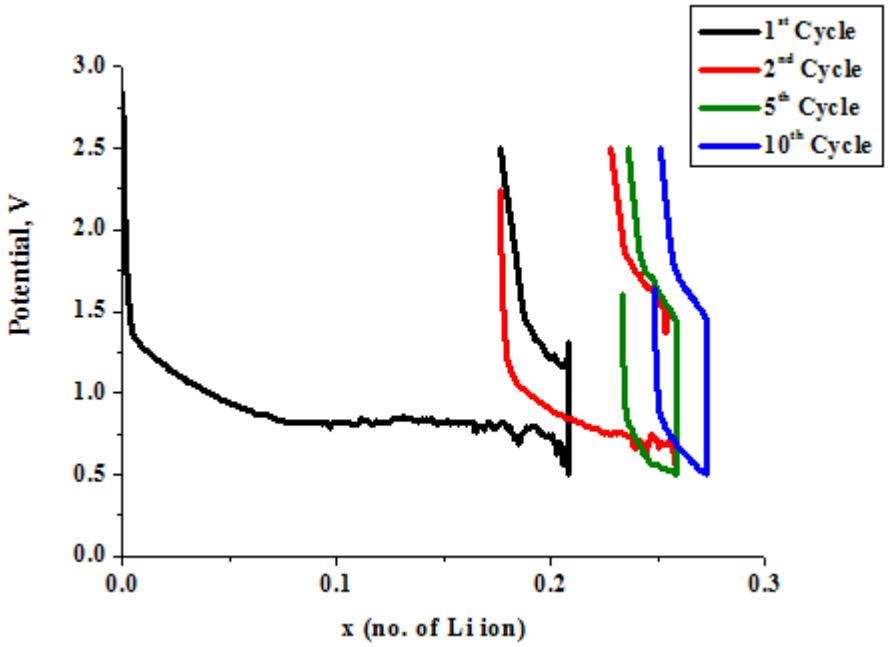

Figure 3-8: Li ion insertion–extraction profile for TiO_2, quenched from 1400°C, for 10 cycles.

The variation of specific capacity with cycle number up to 20 cycles is shown in Figure 3-9. A significant capacity loss occurs in the first cycle and 85% of the original capacity is lost during the initial cycles. After 3 cycles, the capacity became constant with good capacity retention; however, the capacity value is less than that for the oxidised rutile.

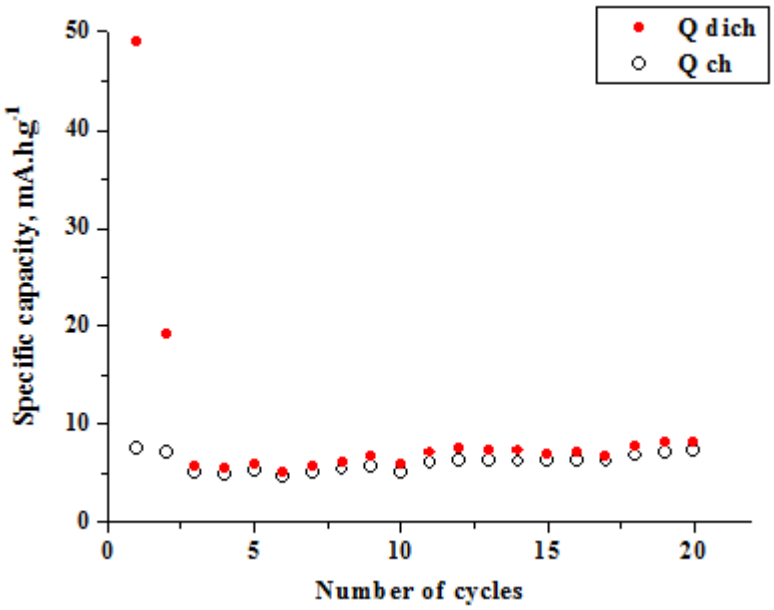

Figure 3-9: Charge-discharge capacities vs. number of cycles for TiO_2, quenched from 1400°C, for 20 cycles.

3.5 Conclusion

Oxygen-deficient rutile $TiO_{2-\delta}$, δ=0.001, behaves differently to fully oxidized rutile during the first cycle. For the quenched sample, a composition of $Li_{0.21}TiO_{2-\delta}$ (49 mA h/g) is obtained during the first reduction, out of which 0.02 lithium ions were extracted during the next oxidation while 0.11Li/TiO_2 was intercalated into the bulk rutile.

The electro-activity of reduced rutile is associated with existence of oxygen vacancies created at high temperature and preserved by the quenching; however the limited activity may be due to the small amount of oxygen loss; 0.001 at 1400°C is too small a change to affect the lattice parameters but it does modify the electronic conductivity of rutile; the oxygen-deficient rutile is a highly conduting material (10^{-1} Scm^{-1}) (228) while pure rutile is an insulator (10^{-13} Scm^{-1}) (265) .

Furthermore, the cycling of this material is stable as a capacity of 15 mA h/g is still obtained after 20 cycles. The capacity loss could due to a large electrode polarization.

It is clear that, oxidized and reduced rutile behave similarly after the first cycle indicating that the increased electronic conductivity of reduced rutile does not improve its reactivity towards lithium intercalation. This result clearly indicates that there may be a kinetic limitation to the insertion of lithium into rutile TiO_2 which is linked to mechanical strains that could be reduced as the unit cell dimensions are expanded, thus allowing a better efficiency of the insertion.

In summary, the anode performance of rutile is not dependent on the level of electronic conductivity of bulk rutile.

4. EFFECT OF RUTILE -TiO_2 STARTING MATERIALS ON THE ELECTROCHEMICAL PERFORMANCE OF $Li_4Ti_5O_{12}$

4.1 Introduction

The huge demand worldwide for low cost, high voltage, high energy density, safe portable electronic devices and electrical vehicles, in addition to environmental concerns, are the main driving forces for the development of advanced materials for new or improved Li-ion batteries (145,266).

Lithium intercalation oxides such as $Li_4Ti_5O_{12}$ (LTO) are considered as promising anode materials (83,145,267–271). Compared to current commercial anodes, LTO offers a stable operating voltage of approximately 1.55 V vs. lithium. With this voltage the formation of a solid electrolyte interface (SEI) and Li plating can be avoided resulting in high charge-discharge rates and high safety level (272). In addition, LTO is a zero-strain lithium insertion material and, therefore, insertion and extraction of lithium ions are extraordinarily reversible (136,267). The zero strain nature of LTO was experimentally evaluated and the study showed the coexistence of two phases $Li_4Ti_5O_{12}$ and $Li_7Ti_5O_{12}$ and also reported that a large volume expansion occurs particularly below 1 V vs. Li/Li^+ (273). This, with its high lithium mobility (270), meets the requirements of high-rate battery applications.

The reversible intercalation/de-intercalation of Li ion occurs at room temperature according to the following equation:

$$Li_4Ti_5O_{12} + 3\,Li^+ + 3e^- \leftrightarrow Li_7Ti_5O_{12} \qquad (1)$$

Three Li ions intercalate into the LTO unit cell leading to a theoretical capacity of 175 mA.h/g as well as transformation from the spinel form of $Li_4Ti_5O_{12}$ to a rock-salt structure and composition $Li_7Ti_5O_{12}$ with a volume change < 0.1%. Very small lattice changes of LTO upon insertion and extraction of Li ions lead to structural stability enhancement and long cycling life (267,271).

$Li_4Ti_5O_{12}$ has a cubic spinel structure in which three of the Li atoms occupy the (8a) tetrahedral positions in the cubic close-packed (ccp) oxygen array, and one Li and all Ti atoms are randomly distributed on (16d) octahedral positions in the ratio Li:Ti

=1:5. This structure provides a three dimensional network of face-sharing tetrahedral and octahedral sites for Li ion diffusion. During intercalation, the additional Li ions insert in the octahedral (16c) sites, and Li ions that initially occupied the (8a) tetrahedral sites migrate to occupy the octahedral (16c) empty sites of the spinel structure.

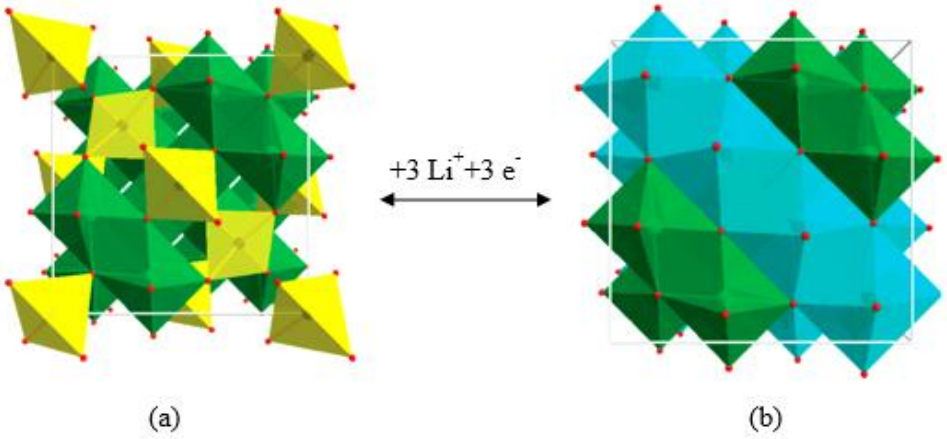

Figure 4-1: Crystal structures of: (a) $Li_4Ti_5O_{12}$ and (b) $Li_7Ti_5O_{12}$. Black spheres symbolise lithium ions, blue spheres symbolise disordered titanium ions and lithium ions (Ti:Li, 5:1), red spheres symbolise oxygen ions. Yellow tetrahedra represent (8a) sites, green octahedra represent (16d) sites and blue octahedra represent (16c) sites, adapted with permission from The Journal of Physical Chemistry C, 113 /16, Ge H, Li N, Li D, Dai C, Wang D., Study on the theoretical capacity of spinel lithium titanate induced by low-potential intercalation, 6324–6. Copyright (2009) American Chemical Society (274).

However, the poor electronic conductivity of $Li_4Ti_5O_{12}$ (≅ 10^{-13}S/cm at room temperature)(147), due to its insulating properties, limits its electrochemical performance. To improve the conductivity and thus electrochemical properties, many strategies have been adopted which include; a) cation doping where transition metal (M^{3+}, M^{4+}, M^{5+})(e.g., Fe^{3+}, La^{3+} ,Sc^{3+} ,Co^{3+}, Cr^{3+}, Mn^{4+}, V^{4+}, Ta^{5+} and Nb^{5+}) and Al^{3+} substitute some of Ti^{4+} atoms (275–286) or substitution of Li^+ with Mg^{2+} (147), b) surface modification either via coating by an electron conductive material such as carbon (287–289) and titanium nitride (290), or fluorination using F_2 gas (291) , c) nanocrystal synthesis to reduce the particle size and consequently minimise the length of Li-ion diffusion and electron transfer paths (273,292–297) and e) heat treatment under reducing atmosphere (H_2/Ar) (298).

A variety of synthesis techniques have been used to prepare $Li_4Ti_5O_{12}$ such as solid state reaction (136,137,267,299,300), the sol–gel method (267,277,292,301–303), the hydrothermal method (296,304–306), molten salt or a flux growth synthesis (307,308), as well as spray pyrolysis processes (138,309). Each has its advantages and drawbacks; high temperature (800°C -1000°C) solid state reaction with long dwell time (12-24 h) results in inhomogeneity, irregular morphology, broad distribution of particle size and the need for longer periods of calcination, whereas the other techniques produce homogeneous materials with fine particle size and good distribution. However, complexity of the synthesis conditions, low yield efficiency as well as use of large quantities of expensive reagents limits the efficiency of these methods (303,308).

In a typical $Li_4Ti_5O_{12}$ synthesis, titanium dioxide (TiO_2) is used as the titanium source due to its advantages in terms of availability, cheapness, non-toxicity and safety (154). Mainly, the anatase polymorph of TiO_2 is used but the rutile form has also been used in several studies (280,289,298,310,311). Rutile is more efficient in obtaining high purity LTO than anatase; a trace of rutile is usually found as impurity with LTO prepared using anatase.

The electrochemical behaviour of both polymorphs is variable; anatase is most active and can accommodate more Li ions compared to rutile which can be considered as inert towards titanium intercalation (154,280,289). Previous studies of $Li_4Ti_5O_{12}$ synthesised from inert TiO_2 have not dealt with its effect on the $Li_4Ti_5O_{12}$ electrochemical performance.

In the present chapter, the aim was to synthesise $Li_4Ti_5O_{12}$ by an economic solid state reaction using rutile as the titanium source, investigate its effects on the electrochemical performance of $Li_4Ti_5O_{12}$ and compare the results with those obtained from $Li_4Ti_5O_{12}$ prepared using anatase.

4.2 Synthesis of LTO

Two $Li_4Ti_5O_{12}$ samples were prepared using anatase, hereafter referred to as A-LTO, and rutile hereafter referred to as R- LTO.

$Li_4Ti_5O_{12}$ was prepared via solid state reaction; the reagents used were Li_2CO_3 (Sigma-Aldrich, 99.9%) and TiO_2 (Anatase, Aldrich, 99.9%). These starting

materials were dried at 180°C and 900°C respectively, and then mixed in stoichiometric amounts; to form a homogenous final product and reduce particle size, the raw materials were ground and mixed using an agate mortar and pestle for 30 minutes. The powder was placed in a gold foil boat, and decarbonated at 650°C for 3 hours followed by calcination at 800°C for 12 hours in air. The sample was reground and fired for a second time at 900°C for 12 hours. Another sample was prepared using TiO_2 (Aldrich, 99+ %) with rutile structure with particle size < 5 micron, following the same procedure as with anatase, but with final overnight heating at 850°C.

4.3 XRD characterization

The X-ray diffraction patterns of the synthesized powders are shown in Figure 4-2. The XRD pattern of the $Li_4Ti_5O_{12}$ adequately corresponds with the XRD pattern of the pure $Li_4Ti_5O_{12}$ sample. The reflections of A-LTO and R-LTO samples match that listed in JCPDS Card No. [49-207] and index in *Fd-3m* space group of the face-centered cubic spinel structure. However, there is a weak additional peak at 2θ near 31.98° in the pattern of the synthesized powder using anatase, which is associated with rutile. This finding is in agreement with Zaghib et al (137). The lattice parameter *a* was calculated to be *a* = 8.3590(3) Å, in good agreement with the reported value.

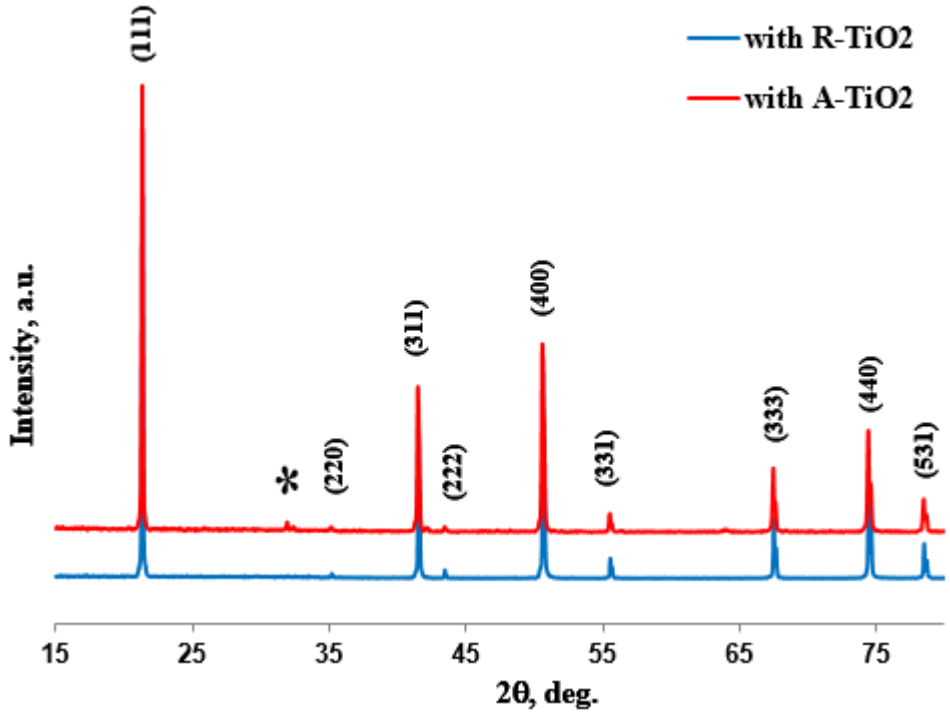

Figure 4-2: X-ray diffraction patterns of $Li_4Ti_5O_{12}$ prepared under different conditions: (a) 900 °C for 12 h with TiO_2 (anatase), (b) 850 °C for 12 h with TiO_2 (rutile), (*) rutile TiO_2. a. u. refers to arbitrary units of intensity as data sets have been offset vertically to show the evolution of the XRD patterns with TiO_2 type.

4.4 Electrochemical measurements

4.4.1 Cyclic voltammetry (CV)

To study the window of electrochemical activity and the species responsible, cyclic voltammetry was performed between 1-3 V cyclic with a scan rate of 0.01 mV/s, on A-LTO and R- LTO. The voltammograms are displayed in Figure 4-3, which clearly show a reversible electrochemical reaction of $Li_4Ti_5O_{12}$. The anodic and cathodic peaks are located at potentials 1.37, 1.70 V for A-$Li_4Ti_5O_{12}$ and 1.38, 1.75 V for R-$Li_4Ti_5O_{12}$. The positions of the reduction and oxidation peaks are consistent with lithium ion insertion and extraction respectively which are reported to be 1.54 and 1.6 V for phase-pure $Li_4Ti_5O_{12}$ (312). This difference in electrochemical performance might be due to electrode polarization. The differences between oxidation and reduction peak potentials for A-$Li_4Ti_5O_{12}$ and R-$Li_4Ti_5O_{12}$ are 0.33 and 0.37 V, respectively. Although both samples reveal polarization resistance of lithium ion insertion/extraction, this difference suggests a lower electrode

polarisation of A-$Li_4Ti_5O_{12}$ than R-$Li_4Ti_5O_{12}$. From the data in Figure 4-3, it is apparent that the current peaks of A-$Li_4Ti_5O_{12}$ are of slightly higher intensity than R-$Li_4Ti_5O_{12}$ which reflects good kinetics.

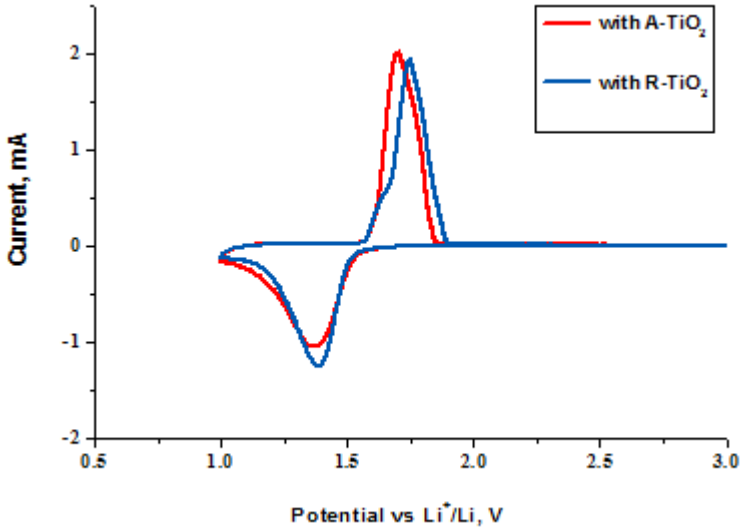

Figure 4-3: Cyclic voltammetric curves of $Li_4Ti_5O_{12}$ electrodes in 1 M $LiPF_6$ /PC. Scan rate: 0.01 mV/s.

4.4.2 Galvanostatic cycling with potential limitation (GCPL)

For the electrochemical characterisation of the Li/ $Li_4Ti_5O_{12}$ cell, the cells (cell 1 and cell 2 with A-$Li_4Ti_5O_{12}$ and R-$Li_4Ti_5O_{12}$ respectively) were cycled between 1.0 and 3.0 V at room temperature and C/10 rate. Figure 4-4 shows extremely flat discharge plateaux for A-$Li_4Ti_5O_{12}$ and R-$Li_4Ti_5O_{12}$ at ~1.55 V which are consistent with the results of previous works (268,269,287,313).

The basis of the flat domain is the coexistence of two phases of lithium titanate $Li_4Ti_5O_{12}$ and $Li_7Ti_5O_{12}$ which suggests a two-phase mechanism for lithium ion insertion/de-insertion into and from the lattice based on the Ti^{4+} /Ti^{3+} redox couple.

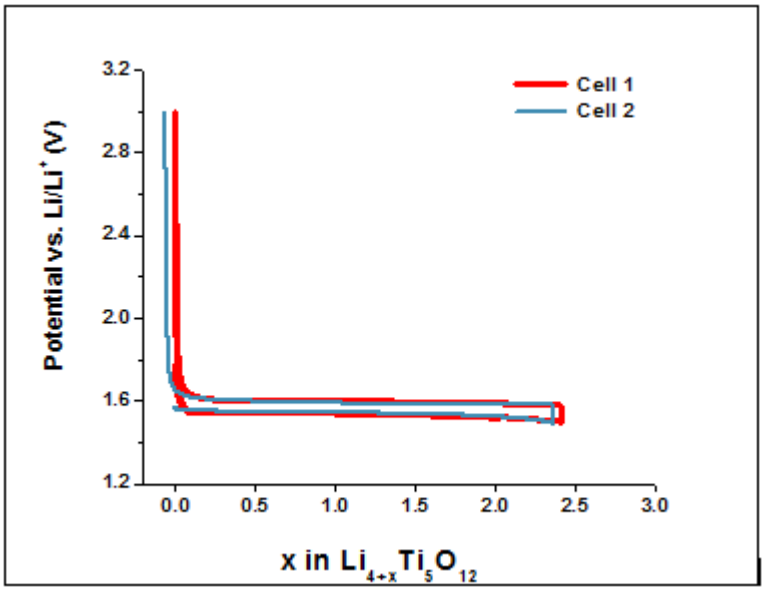

Figure 4-4: First cycle charge-discharge curve of A-LTO (red line is cell 1) and R-LTO (blue line is cell 2).

In both cells, about 2.35 and 2.40 lithium ions were intercalated into R-LTO and A-LTO respectively, during the first discharge process corresponding to a capacity of about 98 and 123 mA.h/g for R-LTO (cell 2) and A-LTO (cell 1), in agreement with that were reported by Yuan et al (289) (86 mA.h/g) and Wang and et al. (313) (103.6 mA.h/g) for $Li_4Ti_5O_{12}$ which was prepared by conventional solid-state reaction. However, the capacity values are much less than that reported in earlier studies in the range 140-165 mA.h/g (136,269,313). The difference may be attributed to many factors such as the synthesis method and thus the particle size; the material: carbon: polymer ratio; trace impurity phases presented in the sample; different thickness of the electrode pellets (272,313)· The difference of the capacity using anatase and rutile may be assoicated to the particle size as small particle size leads to high surface area and hence improve the electrochemical performance. Another possibility may correspond to crystallinity of LTO product and also the presence of impurity.

LTO synthesized with anatase exhibits a higher capacity than that synthesized with rutile, Figure 4-5. A recent study by Kiliç Dokan (310) reports similar finding that the LTO synthesised by traditional solid state method using anatase TiO_2 shows best capacity value. On the other hand, Kiliç Dokan (310) showed data that the specific

capacity of LTO using anatase is higher than that of using rutile TiO_2. Hong et al (311) reported that the specific capacity of LTO using anatase depends significantly on the synthesis process and heat temperature but not on the starting materials.

The correlation of the charge and discharge capacities of $Li_4Ti_5O_{12}$ with cycle number is shown in Fig. 5. Except the initial cycle for A-$Li_4Ti_5O_{12}$, and the first six cycles for R-$Li_4Ti_5O_{12}$, there is no significant difference in the capacity up to 16th and 43rd cycles for A-$Li_4Ti_5O_{12}$ and R- $Li_4Ti_5O_{12}$ respectively. Both cells reveal excellent cycling stability with high capacity retention (100% and 99% for A-$Li_4Ti_5O_{12}$ and R- $Li_4Ti_5O_{12}$ cells respectively). The very stable cyclability is attributed to the stability of the $Li_4Ti_5O_{12}$ spinel structure and to the minimal change of the lattice dimension occurring during insertion and de-insertion of lithium (136,269,313).

As Figure 4-5 shows, there is a clear drop in the initial capacity of cell 1, before the capacity reaches 106 mA.h/g and remains constant with further cycling. This difference can be explained by SEI formation and the presence of R-TiO_2 impurity as shown in the XRD. On the other hand, the initial capacities of cell 2 display an increasing trend during the first four cycles before dropping significantly to a constant value of ~ 98 mA.h/ g over the next 38 cycles.

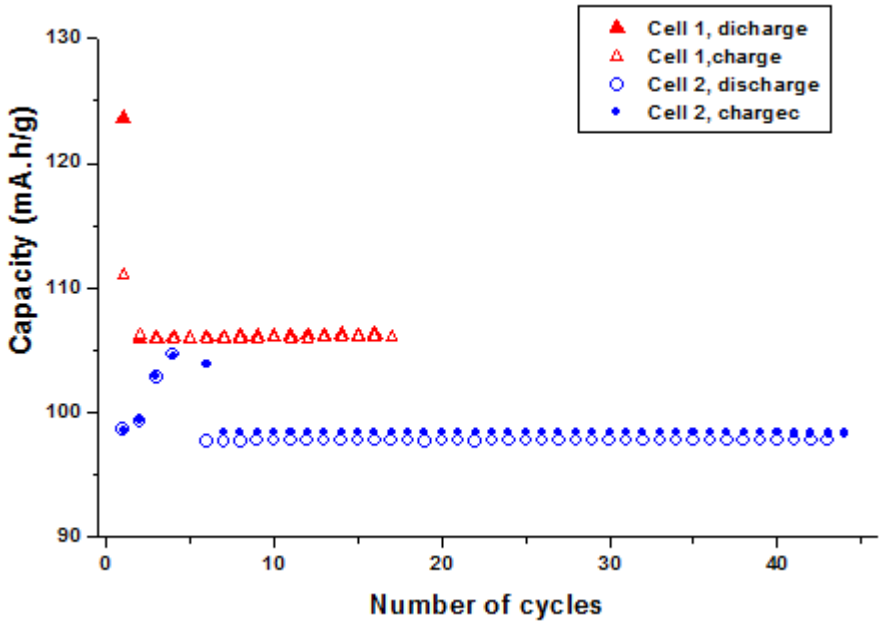

Figure 4-5: Charge and discharge capacities vs. cycle number for A-LTO (cell 1) and R-LTO (cell 2).

4.5 Conclusion

$Li_4Ti_5O_{12}$ was synthesised using anatase and rutile forms of TiO_2 via a solid-state route. $Li_4Ti_5O_{12}$ with rutile TiO_2 was phase-pure at lower temperature Both materials show a stable operating voltage at 1.55 V and a pair of reversible redox peaks. However, using anatase as the TiO_2 source effectively leads to high lithium storage capacity. The capacity delivered by these materials was lower than that reported in previous studies; A-LTO and R-LTO exhibit excellent reversible capacity and cycling stability with very small initial irreversible capacity for A-LTO. These results reveal a significant difference in electrochemical performance of R-LTO and A-LTO. The most significant finding to emerge from the present study is that the synthesis of LTO using rutile as the titanium source without surface activation or ball milling leads to different electrochemical behaviour than using anatase.

Since this work was carried out (Anode Materials for Li-Ion Batteries, 1st year report, university of Sheffield, 2010) reports have been published describing the effect of rutile on the electrochemical performance of LTO (310,311). In their work, they compared the specific capacity of LTO material which has synthesised by solid state reaction with different milling methods: without and with ball milling (310), with ball milling and with high energy milling (311) using anatase and rutile as starting materials.

5. SYNTHESIS AND ELECTROCHEMICAL PERFORMANCE OF $Cu_XM_{2X}Ti_{1-3X}O_2$; M=Nb^{5+}, Ta^{5+}

5.1 Introduction

Titanium dioxide (TiO_2) has many characteristics that make it a potential anode material for lithium-ion batteries (232); however; the dense close packing of the structure reduces the electrochemical performance of rutile-TiO_2 (314). Considerable efforts have been made to enhance the electrical conductivity including doping with aliovalent ions which can modify the electronic properties of TiO_2. It is well known that aliovalent ions have significant effects on the electronic conductivity and/or crystalline structures leading to improvements in the physical and chemical properties of other metal-doped systems (315–317). These effects have been widely studied for both donor and acceptor dopants.

n-type dopants for TiO_2 are the group-V elements; vanadium, niobium, and tantalum. These elements can be substitutionally incorporated within the rutile lattice to occupy at least 50% of the cation sites (318,319) and form a homogeneous solid solution with TiO_2. When M^{5+} substitutes for Ti^{4+}, the charge compensation is achieved either by the creation of Ti cation vacancy, or by the stoichiometric reduction of Ti^{4+} to Ti^{3+} (320). So, M^{5+} introduction can contribute to the generation of electrons or cation vacancies which can give rise to an increase in either electronic or ionic conductivity (321–324). Recent attention to Nb-, Ta-doped TiO_2 particles or films for different applications derives from the fact that Nb, Ta with limited amounts of doping leads to an increase in the electrical conductivity of titanium dioxide (232,324) , enhanced photocatalytic activity (325), enhanced catalytic activity and improved sensing response (95,326). Because the ionic radii in octahedral coordination are about the same, Ta^{5+} and Nb^{5+} can substitute for Ti^{4+} (Ta^{5+}=0.064 nm, Nb^{5+} 0.064 nm and Ti^{4+} = 0.0605 nm) (327) in the crystal lattice (321).

Substitution of acceptor dopants as low valence ions (M^{3+} or M^{2+} such as Cr, Fe, Ba, Cu) on the Ti sites, increases hole concentration and thus *p*-type conductivity (195). The influence of cations with an oxidation state lower than Ti^{4+} on the oxygen vacancy concentration will depend on their position in the TiO_2 lattice. If the cations are present at the Ti sites, they increase the oxygen vacancies in the TiO_2

lattice but if located in interstitial positions, they decrease the oxygen vacancy concentration. In cases of the similarity in ionic size, dopants can easily substitute for Ti^{4+} but the larger sized dopant may need to occupy interstitial positions (328).

In Cr-doped TiO_2 Cr is introduced into the TiO_2 lattice, although a minor part is still present on the surface, and this modified the photocatalytic properties of TiO_2 by extending the visible light absorption (329).

Cu-doped TiO_2 has much application as an efficient photocatalytic material (330,331), as anode materials in Li-ion batteries (332) CO gas sensor (333) and in photocatalytic reduction of CO_2 and NO (334,335). It was proposed by Ni et al. (336) that because Cu has a similar ionic radius, 0.73A° to that of Ti, 0.605A°, it is possible for Cu substitutional incorporation into the rutile TiO_2 lattice.

Pentavalent dopants Nb and Ta, readily dissolve in the TiO_2 lattice, reducing its resistivity by donating conduction electrons (337). Other additives, such as BaO, Cr_2O_3 and Bi_2O_3 help densification during sintering of TiO_2 probably by increasing the defect concentration in the TiO_2 lattice through the formation of a solid solution or a liquid phase (338,339). Co-doping of acceptor and donor impurities is widely practiced to improve the stability. Ba- Nb-, Cr-Nb and Bi- Nb codoped TiO_2 alter the electrical characteristics of TiO_2 based-varistors (338,340). Other authors have studied the effect of CaO (341) and Ta_2O_5 and BaO (342) on the electrical and dielectric properties of the TiO_2-Ta_2O_5 varistor material, and have found that the dopant has significant effects on the nonlinear electrical behaviour and dielectric properties of doped TiO_2 ceramics, and also, increases the electronic conductivity (342).

Theoretical and experimental studies have shown that TiO_2 can be doped with these metals. The stability of doped TiO_2 was determined from the calculation gave a negative free energy for the substitution (343). On the other hand, experimental data reported that Nb forms a homogeneous solution with rutile TiO_2 (323) and Ta is more soluble than Nb in the TiO_2 lattice (344).

In short, the introduction of Nb, Ta into TiO_2 can modify the microstructure of the material and introduce electronic states at the surface or into the bulk of the grain leading to a modification of the material conductivity. Also, Ta is stable in harsh electrochemical environments.

CuO affects the grain size, the electrical properties and dielectric properties of SnO_2-based varistors for CuO concentration from 0.00 to 1.00 mol % (345).

For this study, Cu, M co-doped TiO_2, M= Nb and Ta, was proposed. A solid solution, $Cu_xNb_{2x}Ti_{1-3x}O_2$ ($0 \leq x \leq 0.9$) (346) and ($0.02 \leq x \leq 0.20$) (347) was prepared by conventional solid state reaction. This increased the electrical conductivity (346). Also, the subsolidus phase relations in the CuO_x–TiO_2–Nb_2O_5 pseudo-ternary system and the crystal structure of the rutile solid solution were determined (236). On the other hand, a rutile solid solution of Cu, Ta co-doped rutile TiO_2 in the range of compositions ($0 \leq x \leq 0.60$) has been briefly investigated by Grandin et al (346). They pointed out that the lattice parameters and the linear evolution of the conductivity vs. 1/T are similar to those observed for the corresponding niobium oxides but no experimental data were reported. Also, the electrochemical performances of these solid solution series have not been addressed and the electrical properties have not been discussed in depth.

In this chapter, solid state synthesis has been used to synthesise different rutile compositions of Cu, M co-doped TiO_2 (M= Nb and Ta) which were characterised by XRD. A new rutile solid solution has been successfully synthesised, $Cu_xTa_{2x}Ti_{3-x}O_2$ ($0 \leq x \leq 0.15$). Synthesis of rutile solid solution, $Cu_xNb_{2x}Ti_{3-x}O_2$ ($0 \leq x \leq 0.23$) has been reported (236), however in this work the electrical and electrochemical properties are studied. The effect of Cu-M codoping on the electrochemical performance of the rutile TiO_2 was investigated by CV and GCPL.

The following equation was adapted to form a solid solution of co-doped TiO_2 using CuO, Nb_2O_5 ,Ta_2O_5 and rutile-TiO_2:

$$3x\ TiO_2 + x\ CuO + x\ Ta_2O_5(Nb_2O_5) \rightarrow Ti_{1-3x}Cu_xTa_{2x}O_2 \qquad (1)$$

Solid solutions of rutile-TiO_2 have been synthesized according to the composition trinagle shown in Figure 5-1 and the following substitution mechanisms:

$$3Ti^{4+} \rightarrow Cu^{2+} + 2M^{5+}, \quad (M= Nb^{5+}, Ta^{5+})$$

The total number of cations is maintained at a constant value to avoid the creation of cation vacancies and interstitials (348).

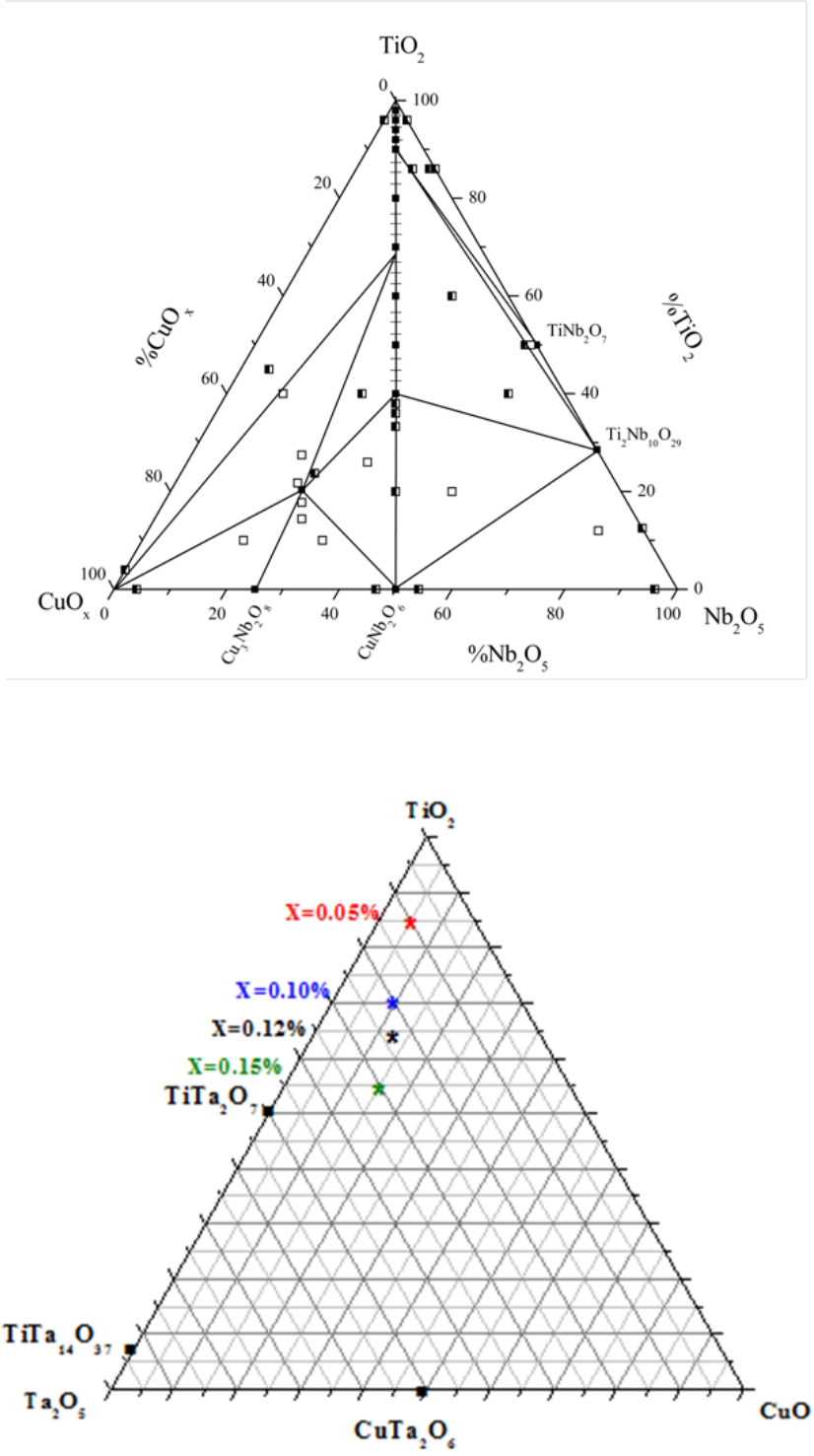

Figure 5-1: The phase diagram of CuO– TiO_2– Nb_2O_5 (top), Reprinted from Solid State Chemistry, 184 /7, Reeves-McLaren N, Ferrarelli MC, Tung Y-W, Sinclair DC, West AR, Synthesis, structure and electrical properties of $Cu_{3.21}Ti_{1.16}Nb_{2.63}O_{12}$ and the CuO_x–TiO_2–Nb_2O_5 pseudoternary phase diagram, 1813–9, Copyright (2011), with permission from Elsevier (236) and the composition trinagle of CuO– TiO_2– Ta_2O_5 (bottom).

5.2 Materials characterization

5.2.1 XRD data

The XRD data of the two solid solution series are shown in Figure 5-2 (a, b). All XRD patterns show well-developed diffraction peaks of rutile phase (JCPDS 21-1276) without the presence of other phases. A significant shift of the diffraction peak positions toward lower 2θ values was observed for doped rutile, and increased when the x value increased.

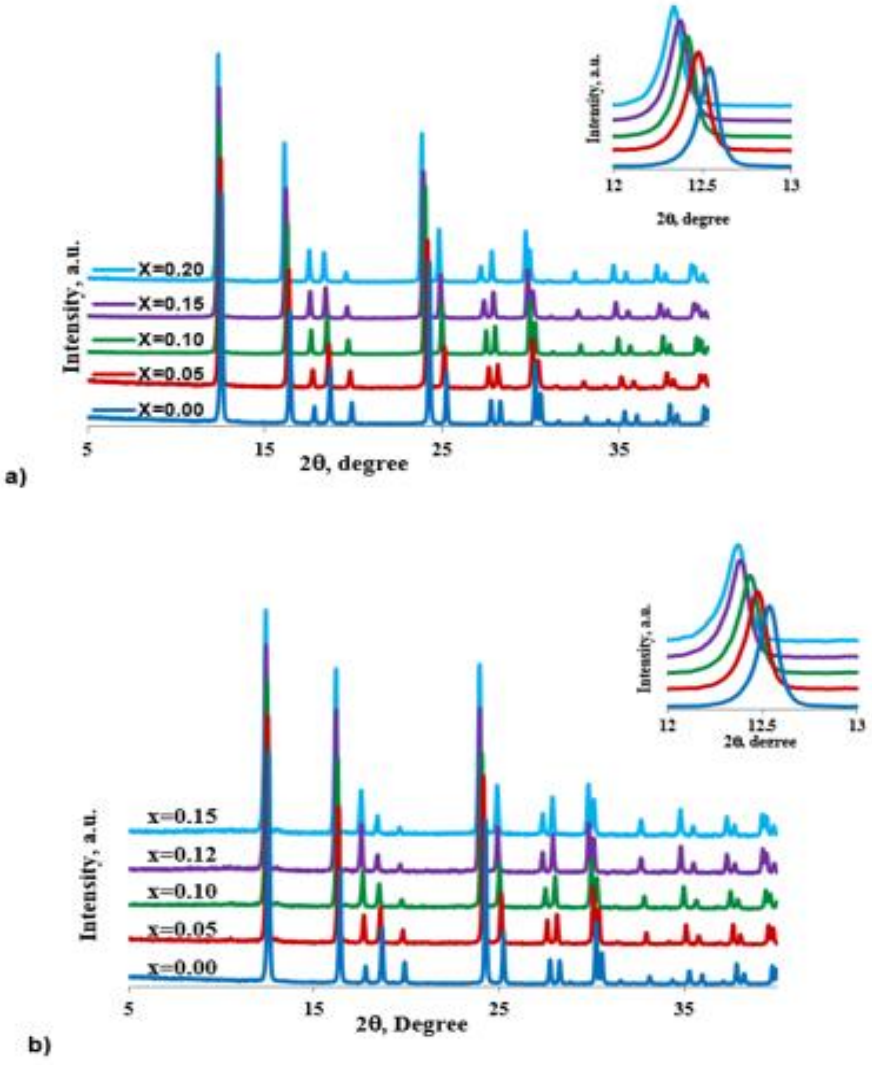

Figure 5-2: XRD patterns of $Cu_xM_{2x}Ti_{1-3x}O_2$: (a) M=Nb^{5+} (0≤ x ≤0.2), (b) M=Ta^{5+} (0≤ x ≤0.15). Inset shows the gradual shift in the 100 diffraction peak. a.u. refers to arbitrary units of intensity as data sets have been offset vertically to show the evolution of the XRD patterns with increasing x content.

5.2.2 Lattice parameters

The variation in lattice parameters and cell volume of the tetragonal unit cell of rutile with composition x, Table 1, are plotted as a function of x and presented in Figure 5-3. The structure parameters (a, c and V) increase gradually with x, leading to expansion of the lattice for all rutile solid solutions. However, the expansion of the unit cell is isotropic as the c/a ratio is almost constant in both systems, as shown in Figure 5-3. From the Figure below, it can be clearly seen that both lattice parameters and the cell volume of the solid solutions reveal a linear relationship obeying Vegard's law.

Table 5-1: Lattice parameters data of the $Cu_xM_{2x}Ti_{1-3x}O_2$ (M= Nb^{5+} and Ta^{5+}) systems, the estimated standard deviation (e.s.d) ≤ ±(3).

$Cu_xNb_{2x}Ti_{1-3x}O_2$	a, Å	c, Å	c/a	V, $(Å)^3$
x= 0.00	4.5933	2.9592	0.64424	62.400
x = 0.05	4.6193	2.9738	0.64378	63.455
x = 0.10	4.6406	2.9868	0.64363	64.32
x = 0.15	4.6661	3.0034	0.64438	65.246
x = 0.20	4.6700	3.0259	0.64794	66.268
$Cu_xTa_{2x}Ti_{1-3x}O_2$	a, Å	c, Å	c/a	V, $(Å)^3$
x = 0.05	4.62029	2.97621	0.64416	63.533
x = 0.10	4.63494	2.98574	0.64418	64.142
x = 0.15	4.65948	3.00309	0.64451	65.199

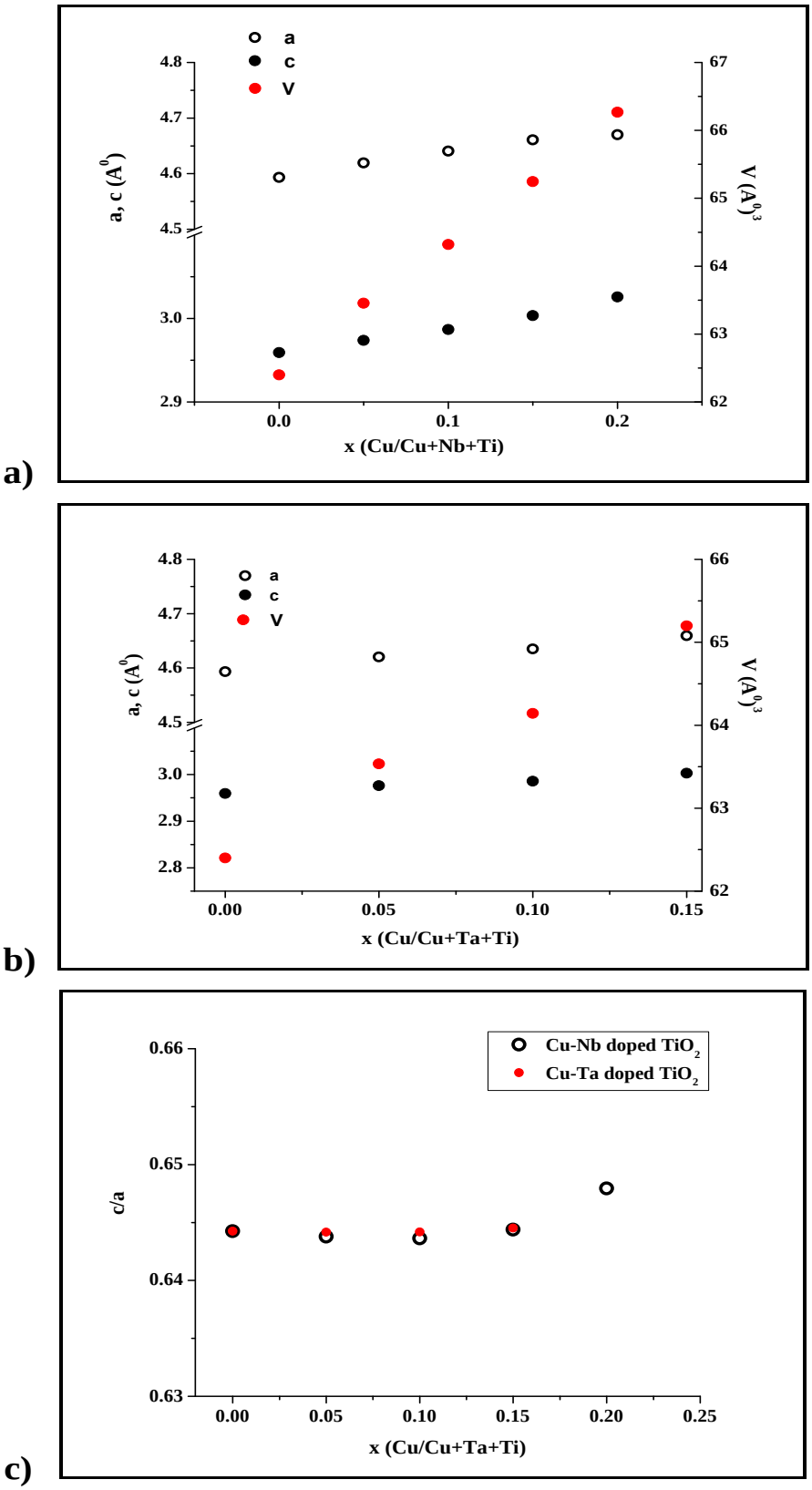

Figure 5-3: Refined lattice parameters, a, c and cell volume, V, of rutile-solid solutions for; a) $Cu_xNb_{2x}Ti_{1-3x}O_2$ and b) $Cu_xTa_{2x}Ti_{1-3x}O_2$, c) c/a ratio. Error bars are smaller than the data points.

5.3 Electrochemical properties

5.3.1 Cyclic voltammetry (CV)

CVs were recorded at a scan rate of 0.01 mV s^{-1}, at room temperature in the potential window of 1-2.8 V vs. Li/Li^+. Figure 5-4 shows the cyclic voltammograms of the first three cycles of Cu, Nb co-doped TiO_2, x=0.2. The first cycle voltammograms show two cathodic peaks during the cathodic scan; a very broad peak at ~1.75 V and second peak at ~1.1V, while the anodic scan shows a broad peak centred at 2.1 V. The following cycles show a different CV shape during the anodic and cathodic sweeps; the anodic and the cathodic parts of the cycles are symmetric, and the values of the anodic and the cathodic peak currents are almost the same in each cycle. The intensity of anodic and cathodic peaks at 1.75 and 2.1 V respectively, increase during CV sweep however the intensity of cathodic peak at 1.1 V significantly decreases in the second cycle and does not exist after.

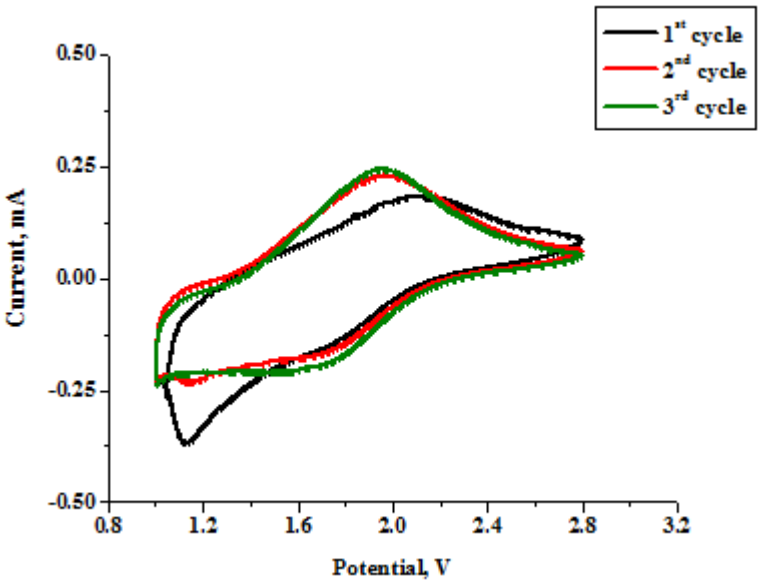

Figure 5-4: Cyclic voltammetric curves of Cu-Nb doped TiO_2 , x=0.20, electrodes in 1 M $LiPF_6$ /PC electrolyte. Scan rate 0.01 mV/s at different cycles.

5.3.2 Galvanostatic cycling with potential limitation (GCPL)

Figure 5-5, Figure 5-6, and Figure 5-7 show the discharge–charge curves of Cu-M co-doped TiO_2 (M=Nb, Ta) at room temperature within the potential window 1.0–3.0 V. All materials showed distinct potential drops during Li insertion from open circuit voltage (OCV) to 2.0 V for $Cu_xNb_{2x}Ti_{1-3x}O_2$ (x=0.20) and 2.2 V for both $Cu_xNb_{2x}Ti_{1-3x}O_2$ (x=0.15), and $Cu_xTa_{2x}Ti_{1-3x}O_2$ (x=0.10); this is followed by a curved solid solution regime up to the cut-off voltage. A negligible amount of Li is inserted into the co-doped TiO_2 before the sloped regime starts. A large amount of Li is inserted during the sloped region between 2.0 V to 1.0 V with capacities 56, 78 and 78 $mAhg^{-1}$ for $Cu_xNb_{2x}Ti_{1-3x}O_2$ (x=0.15 and 0.2) and $Cu_xTa_{2x}Ti_{1-3x}O_2$ (x=0.1) respectively. The subsequent charging (Li^+ extraction) show increase in the capacity up to 2.2 V and this region is complementary to the Li insertion during the sloped region followed by a curved solid solution regime up to 3.00 V. However, the amount of Li^+ extracted at up to ~ 2.2 V is less than that inserted during the sloped region on discharge. The extraction capacity was 12, 19 and 12 mAh g^{-1} for $Cu_xNb_{2x}Ti_{1-3x}O_2$ (x=0.15 and 0.2) and $Cu_xTa_{2x}Ti_{1-3x}O_2$ (x=0.1) respectively. From the tenth cycle, the capacity of all systems became reversible and the capacity loss is smaller, Figure 5-5.

Figure 5-6 represent the discharge–charge capacities versus cycle number within the voltage window 1.0–3.0 V. Cu-Nb doped TiO_2 samples show good reversibility with good performance upon subsequent cycling. Reversible capacities observed for the cycles from the 10^{th} in the case of $Cu_xNb_{2x}Ti_{1-3x}O_2$ (x= 0.2) whereas, it was observed for the cycles from the 3^{rd} in the case of $Cu_xTa_{2x}Ti_{1-3x}O_2$ (x=0.10) with gradually fading.

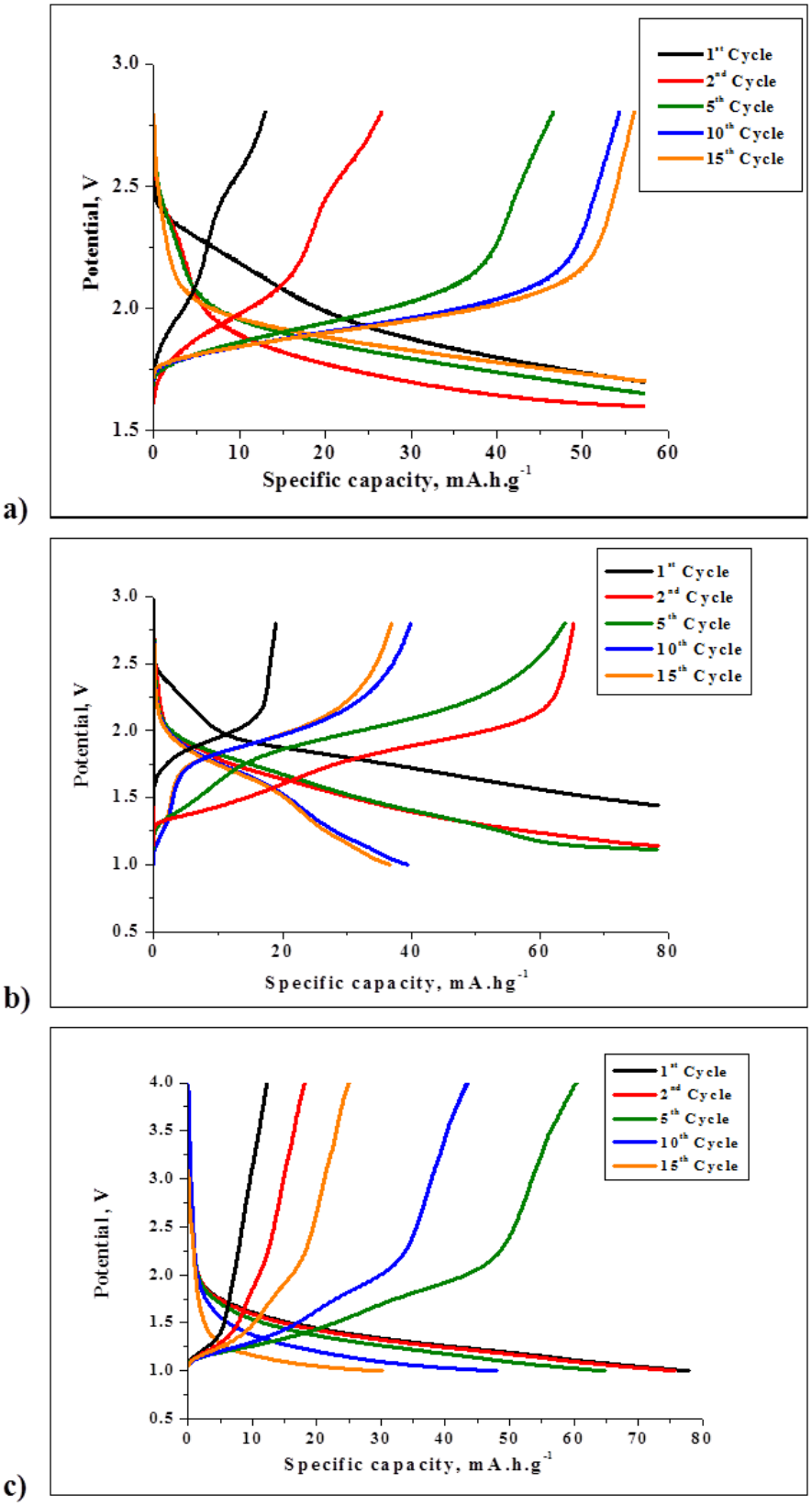

Figure 5-5: Charge-discharge voltage profile of: (a) $Cu_xNb_{2x}Ti_{1-3x}O_2$ (x=0.15), (b) $Cu_xNb_{2x}Ti_{1-3x}O_2$ (x=0.2) and (c) $Cu_xTa_{2x}Ti_{1-3x}O_2$ (x=0.10) at room temperature for representative cycles (1^{st}, 2^{nd}, 5^{th}, 10^{th} and 15^{th}).

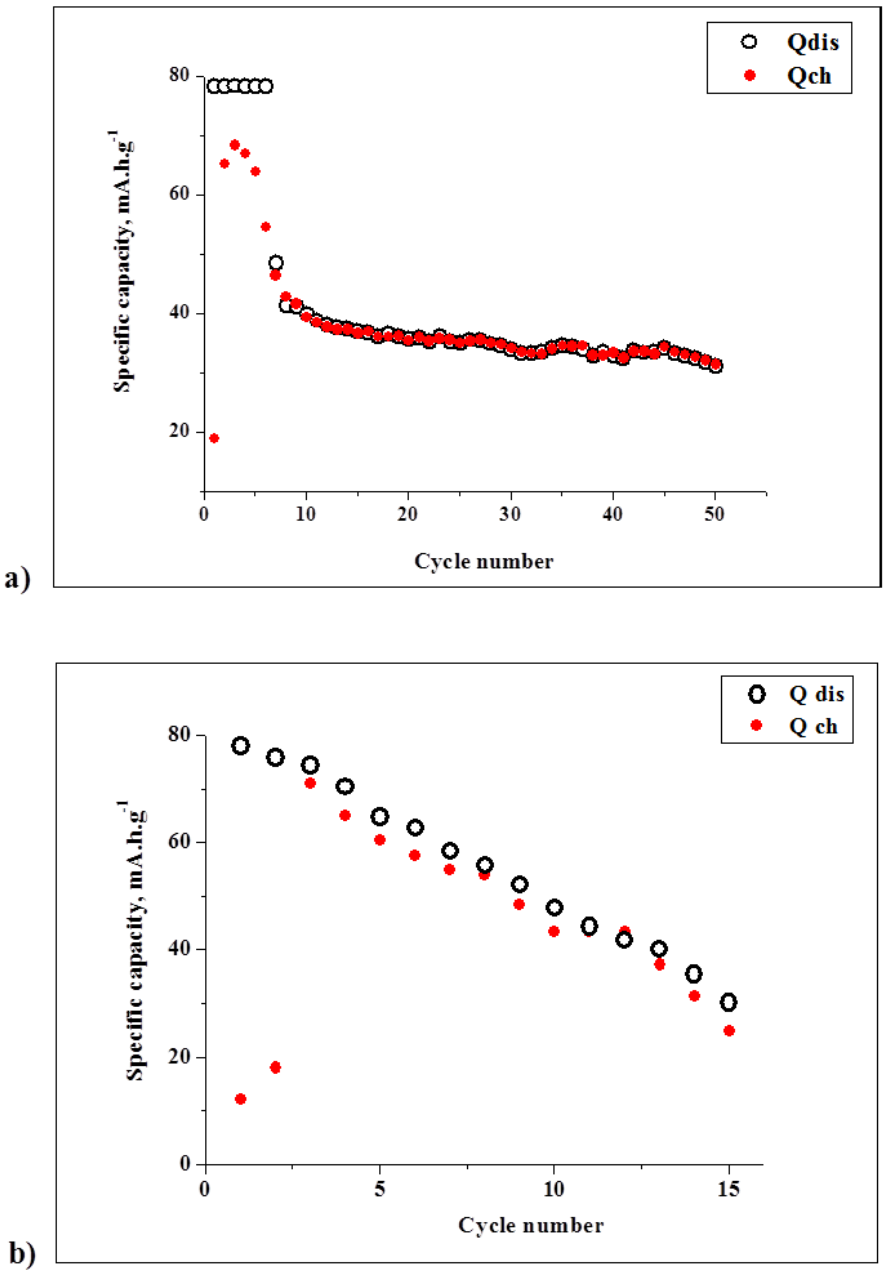

Figure 5-6: Specific capacity versus cycle number for: (a) $Cu_xNb_{2x}Ti_{1-3x}O_2$ (x=0.2) and (b) $Cu_xTa_{2x}Ti_{1-3x}O_2$ (x=0.10) at room temperature.

One mole of Li^+ inserted during the first discharging step, Figure 5-7, and only around 0.2-0.3 mole of Li^+ was extracted during this cycle for all materials. The subsequent discharging showed almost similar amounts of Li^+ intercalated on both $Cu_xNb_{2x}Ti_{1-3x}O_2$ (x=0.15) and $Cu_xTa_{2x}Ti_{1-3x}O_2$ (x=0.1) while only 0.2 mole inserted on the $Cu_xNb_{2x}Ti_{1-3x}O_2$ (x=0.2). Varied amount of Li^+ de-intercalated in sequence charging, however the lithium extraction increase during cycling.

The shape of charge-discharge curve consists of multi-processes; first drop from OCV to voltage at ~ 2.2V, second sloped curve correspond to reversible solid solution transitions and finally oxidation towards a smooth voltage variation associated with a solid solution domain reaction (154). A short voltage plateau at 1.2 V which was observed for $Cu_xNb_{2x}Ti_{1-3x}O_2$ (x=0.2) may be due to side reaction with electrolyte which is irreversible and this plateau disappeared in subsequent cycles.

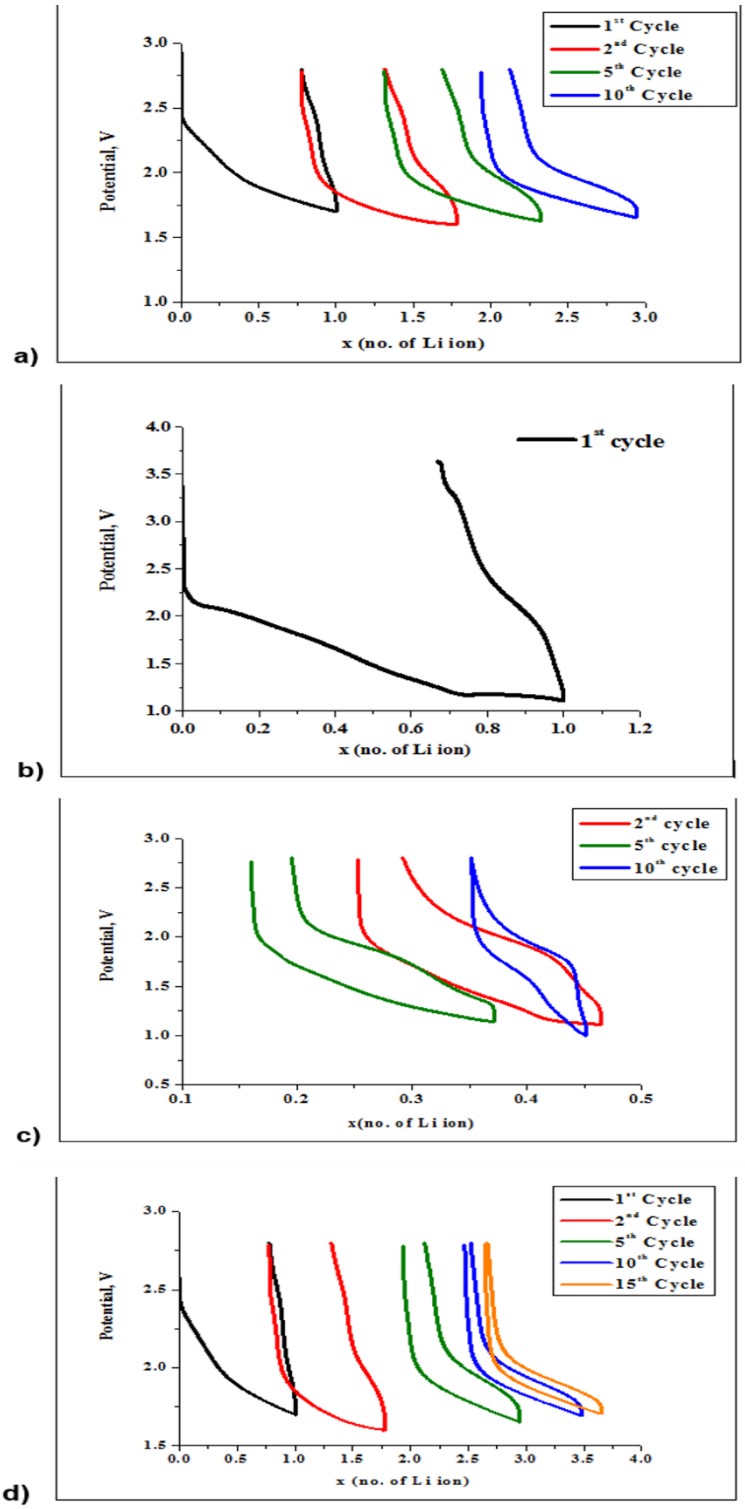

Figure 5-7: Galvanostatic cycling curves of: (a) $Cu_xNb_{2x}Ti_{1-3x}O_2$ (x=0.15), (b and c) $Cu_xNb_{2x}Ti_{1-3x}O_2$ (x=0.2) and (d) $Cu_xTa_{2x}Ti_{1-3x}O_2$ (x=0.10) for representative cycles (1^{st}, 2^{nd}, 5^{th}, 10^{th} and 15^{th}).

5.3.3 Ex-situ XRD

It is essential to identify the mechanism of Li ion intercalation into the doped rutile structure and to investigate the stability of the structure during cycling. XRD was used to study the $Cu_xNb_{2x}Ti_{1-3x}O_2$ (x=0.2) electrode after cycling at a different number of cycles. A Swagelok cell was used instead of coin cell. After cycling to a specific number of cycles, the cell was stopped and opened in the glove box. The electrode was washed using anhydrous dimethyl carbonate (DMC), and then the powder was dried and sealed to avoid contact with air during the XRD run. From the data in Figure 5-8, it is clear that there is no change in the XRD pattern during cycling, which indicates a good structural stability.

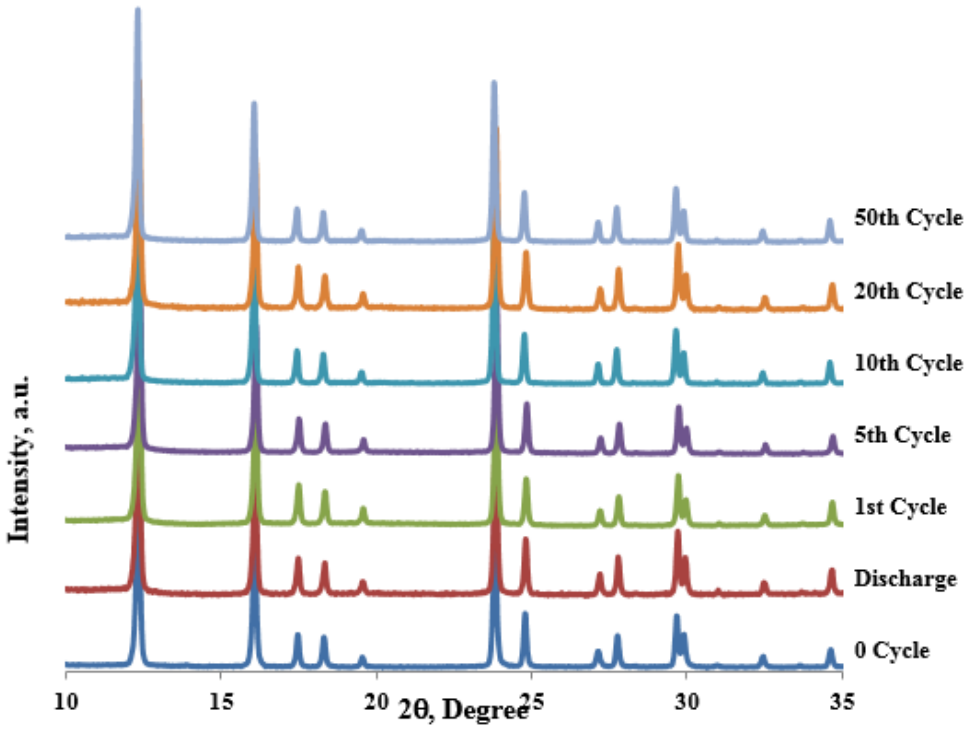

Figure 5-8: Ex-situ XRD patterns of $Cu_xNb_{2x}Ti_{1-3x}O_2$ (x=0.2) at different discharge and charge state. a. u. refers to arbitrary units of intensity as data sets have been offset vertically to show the evolution of the XRD patterns with cycle number.

The calculated lattice parameters and cell volume of Cu-Nb co-doped rutile, Figure 5-9, show a decreasing trend in the initial cycles. Upon the first discharge process, a very slight expansion of the lattice parameters occured from a= 4.6716Å, c= 3.019 Å to a= 4.6732Å and c= 3.02 Å, corresponding to Li^+ intercalation. Upon the first charge process, the lattice parameters return to a= 4.6711Å and c= 3.0185 Å. The constant variation of lattice parameters and cell volume during discharge in subsequent cycles (5th cycle and above) reveals the reversibility of Li ion (de)intercalation.

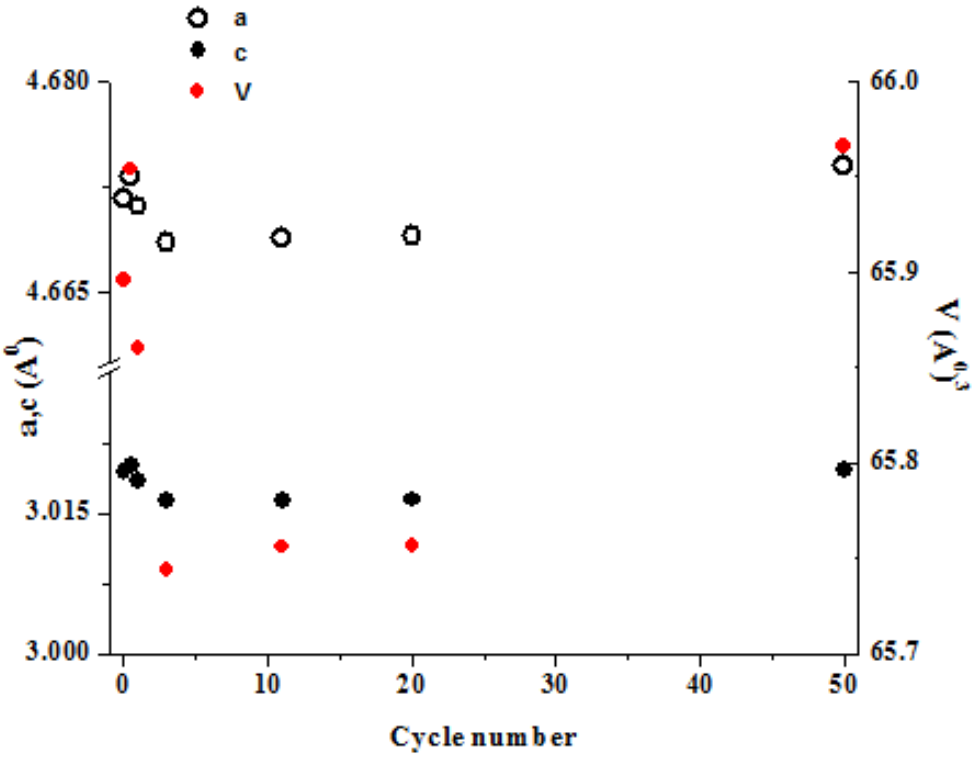

Figure 5-9: Variation in lattice parameters and cell volume of $Cu_xNb_{2x}Ti_{1-3x}O_2$ (x=0.2) with number of cycles and e.s.d ≤ ±(4).

5.4 Discussion

The XRD patterns clearly reveal the formation of pure- phase rutile solid solutions. The diffraction peaks were shifted towards smaller angles with increasing x.

The calculated cell parameters are consistent with those reported earlier (236,346) which increase with x. It indicates that the presence of dopants in the crystalline structure of rutile causes crystal lattice expansion. Lattice parameters in both systems increase linearly obeying Vegard's law, consistent with the result of previously published study (346). Although deviation from Vegard's law has been reported for $Cu_xNb_{2x}Ti_{1-3x}O_2$ (236) system, the variation in unit cell parameters of the $Cu_xTa_{2x}Ti_{1-3x}O_2$ system is not published before.

The voltammogram of Cu, Nb co-doped TiO_2 is clearly different to that of rutile TiO_2; the position of both cathodic and anodic peaks are shifted to higher voltage, 1.75 and 2.1 V respectively compared to those for rutile-TiO_2, 1.35 and 1.85V. In general, the shift could be ascribed to either the formation of solid solutions or change in particle size (349). The increase in the peak intensity indicates greater incorporation of Li in the electrode. An additional cathodic peak at 1.1V disappeared in the following cycles which indicated an irreversible phase transformation during cycling as reported in previous studies for rutile (154,177,194,216,350).

All the Cu, M co-doped TiO_2 (M= Nb, Ta) materials synthesized using the solid state method show higher storage capacities and better stabilities when compared with undoped-TiO_2. Under the same cycling conditions, up to 1 mole Li^+ intercalated during the first cycle for both systems with a capacity of 56-78 mAh g^{-1}.

The significant irreversible loss of capacity is probably not attributed to a solid electrolyte interface (SEI) formation since the cycling potential was restricted to be above 1.0V, which is above the reduction potential of electrolyte (194). The studies of significant irreversible loss of capacity in nano-sized rutile electrodes suggest that the complete extraction of the Li^+ ions inserted at the beginning is impossible. This may be due to a major structural change related to a new phase formation around $Li_{0.4}TiO_2$ in either a hexagonal(*R-3m*) or a cubic salt (*Fm-3m*) structure, but the accurate structure of this phase is still under investigation by others groups. X-ray diffraction data and calculation methods suggest that the new phase can be indexed by a hexagonal structure(*R-3m*) (154,194,216). On the other hand, the

neutron diffraction results and simulation of a chemically-lithiated rutile (about 0.43 Li/Ti at room temperature) indicate the formation of a layered phase having a monoclinic structure (*P*2/*m*) closely similar to the hexagonal phase (194,216). In Cu, Nb co-doped rutile system, ex-situ XRD study does not confirm any major structural change during cycling.

Large capacity fading cannot be caused by structural change during cycling but the disappearance of the cathodic peak at 1.1 V in the subsequent cycles can be suggested as the main contribution to irreversible capacity loss in the first two cycles. A possible explanation for an irreversible capacity loss in subsequent cycles could be that it is associated with either an irreversible surface reaction or electrode polarization due to poor electronic conductivity (350). From the 3^{rd} and 10^{th} cycle, the capacity of Cu, Ta and Cu, Nb systems respectively became reversible and the capacity loss is smaller. However, in all cycles, full removal of the Li ions intercalated during the cycling is difficult. It is speculated that the slow diffusion in the *ab* planes ($D_{ab}=10^{-15}cm^2/s$) and Li-Li repulsive interactions in the *c* direction provide a trapping mechanism; therefore, the *c* channel is blocked and traps a considerable amount of the intercalated Li^+ ions (193,194,216).

The Cu, Ta co-doped system has poor electrochemical performance and degradation in terms of capacity fade which is the major limitation. The drastic capacity fading leads to poor cyclability and limits its application as anode for Li ion battery.

In the current systems, ex-situ XRD data confirmed that there is no significant change in the XRD patterns which indicates that the lithium intercalation into co-doped TiO_2 remains in a single phase and the strong intensity of the diffraction peaks indicates that the electrode material has a stable crystalline structure during the charge-discharge process. However, the identification of the lithium ion positions by XRD is difficult due to low signal strength, the low sensitivity to light weight elements such as Li which are essentially non scattering in X-rays and it is significant to estimate their position in the crystal structure.

5.5 Conclusion

Considering the comparable ionic radii of Ti^{4+}, Cu^{2+}, Ta^{5+} and Nb^{5+} ions, we conclude that there is a complete substitution of titanium by copper and niobium ($0.05 \geq x \leq 0.2$) or copper and tantalum (($0.05 \geq x \leq 0.15$), respectively, at all concentrations studied and a series of solid solution has been synthesised as confirmed by XRD.

The shift in the XRD peak positions may occur due to the lattice distortion; hence, the expansion of the TiO_2 unit cell caused by the substitution of elements with different ionic radii onto Ti sites, Cu^{2+}, Nb^{5+} and Ta^{5+}, are bigger than Ti^{4+}.

Results of electrochemical measurements show that the electrochemical properties of the rutile TiO_2 have been modified by the co-doping. High capacity value was obtained for co-doped rutile (56- 78 mAh/ g) compare with undoped (26 mAh/ g) which is attributed to the increasing of the lattice dimensions of co-doped materials.

Despite considerable changes in the material structure after the first cycle, the highly reversible and stable charge-discharge capacity in the subsequent cycles suggests that a good stability of the electrode has been achieved during the subsequent cycles.

No structural transformations were detected by ex-situ XRD at different cycles; also the strong intensity of the diffraction peaks point to the electrode material maintaining a good crystalline structure during the charging-discharging process. However, it is important to clarify the solid solution behaviour and structure evolution mechanism by efficient technique such as neutron diffraction as it has an advantage over the XRD for the study of the material structure due to their relative sensitivity to Li ions, which allows the detailed determination of Li-ion positions and fractions.

TiO_2 is becoming increasingly a hot topic in LIBs research with several possible TiO_2 polymorphs considered in these ‘rocking-chair’ Li-ion batteries (152). Doping of rutile with the objective of increasing the lattice parameters and easy intercalation of lithium ions has not been reported previously.

6. THE ELECTRICAL BEHAVIOUR OF $Cu_XM_{2X}Ti_{1-3X}O_2$; $M=Nb^{5+}$, Ta^{5+}

The electrical properties of the $Cu_xM_{2x}Ti_{1-3x}O_2$; $M=Nb^{5+}$, Ta^{5+} solid solutions were investigated by IS measurement with various kinds of electrodes, sputtered Au, Pt and paste Au and paste Pt by using two sets of equipment; an Agilent E4980A LCR meter for low temperature measurements (10 – 320 K) and an Agilent 4294A for high temperature measurements (25 – 350 ºC). The variations in the electrical properties with atmosphere and also the effect of dc bias application are reported.

6.1 Impedance data for $Cu_xTa_{2x}Ti_{1-3x}O_2$ (x = 0.10)

6.1.1 With sputtered electrodes

Impedance data for $Cu_xTa_{2x}Ti_{1-3x}O_2$ (x = 0.10) sputtered with gold are illustrated in Figure 6-1. Two components can be seen in the Z* plot, Figure 6-1 (a), as two well-defined semicircular arcs at high and low frequency which can be assigned to an equivalent circuit composed of two parallel RC elements. With an increase in temperature, a semicircle with non-zero intercept is observed at high frequency. The electrical properties can be described as a series combination of two parallel RC elements in which R represents the resistance and C the capacitance and interpreted according to “brick layer” impedance model. The corresponding equivalent circuit is given in Figure 6-1(b).

In the Z″/M″ plot, Figure 6-1 (c), two overlapping peaks at high frequency and another peak at low frequency can be clearly seen; at high temperature, the Z″/M″ plot shows one peak which might belong to the grain boundary contribution.

The admittance plots in Figure 6-2 (a) shows two plateaux at high and low frequency separated by dispersion over a range of intermediate frequencies. The activiation energy of the two plateaux in Figure 6-2 (a) are very different and above ~235°C the two resistances became comparable. Spectroscopic plots of capacitance at different temperatures are presented in Figure 6-2 (b). Two different electrical regions can be distinguished at 10^{-12} and 10^{-10} F suggesting that they belong to bulk and grain boundary response respectively (351). The capacitance of the low frequency plateau decreases with increasing temperature. At low

temperature, subambient, the sample bulk has a capacity value ~ 7.1 pF/cm, Figure 6-2 (b) left.

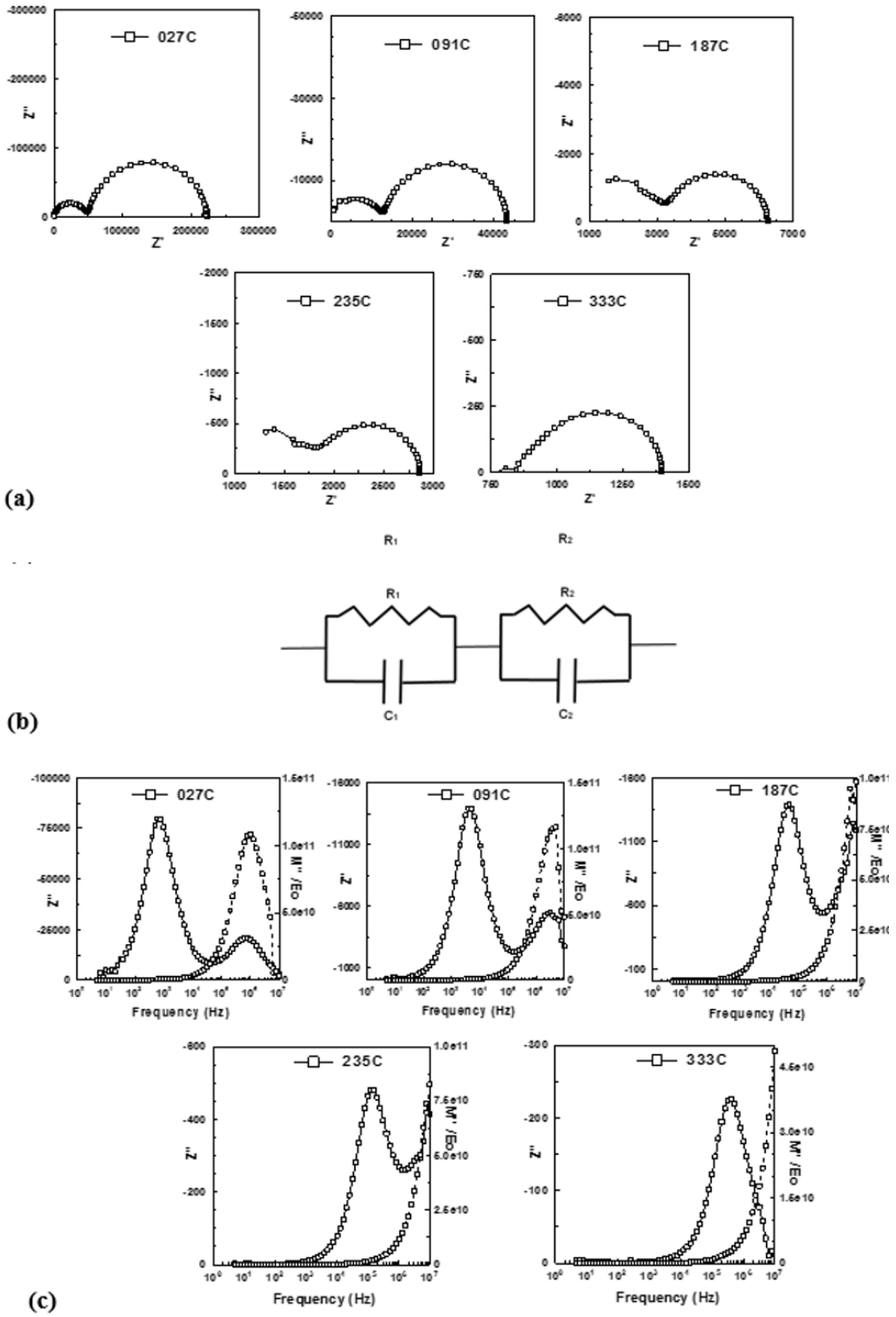

Figure 6-1: Impedance data for $Cu_xTa_{2x}Ti_{1-3x}O_2$ (x =0.10) with sputtered Au electrodes at different temperatures in air: (a) Z* plots, (b) the corresponding equivalent circuit and (c) Z″/M″ spectroscopic plots.

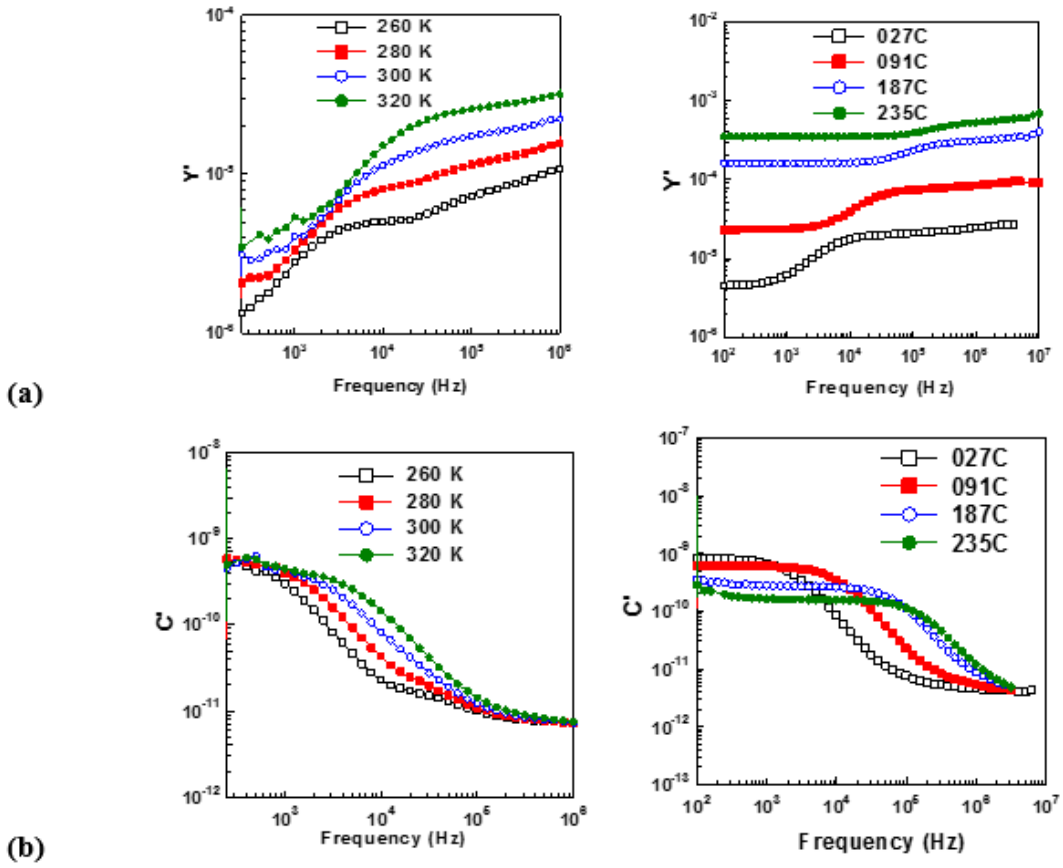

Figure 6-2: Spectroscopic plots of: (a) admittance and (b) capacitance for $Cu_xTa_{2x}Ti_{1-3x}O_2$ (x =0.10) with sputtered Au electrodes at subambient temperatures (left) and high temperature (right) in air.

The relative dielectric permittivity ε_r was determined through capacitance measurements performed at 1.0 MHz, and calculated from equation (351):

$\varepsilon_r = C.d/\varepsilon_o.A,$ (1)

where C is the capacitance, *d* is the sample thickness, *A* is the sample area and ε_o is the vacuum permittivity, 8.854x 10^{-14} F/cm.

The relative dielectric permittivity is 80.19 which is in fairly good agreement with the permittivity value of rutile TiO_2 reported by Moulson, ~100 (352) .

Impedance data for the same material with sputtered Pt electrodes are presented in Figure 6-3 and Figure 6-4. It can be seen that the sample has a similar electrical behaviour to that with sputtered Au electrodes.

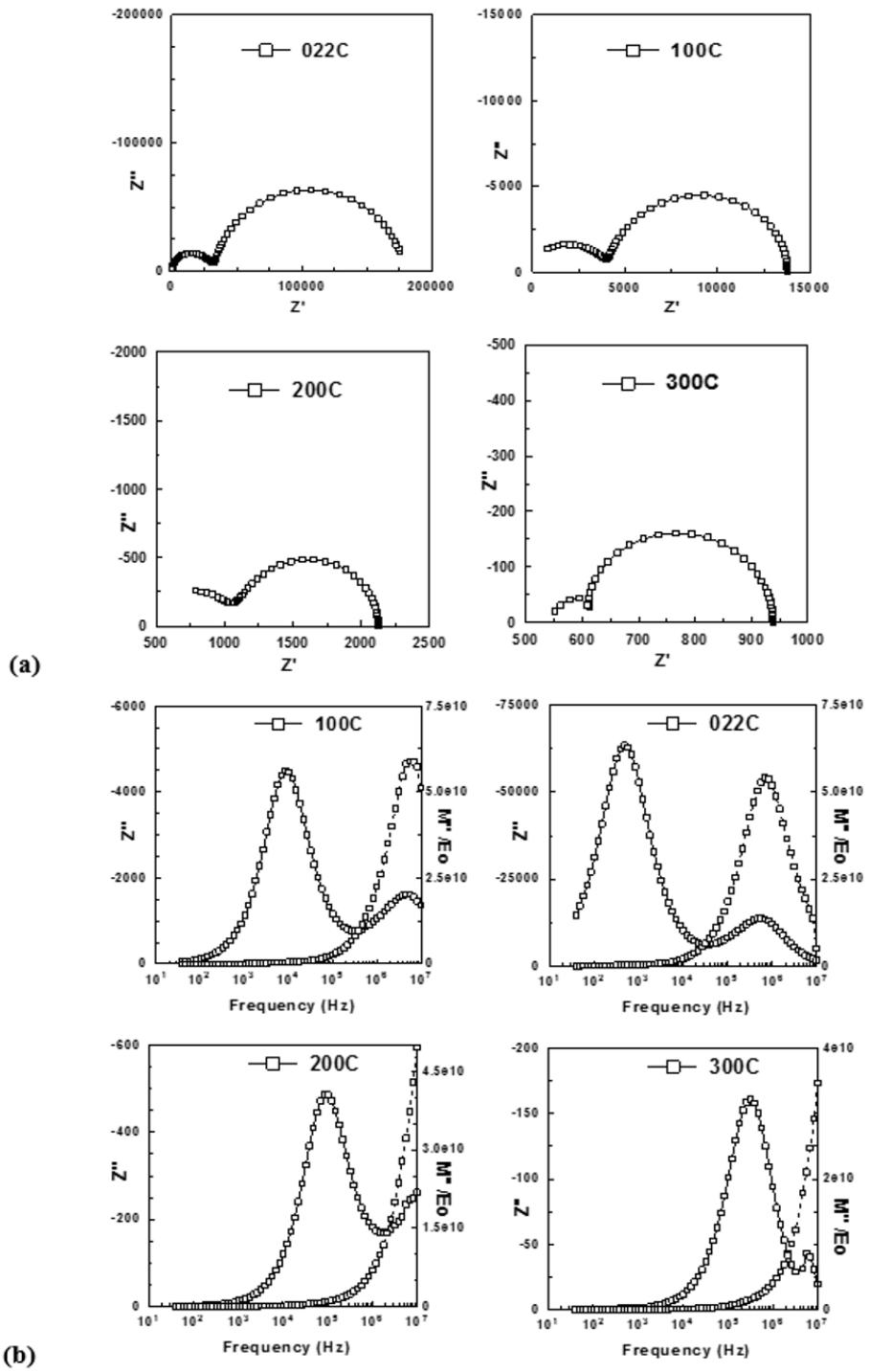

Figure 6-3: Impedance data for $Cu_xTa_{2x}Ti_{1-3x}O_2$ (x =0.10) with sputtered Pt electrodes: (a) Z* plot, and (b) Z″/M″ spectroscopic plot at different temperatures in air.

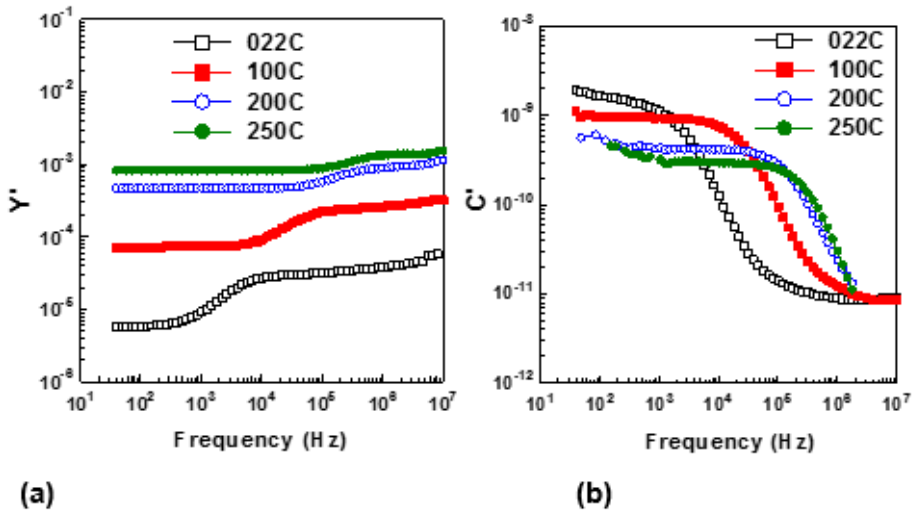

Figure 6-4: Spectroscopic plots of: (a) admittance and (b) capacitance for $Cu_xTa_{2x}Ti_{1-3x}O_2$ (x =0.10) with sputtered Pt electrode at different temperatures in air.

A significant change in the low frequency (grain boundary) capacitance values with temperature was observed in the spectroscopic plots of capacitance and is illustrated in Figure 6-5 for both Au and Pt electrodes. The capacitance decreases with increasing temperature. There are two (at least) possible explanations for this variation in capacitance. One possibility is that the grain boundary, but not the bulk, shows a large, negative temperature coefficient of capacitance. Another possibility arises from the fact that the low frequency plateau does not correspond simply to the grain boundary capacitance but is a more complex function of the equivalent circuit parameters. This is discussed in more detail in section 6.3.1.

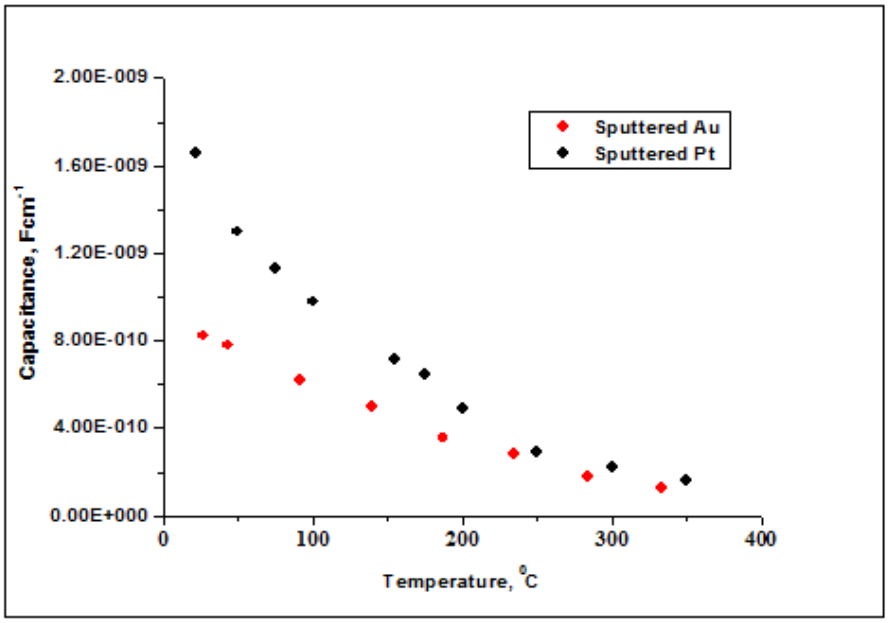

Figure 6-5: The variation of the low frequency capacitance with temperature in air for x=0.10 with sputtered Au (red) and Pt (black) electrodes.

Figure 6-6 (a) shows the electrical conductivities of both components of the sample sputtered with Au in Arrhenius format. The temperature dependence of the electrical conductivity was plotted based on the Arrhenius equation with the following expression:

$$\log(\sigma) = -Ea/k_BT + \log A \qquad (2)$$

where σ is the electrical conductivity in S/cm, Ea is the activation energy, k_B is the Boltzmann constant, T is temperature in K (absolute temperature), and A, the intercept, is the pre-exponential factor. The electrical conductivity is calculated from electrical resistance. The experimental value of bulk and grain boundary resistance (R_b and $R_{g.b}$) at different temperatures were obtained from the intercepts of the semicircular arcs on the real axis (Z′). The procedures for calculating bulk and grain boundary conductivities are based on a brick layer model since the resistance of the grain boundary is higher than the bulk resistance.

The grain boundary conductivity has higher activation energy than the bulk conductivity and the Arrhenius plots cross at 1000/T ≅ 2.2, i.e. T≅ 180°C. At this temperature, the arcs in Z* plots became of equal size and the distinction between high and low frequency plateaux in log Y/ log f plots disappears. At high temperature, the sample exhibited nonlinear behaviour which might due to a

change in conduction mechanism or crystal structure during the measurement. The sample sputtered with Pt exhibits a similar electrical behaviour as shown in Figure 6-6 (b).

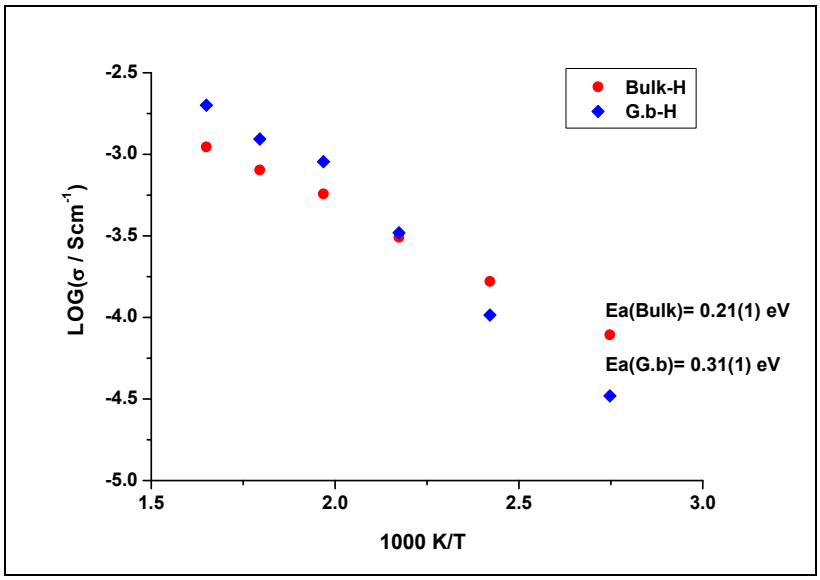

(a)

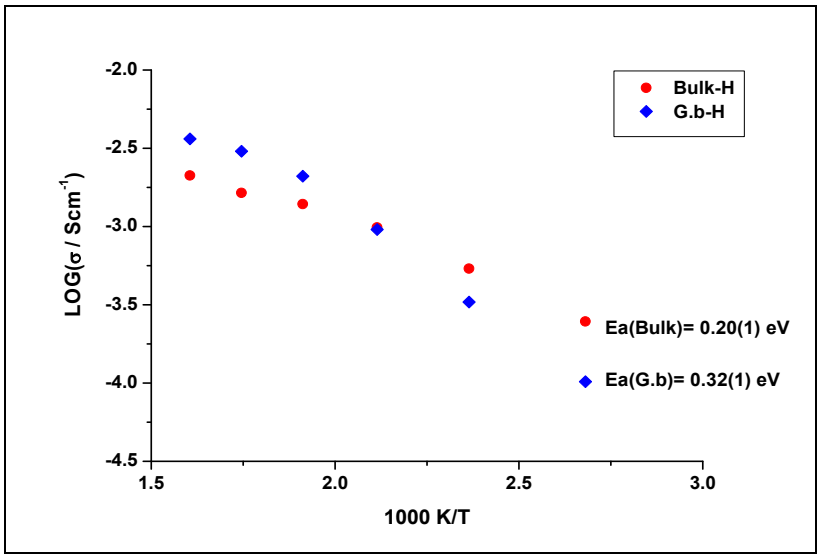

(b)

Figure 6-6: Arrhenius plot of electrical conductivity,σ showing activation energies, Ea, for $Cu_xTa_{2x}Ti_{1-3x}O_2$ (x =0.10) sputtered with: (a) Au and (b) Pt electrodes in air.

In order to check the reproducibility and reversibility on cooling, impedance data were collected at different temperatures upon heating and cooling in air for a

sample sputtered with different types of electrodes, Au and Pt; data are presented in Appendix A.

Arrhenius plots obtained on heating- cooling are presented in Figure 6-7.

A slight difference can be seen in the conductivity of grain boundary, however both bulk and grain boundary on cooling have almost the same activation energies.

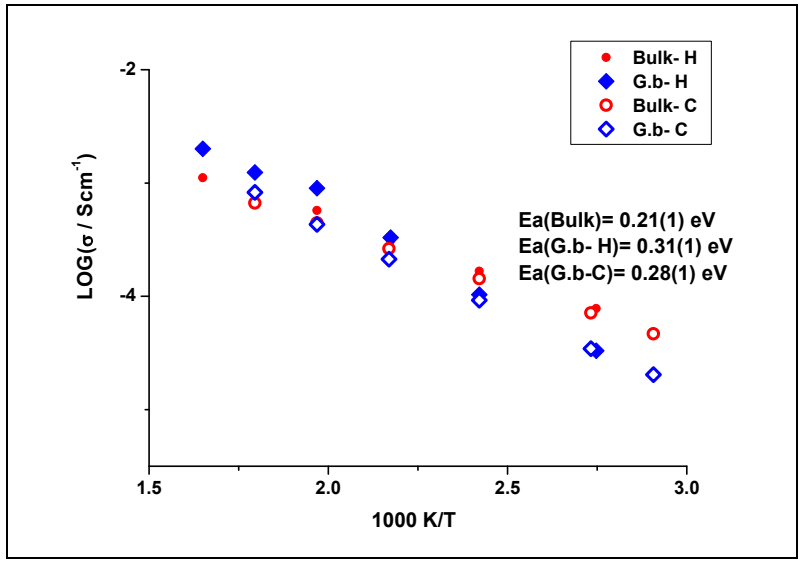

(a)

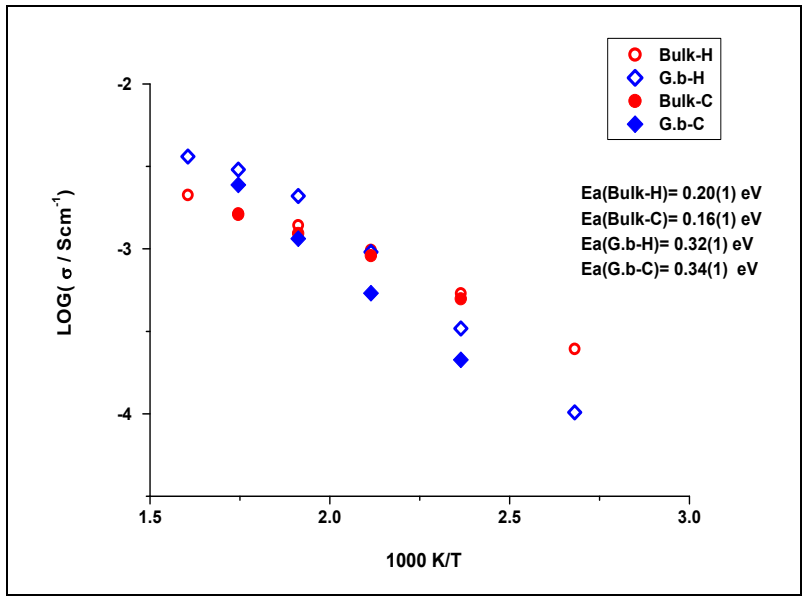

(b)

Figure 6-7: Arrhenius plot of conductivity, σ for $Cu_xTa_{2x}Ti_{1-3x}O_2$ (x =0.10) with: (a) sputtered Au and (b) sputtered Pt electrode on heating (H) and cooling (C) at different temperatures in air.

To determine whether atmosphere during impedance measurements had any effect on the impedance data, impedance measurements were performed in atmospheres of either N_2 or O_2, at different times. The variation in the resistance of bulk and grain, Figure 6-8, shows that N_2 has no effect on the bulk and grain boundary impedance. When the sample was exposed to O_2, a slight change in the grain boundary resistance was observed due to the fluctuation of temperature in the furnace chamber.

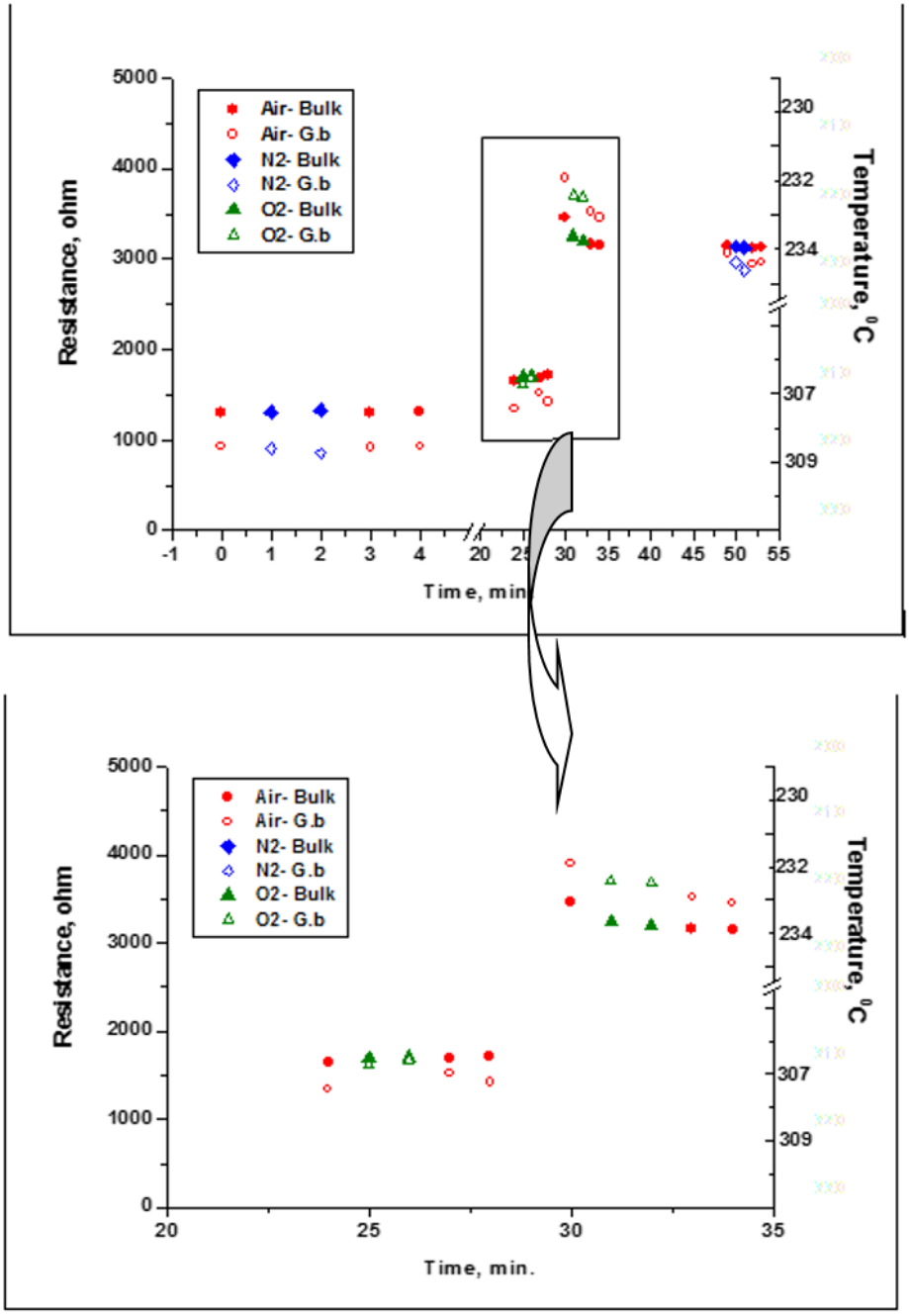

Figure 6-8: Variation in the resistance of bulk and grain boundary for $Cu_xTa_{2x}Ti_{1-3x}O_2$ (x = 0.10) with sputtered Au electrode in different atmosphere at different times.

6.1.2 Influence of the electrode type

In order to study the effect of type and electrode processing on the electrical behaviour, impedance measurements were performed for $Cu_xTa_{2x}Ti_{1-3x}O_2$ (x = 0.10) coated with Au and Pt paste electrodes.

Impedance data with Au paste electrode, Figure 6-9 and Figure 6-10, show one semicircle in Z* at low temperature (120-200K). With increasing temperature, an inclined spike is seen at low frequencies which became semicircular arc at high temperature, 200° and 300°C. Spectroscopic plots of Z″/M″, Figure 6-9 (b), show overlapping peaks at low temperature (120-140K). With increasing temperature, a second, low frequency peak appears in Z″.

The admittance plot, Figure 6-10 (a), reveals a plateau at high frequency which might correspond to the bulk conductivity, and emergence of a plateau at low frequency.

Spectroscopic plots of capacitance, Figure 6-10 (b), show a plateau at high frequency in picofarads region and a second plateau at low frequency with a capacitance value in range of nanofarads to reach 1.9 E-8 F at 300 °C. The capacitance plot at high temperature, 200° and 300°C, shows the presence of third component at low frequency which might associated with a surface layer component.

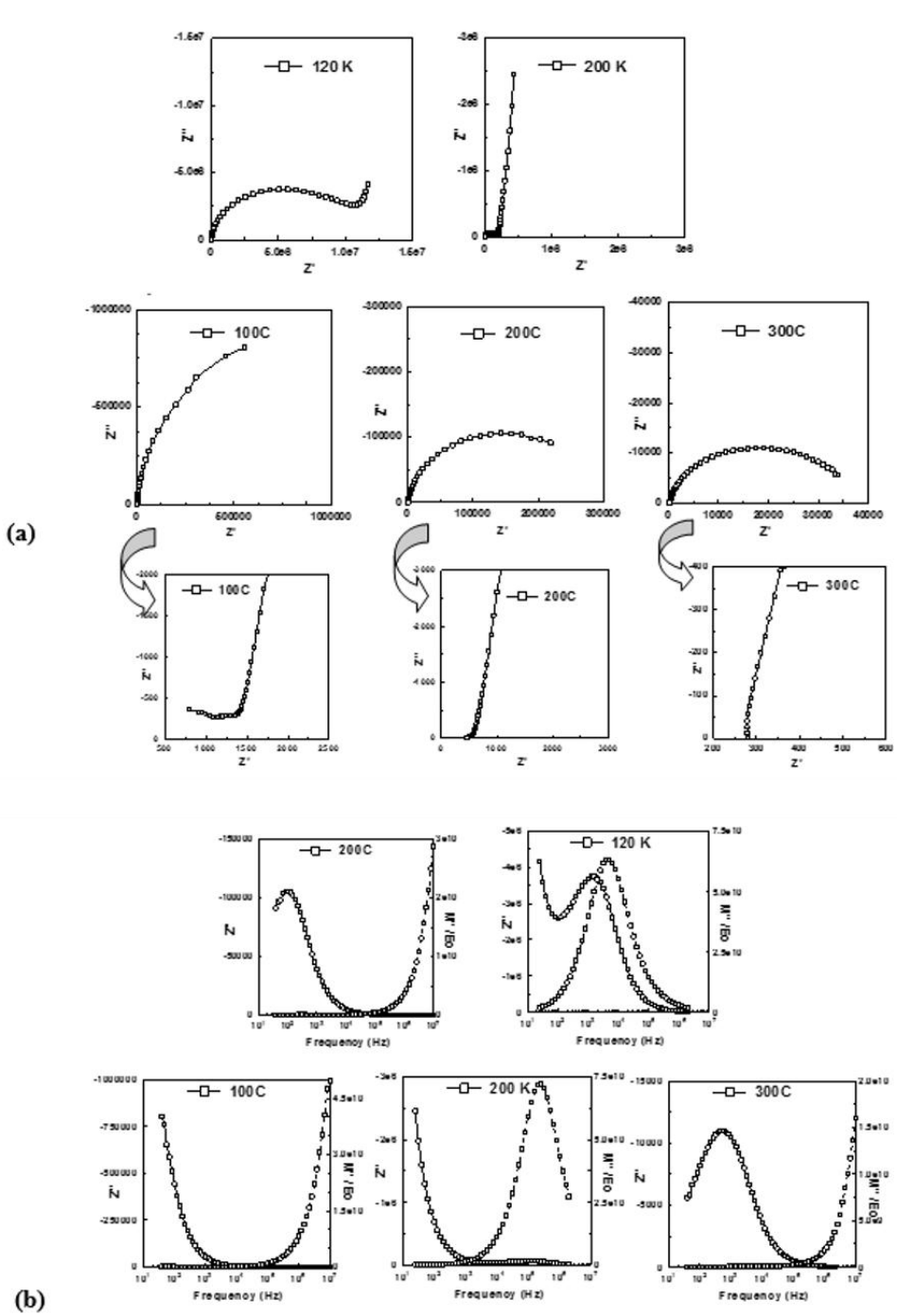

Figure 6-9: Impedance data of: (a) complex plane, Z* and (b) Z″/M″ spectroscopic plot for $Cu_xTa_{2x}Ti_{1-3x}O_2$ (x =0.10) with Au paste electrode at different temperature in air.

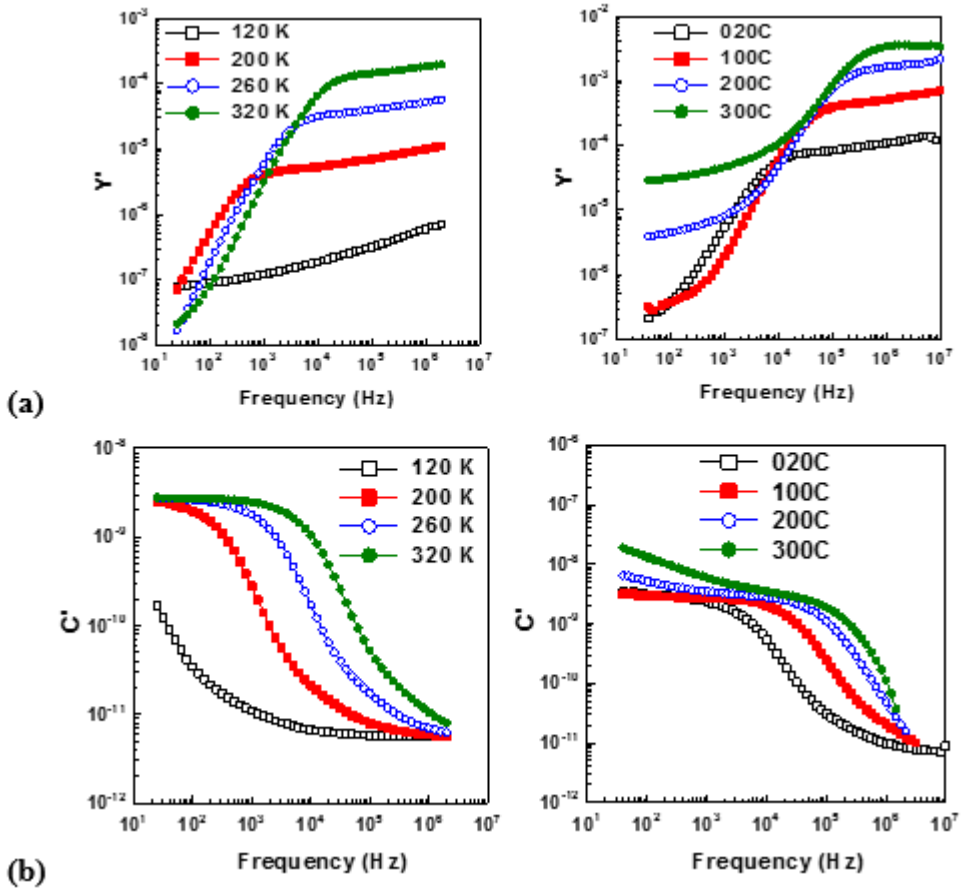

Figure 6-10: Spectroscopic plots of: (a) admittance and (b) capacitance for $Cu_xTa_{2x}Ti_{1-3x}O_2$ (x =0.10) with Au paste electrodes at different temperature in air.

The capacitance values at different temperature were corrected for sample geometry and blank capacitance of the jig, and are summarised in Table 6-1. The sample bulk has a capacitance value ~ 5.6 $pFcm^{-1}$; the permittivity was calculated to be 63.25 which is lower than that of rutile TiO_2, ~100.

Table 6-1: The capacitance values of $Cu_xTa_{2x}Ti_{1-3x}O_2$ (x = 0.10) with Au paste electrode at different temperature in air, corrected from blank jig capacitance.

Temperature	C_1, Fcm^{-1}	C_2, Fcm^{-1}	Temperature	C_1, Fcm^{-1}	C_2, $Fcm^{-1}m$
100K	5.7 E-12	-	320K	8.0 E-12	2.8 E-9
120K	5.65 E-12	-	20°C	8.8E-12	3.4E-9
140K	5.6 E-12	-	100°C	7.7E-12	3.4E-9
200K	5.7E-12	2.5 E-9	200°C	4.8E-12	6.5E-9
240K	6.0 E-12	2.7 E-9	300°C	-	1.9E-8
260K	6.3 E-12	2.7E-9			

Impedance data for the same material coated with Pt electrodes are presented in Figs.11-12. At low temperature, $140 \leq T \leq 320K$, the sample has a similar electrical behaviour to that with Au paste electrode. A third component can be distinguished at 320K as a spike in Z* plot, Figure 6-11 (a) and the emergence of a second peak in Z″ plot, Figure 6-11 (b). At high temperature (80-350°C) two semicircle can be seen in Z*. A third arc can be followed before it disappears at high temperature, 350°C. The spectroscopic plot of Z″/M shows a presence of two peaks and reflects the formation and disappearance of third component as an additional peak and disappears at high temperature.

Impedance spectra of the sample with Pt paste electrodes can be modelled by an equivalent circuit with series combination of three parallel RC elements including bulk, grain boundaries, and the surface layer.

The same Impedance data are shown in Figure 6-12 in term of spectroscopic plot of admittance and capacitance. Two plateaux were observed during the measurement in both admittance and capacitance plots at temperature above 200 K. However, three different electrical regions can be distinguished in the capacitance plot with capacitance values of ~10^{-12}, 10^{-10} and 10^{-9} F.

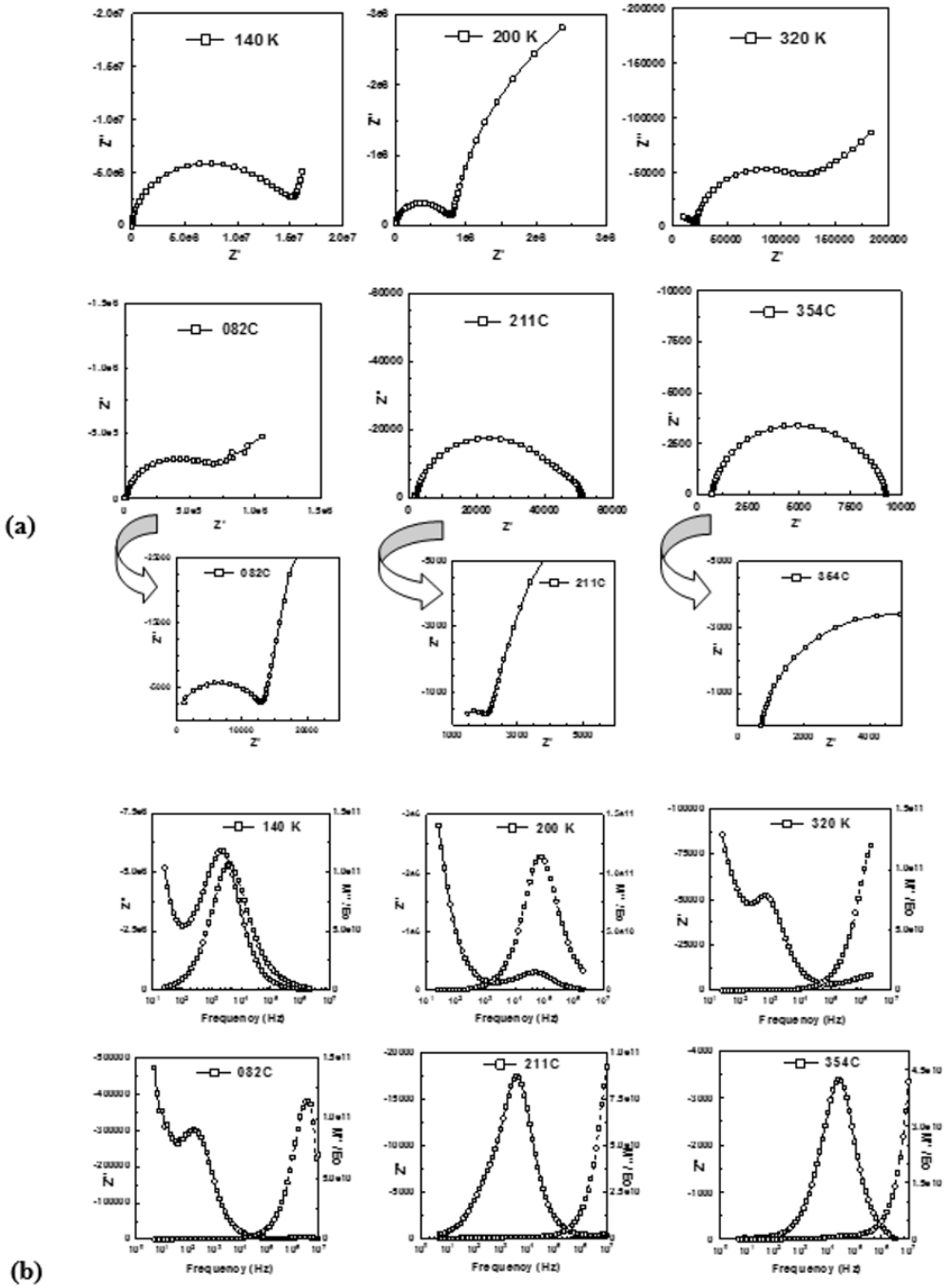

Figure 6-11: Impedance data of: (a) Z^* plot and (b) Z''/M'' for $Cu_xTa_{2x}Ti_{1-3x}O_2$ (x =0.10) with Pt paste electrode at different temperature in air.

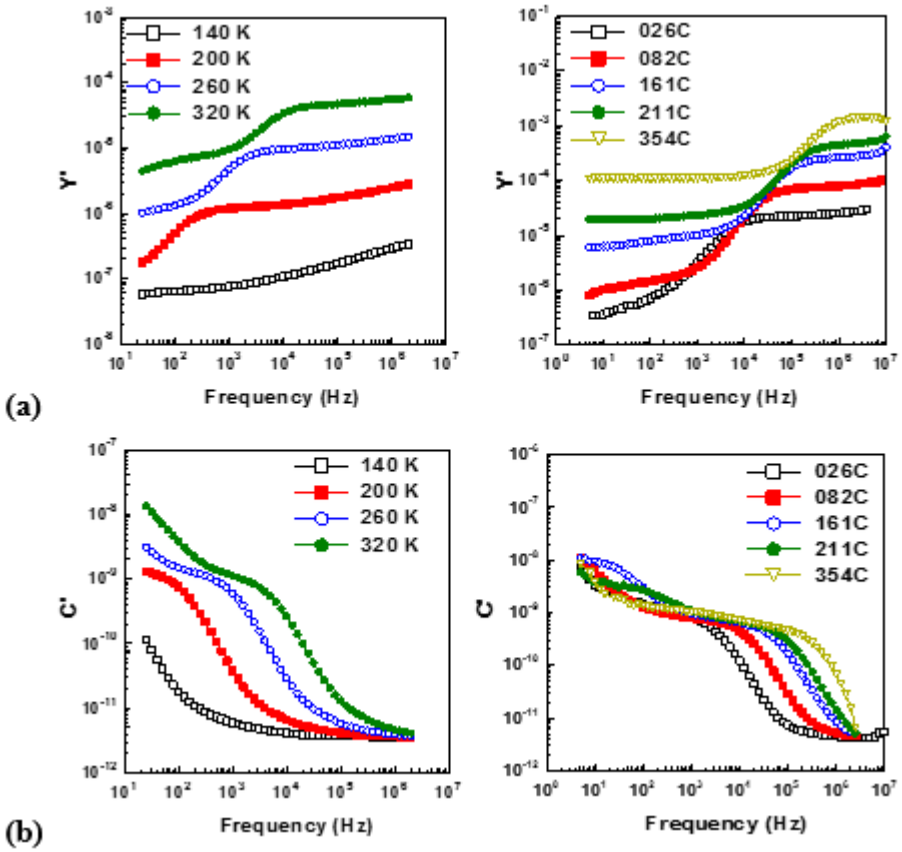

Figure 6-12: Spectroscopic plot of: (a) admittance and (b) capacitance at different temperatures for $Cu_xTa_{2x}Ti_{1-3x}O_2$ (x = 0.10) with Pt paste electrode at different temperature in air.

Arrhenius plot for conductivity of bulk and surface layer at low and high temperature were constructed as shown in Figure 6-13 (a) and (b) respectively. Note that the there is no visible grain boundary semicircle in the impedance spectra. Both components reveal a linear response with a break in the slope of Arrhenius plot for the bulk conductivity with activation energy of ~0.12 eV below 320K (-47°C) and 0.18 eV above. The bulk conductivity is higher than that of surface layer and the difference decreases when temperature increases, from 3 orders of magnitude at 200°C to 1.5 order of magnitudes at 400°C. The activation energy was 0.48 eV for the surface layer.

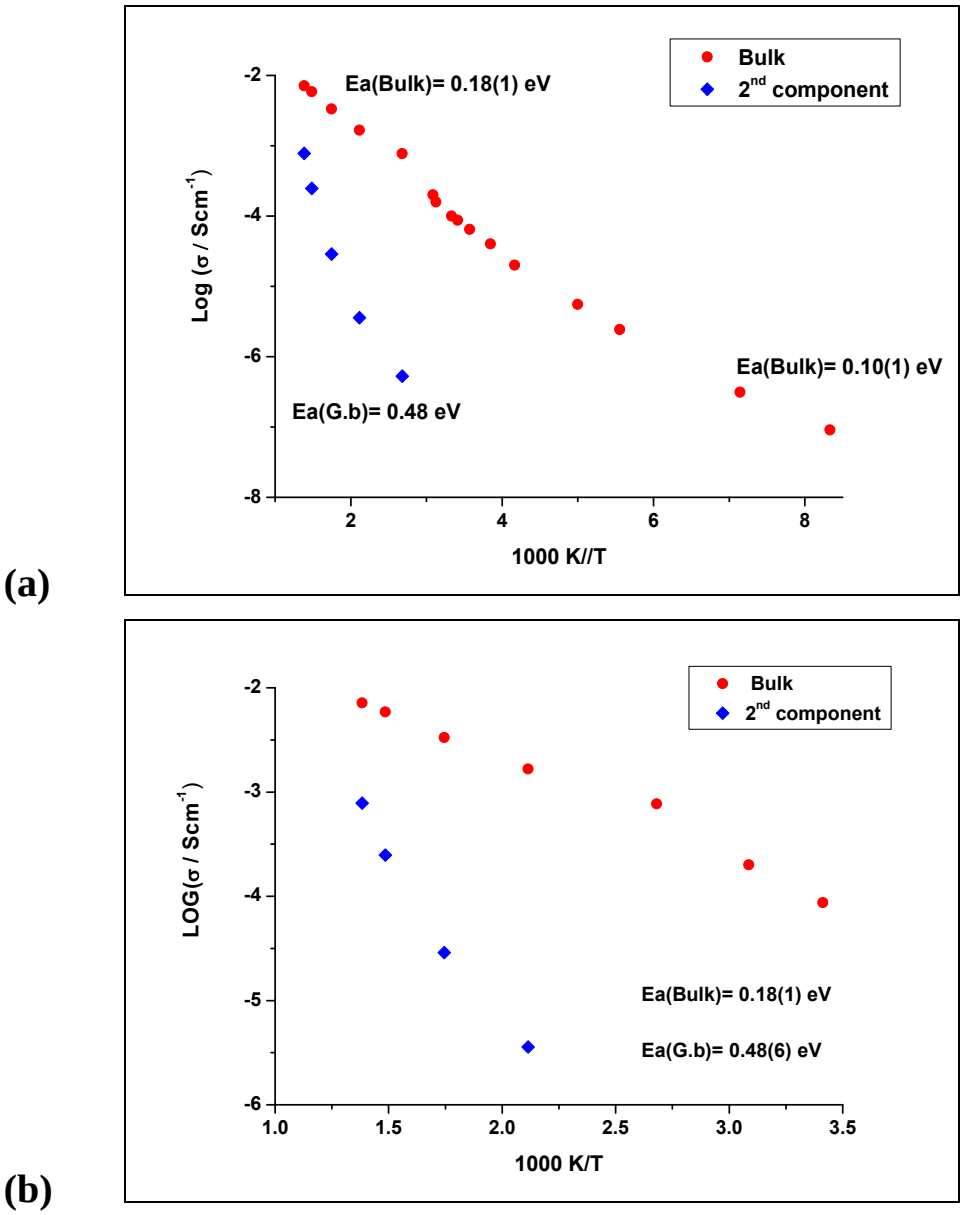

Figure 6-13: Arrhenius plot of bulk and grain boundary conductivities, showing activation energies, Ea, for $Cu_xTa_{2x}Ti_{1-3x}O_2$ (x =0.10) with Au paste electrode at different temperature: (a) low and high temperature and (b) high temperature in air.

The electrical conductivities of the sample with Pt paste electrode at low and high temperature are shown in Figure 6-14 (a) and (b) respectively. The electrical conductivity of bulk exhibits a similar behaviour to the sample with Au paste electrode. The activation energy for the bulk increased from ~0.10 eV below 220K (-53°C) to 0.20 eV beyond. A break in the slope of Arrhenius plot was observed for

grain boundary with increase in activation energy from ~0.21 eV below 320K (-47°C) to 0.32 eV beyond. In addition, the conductivity of the third component, which appears at high temperature due to the surface layer effect, increases rapidly when temperature increases with activation energy of 0.78 eV.

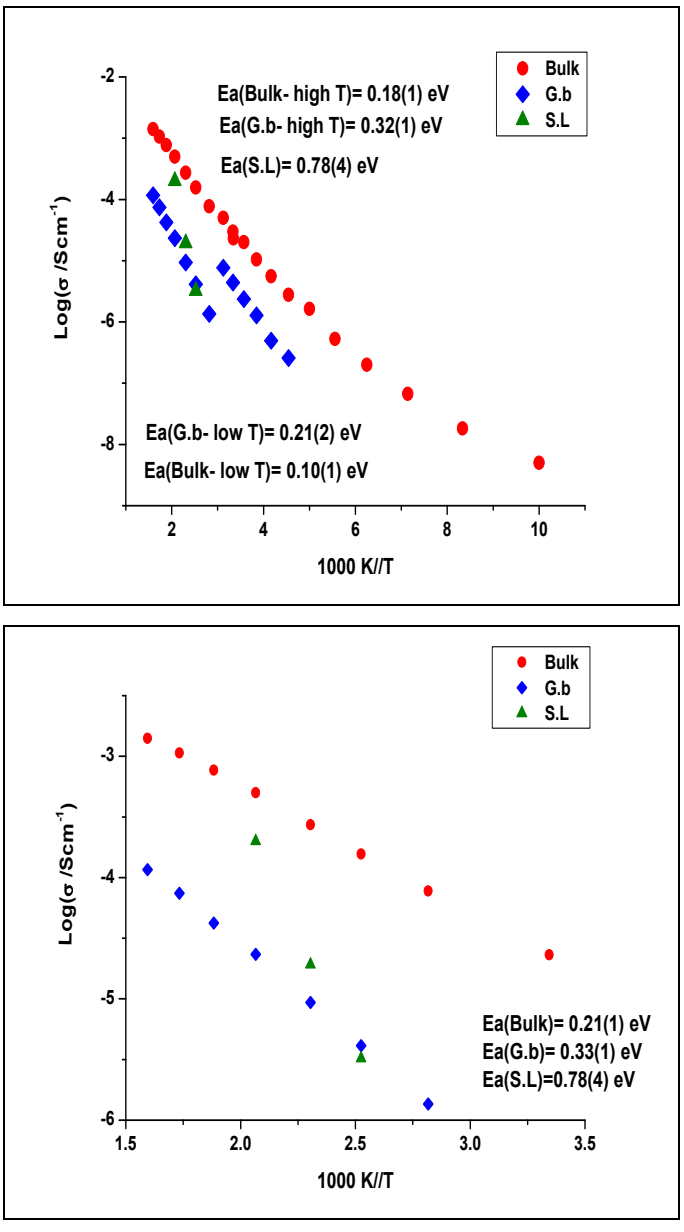

Figure 6-14: Arrhenius plot of bulk and grain boundary conductivities showing activation energies for $Cu_xTa_{2x}Ti_{1-3x}O_2$ (x =0.10) with Pt paste electrode at different temperature: (a) low and high temperature and (b) high temperature in air.

Impedance data on heating and cooling in air with Au paste and Pt paste electrodes are presented in Appendix A. The samples were heated stepwise to 500°C and then cooled stepwise at the same temperature intervals. There was no significant change in the bulk but a slight change in grain boundary and/ or surface layer resistancees.

Arrhenius plots with Au, Pt paste electrodes upon heating-cooling are illustrated in Figure 6-15. The conductivities are identical during heating and cooling with same activation energy for bulk and grain boundary while the activation energy of surface layer decreases during cooling.

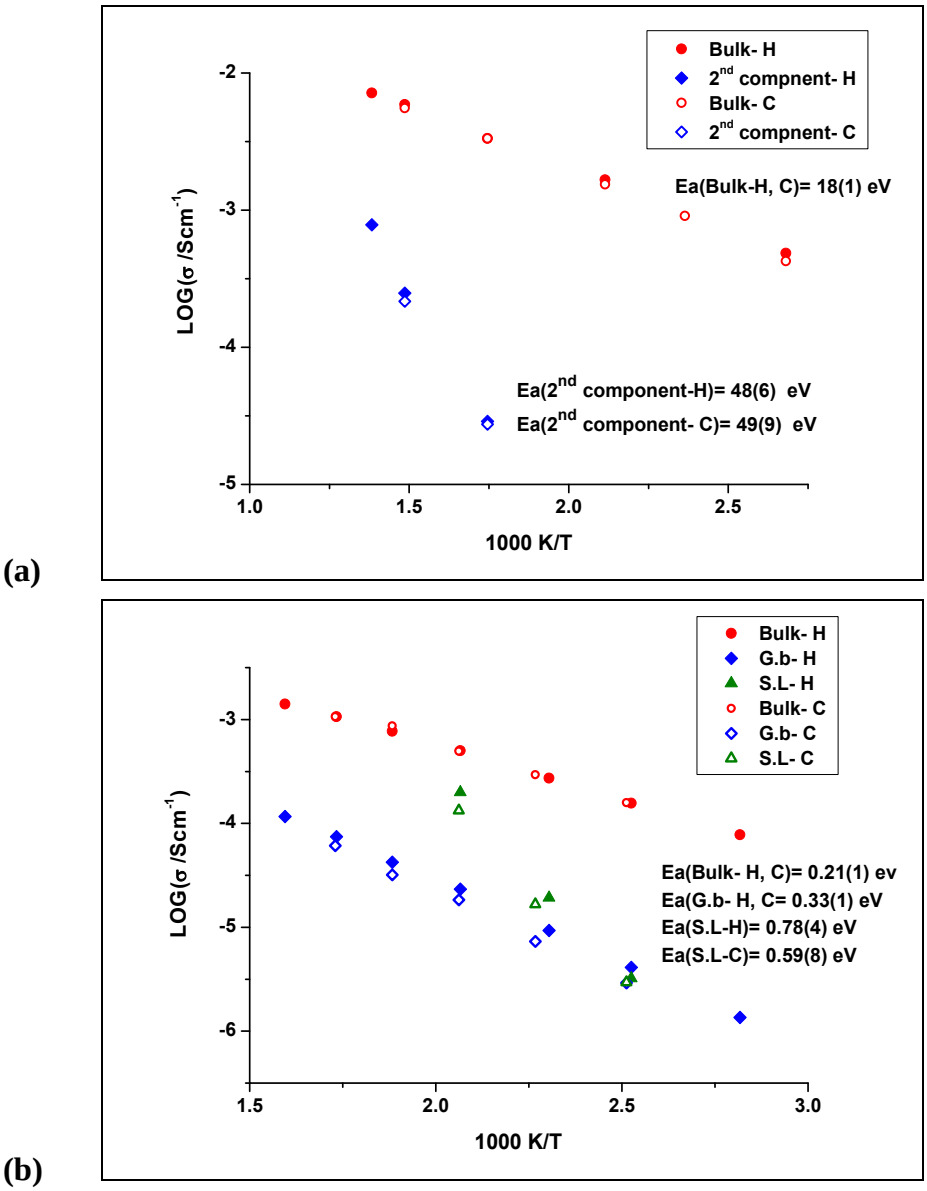

Figure 6-15: Arrhenius plot of conductivity,σ showing activation energies, Ea, for $Cu_xTa_{2x}Ti_{1-3x}O_2$ (x =0.10) upon heating (H) and cooling (C) at different temperature in air with: (a) Au paste and (b) and Pt paste electrode.

A comparison of results obtained with different electrodes is shown in Figure 6-16. The bulk conductivity for various electrode materials in Figure 6-16 (a) shows that the conductivity with sputtered Au and Pt paste electrode are similar and lower than that with Au paste and sputtered Pt. This observed behaviour is different for the conductivity of grain boundary; it is similar with sputtered Au and sputtered Pt

and both higher than that with Pt paste. Surface layer conductivities with Pt paste is higher than that with Au paste, as shown in Figure 6-16 (b).

The bulk and grain boundary have similar activation energy for all different types of electrode while that of surface layer with Pt paste electrode is higher. The activation energy of bulk, grain boundary and surface layer with different kinds of electrodes are illustrated in Table 6-2.

The parallel plots in Figure 6-16 (a) suggest that either the carrier concentration varies; perhaps by oxidation/reduction during electrode fabrication, or the electrode contact area may have varied. The differences are not great, $<$ 1 order of magnitude.

Table 6-2: Activation energies of grain, grain boundary and surface layer for the $Cu_xTa_{2x}Ti_{1-3x}O_2$ (x = 0.10) materials with different electrodes.

Electrode Type	Ea (Bulk), eV	Ea (G.b), eV	Ea (S.L), eV
Au paste	0.18	*	0.48
Pt paste	0.21	0.33	0.78
Sputtered Au	0.21	0.31	-
Sputtered Pt	0.20	0.32	-
In - Ga	0.18	0.25	-

* Electrical response from grain boundary is not resolved.

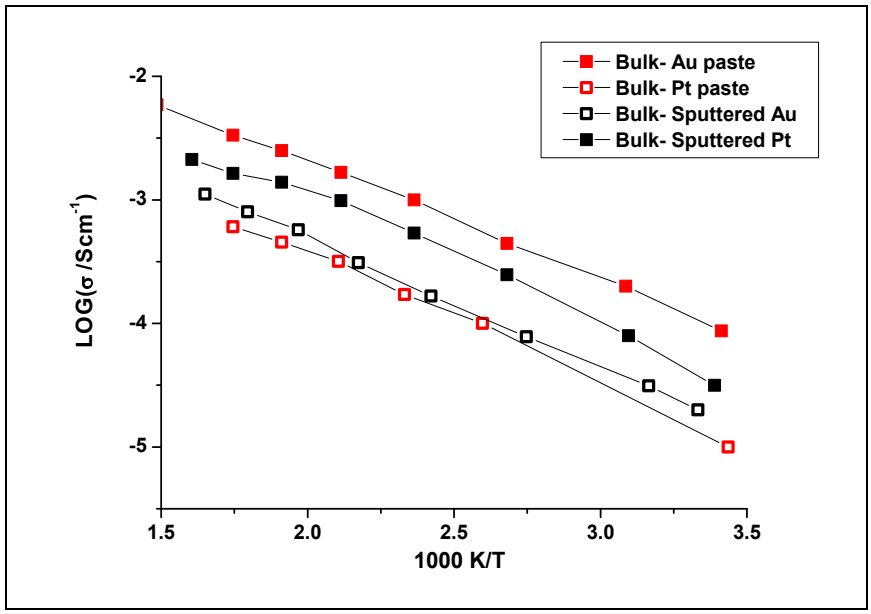

(a)

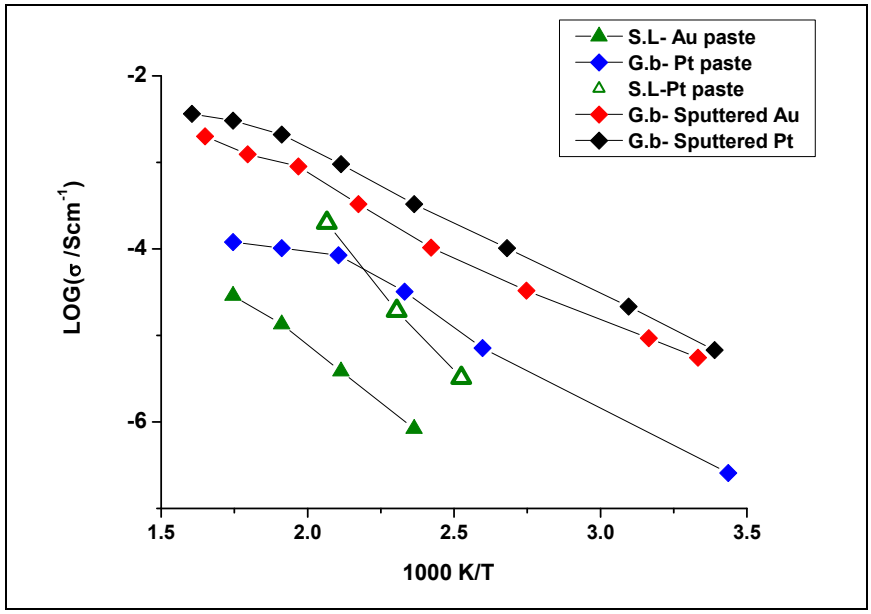

(b)

Figure 6-16: Arrhenius plot of: (a) bulk conductivity,σ_b and (b) grain boundary conductivity ($\sigma_{g\cdot b}$) and surface layer ($\sigma_{S.L}$) for $Cu_xTa_{2x}Ti_{1-3x}O_2$ (x =0.10) with different types of electrode; Au paste, Pt paste, sputtered Au and sputtered Pt at different temperature.

Since rather different results were obtained with sputtered/ paste Au/Pt electrodes, additional measuraments were carried out using In-Ga electrodes, Figure 6-17- Figure 6-18. The impedance results were similar to those reported here with sputtered Au, Pt electrodes.

In/Ga liquid alloy is used as electrodes in impedance measurements. It is quick and easily applied and works over a wide temperature range, -100 to 300°C (353). It does not require any thermal treatment when it is applied.

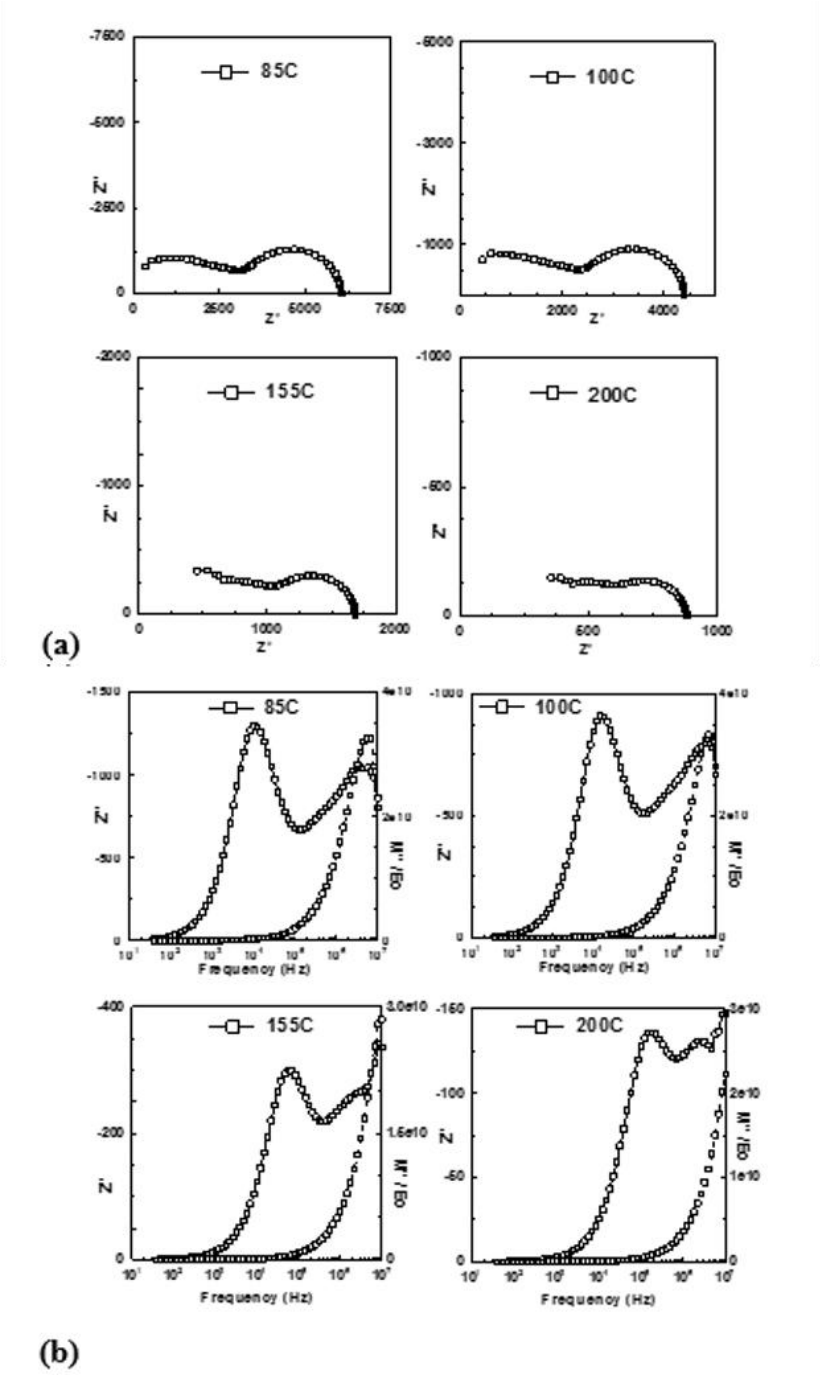

Figure 6-17: Impedance data for $Cu_xTa_{2x}Ti_{1-3x}O_2$ (x =0.10) with In-Ga electrode at different temperature in air: (a) Z* plot and (d) Z″/M″ spectroscopic plot.

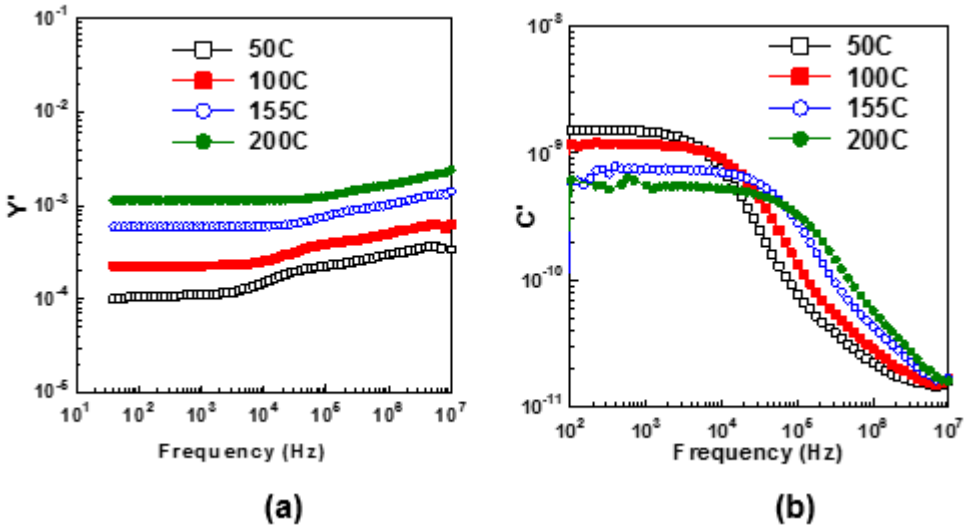

Figure 6-18: Spectroscopic plot of: (a) admittance and (b) capacitance for $Cu_xTa_{2x}Ti_{1-3x}O_2$ (x =0.10) with In-Ga electrode at different temperature in air.

In the Arrhenius plots, Figure 6-19 (a), the grain boundary conductivity has higher activation energy than the bulk conductivity and the Arrhenius plots cross at 1000/T ≅ 2.8, i.e. T≅ 85°C. At this temperature, the arcs in Z* plots became of equal size.

Comparison of the conductivities with In- Ga and sputtered Au are shown in Figure 6-19 (b). Bulk and grain boundary with In- Ga has a higher conductivity than those with sputtered Au. Activation energies of bulk and grain boundary with In- Ga, 0.18 eV and 0.25 eV respectively, are slightly lower compared to those with sputtered Au.

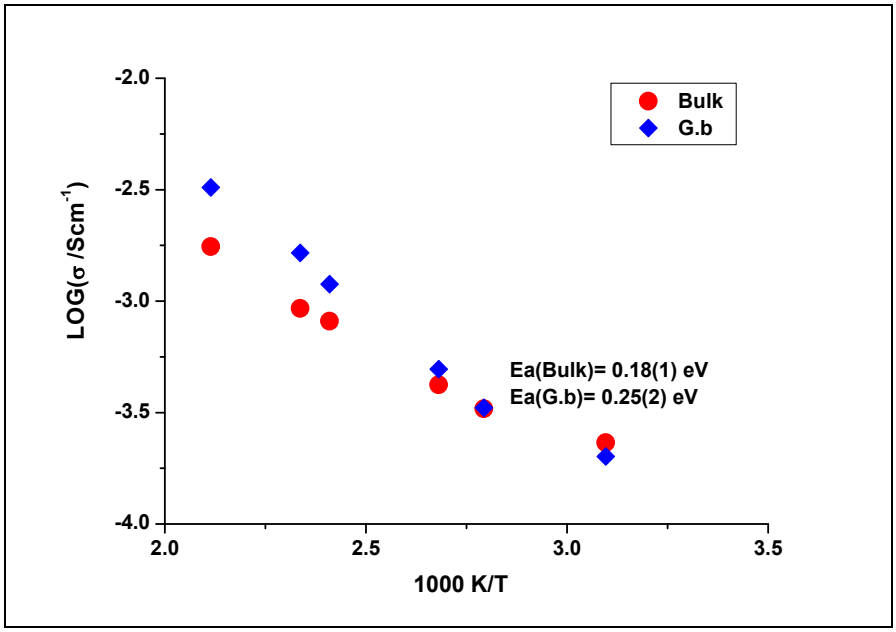

(a)

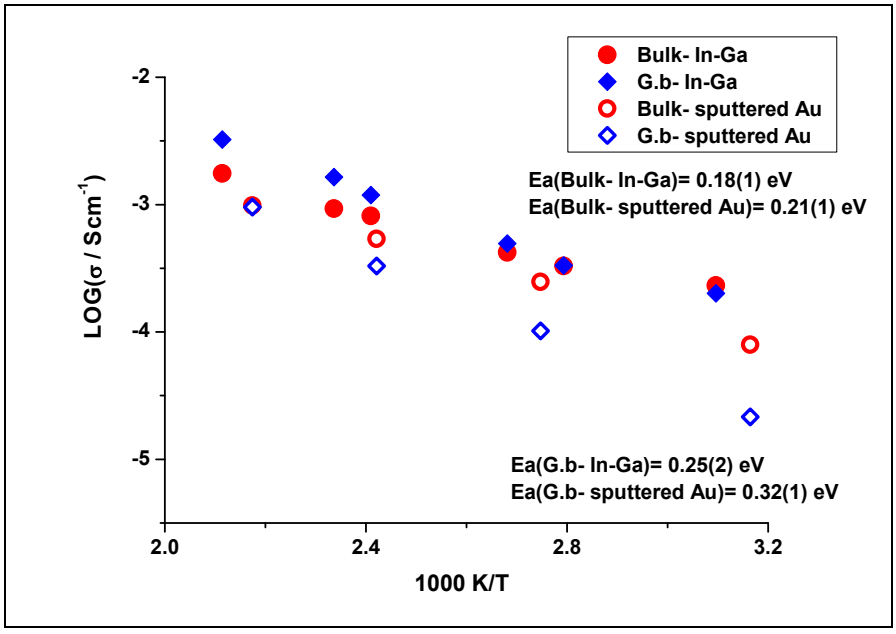

(b)

Figure 6-19: Arrhenius plot of electrical conductivity showing activation energies for $Cu_xTa_{2x}Ti_{1-3x}O_2$ (x =0.10) with: (a) In-Ga and (b) In-Ga and sputtered Au at different temperature in air.

6.1.3 Effect of solid solution composition

The effect of the chemical composition of the material was investigated for $Cu_xTa_{2x}Ti_{1-3x}O_2$ by comparing results for x=0.10 with x= 0.12. Impedance data at different temperatures with Au paste electrodes, Appendix B, are similar to that with x= 0.10. An intermediate Z* semicircle can be observed at high temperature, 200 and 300°C in addition to the appearance of a shoulder peak at 300°C in Z″/M″. When temperature increases, an intermediate plateau can be distinguished in the admittance and capacitance plots.

Impedance data for the same sample with Pt paste electrode show a similar behaviour to that with Au electrode. A significant observation is that the grain boundary contribution is more visible in Z″/M″ plot. In addition, the component at low frequency is temperature dependent as it is clearly seen at 200°C and 300°C.

The conductivities of bulk, grain boundary and surface layer with Au, Pt paste electrodes, Figure 6-20, follow the Arrhenius law. The grain boundary and surface layer conductivities are lower than that for bulk but with Pt paste electrode, Arrhenius plots of bulk and surface layer cross at 1000/T ≅ 2.11, i.e. T= 200°C, Figure 6-20 (b). With Au and Pt paste electrodes, the bulk conductivities are similar with activation energy of ~ 0.20 eV and higher than that for grain boundary. The conductivities of both grain boundary and surface layer are higher with Pt paste electrode than with Au paste electrodes. The surface layer has a high activation energy.

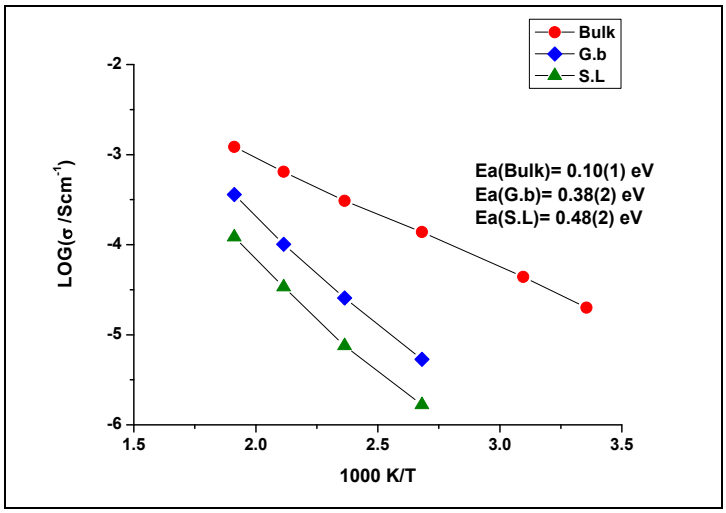

(a)

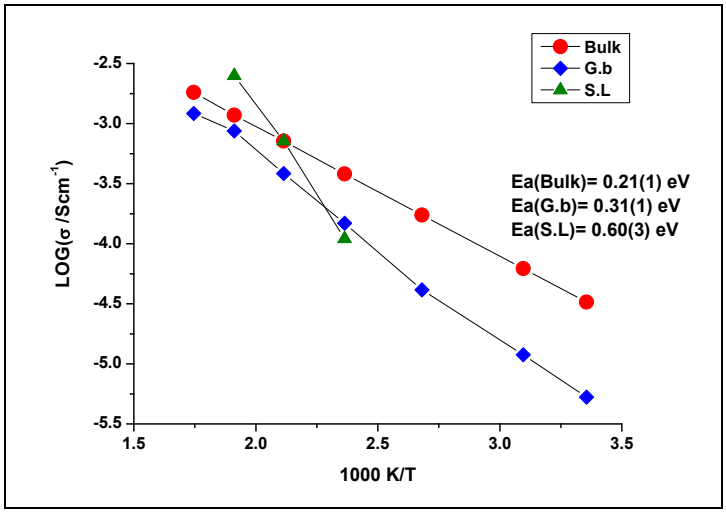

(b)

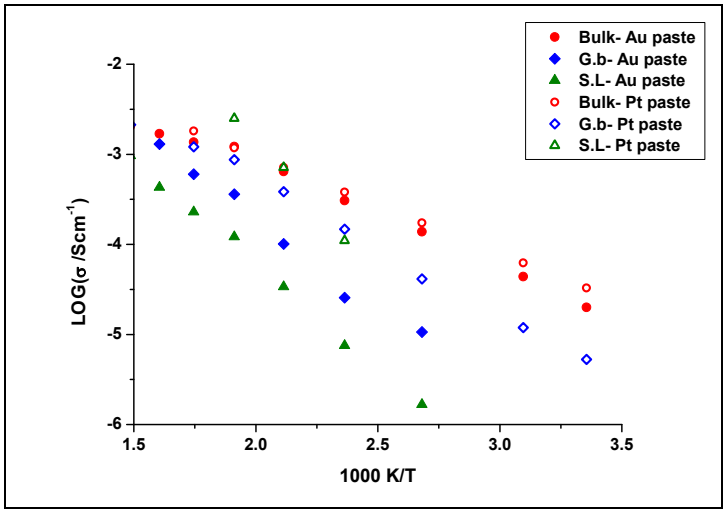

(c)

Figure 6-20: Arrhenius plot of electrical conductivity, σ showing activation energies, E_a, upon heating at different temperature in air for $Cu_xTa_{2x}Ti_{1-3x}O_2$ (x =0.12) with: (a) Au paste, (b) Pt paste electrode and (c) both. Lines serve as a guide to the eye.

The impedance data for the x=0.12 sample with Au and Pt paste electrode at different temperatures during heating-cooling cycle reveal a similar behaviour to those with x= 0.10.

The electrical conductivity during heating and cooling with different types of paste electrode in air is given in Figure 6-21. The grain conductivity exhibits a similar behaviour on heating and cooling. The grain boundary and surface layer conductivities with Au paste electrode exhibit a slight difference upon cooling, Figure 6-21(a), while no obvious change can be observed with Pt paste electrode, Figure 6-21(b). The activation energies for all components are similar on heating and cooling.

Arrhenius plots of conductivity for the sample with x=0.10 and x=0.12 with different types of paste electrode in air are given in Figure 6-22. With Au paste, the bulk conductivity of the sample with low level of dopant (x=0.10) is higher while the observed behaviour is different for the conductivity of surface layer which is higher for high level of dopant (x=0.12), Figure 6-22(a). With Pt paste electrode, grain, grain boundary and surface layer conductivities of sample with x=0.12 are higher than those of sample with x=0.10, Figure 6-22(b).

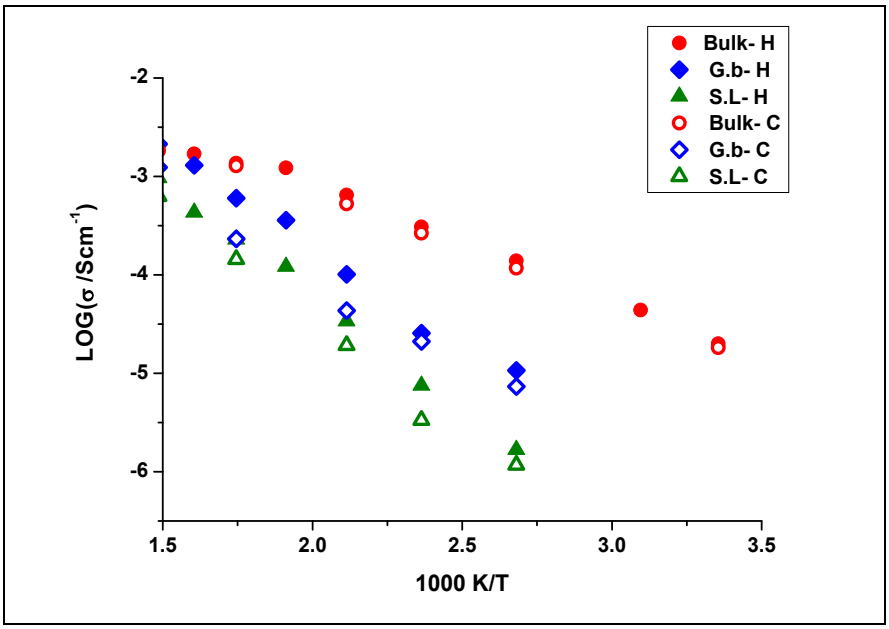

(a)

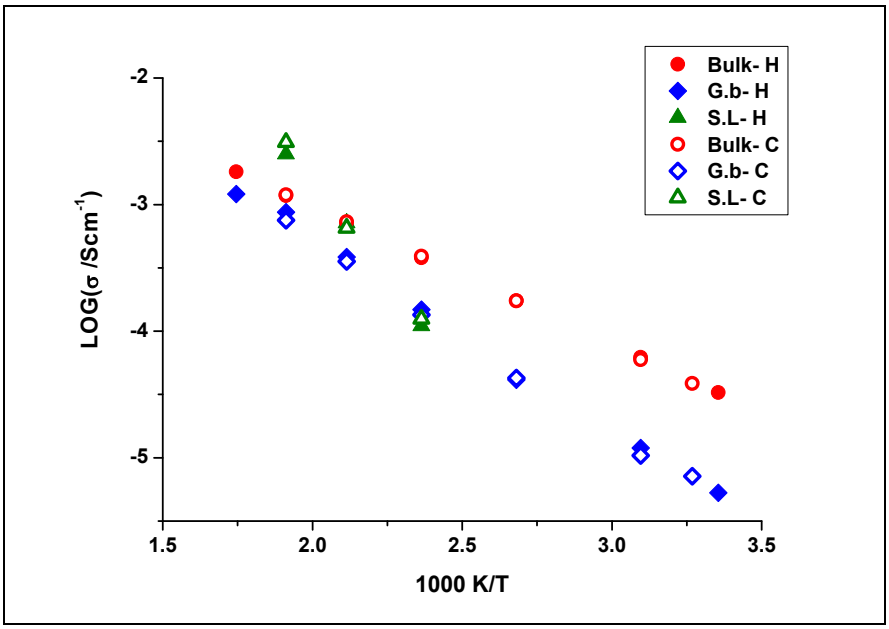

(b)

Figure 6-21: Arrhenius plot of conductivity for $Cu_xTa_{2x}Ti_{1-3x}O_2$ (x =0.12) with: (a) Au paste and (b) and Pt paste electrode on heating (H) and cooling (C) at different temperatures in air.

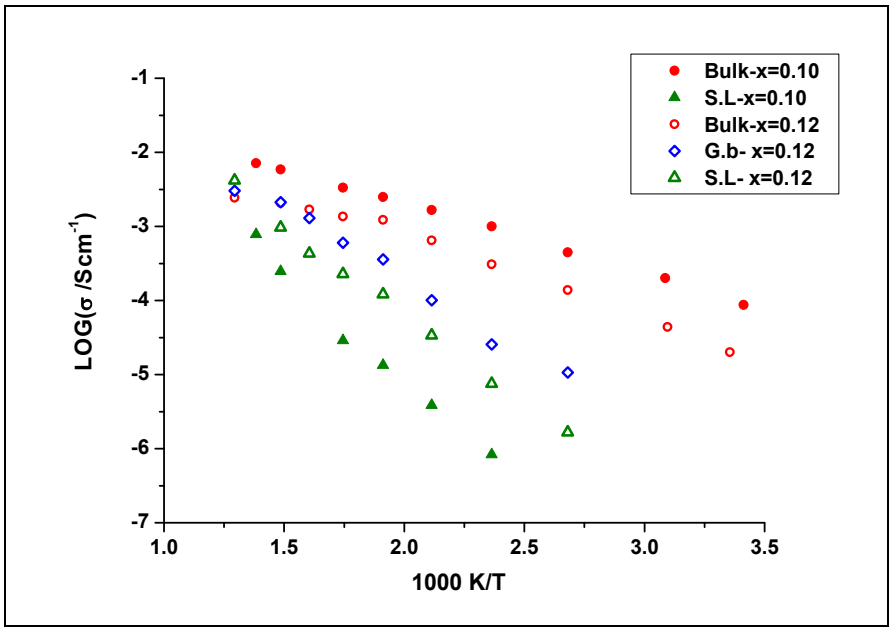

(a)

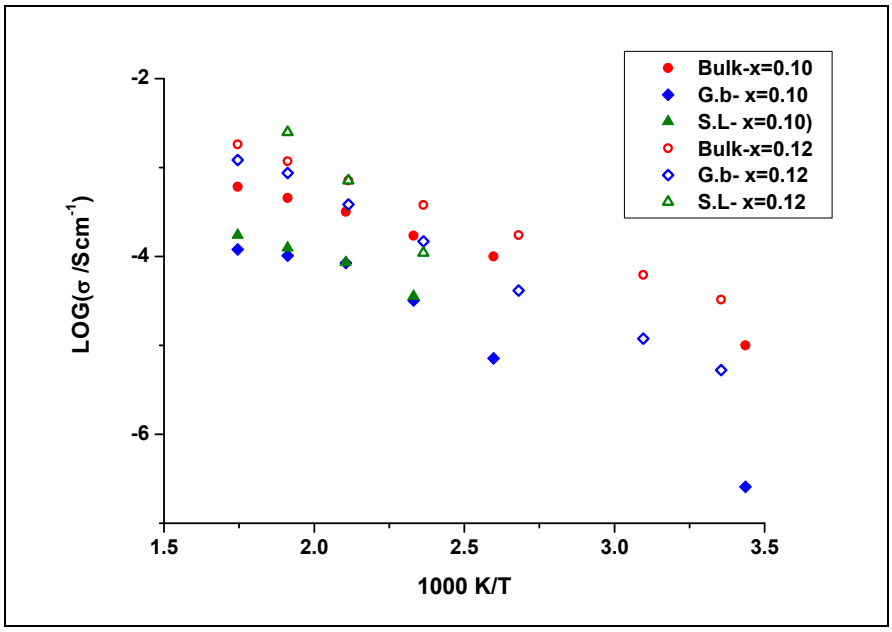

(b)

Figure 6-22: Arrhenius plot of electrical conductivity, σ for $Cu_xTa_{2x}Ti_{1-3x}O_2$, x =0.10 and 0.12 with: (a) Au paste and (b) Pt paste electrode on heating at different temperature in air.

The activation energy for bulk, grain boundary and surface layer of two samples with different kinds of electrode are summarised in Table 6-3. The activation energy has a value in range 0.18 - 0.21eV for bulk and in the range of 0.30 - 0.40 eV for grain boundary. The activation energies of bulk interface with Au and Pt paste electrode was found in range 0.47-0.78 eV.

Table 6-3: Activation energies for grain, grain boundary and surface layer in the $Cu_xTa_{2x}Ti_{1-3x}O_2$ with x= 0.10 and 0.12 with different types of paste electrodes.

Electrode Type	Au paste		Pt paste	
Composition, x	0.10	0.12	0.10	0.12
$Ea_{(Bulk)}$, eV	0.18(1)	0.20(1)	0.21(1)	0.21(1)
$Ea_{(G.b)}$, eV	*	0.38(2)	0.33(1)	0.31(1)
$Ea_{(S.L)}$, eV	0.48(6)	0.48(2)	0.78(4)	0.60(3)

* Electrical response from grain boundary is not resolved.

6.2 Impedance data for $Cu_xNb_{2x}Ti_{1-3x}O_2$, (x=0.10)

6.2.1 With Au sputtered electrode

Impedance data for the sample with sputtered Au electrode are given in Figure 6-23 and Figure 6-24 at low and high temperature. Well- defined semicircle is clearly seen at low temperature (≥ 200K) in Z* plot, Figure 6-23 (a), as well as a spike which can be considered as a part of a second semicircle, as seen at high temperature, ≥ 260K. At high temperature, ≥ 320K, the high frequency arc starts to disappear while that at low frequency becomes well- defined. At low temperature, the spectroscopic plot of Z″/M″, Figure 6-23(b), shows overlapping peaks which shift to high frequency by increasing the temperature. At 200K, a shoulder appears at low frequency then become a peak at high temperature. One peak can be seen in M″ plot at temperature > 320K. Two plateaux appear in the spectroscopic plots of admittance, Figure 6-24(a), but when temperature increases, > 150°C, the high frequency plateau became hardly visible due to limited frequency measurements.

The capacitance plot, Figure 6-24(b), reveals two plateaux at high and low frequency. The capacitance value of $5.65x10^{-12}$ F/cm related to the sample bulk was obtained from the smooth plateau at low temperature while the capacity value in range of 0.1-1 nF/cm for low frequency plateau was obtained from the flat plateau at high temperature and suggests that the second component might be a grain boundary or surface layer. The capacitance of the second component decreases when temperature rises. The relative permittivity was calculated, from the corrected capacitance of the bulk over the temperature range 10–320 K, to be ~ 63.81 which is lower than that of bulk rutile- TiO_2, ~100. This value for relative permittivity along with slight temperature-dependence was previously reported for $Cu_{3.21}Ti_{1.16}Nb_{2.63}O_{12}$ (236).

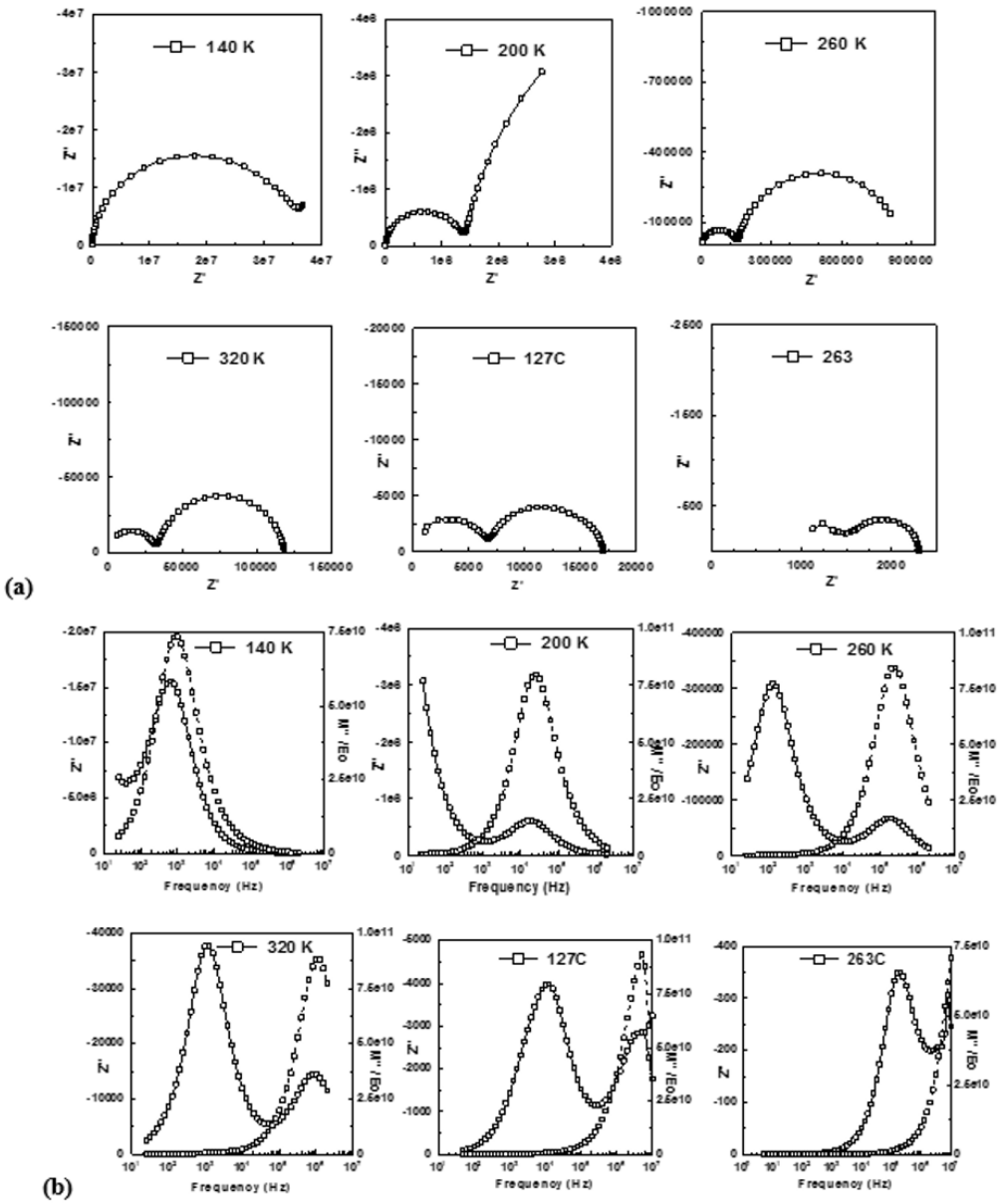

Figure 6-23: (a) Z* plot and (b) spectroscopic plot of Z″/M″ for $Cu_xNb_{2x}Ti_{1-3x}O_2$ (x =0.10) with sputtered Au electrode at different temperature in air.

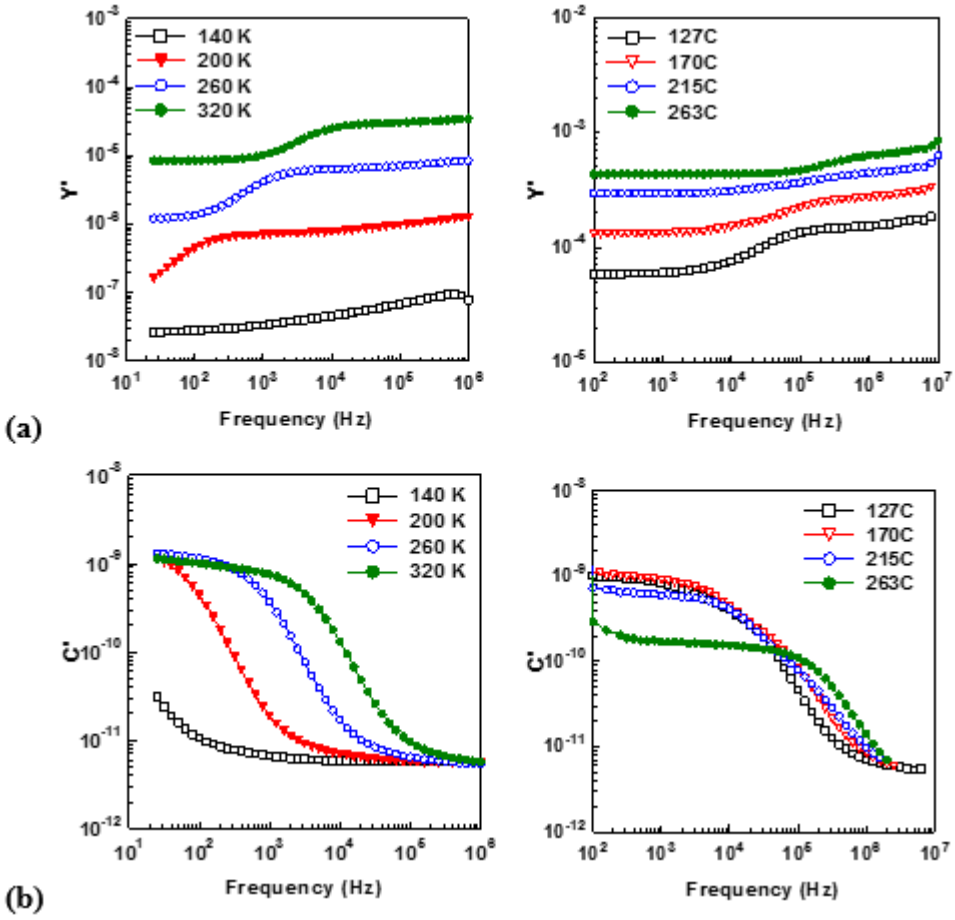

Figure 6-24: Spectroscopic plot of: (a) admittance and (b) capacitance for $Cu_xNb_{2x}Ti_{1-3x}O_2$ (x =0.10) with sputtered Au electrode at low and high temperature in air.

Electrical conductivity of two components, Figure 6-25, shows a non-linear response deviating from Arrhenius law with activation energy of 0.14 and 0.24 eV for bulk and second component respectively at low temperature, at high temperature it became 0.21 eV for bulk and 0.34 eV for grain boundary.The Arrhenius plots cross at 1000/T ≅ 2.2, i.e. T≅ 180°C. At this temperature, the arcs in Z* plots became of equal size and the distinction between high and low frequency plateaux in log Y/ log f plots disappears.

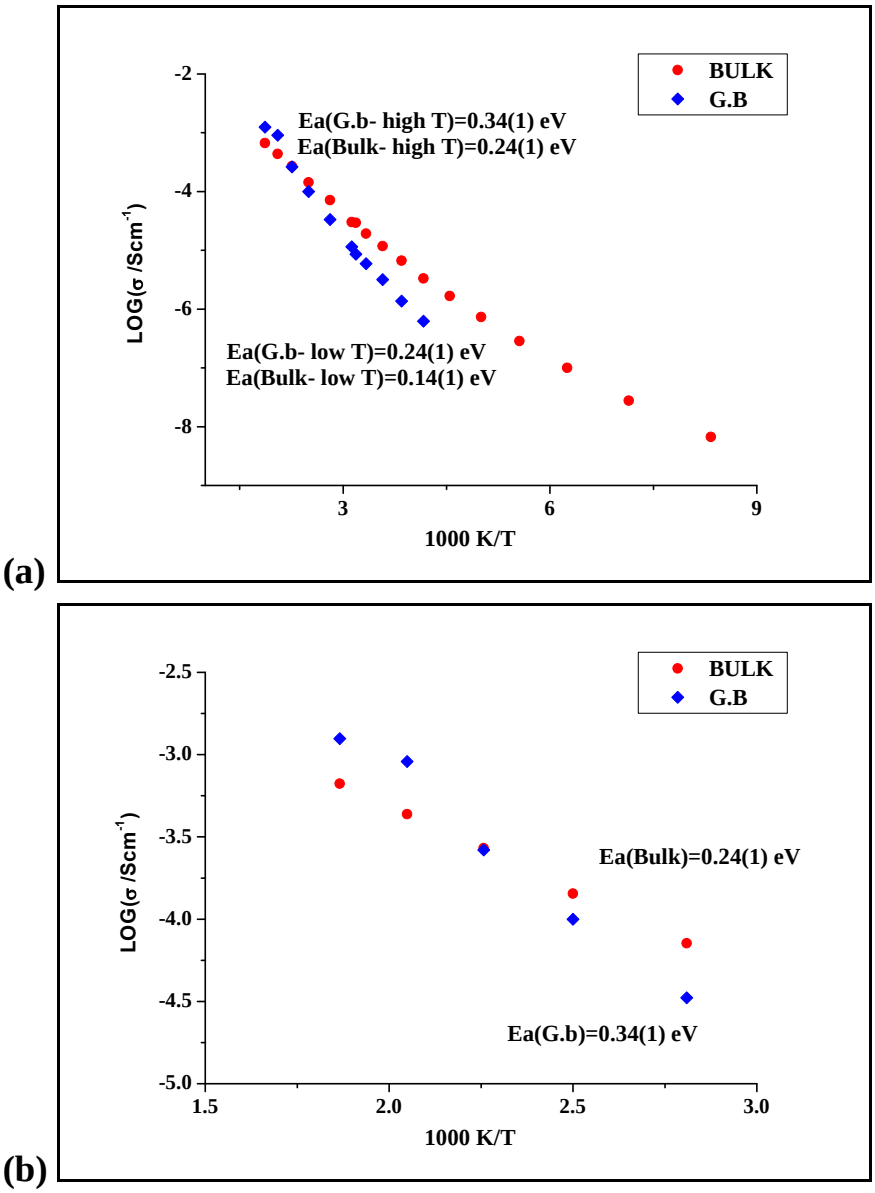

Figure 6-25: Arrhenius plot of electrical conductivity, σ showing activation energies, Ea, for $Cu_xNb_{2x}Ti_{1-3x}O_2$ (x =0.10) with sputtered Au electrode at: (a) low and high temperature and (b) high temperature in air.

6.2.2 Impedance data for $Cu_xNb_{2x}Ti_{1-3x}O_2$, (x=0.10) with paste electrodes

Impedance measurements were carried out on the sample with x =0.10, and Au, Pt paste as electrodes. The impedance behaviour are similar for the $Cu_xTa_{2x}Ti_{1-3x}O_2$ (x =0.10) sample with Au and Pt paste electrode.

Arrhenius plots of all components and the total conductivities are constructed for samples coated and sputtered by different metals; Au and Pt, Figure 6-26. The bulk conductivities are identical, Figure 6-26(a), and have activation energy with value in range of 0.18 - 0.20 eV. Also, the grain boundary conductivities are identical and higher than that for surface layer with activation energy in range of 0.30 - 0.34 eV. On the other hand, the conductivity of surface layer with Pt paste electrode is higher than that with Au paste electrode, Figure 6-25(b), with activation energy of 0.31 and 0.43 eV respectively.

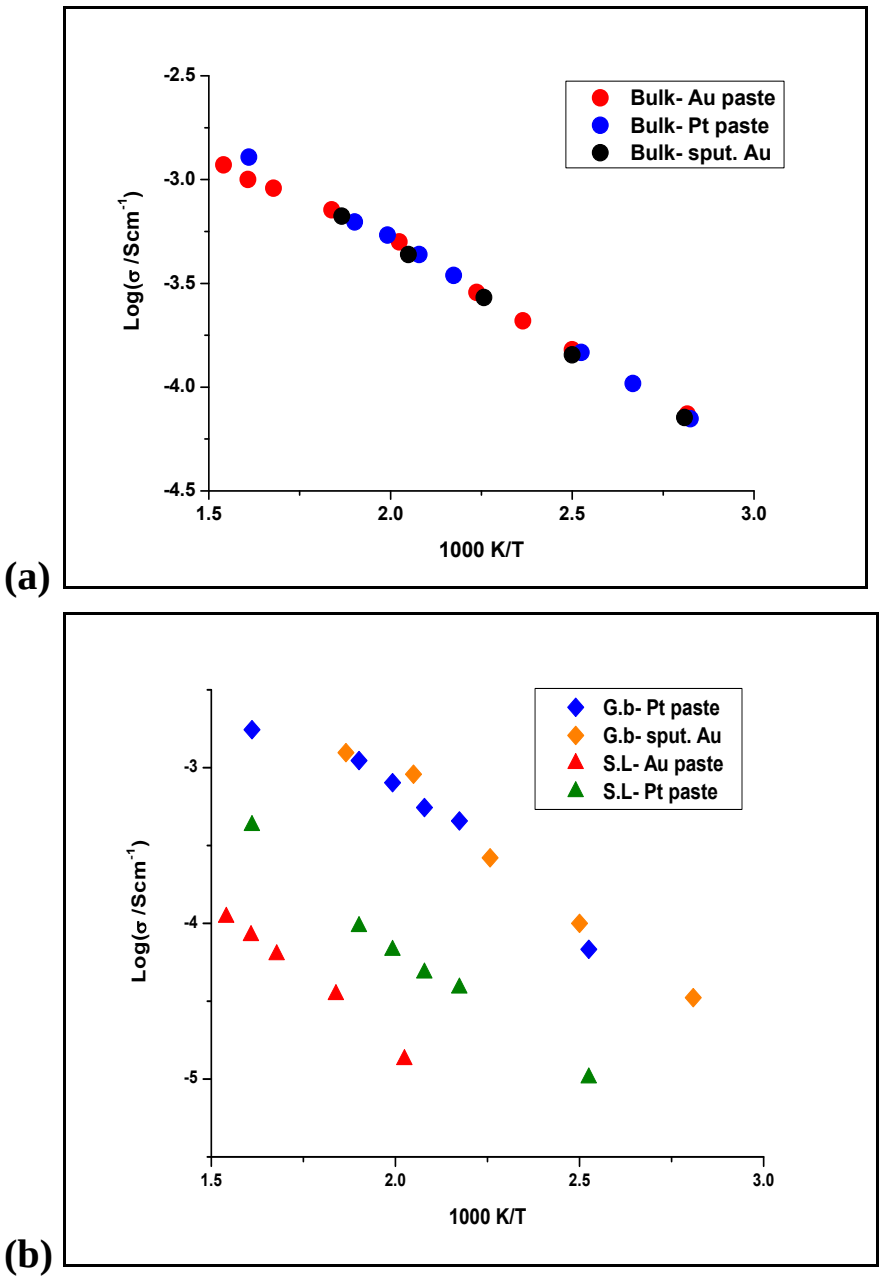

Figure 6-26: Arrhenius plot of: (a) bulk conductivity, σ_b, (b) and grain boundary for $Cu_xNb_{2x}Ti_{1-3x}O_2$ (x =0.10) on heating in air at different temperature with different types of electrode: Au paste, Pt paste and sputtered Au.

6.2.3 Impedance data for $Cu_xNb_{2x}Ti_{1-3x}O_2$, (x=0.20) with Au sputtered electrode

To study the effect of chemical composition change on the electrical behaviour, the impedance measurements were performed on a sample with composition x=0.20 and sputtered Au electrode. It exhibits a similar impedance response to that observed with x= 0.10 and sputtered Au electrode. Arrhenius plots of bulk and grain boundary are constructed and plotted in Figure 6-27 at different temperatures for samples with different compositions; x=0.10 and 0.20, sputtered with Au. The conductivity of bulk is higher at low temperature for x=0.20, Figure 6-27(a). The same trend can be seen for grain boundary, Figure 6-27(b).

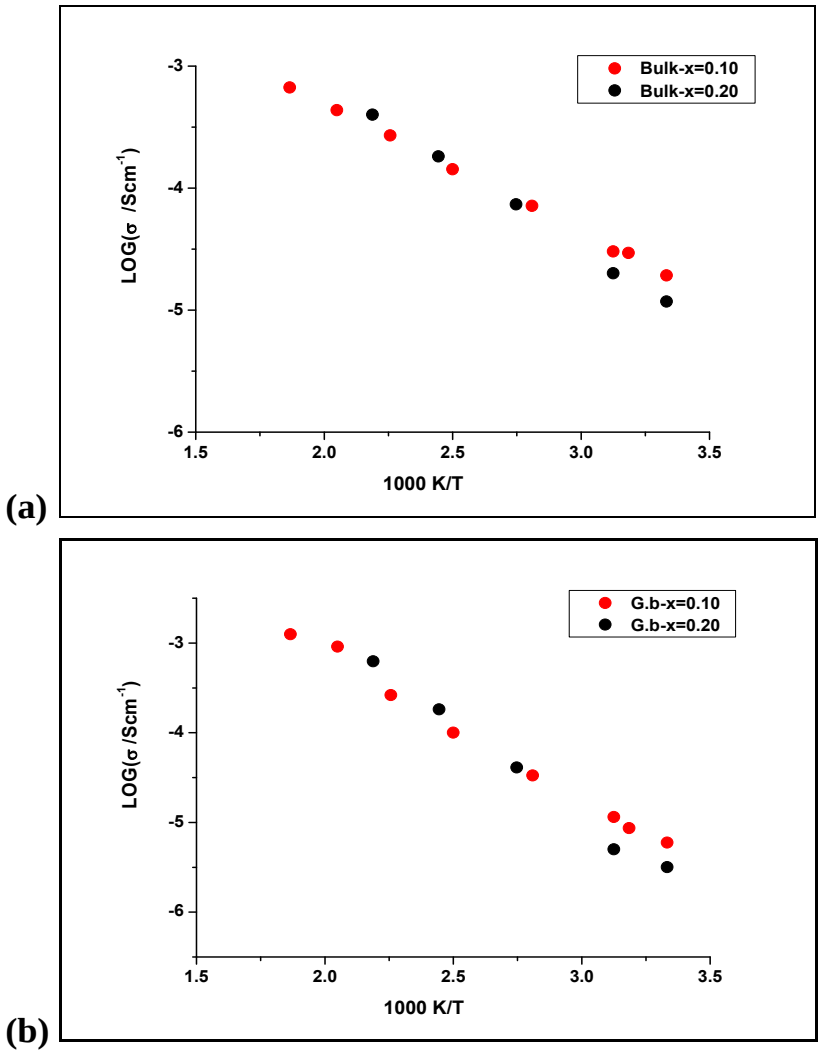

Figure 6-27: Arrhenius plot of: (a) bulk conductivity and (b) grain boundary conductivity for $Cu_xNb_{2x}Ti_{1-3x}O_2$; x =0.10 (red) and x=0.20, with sputtered Au electrode on heating at different temperature in air.

6.3 Discussion of impedance data of samples with different types of electrodes

The electrical behaviour of $Cu_xTa_{2x}Ti_{1-3x}O_2$ (x =0.10 and 0.12) and $Cu_xNb_{2x}Ti_{1-3x}O_2$ (x =0.10 and 0.20) with different types of electrode were studied over a wide range of frequency and temperature using a complex impedance spectroscopy technique. According to the specific features observed in the impedance data, the samples can be classified into two categories: sputtered or paste by electrode metal.

6.3.1 With sputtered electrodes

6.3.1.1 Impedance data

$Cu_xM_{2x}Ti_{1-3x}O_2$ (M= Nb^{5+} and Ta^{5+}) sputtered by Au and Pt as electrodes show a very similar electrical behaviour. Impedance data indicate that two components are present in the electrical response of the material which can be identified as bulk and grain boundary according to the capacitance measured at several temperatures which were in the order of 10^{-12} and 10^{-10} F respectively (351). The impedance spectra are composed of a two semicircular arcs, each semicircle is a representative of an RC circuit that corresponds to individual component of the material. The bulk and grain boundary response is expressed in an equivalent circuit with a parallel combination of a resistor and a capacitor: (R_bC_b) and ($R_{gb}C_{gb}$) respectively (250). The electrical behaviour of $Cu_xM_{2x}Ti_{1-3x}O_2$ (M= Nb and Ta) is well represented by two parallel RC equivalent elements connected in series.

The $Cu_xM_{2x}Ti_{1-3x}O_2$ (M= Nb and Ta) with sputtered Au and Pt electrodes exhibits a dielectric constant ranging from 63 to 80 at 1 MHz and at room temperature. These values are lower than the static dielectric constant reported for pure rutile TiO_2, ranging from 80 to 100, depending on the lattice orientation (352). On the other hand, these values are in agreement with those previously reported at 1.15 MHz at 20°C for rutile TiO_2 obtained from three different synthesis methods with low relative density, 74% (354) . Marinel et al. (355) reported a value of ~ 100 at 100 Hz and at room temperature for highly dense rutile TiO_2 (~ 94 %) which was microwave and conventionally sintered at a temperature ranging from 1000 °C to 1300 °C.

Structural features (phase composition, deviations from stoichiometry, grain size, ceramic density and therefore porosity) have characteristic effects on ceramic properties. The reason for the lowest dielectric constant may be due to low relative density of the investigated samples which are in the range of 75- 85%. Another reason would seem to be that the $Cu_xM_{2x}Ti_{1-3x}O_2$ (M= Nb and Ta) system can show deviations from stoichiometry as it is generally believed that TiO_2 can show a significant deviations from stoichiometry (356) which affect the dielectric constant. The presence of moisture, residual -OH, may also be a factor

Grain boundary capacitance shows a step-like decrease in C_2 vs. *f* with movement to higher *f* with increasing temperature, T. Moreover, the variation of the grain boundary capacitance shows a nonlinear decrease in C_2 vs. temperature, Fig.6.5. It is possible to demonstrate that the employed Cu-M co-doped in TiO_2 exhibit negative temperature coefficient (NTC) values which mean that the temperature increase causes a decrease in the grain boundary capacitance.

A small change in the grain boundary resistance during heating-cooling cycle is more pronounced at high temperature. This difference in the impedance result might generally be due to: (1) change in electrode-sample contact area, or (2) change in the conductivities of grain boundary due to oxidation-reduction. Similar behaviour with Au and Pt electrodes suggests that the second reason is more likely. This irreversible behaviour in heating and cooling was investigated by measuring the impedance response of $Cu_xTa_{2x}Ti_{1-3x}O_2$ (x= 0.10) with sputtered Au electrode in various atmospheres at different temperatures and time. Resistance values of both bulk and grain boundary exhibit no change by changing from air to N_2. When the sample is exposed to O_2, a slight change in the grain boundary resistance was observed; however we believe that this change is due to temperature fluctuations inside the furnace chamber when it is exposed to the different gases. According to these results, the change in the grain boundary conductivity does not seem to be related to any oxidation-reduction reaction suggests that the grain boundary conductivity practically at high temperatures might be dependent upon the length of time the sample was allowed to reach equilibrium and it was not sufficient to obtain equilibrium.

Electrical conductivity indicates a pattern in which conductivity increases gradually with rise in temperature suggesting a thermally activated process in the materials. All the investigated samples follow the Arrhenius law behaviour at low and high

temperature but in the whole temperature range investigated since the plot presents a small deviation from the linear behaviour as a result of two different measurements set up below and above room temperature. Activation energy of $Cu_xM_{2x}Ti_{1-3x}O_2$ (M= Nb and Ta) for different composition of x with sputtered Au, Pt electrodes is in the range from 0.20 eV to 0.24 eV for bulk and from 0.31 eV to 0.42 eV for grain boundary.

The activation energy over the range RT to 350 °C is 0.20 ±0.01 eV and the conduction mechanism is interpreted as n-type electronic due to presence of shallow donor levels in the order of 0.1–0.2 V which are commonly reported in literature for TiO_2 (357–360).

6.3.1.2 Temperature dependence of the low frequency capacitance plateau

Several of the data sets show that the low frequency capacitance with sputtered metal electrodes, $C_{l.f}$, decreased significantly with increasing temperature. One possibility is that this could be an NTC effect with very temperature dependent, temperature coefficient of permittivity, however, this is not compatible with that the bulk capcitance, C_1 shows a very small temperature dependent. An alternative explanation is that this temperature dependent capacitance is a consequence of the temperature dependence of resistances, R_1, R_2, since the equation for low frequency capacitance, $C_{l.f}$ is in general a complex function of R_1, R_2, C_1 and $C_{l.f}$:

at $\omega = 0$, $\varepsilon' = [C_1(R_1)^2 + C_{l.f}(R_2)^2]/ [C_0 (R_1+R_{l.f})^2]$

A simulation was therefore carried out to demonstrate the magnitude of $C_{l.f}$ and its possible dependency on the resistance values of R_1, R_2. For this assumption it was assumed that C_1= 4.3 $pFcm^{-1}$ and $C_{l.f}$= 8.66E-10 Fcm^{-1} . R_1 and R_2 values at each temperature were taken from the experimental data. Simulation results are shown in Table 6-4 at four temperatures given calculated and observed data of the $C_{l.f}$. As can be seen, the calculated data show a decrease of a factor of five over the range 27- 333°C which is qualitatively similar to observed decrease in $C_{l.f}$. over the same temerature range. We therefore conclude that the temperature dependence of $C_{l.f}$. is a consequence of where the two resistance, R_1 and R_2, having very different activation energies, and that there is no evidence of any NTC behaviour in the material.

Table 6-4: The permittivity of the material and the capacitance of low frequency component, calculated and observed, at different temperature.

T, °C	$C_{l.f}$ Calculated, E-10/ Fcm^{-1}	$C_{l.f}$ Observed, E-10/ Fcm^{-1}
27	5.40	8.66
140	3.30	4.50
235	1.14	1.60
333	1.23	1.20

6.3.2 Impedance data with paste electrodes

Impedance data for x=0.10 with a Au paste electrode indicates that the electrical response is composed of, at least, two components. The appearance of two semicircles in the complex plane suggests the presence of bulk as well as grain boundary effects in the studied samples. However, the magnitude of the second components capacitance, C_2, in the range of nF, suggests either a grain boundary or thin surface layer. With Pt paste electrode, the electric response of the sample is separated to three arcs corresponding to bulk, grain boundary and surface layer. Each semicircle is a representative of an RC circuit that corresponds to an individual component of the material which are connected in series.

Electrical conductivity indicates a pattern in which conductivity increases gradually with rise in temperature suggesting a thermally activated process in the materials.

The large difference displayed in E_a as well as in the conductivity between grain boundary, surface layer and bulk is an evidence of remarkable chemical differences between grain boundary and surface layer, and bulk regions results in different charge transport mechanisms.

Moreover, the activation energy of 2^{nd} components in the sample with x=0.10 (~ 0.48 eV) confirms that no grain boundary effect can be seen in the impedance spectra with Au paste electrodes; this might be either due to very thin grain boundaries in the materials, or because of the similar electrical properties of the grain boundary and surface layer, this means that electrical responses from some microstructural factors may overlap, or do not give significant contributions to the

impedance in the measuring frequency range. Semicircles will overlap to form one single semicircular arc similar to a depressed semicircle when the relaxation frequencies of different RC elements are close.

The impedance response of the bulk is reproducible and reversible in thermal cycle and bulk conductivity shows a good linearity over the temperature range studied. In contrast, the resistance and conductivity variations of grain boundary and/ or surface layer with Au, Pt paste electrodes detected during the measurements taken on the heating and cooling cycle indicate that these changes might due to oxidation- reduction reaction.

Compare conductivity of samples with all types of electrode at T≥ room temperature; show that the bulk conductivity has linear characteristic following Arrhenius law. The bulk with Au paste electrode has a higher conductivity than that with sputtered Pt which is higher than that sputtered with Au. Sample with paste Pt and sputtered Au has similar bulk conductivity.

The conductivity of grain boundaries with sputtered Au, Pt electrodes are similar and higher than that with Pt paste electrode. The second components in the impedance response with Au paste electrode has a lower conductivity than that with Pt paste electrode and this suggests that the second component is surface layer rather than grain boundary which is not visible in complex impedance data as the grain boundary and surface layer semicircles might exhibit a high overlapping degree.

The difference in conductivity between the bulk and surface layers is high and reaches 3 order of magnitude in the case of Au paste electrode at 200°C indicates the bulk is more conductive.

The activation energy of grain boundaries and surface layers are found to be higher than that of grains indicating higher resistive behaviour than that of the grains. This large difference displayed in the conductivity of grain boundary along with appearance of non-stoichiometric surface layer are an evidence of remarkable effect of electrode processing suggests that the heat treatment during the application of Au, Pt paste electrodes can induce the formation of potential barriers at grain boundaries.

In order to make clear whether or not the electrode processing is mainly responsible for the different impedance response of materials with sputtered and coated electrodes, In-Ga electrode selected for a comparison of different electrode processing conditions. The responses are similar with electrodes that were applied without the need for thermal treatment. The Arrhenius curves of samples with sputtered electrodes and In-Ga electrodes are also very similar. The distinguishing feature is a temperature at which the Arrhenius plots cross. A comparison of three different electrode processing methods indicates that the electrode effects play a major role in determining the impedance response at low frequency characteristic of grain boundary and/ or surface layer of the materials.

One explanation would seem to be that the thermal treatment conditions when Au, Pt paste electrodes are applied to ceramic material creates a thin surface layer which displays different properties to those of the bulk probably because the stoichiometry at the surface may not be identical to the average value of the grains. Oxidation-reduction might take place under the thermal treatment with organic solvents which produces physical and chemical changes on the ceramic surface.

In general, two observations can be made from the impedance spectra: (1) the interfacial impedance dominates the overall impedance, and (2) the interfacial impedance depends critically on the manner in which the electrodes were applied to the sample, i.e. the processing of the electrode.

6.3.3 Effect of solid solution composition

One significant finding can be determined from impedance data of the sample with composition $x > 0.10$ with Au paste electrode is the appearance of a grain boundary response in the impedance spectra. Another important observation is related to the electrical conductivity of these samples; bulk of sample with lower x= 0.10 has a higher conductivity while the conductivity of the surface layer is higher with $x > 0.10$. These results indicate that the copper species has a role in the electrical properties of both grain boundary and/or surface layer. It is observed that the grain boundary conductivity could be increased either by increasing the temperature or increasing the dopant level in the TiO_2.

In general, impedance measurements of 4 rutile-based solid solutions were carried out with different types of electrodes: sputtered, paste, Au and Pt. The data show that the materials are electronic semiconductors as there is no evidence for an

electrode spike. The bulk and grain boundary conductivities are similar for $Cu_xTa_{2x}Ti_{1-3x}O_2$ and $Cu_xNb_{2x}Ti_{1-3x}O_2$ with sputtered Au electrodes while with Au paste electrodes, the conductivities of $Cu_xNb_{2x}Ti_{1-3x}O_2$ are slightly smaller than that for $Cu_xTa_{2x}Ti_{1-3x}O_2$ (less than 1 order of magnitude). However, for same material, the bulk conductivity is almost similar with all types of electrodes and has similar activation energy in range 0.18-0.21 eV. The conductivity of grain boundaries is similar for same type of electrodes: sputtered or paste however, it has similar activation energy in range 0.31-0.38 eV with all types of electrodes. The significant difference between IS data is that the appearance of third component (surface layer) with paste electrodes than with sputtered electrodes. The surface layer conductivity and activation energy of this third component depend on the type of the metal electrodes; with Pt paste is higher than that with Au paste electrodes.

The origin of conductivity of doped-rutile $Cu_xM_{2x}Ti_{1-3x}O_2$ (M=Nb or Ta) with sputtered electrodes does not affect with atmosphere changes suggests that it is intrinsicly correlated to a presence of Cu^{2+} in the samples.

By applying paste electrodes (with organic solvents at high temperature), the reduction of Cu^{2+} occurs with effects on conductivity at grain boundaries and/or surface layers: mixed valances of Cu ($Cu^{2+/}$ Cu^{0+} or $Cu^{2+/}$ Cu^0); reduced Cu^{1+} which does not oxidized during slow cooling or the presence of segregation phase/s (CuO and/or TiO_2).

6.3.4 Explanation of semiconducting bulk-insulating surface layer in Cu-M co-doped TiO_2 system, M= Nb^{5+} and Ta^{5+}

It is generally accepted that dopant segregation, grain boundary thickness and secondary phases can create blocking effect at grain boundaries due to the different chemical potential between the grain and grain boundary (361). For Cu-doped TiO_2, the segregation of CuO at the grain boundaries is confirmed by TEM from several studies (362)(326). Moreover, copper formed asperities <5 nm in size were reported for flame spray pyrolysis made Cu doped TiO_2 nanoparticles (326). Consequently, CuO dopant performs a role of formation of insulated depletion layer in which the CuO intergranular insulating layer exhibits p-type character and separates two n-type semiconductive TiO_2 grains giving rise to a negative surface

due to the electron localization on the surface. The potential barrier, therefore, can be seen as a result of the formation of intergranular secondary phase layer.

n-type-*p*-type model suggests that the grain boundary region has a *p*-type characteristic due to the precipitated phase at the grain boundary, while the bulk is *n*-type TiO_2-. The positive charged donors, extending from the side of grain boundary, are compensated by the negative charged acceptor at the grain boundary interface. As a result, electron depletion layers are formed and act as potential barriers with Schottky-like nature due to negative interfacial states (363).

This Schottky-like nature with n-type-p-type model was reported for several metal oxide varistors and inmost metal oxide gas sensors at higher temperatures (363). Other varistor systems based on TiO_2 (337,364–366) have been reported; however the varistor behaviour of these systems is lower compared to that of the ZnO varistors.

Application of paste electrode requires a high temperature; 800-900°C to remove the organic solvent.

During the application of paste electrodes, Cu^{2+} can partially undergo a reduction to form Cu^{+} and/or Cu^{0}. Upon cooling, an internal redox process may takes place in which the reoxidation of Cu^{+} to Cu^{2+} accompanies the partial reduction of Ti^{4+} to Ti^{3+}. The formation of a segregated phase induced by thermal treatment at high temperature results in an insulating surface layer.

6.4 The effect of atmosphere

In order to investigate the effect of the atmosphere on the electrical properties of the material with x= 0.10, coated with Au and Pt, impedance measurements were carried out in different atmospheres upon heating and cooling and data are presented in Figure 6-28 -Figure 6-28.

The impedance measurements were carried out in air and then in N_2 atmosphere for the sample coated with Au and data are presented in Figure 6-28. Impedance data in both gases has the same features in which two components are present in the sample; bulk and surface layer. The bulk of the sample has an identical impedance response in air and N_2 but the change was observed for the surface layer of the sample in which resistance decreases in N_2 and the difference in the resistance became larger when temperature increased, Figure 6-28 (a). In Z″/M″ plot, Figure 6-28 (b), overlapping peaks, at high frequency associated with the bulk of the sample can be seen at room temperature with an decrease in intensity of the peak in N_2. At high temperature, 200°C, the overlapping peaks were observed at low frequency associated with the surface layer effect. It clearly seen that the peak intensity declines and shifts to high frequency when impedance measurement was performed in N_2. The admittance plot Y′, Figure 6-28 (c), shows that Y′ value increase in N_2 and the difference in the admittance became larger when temperature increases. The spectroscopic plot of the capacity, Figure 6-28(d), shows that the capacitance remains constant in the range of picofarads for the bulk and nanofarads for the surface layer.

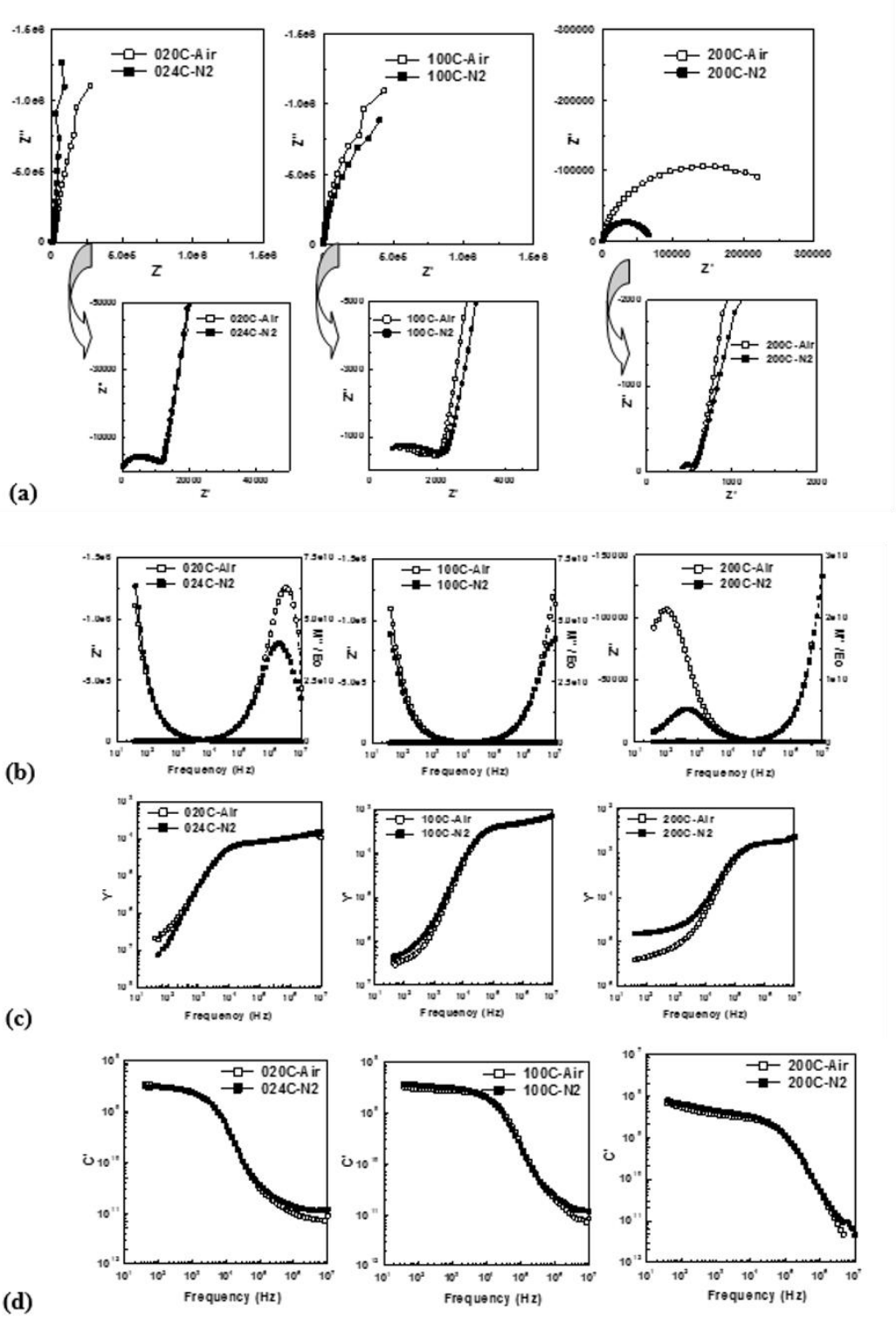

Figure 6-28: Impedance data of: (a) Z* plot, (b) Z″/M″, (c) admittance and (d) capacitance for $Cu_xTa_{2x}Ti_{1-3x}O_2$ (x =0.10) with Au paste electrode at different temperature in Air and N_2.

During the measurements, x= 0.10 with Pt paste electrode was exposed to flowing different type of gases in the following sequence; air, N_2, air, O_2 and air upon heating and cooling. Impedance data were measured at different temperature and three of these measurements at 150, 200, and 250°C were chosen to investigate the atmosphere effect more deeply as the third component is incomplete at $<$ 200°C and it disappears at $>$ 250°C. Impedance data in N_2 and O_2 after air are given in Figure 6-29 and Figure 6-30 respectively. At all conditions, three components can be distinguished. Impedance data in N_2, Figure 6-29, was found to be similar to that was obtained for the sample with Au paste in N_2. On the other hand, the electrical behaviour in O_2, Figure 6-30, shows no change can be considered; however, a slight change in the surface layer can be observed at 200°C.

The capacitance value for the low frequency component with Au paste electrode is almost constant when the atmosphere was changed from air to N_2. On the other hand, a decrease in the capacitance was observed for the same component with Pt paste electrode when the atmosphere was changed from air to N_2 and this difference in the capacitance becomes high with increasing temperature.

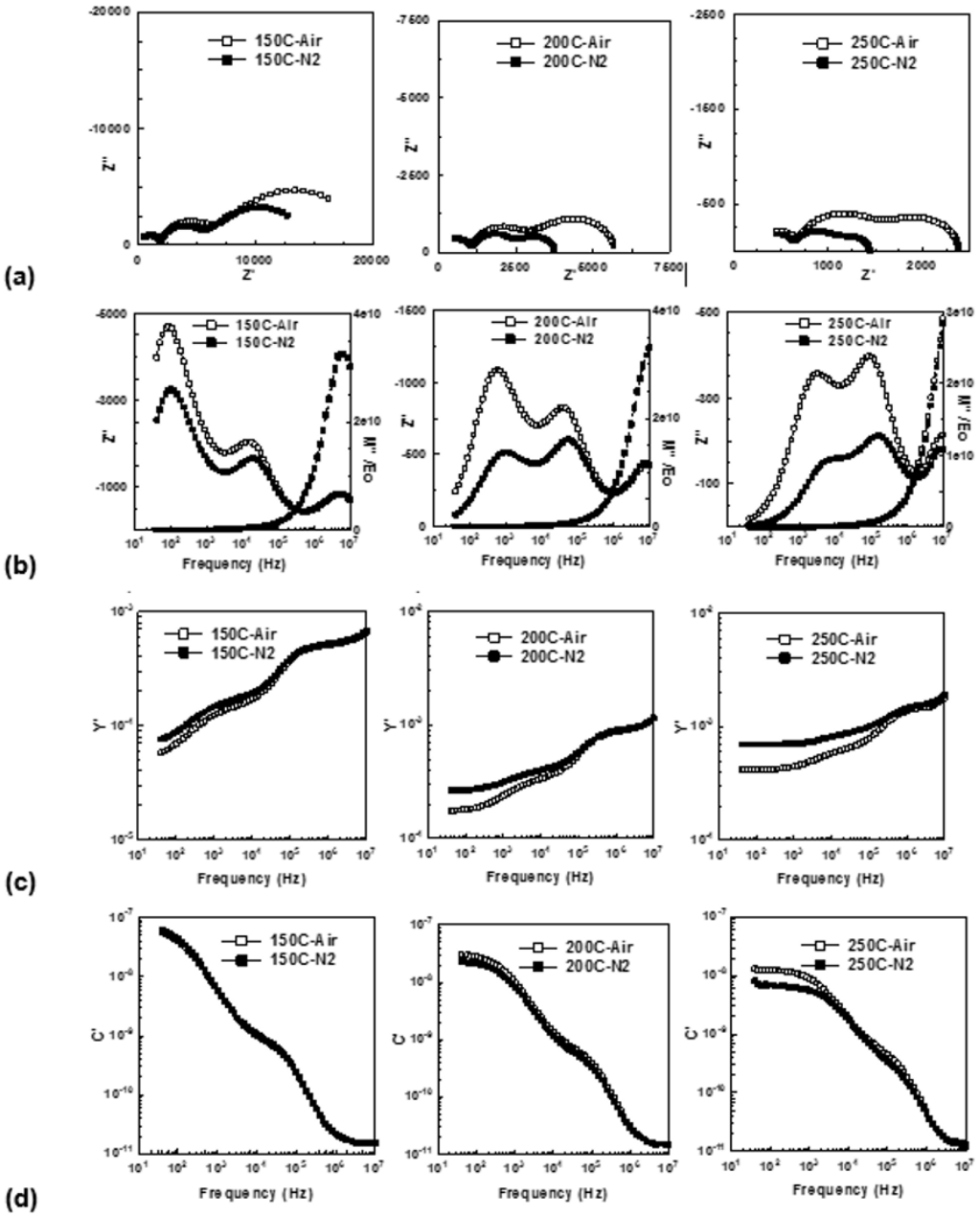

Figure 6-29: Impedance data of: (a Z* plot, (b) Z″/M″ spectroscopic plot, (c) admittance and (d) capacitance for $Cu_xTa_{2x}Ti_{1-3x}O_2$ (x =0.10) with Pt paste electrode at 150, 200 and 250°C in air and N_2 atmosphere.

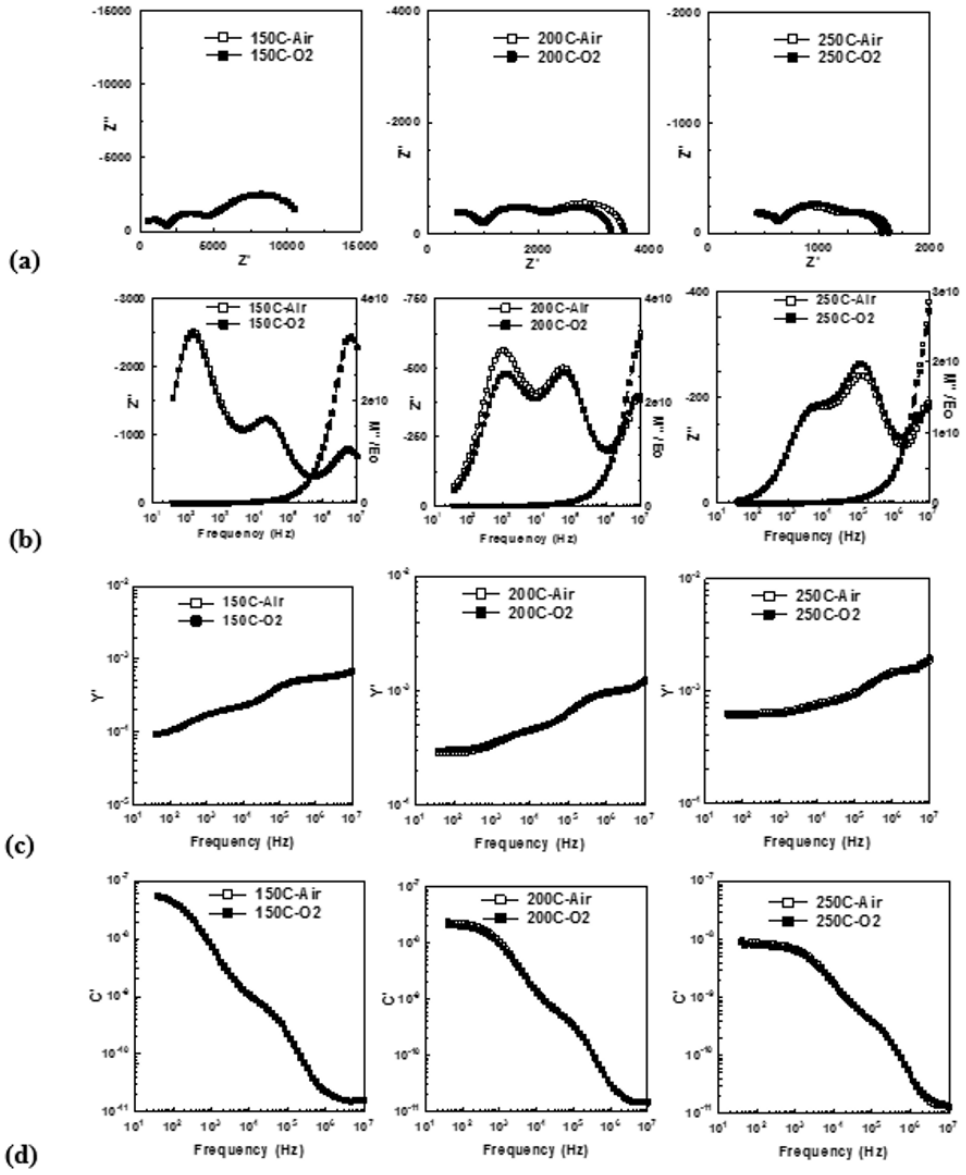

Figure 6-30: Impedance data of: (a Z* plot, (b) Z″/M″ spectroscopic plot, (c) admittance and (d) capacitance for $Cu_xTa_{2x}Ti_{1-3x}O_2$ (x =0.10) with Pt paste electrode at 150, 200 and 250°C in air and O_2 atmosphere.

The electrical conductivity in different atmosphere can be analyzed within the whole temperature range by using an Arrhenius diagram, Figure 6-31 and Figure 6-32. The conductivity of the bulk with Au paste electrode is identical in air and N_2 and higher than that for surface layer. There is a slightly increase in the conductivity of the surface layer when measured in N_2 gas. The activation energy has a value of 0.18, 0.21 eV for the bulk and 0.63, 0.70 eV for the surface layer in air and N_2, respectively.

The electrical conductivity of the sample with x= 0.10 with Pt paste electrode shows that at all investigated atmosphere. The bulk conductivity remains unchanged when the atmosphere was changed while the conductivities of the grain boundary and surface layer increases when the gas was changed from air to N_2, Figure 6-32(a), however both were constant in the case of O_2, Figure 6-32(b). The corresponding activation energy, in all atmospheres, has a value of ~ 0.21 and ~ 0.34 eV for the bulk and the grain boundary respectively while the surface layer has activation energy of 0.64 and 0.49 eV in N_2 and O_2, respectively.

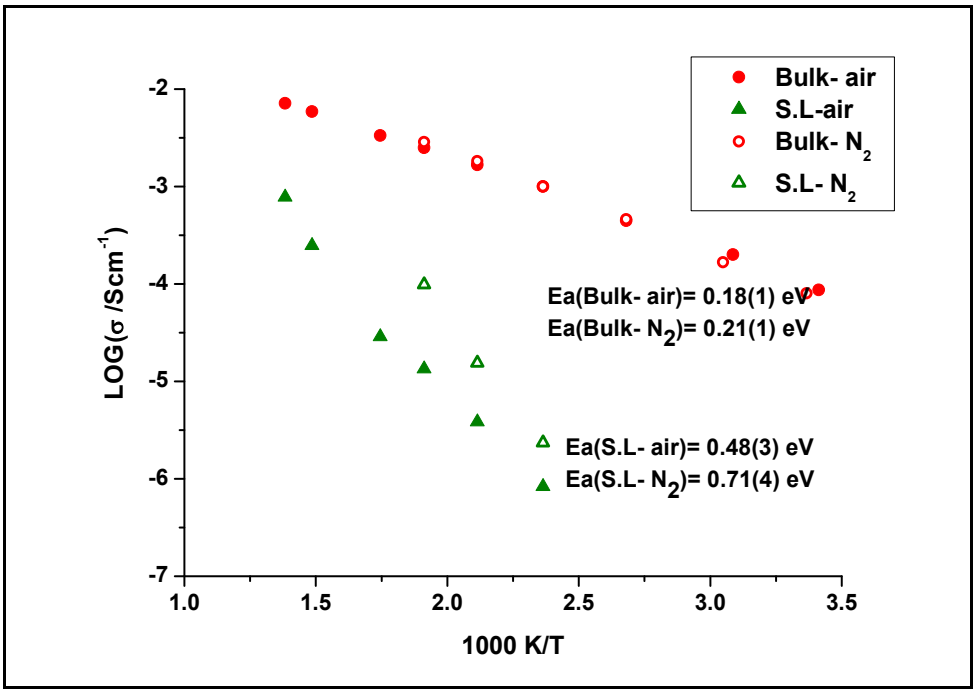

Figure 6-31: Arrhenius plot of conductivity, σ, showing activation energies, E_a, for $Cu_xTa_{2x}Ti_{1-3x}O_2$ (x=0.10) with Au paste electrode in air and N_2 at different temperatures.

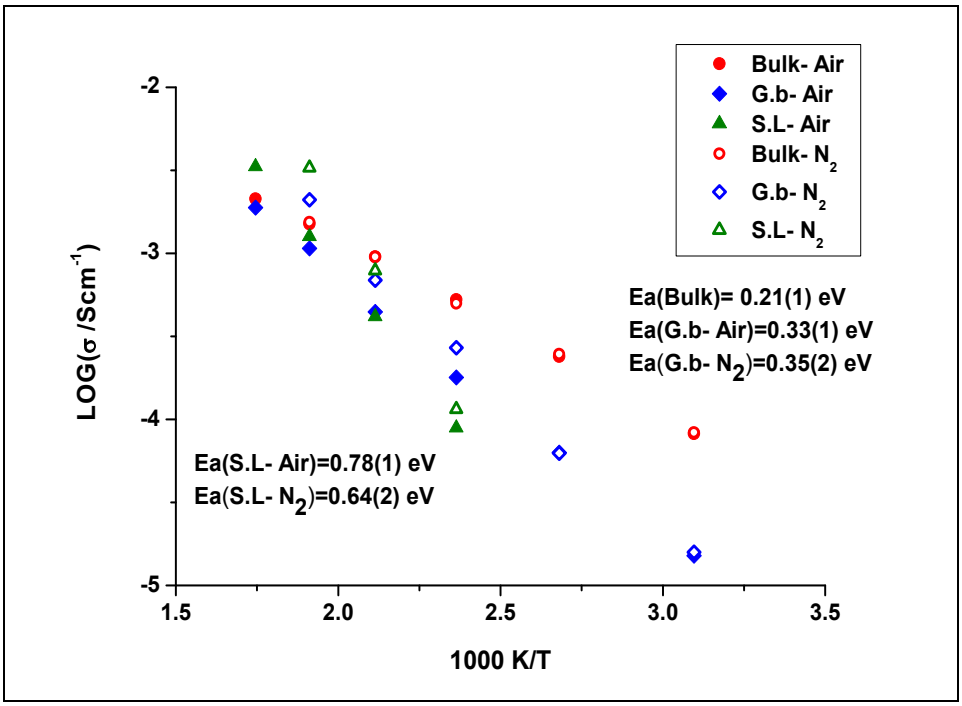

(a)

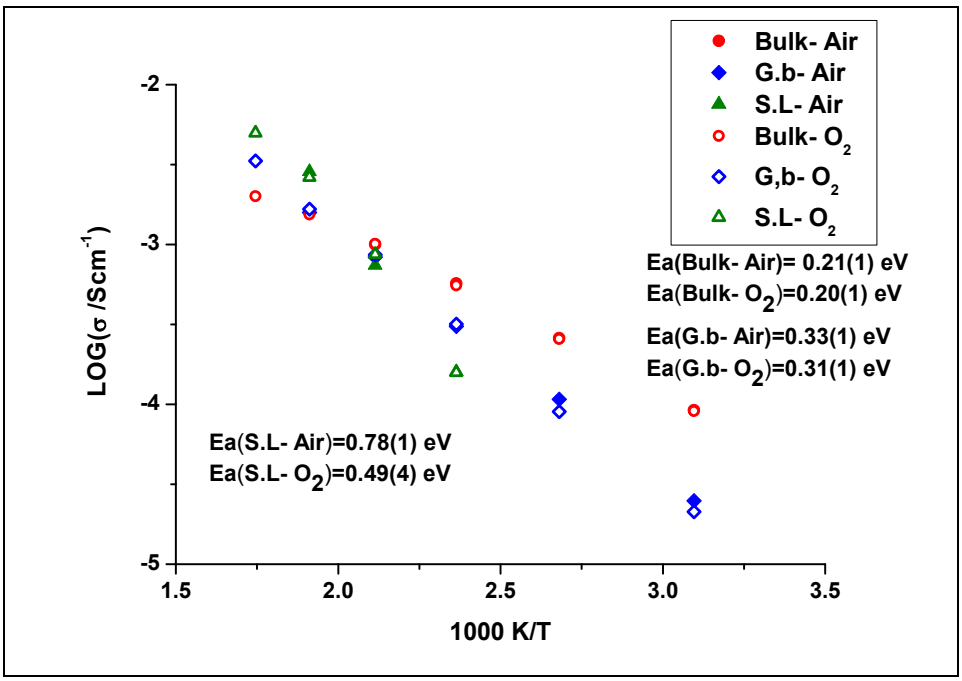

(b)

Figure 6-32: Arrhenius plot of electrical conductivityσ for $Cu_xTa_{2x}Ti_{1-3x}O_2$, (x =0.10) with Pt paste electrode in: (a) air/N_2 and (b) and air/O_2 at different temperatures.

Impedance data upon heating and cooling for x=0.10 with Au paste electrode in N_2 and Pt paste electrode in N_2 and O_2 are given in Appendix C. There is no change in the impedance data for the sample bulk with Au paste electrode but a decrease in the resistance of the surface layer during cooling as seen in Z* plot was observed

associated with: a decrease in the intensity of Z″/M″ peak, increase in Y′ value and increase in the capacitance during cooling. Upon heating-cooling cycle, the impedance data for the sample with Pt electrode in N_2 is similar to that with Au paste electrode in N_2.

The impedance data of the thermal cycle with Pt paste electrode in O_2 shows different behaviour on cooling compared to heating in terms of R, Z″/M″ and Y values of grain boundary and surface layer compared to that in N_2. These effects became more pronounced when temperature increases, ≥ 200°C. In the heating-cooling cycle, the capacitance values of the sample in O_2 atmosphere are almost constant.

Conductivity values obtained in the heating–cooling cycle in different atmosphere are given in Figure 6-33, for x= 0.10 with Au and Pt paste electrodes. The conductivity of the bulk is identical upon heating and cooling in N_2 with Au paste electrode and in O_2 with Pt paste electrode, but there is a very small difference in the bulk conductivity with Pt paste electrode in N_2. With Au and Pt paste electrodes, a change in both grain boundary and/ or surface layer conductivities was observed during cooling in N_2 and O_2. Similar activation energy was found during heating- cooling cycle for the bulk, the grain boundary and the surface layer of sample.

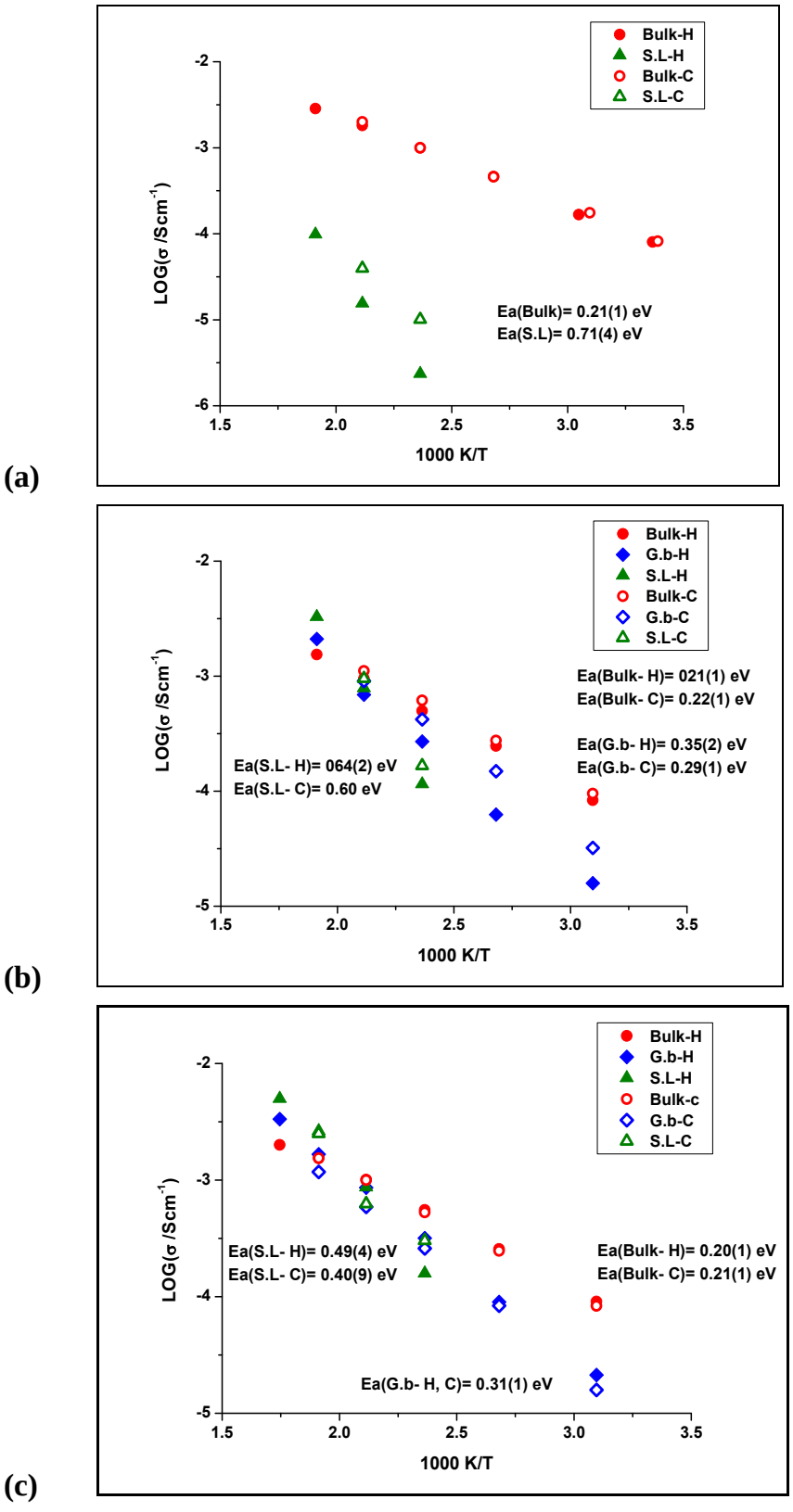

Figure 6-33: Arrhenius plot of electrical conductivity,σ showing activation energies, E_a, for $Cu_xTa_{2x}Ti_{1-3x}O_2$ (x =0.10) upon heating (H) and cooling (C) at different temperature with: (a) Au paste electrode in N_2, (b) Pt paste electrode in N_2 and (c) Pt paste electrode in O_2.

6.5 Discussion of the atmosphere effect

Impedance data for the $Cu_xM_{2x}Ti_{1-3x}O_2$, M=Nb^{5+} and Ta^{5+} (x =0.10) with paste electrodes in different gas environments show that the electrical properties of the bulk persists with no change by changing the measurement gases. In contrast, the atmosphere effect was readily observed for grain boundaries and/or surface layers with low resistance values by exposing to N_2. In addition, the capacitance of the surface layer decreases with increasing the temperature for the sample with Pt paste electrode, indicating that the thickness of the surface layer increased. On the other hand, the effect of the O_2 atmosphere on the electrical behaviour of the sample can be considered negligible.

These variations in the electrical properties with atmosphere can be explained as N_2 eliminates excess oxygen at grain boundary and surface layer, allowing the metal atoms to remain (367) and, thus, decreasing the resistivity of the material. Moreover, the increase of grain boundary and/or surface layer conductivities can be also related to the formation of a highly conductive Cu_2O, surface film; this film is formed by CuO at high temperature ~ 250°C (368), particularly in the presence of a reducing agent such as N_2. In addition, atmosphere effect of N_2 tends to be more pronounced with Pt paste electrode may due the well known catalytic effect of Pt which might be induced the formation of Cu_2O, surface film, the capacitance drop would indicate that the surface layer thickness increases and can be an evident of the significant contribution of Cu_2O, surface film. When the material is submitted to air atmosphere, the segregated metals at grain boundaries become saturated with negative species, i.e., oxygen species, so that the oxidizing gas, O_2 does not change the electrical behaviour of grain boundary and surface layer (363).

Impedance data of thermal cycle, heating-cooling, in N_2 and O_2, in appendices 8 and Figure 6-33, show difference in resistance and conductivity of the grain boundary and/or surface layer, this difference become greater with a temperature decrease. Although the temperature was held constant for 30-60 min, it seems not sufficient to establish equilibrium and this makes the atmosphere effect non-fully reversible on heating and cooling.

6.6 Effect of electrical field (DC bias)

To study DC bias effect, different voltages, 1, 5 and 10 V, were applied to the $Cu_xM_{2x}Ti_{1-3x}O_2$; M=Nb^{5+} and Ta^{5+}, (x = 0.10) sample in air at 200°C. The impedances were measured with different types of electrodes; sputtered and coated.

6.6.1 Impedance data with sputtered Au electrodes

Impedance data with sputtered Au electrodes, Figure 6-34, Figure 6-35, Figure 6-36 and Figure 6-37, with 1 and 5 volt, show no change in the bulk and grain boundary impedance. A small change can be seen before and after application/removal of 10 V dc bias. The variation in the total resistance with time before and after application of a dc bias voltage of 10 V, Figure 6-36(e), shows a decrease in the total resistance when 10 V was applied then became constant with time.

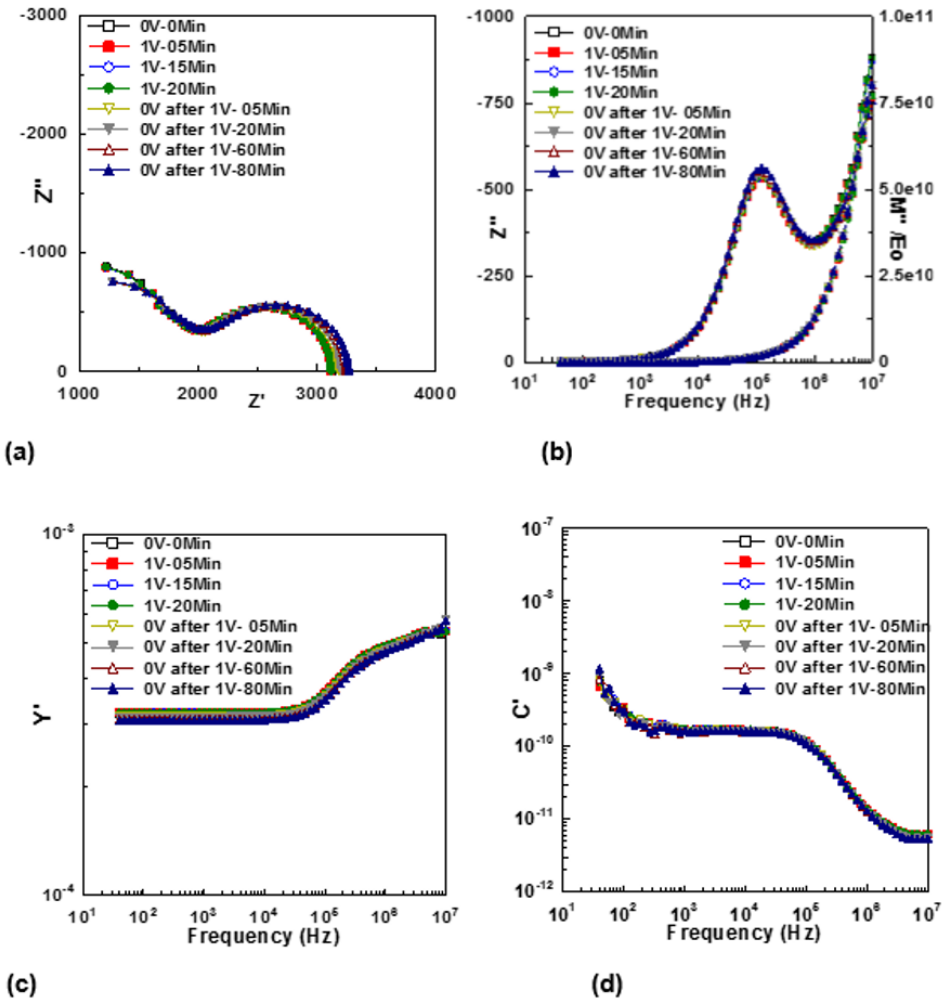

Figure 6-34: Impedance data for $Cu_xTa_{2x}Ti_{1-3x}O_2$ (x = 0.10) with sputtered Au electrodes before and after applying DC bias with 1V after different times: (a) Z^* plot, (b) Z″/M″ (c) admittance and (d) capacitance, at 200°C in air.

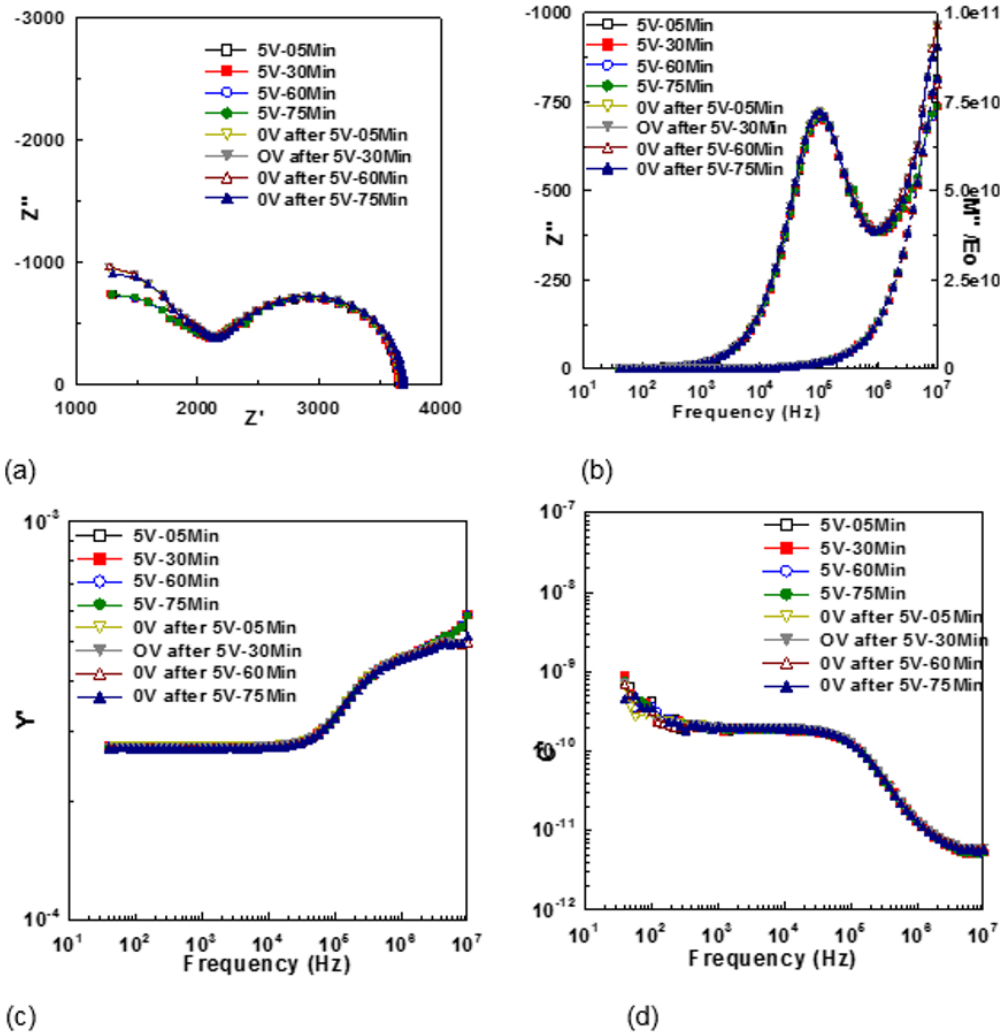

Figure 6-35: Impedance data for $Cu_xTa_{2x}Ti_{1-3x}O_2$ (x = 0.10) with sputtered Au electrode before and after applying DC bias with 5V after different times: (a) Z^* plot, (b) Z″/M″ (c) admittance and (d) capacitance, at 200°C in air.

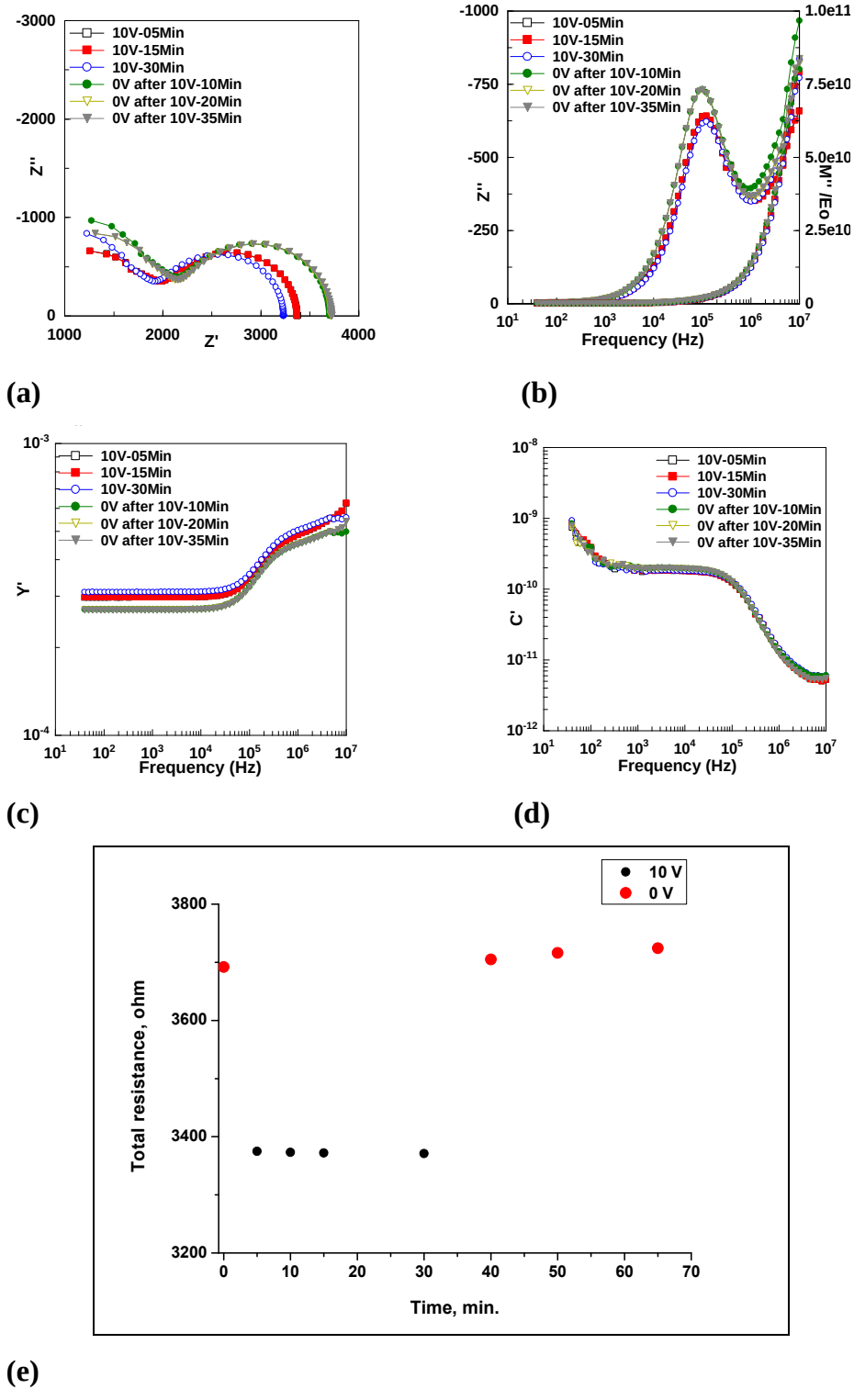

Figure 6-36: Figure 36: Impedance data for $Cu_xTa_{2x}Ti_{1-3x}O_2$ (x = 0.10) with sputtered Au electrode before and after applying DC bias with 10 V after different times at 200°C in Air: (a) Z^* plot, (b) Z″/M″ (c) admittance, (d) capacitance and (e) variation in the total resistance.

The effect of the electrical field on the electrical properties of the sample under dc bias was studies for $Cu_xNb_{2x}Ti_{1-3x}O_2$ (x= 0.10) with sputtered Au electrode at 200°C in air. Impedance data before and after applying dc bias with different voltage (1, 5 and 10V) at different time are illustrated in Figure 6-37. A small change can be observed by applying dc bias voltage, an increase in the resistance was observed under 1V while a slightly decrease in resistance, either for bulk and grain boundary, was observed when a voltage of 5 or 10V is applied. However, There is no considerable effect of dc bias voltage on the capacitance of the sample, this effect is a similar before was observed for $Cu_xTa_{2x}Ti_{1-3x}O_2$ (x= 0.10).

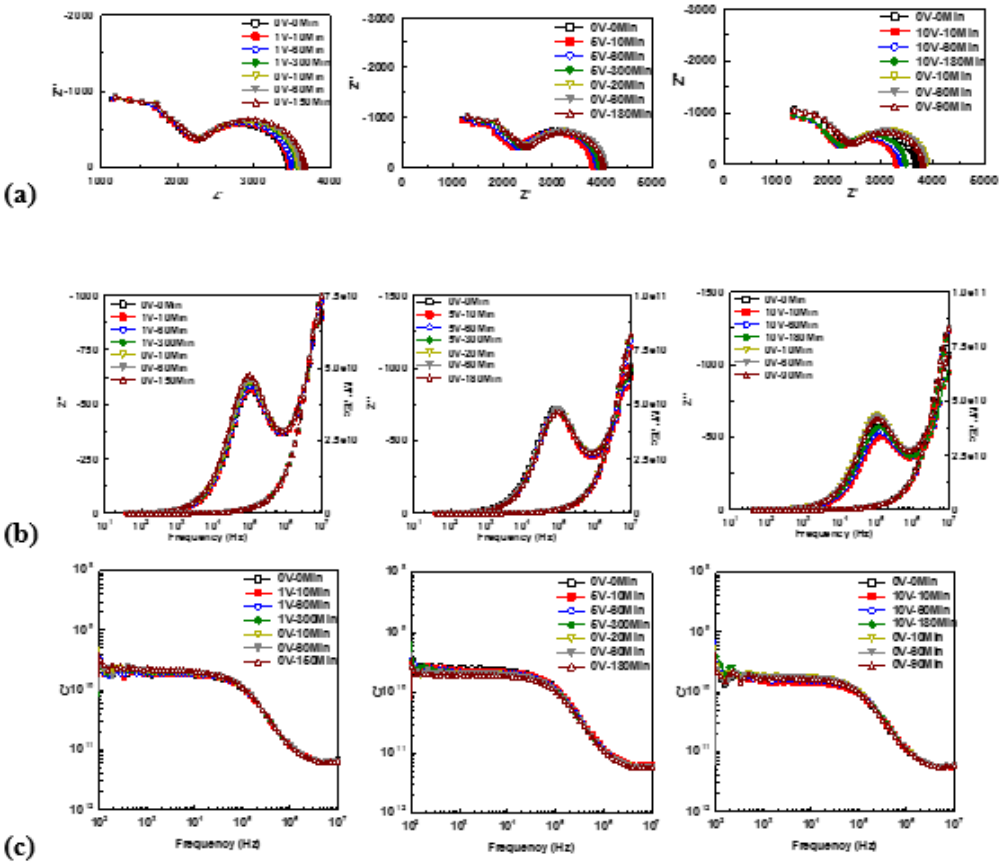

Figure 6-37: Impedance data for $Cu_xNb_{2x}Ti_{1-3x}O_2$ (x = 0.10) with sputtered Au electrode, before and after applying a dc bias with 1, 5 and 10V at different time; (a) Z^* plot, (b) Z″/M″ (c) capacitance at 200°C in air.

6.6.2 Impedance data with Au and Pt paste electrodes

Impedance results of sample with Au paste electrodes, Figure 6-38, Figure 6-39 and Figure 6-40, reveal that the sample has three different components; bulk, grain boundary and surface layer. A dc bias of different voltage has no effect on the electrical properties of bulk and grain boundary. However, surface layer component shows clear effect of dc bias on its electrical performance and exhibits different behaviour by applying different voltage.

Impedance data when 1V was applied show increase in the resistance and intensity of peak in Z″/M while no change can be seen in spectroscopic plots of admittance and capacitance. The sample has recovered its electrical properties after removing a dc bias indicating that the application of a dc bias was reversed on removal of the dc bias.

After applying a dc bias of 5 and 10 V, the surface layer resistance gradually decreases until it became constant with time. A significant decrease in the resistance of the surface layer can be seen after application 10 V. Z″/M″ data show decrease in the peak's intensity with shift to high frequency. When a dc bias of 5 V was applied, spectroscopic plot of admittance show increases in Y′ value while value of capacitance decrease gradually with time. After removal of the dc bias, electrical properties of the sample almost recovered.

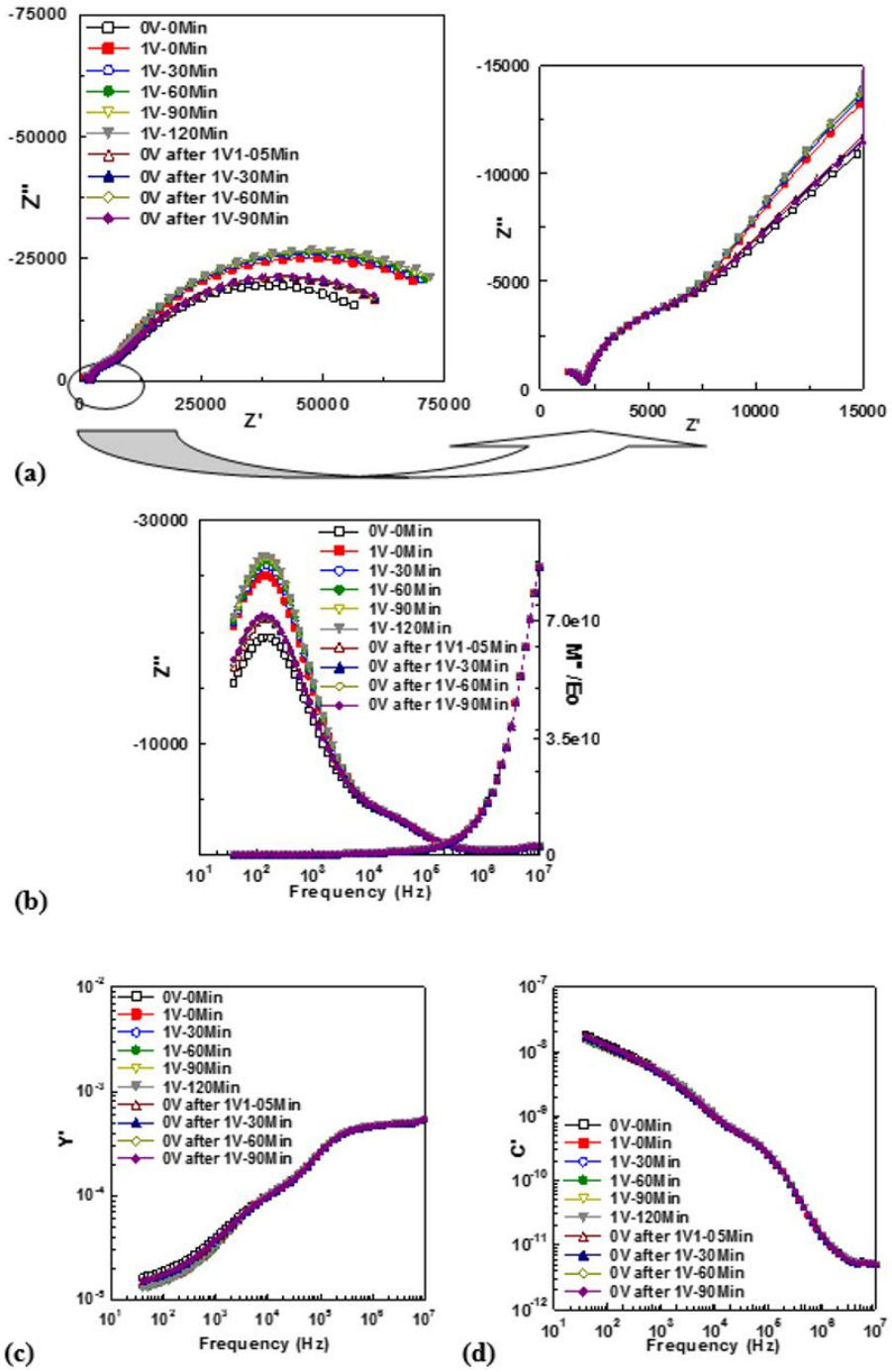

Figure 6-38: Impedance data for $Cu_xTa_{2x}Ti_{1-3x}O_2$ (x = 0.10) with Au paste electrode before and after applying DC bias 1V after different times: (a) Z^* plot, (b) Z″/M″ (c) admittance and (d) capacitance, at 200°C in air.

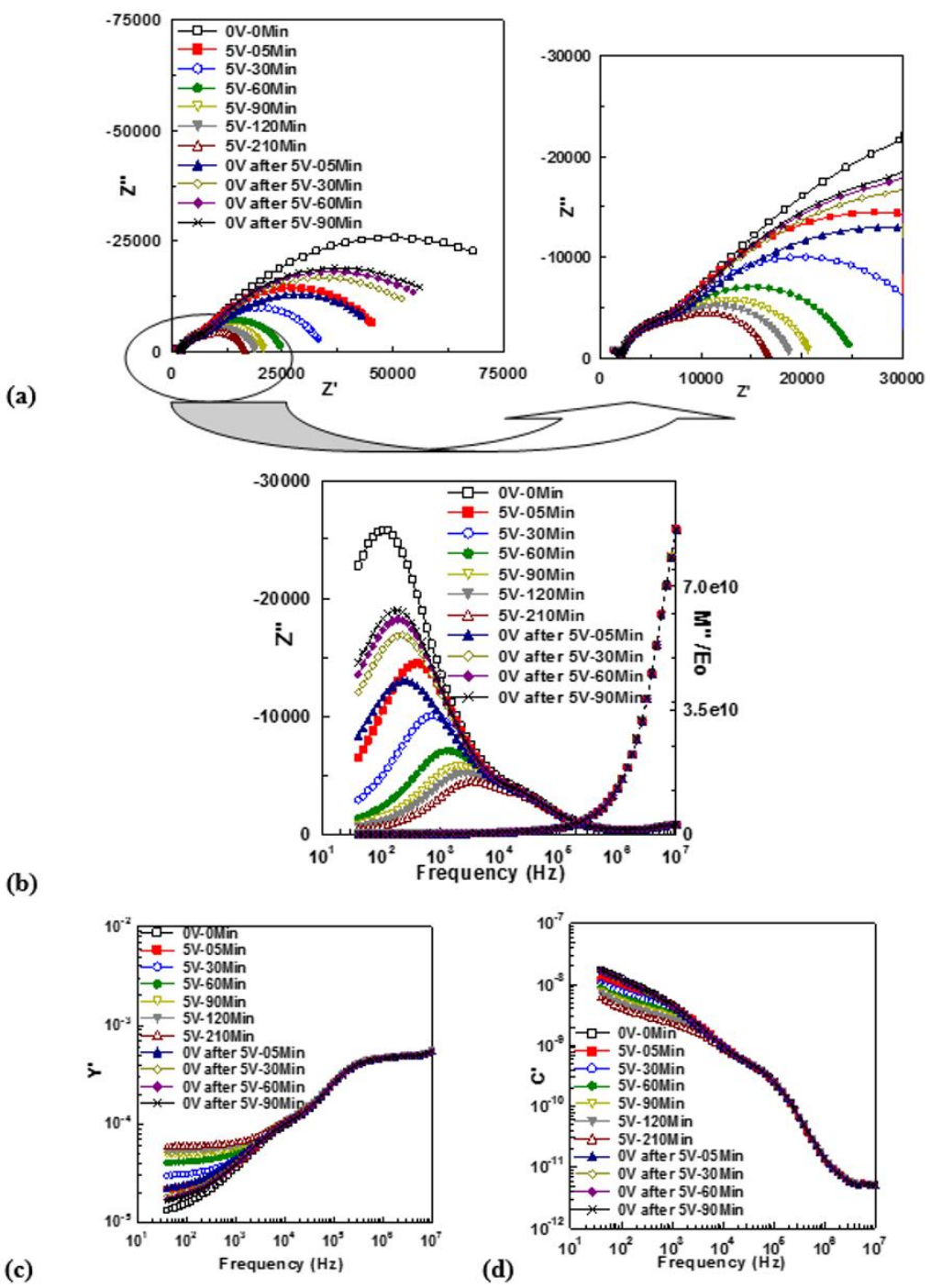

Figure 6-39: Impedance data for $Cu_xTa_{2x}Ti_{1-3x}O_2$ (x = 0.10) with Au paste electrode before and after applying dc bias 5V after different times: (a) Z^* plot, (b) Z″/M″ (c) admittance and (d) capacitance, at 200°C in air.

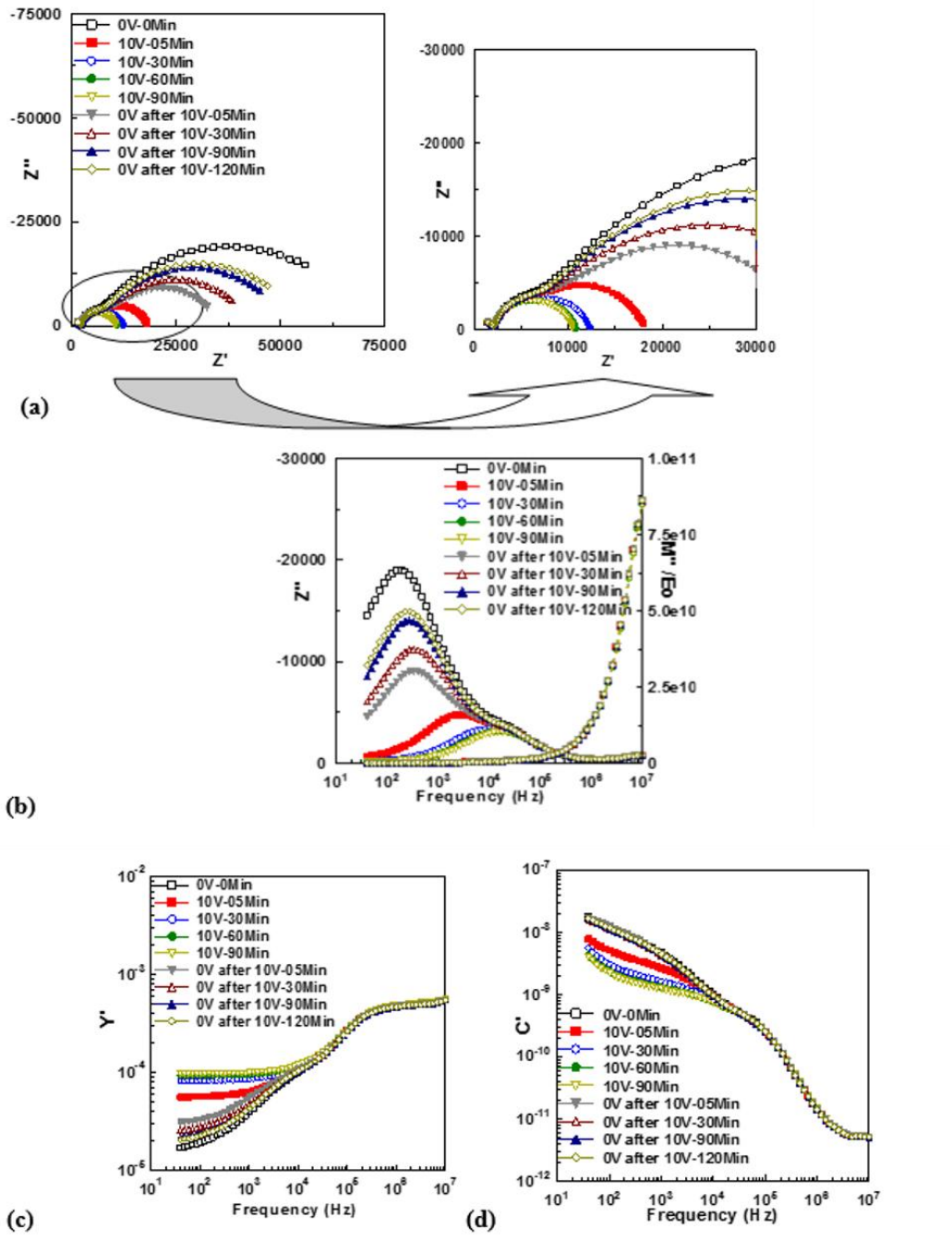

Figure 6-40: Impedance data for $Cu_xTa_{2x}Ti_{1-3x}O_2$ (x = 0.10) with Au paste electrode after applying and removing a dc bias of 10V after different times: (a) Z^* plot, (b) Z″/M″ (c) admittance and (d) capacitance, at 200°C in air.

The effect of dc bias of all different voltage applied on the sample coated with Au is summarized in Appendix D.

The effect of dc bias of 1, 5 and 10 V, of same sample with Pt paste. Impedance data in Appendix D exhibits a similar behaviour observed before for the sample coated with Au, however, a slight increase in the capacitance of the sample when dc bias of 1V voltage was applied.

The effect of an applied dc bias on the impedance response of $Cu_xNb_{2x}Ti_{1-3x}O_2$ (x= 0.10) with Au paste electrode was investigated. The impedance data are given in Figure 6-41. The resistance decreases slightly when a voltage of 1V was applied for one hour then increase gradually with time, this increasing in the resistance with the time continues even after the removal of dc bias voltage. The capacitance of sample remains constant under 1 V. However, the sample exhibits a similar behaviour as observed previously for $Cu_xTa_{2x}Ti_{1-3x}O_2$ when dc bias voltage of 5 and 10 V were applied.

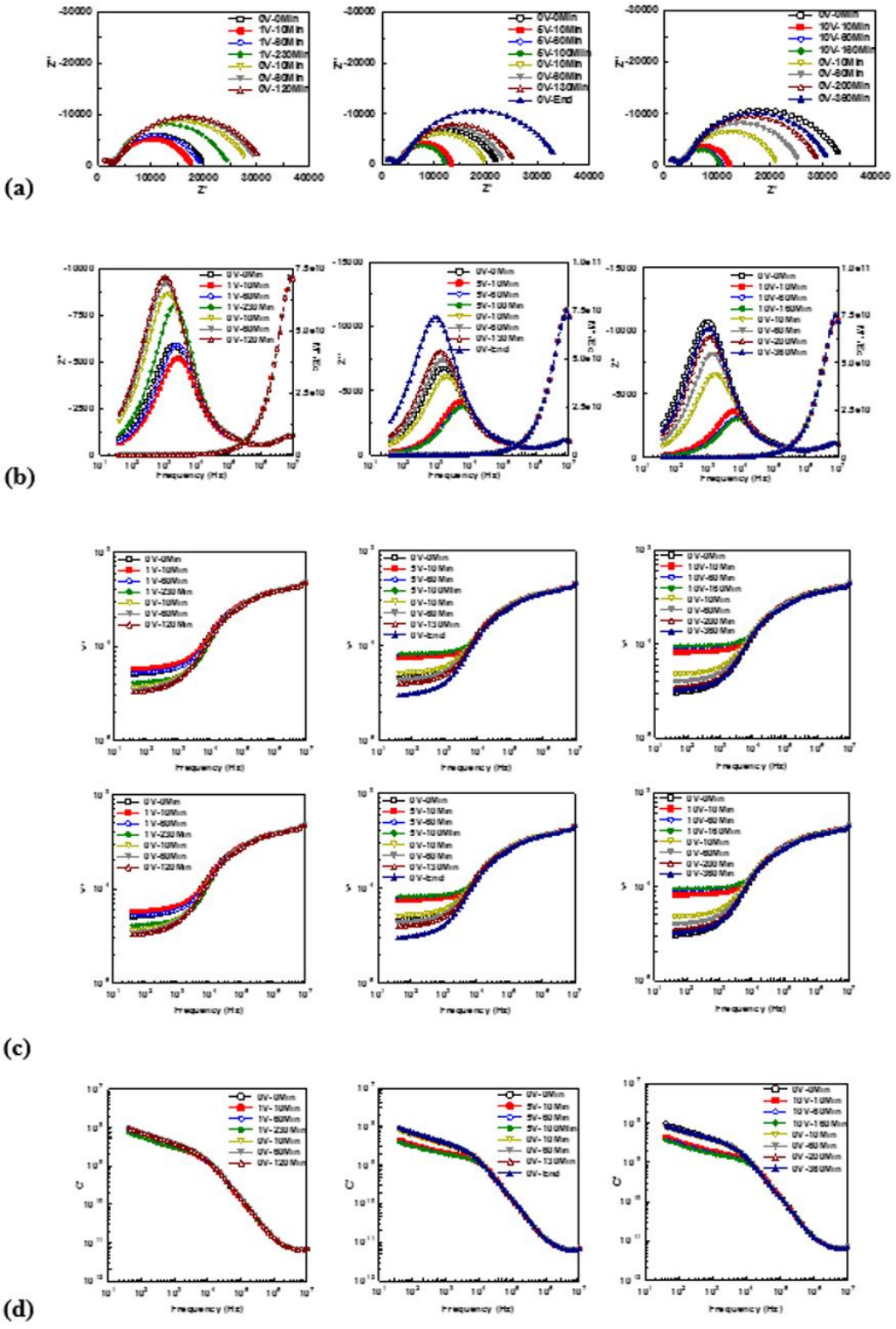

Figure 6-41: Impedance data for $Cu_xNb_{2x}Ti_{1-3x}O_2$ (x = 0.10) with Au paste electrode, before and after applying dc bias with 1, 5 and 10V at different time; (a) Z^* plot, (b) Z″/M″ (c) admittance and (d) capacitance at 200°C in air.

In summary, impedance data after applying and removing a dc bias of 1, 5 and 10 V reveals that the dc bias has no effect on the electrical property, resistance and capacitance, of both bulk and grain boundary while the electrical properties of the surface layer at low frequency are different depending on the value of voltage. A small change observed when dc bias of 1V was applied. Significant change in the electrical properties of surface layers can be observed after applying a dc bias of 5 and 10 V; however, 10 V has more pronounced effect.

$Cu_xTa_{2x}Ti_{1-3x}O_2$ (x = 0.10) coated either with Au or Pt exhibits a change in the surface layer resistance, capacitance and therefore its thickness with time when a dc voltage was applied. The changes in these properties with time and an applied dc voltage are given in Figure 6-42, Figure 6-43, Figure 6-44, Figure 6-45, Figure 6-46, Figure 6-47 and Figure 6-48.

The change in rate of surface layer resistance with Au paste electrodes versus time under a dc bias voltage of 1, 5 and 10 V are shown in Figure 6-42. The resistance value increases when 1 V was applied then became constant with time but a distinct decrease can be observed on application of a 5 and 10 V bias voltage which became constant with time. The change in rate of surface layer resistance for the sample with Pt paste electrode with time under a dc bias voltage of 1, 5 and 10 V, Figure 6-43, is similar to that with Au paste electrodes.

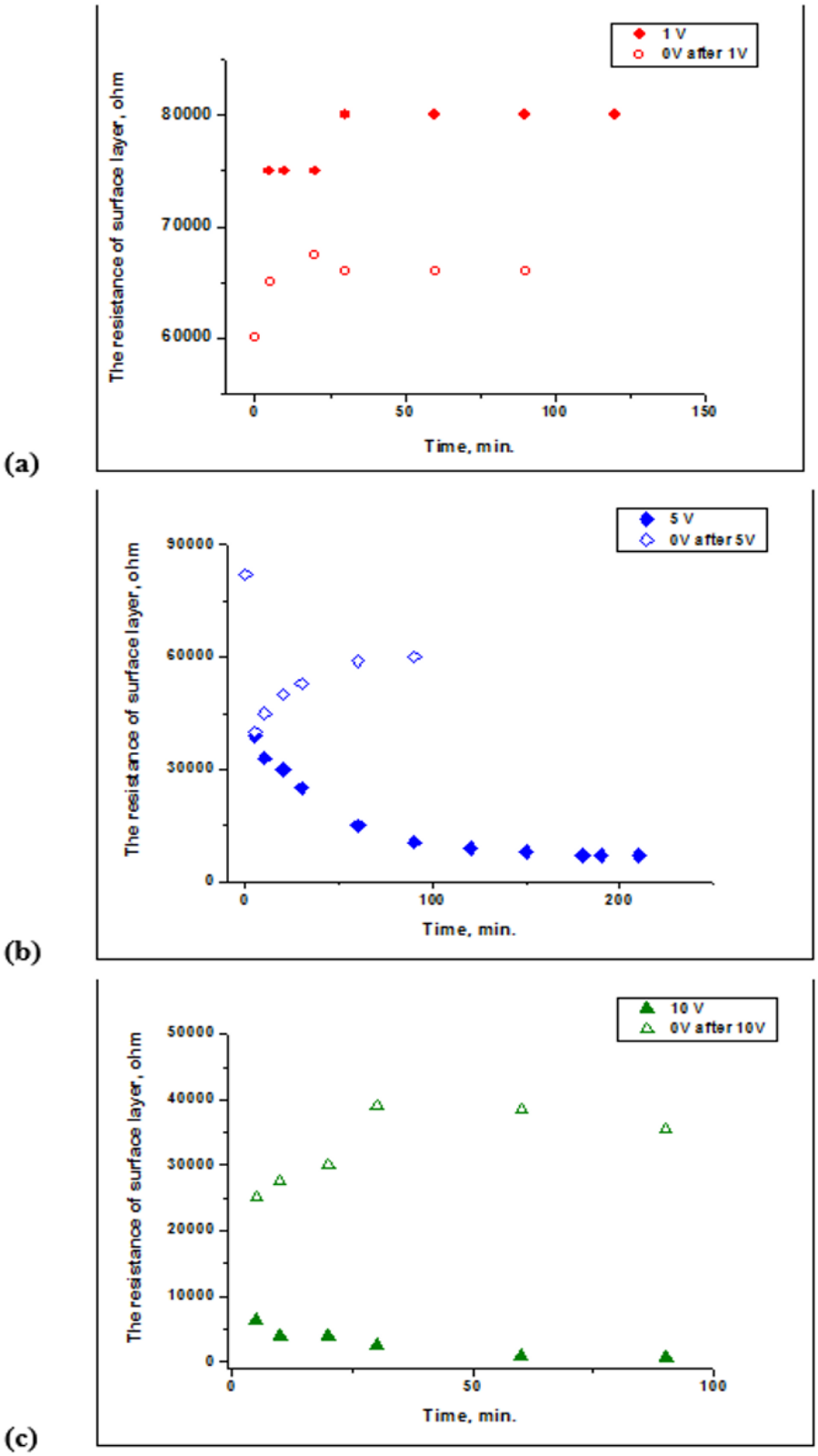

Figure 6-42: The variation of resistance of the surface layer for $Cu_xTa_{2x}Ti_{1-3x}O_2$ (x = 0.10) with Au paste electrode applying DC bias with: (a) 1, (b) 5 and (c) 10 V after different times at 200°C in air.

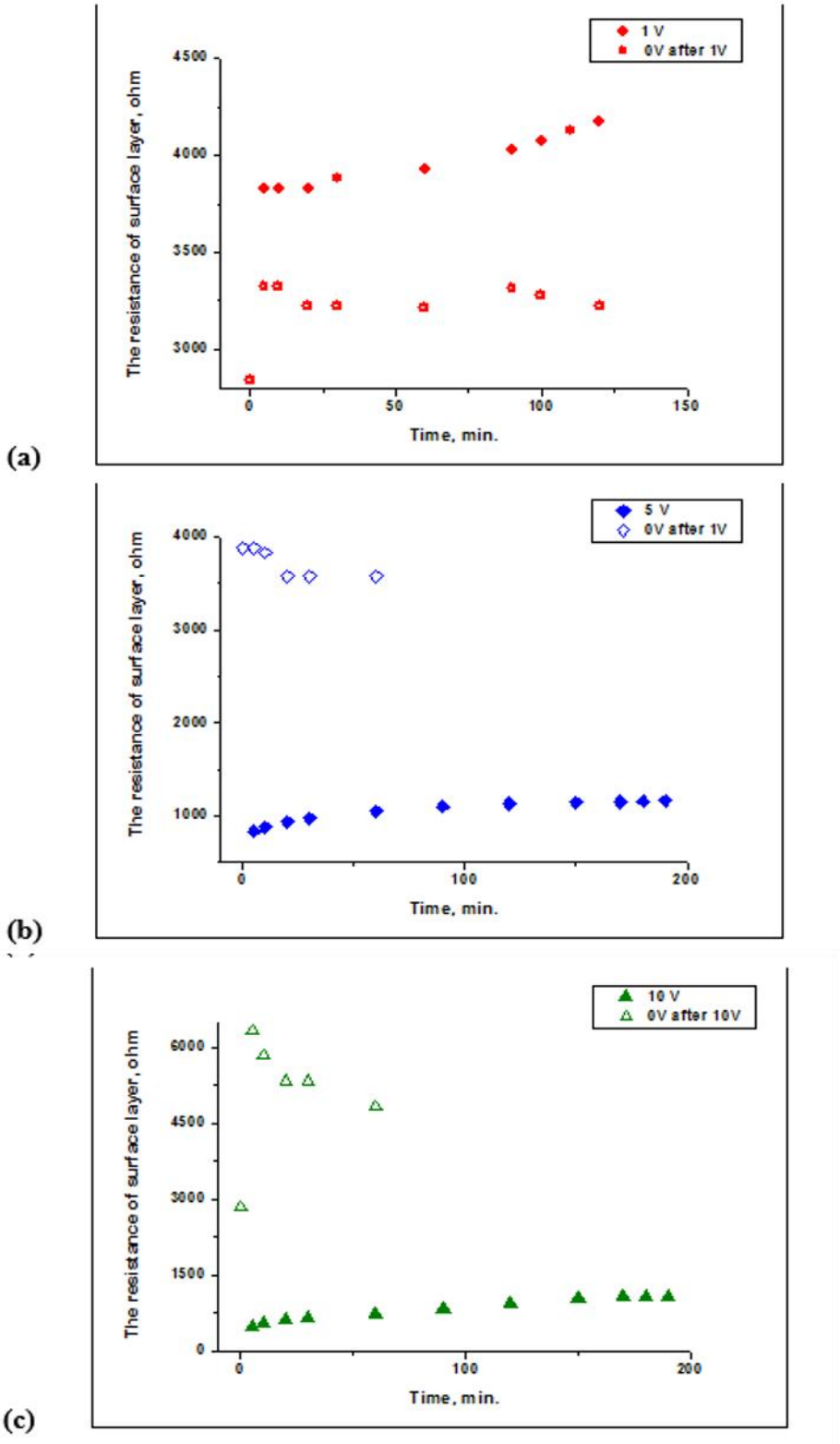

Figure 6-43: The variation of resistance of the surface layer for $Cu_xTa_{2x}Ti_{1-3x}O_2$ (x = 0.10) with Pt paste electrode applying DC bias with: (a) 1, (b) 5 and (c) 10 V after different times at 200°C in air.

Variations with total time in the change rate of surface layer resistance, the capacitance value and therefore thickness of surface layer for sample with Au and Pt paste electrode are shown in Figure 6-44 and Figure 6-45 respectively.

The change rate of surface layer resistance with total time under all voltage; 1, 5 and 10 V was summarised in Figure 6-44 and Figure 6-45(a).

The surface layer thicknesses ($l_{g.b}$) were estimated from the capacitance ratios assuming that the dielectric constant of the boundary region is equal to the bulk value, $\varepsilon_b = \varepsilon_{g.b}$, equation 3. The grain sizes thickness (l_b) was obtained from pellet thickness.

$$\frac{C_b}{C_{g.b}} = \frac{l_{g.b}}{l_b} \qquad (3)$$

By application of 1V dc bias voltage, the capacitances vary depending on the type the of electrode metal: it decreases for the sample with Au paste electrode while it slightly increases for that with Pt paste. A significant decrease in the capacitance value was observed when a dc bias voltage of 5 and 10 V were applied, Figure 6-44 and Figure 6-45 (b). The variations in the thickness with time are in opposite way, Figure 6-44 and Figure 6-45 (c). It can be seen that these changes became constant with time. The resistance and capacitance was retained to original state after the removal of dc bias of 1, 5 and 10 V.

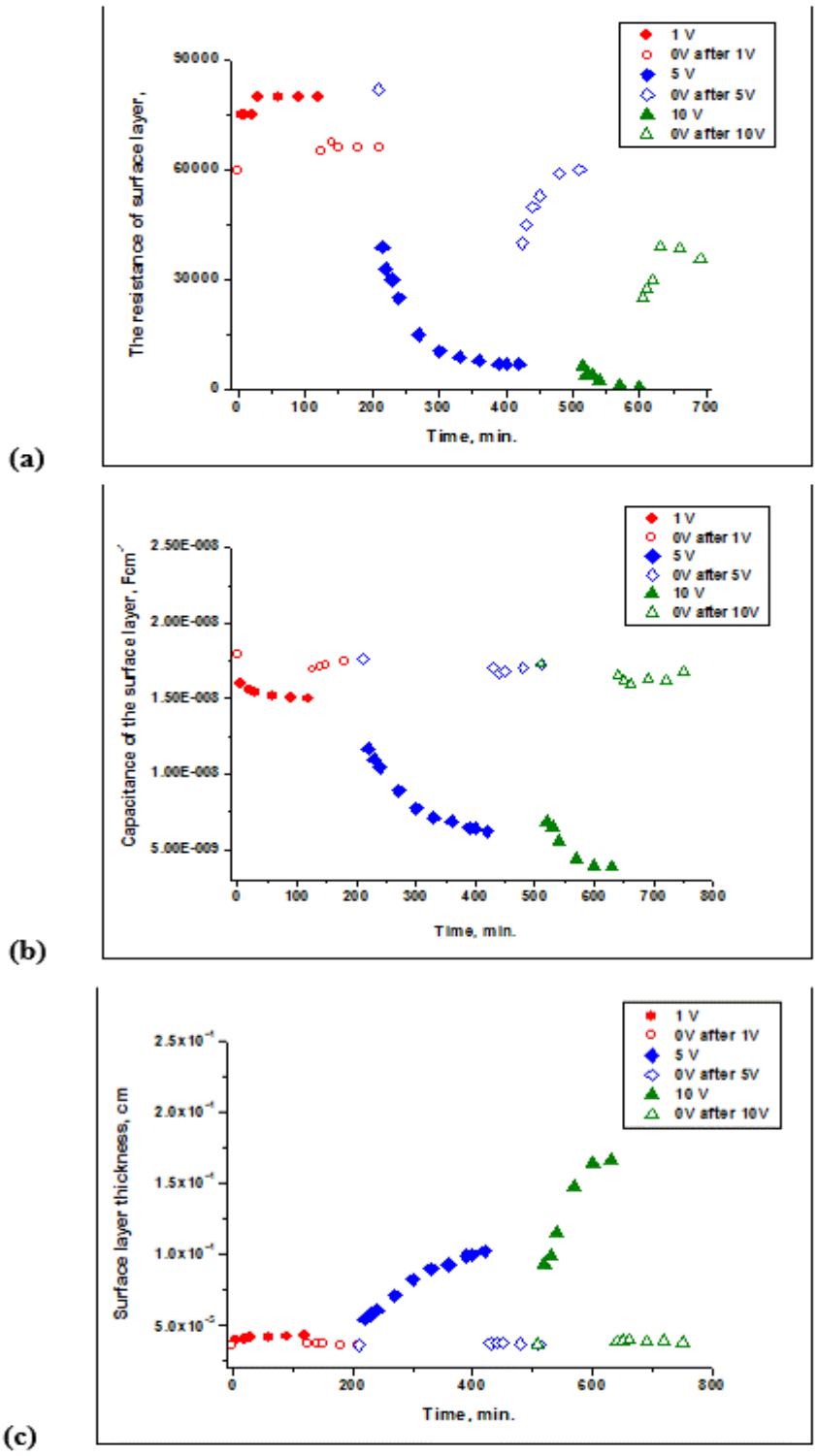

Figure 6-44: The variation of: (a) resistance of the surface layer, (b) capacity value and (c) the thickness of surface layer for $Cu_xTa_{2x}Ti_{1-3x}O_2$ (x = 0.10) with Au paste electrodes at 200°C in air before and after applying/removal dc bias with different voltage.

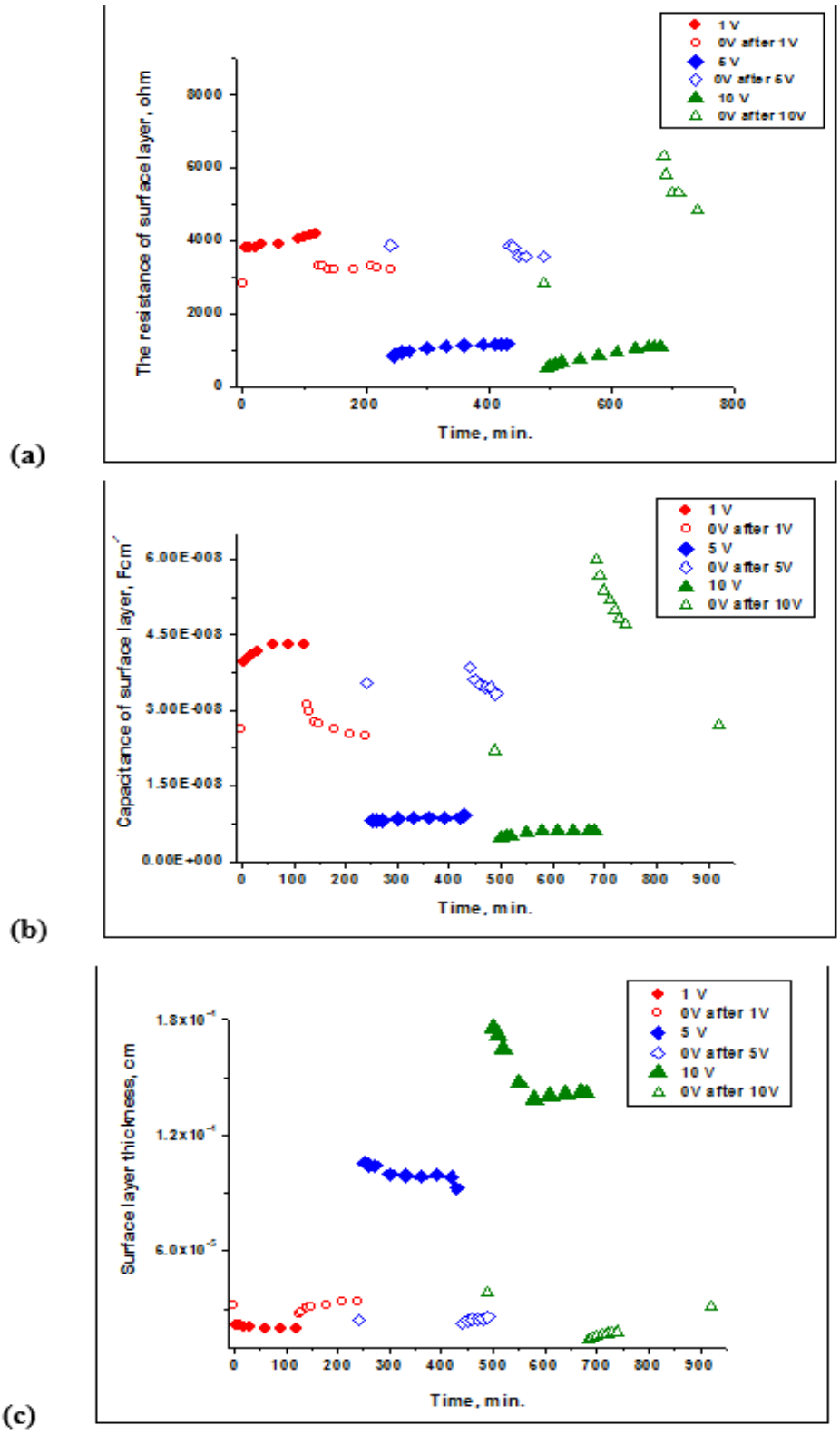

Figure 6-45: The variation of: (a) resistance of the surface layer, (b) capacity value and (c) the thickness of surface layer for $Cu_xTa_{2x}Ti_{1-3x}O_2$ (x = 0.10) with Pt paste electrode applying dc bias with 1, 5 and 10 V after different times at 200°C in air.

The change in the resistance value of the surface layer versus the voltage applied on the sample with Au and Pt paste electrode is given in Figure 6-46 (a) and (b) respectively. In both cases, the resistance slightly increases under 1V and significant decreases by application of 5 and 10V.

The change in the capacitance of the surface layer versus the voltage applied on the sample with Au and Pt paste electrode is given in Figure 6-47 (a) and (b) respectively. For the sample with Au paste electrode, the capacitance decreases at the all applied voltages. On the other hand, the capacitance increases when 1V was applied and decreases when 5 and 10 V was applied for the sample with Pt paste electrode.

Variations in voltage have an effect on the thickness of the surface layer but in opposite manner to that of capacitance, as shown in Figure 6-48(a) and (b) for the sample with Au and Pt paste electrode respectively.

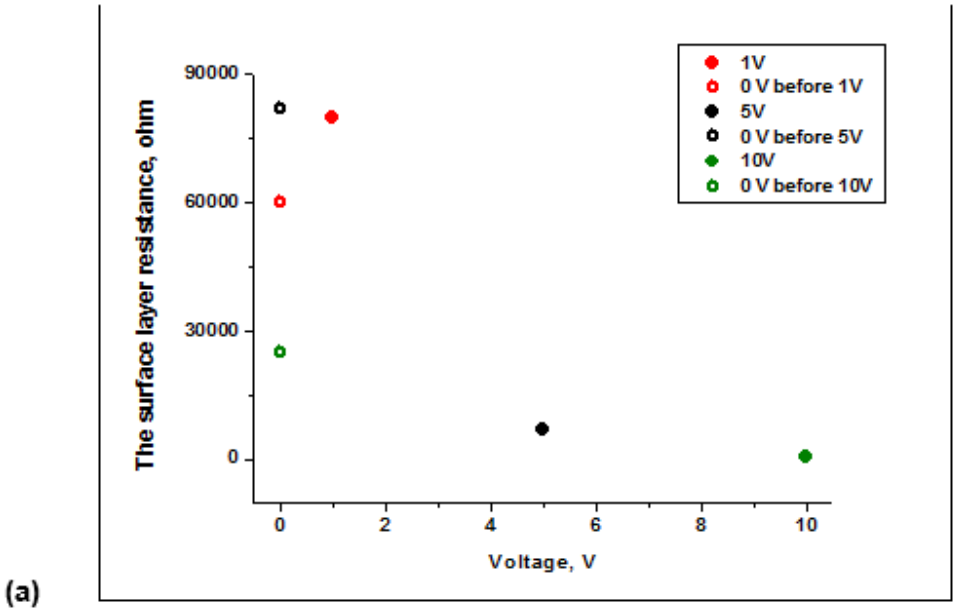

(a)

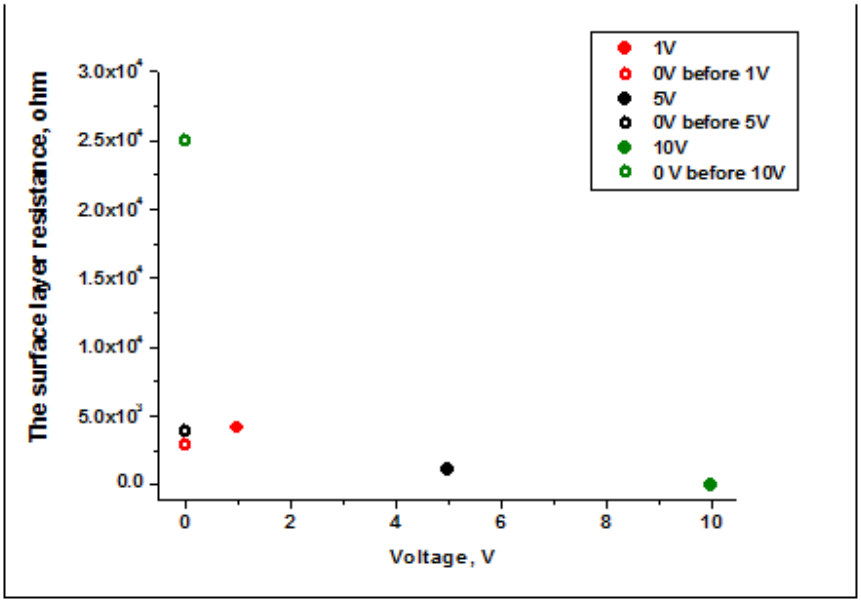

(b)

Figure 6-46: the variation in the resistance of the surface layer after reach steady state with applied voltage for $Cu_xTa_{2x}Ti_{1-3x}O_2$ (x = 0.10) with: (a) Au paste and (c) Pt paste electodes at 200°C in air.

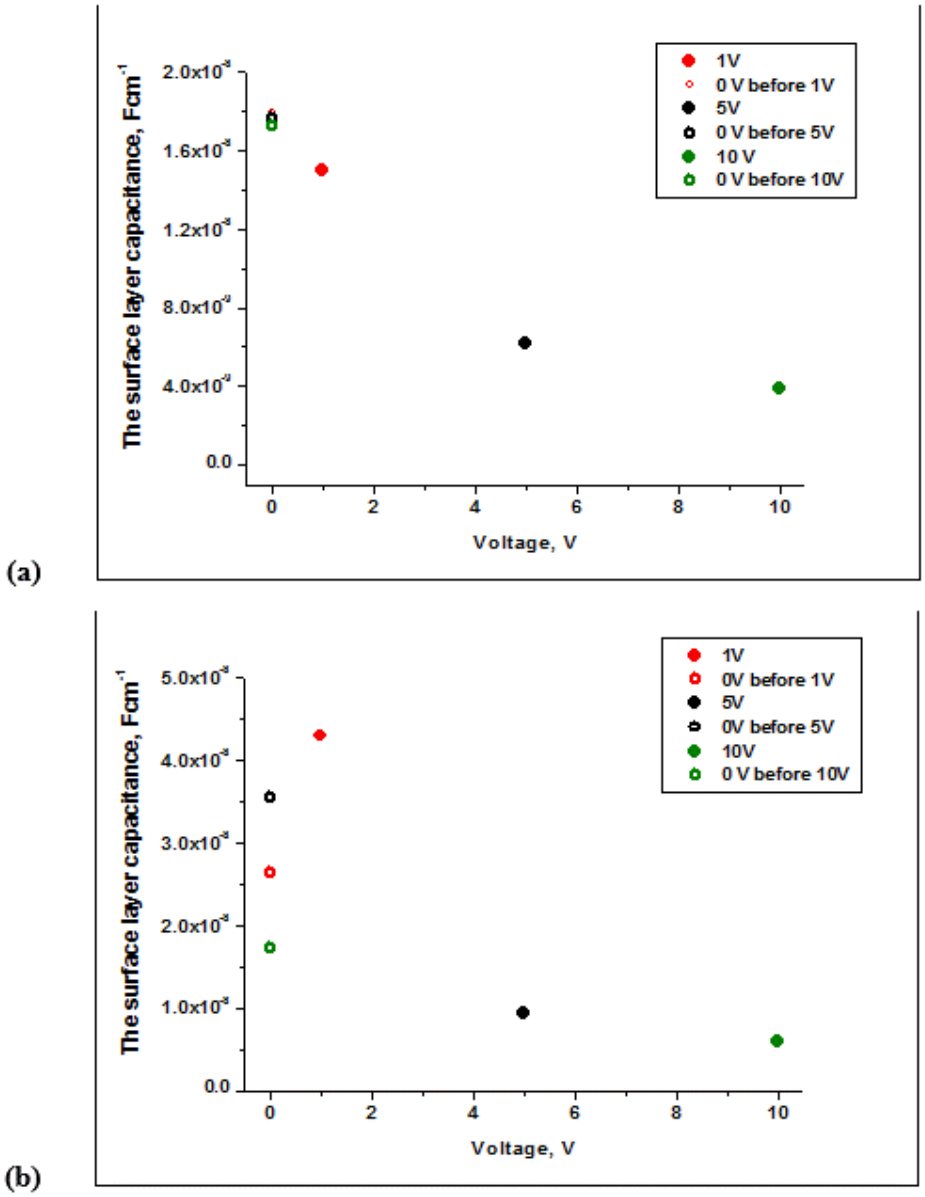

Figure 6-47: the variation in the capacity value of surface layer after reach steady state with applied voltage for $Cu_xTa_{2x}Ti_{1-3x}O_2$ (x = 0.10) with: (a) Au paste and (b) Pt paste electrodes at 200°C in air.

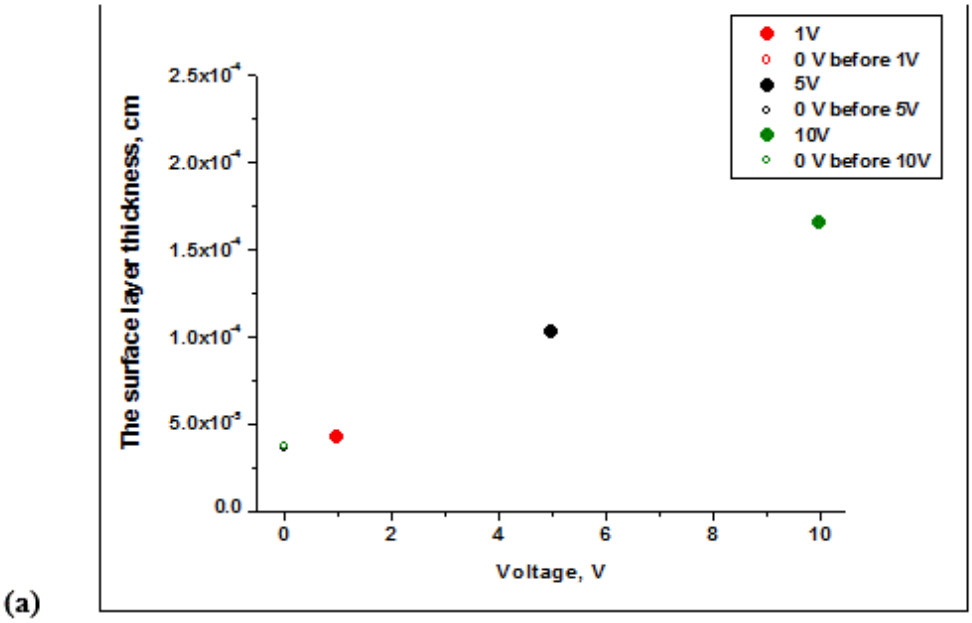

(a)

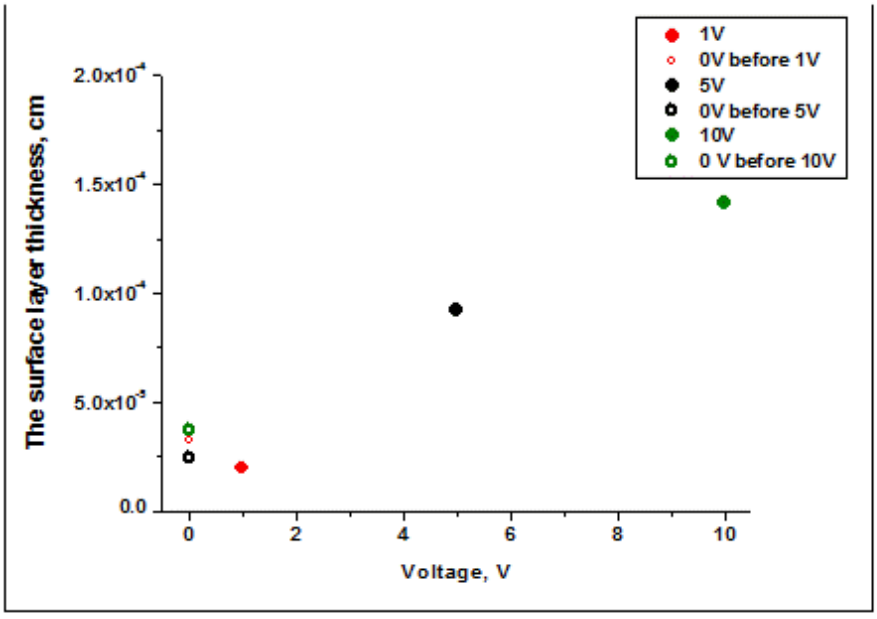

(b)

Figure 6-48: the variation in the surface layer thickness after reach steady state with applied voltage for $Cu_xTa_{2x}Ti_{1-3x}O_2$ (x = 0.10) with: (a) Au paste and (c) Pt paste electrodes at 200°C in air.

6.7 Discussion of electric field effect

The DC bias dependent measurements are appropriate to elucidate the nature of the grain boundary influence on electrical properties (369–371). For that, different voltages, 1, 5 and 10 V, were applied to the $Cu_xM_{2x}Ti_{1-3x}O_2$; M=Nb^{5+} and Ta^{5+} (x=0.10) sample in air at 200°C with different type of electrodes; sputtered and coated.

The application or removal of dc bias voltage has no effect on both bulk and the grain boundary of the sample with sputtered electrode. No evidence of a dc bias effect on the resistance or capacitance of the sample was observed. The constant resistance is because mobility and concentration of carriers are unaffected by small applied voltages indicates the absence of interfacial effects. 10V, a change was observed in term of the resistance decreasing, see Fig. 36; however, the capacitance is uninfluenced by applied voltage of 10 V.

A system with Schottky-like barrier is supposed to show a decrease in the capacitance of grain boundaries with increasing dc bias voltage due to an increase in the depletion layer width. The constant resistance and capacitance of a sample with sputtered electrodes under dc bias voltage is evidence of the absence of the potential barrier. This result is in good agreement with the impedance data in different atmospheres, section 6.1.1.

The application or removal of dc bias voltage has no effect on both bulk and the grain boundary of the sample with paste electrodes. However, the lower frequency response was affected and was dependent upon the magnitude of the applied voltage. A small change was observed when 1V was applied while a significant change in the electrical property of surface layer can be observed after applying a dc bias of 5 and 10 V; however, 10 V has more pronounced effect. The change in the resistance and capacitance reveal a decrease in the resistance and capacitance for both systems with all types of paste electrodes fewer than 5 and 10. By contrast, the resistance shows an increase under 1V while the very small change in the capacitance can be considered as constant. After removal of the dc bias voltage, the electrical properties of the sample almost recovered and regained their original state.

The low frequency responses show significant voltage dependence. The effect of increasing the bias voltage is to decrease the low frequency intercept in complex

plane Z* and the magnitude of the peak in Z″/M″; this suggests that in this region the resistance is highly non-ohmic. This behaviour is also clearly demonstrated in the spectroscopic plot of capacitance: where the low frequency capacitance is voltage dependent. The voltage dependent on both the resistance and capacitance can be attributed to a dependence of the effective barrier height on the applied voltage. This would indicate, for such a model, that the layer thickness essentially increases by increasing the bias voltage.

In general, the dc bias behaviour of $Cu_xM_{2x}Ti_{1-3x}O_2$; M=Nb^{5+} and Ta^{5+} with paste electrodes is consistent with semiconducting bulk-insulating surface layer model, that has Schottky-like barrier as we suggest previously.

6.8 Conclusion

- The electrode applied effect was readily observed in terms of the type of metal electrode and the processing of the electrode.
- The different behaviours between samples with paste and sputtered electrodes should be attributed to their different microstructures.
- In the absence of interfacial effects, $Cu_xM_{2x}Ti_{1-3x}O_2$; M=Nb^{5+} and Ta^{5+} exhibits two electrical responses: bulk and grain boundary. An additional (lower frequency) response associated with a surface layer effect was observed and was dependent upon the type of electrode processing.
- The dc bias behaviour with paste electrodes is consistient with a Schottky-like barrier nature.
- Further study is needed to investigate the electrical properties of $Cu_xM_{2x}Ti_{1-3x}O_2$; M=Nb^{5+} and Ta^{5+}, in particular, the origin of the semi-conductivity bulk and the nature of the grain boundary and surface layer regions.

7. ELECTRICAL AND ELECTROCHEMICAL BEHAVIOUR OF Sn-DOPED RUTILE TiO_2

7.1 Introduction

Mixed oxides of SnO_2/TiO_2 are promising materials for use in a range of applications, particularly as gas sensors (372) and in photocatalysis (373). The response of SnO_2-TiO_2 mixtures shows higher sensitivity towards H_2 and CO compared to the sensitivity of the individual oxides (374). It has also been reported that the substitution of Sn for Ti in the TiO_2 lattice improves photocatalytic activity; for example, the photocatalytic activity of $Sn_xTi_{1-x}O_2$ for the oxidation of acetone is higher than that of pure rutile TiO_2 by 15 times (375).

TiO_2 and SnO_2 are *n*-type semiconductors with a tetragonal rutile structure and space group $P4_2/mnm$, Figure 7-1. Both cations are in octahedral coordination with oxygen with lattice parameters, for SnO_2, a = 4.737Å and c = 3.360 Å, and for TiO_2, a = 4.594Å and c =2.959 Å (376). Ti^{4+} and Sn^{+4} ions have a comparable ionic radius (Ti^{4+} =0.68 Å, and Sn^{4+}= 0.71 Å), but Sn^{4+} is slightly larger. Therefore, the substitution of Sn^{4+} by Ti^{4+} (or vice versa) in the binary system lattice is unlikely to create oxygen vacancies or another kind of defect chemistry but to be a simple substitution of the kind shown in equation 1:(372,376).

$$TiO_2 \xrightarrow{SnO_2} Sn_{Ti}^{x} + 2O_O^x \qquad (1)$$

However, an expansion of the rutile lattice is expected on the partial replacement of Ti by Sn.

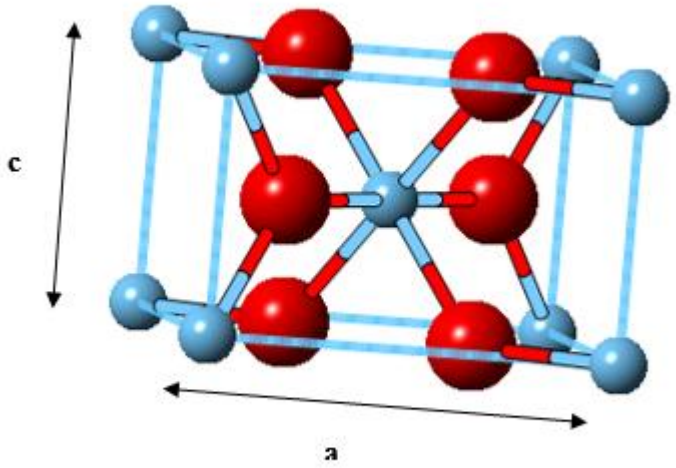

Figure 7-1: Primitive unit cell of the rutile structure, space group *$P4_2/mnm$.* Small blue balls correspond to titanium (or tin) atoms, and big red balls to the oxygen atoms.

The binary phase diagram for TiO_2-SnO_2 shows a complete range of solid solutions at high temperatures but at lower temperatures, a nearly symmetric spinodal dome with a critical temperature centred at about 50 % of each component (377). The upper consolute temperature reported by different authors is: 1330°C, 1430°C, and 1475°C (378), Figure 7-2. Above this critical temperature, solid solutions of $Sn_xTi_{1-x}O_2$ are thermodynamically stable and occur over the entire range of compositions ($0.0 \leq x \leq 1.0$). However, TiO_2-SnO_2 solid solutions undergo spinodal decomposition upon cooling from high temperature as they enter the miscibility gap, which results in separation into Ti-rich and Sn-rich phases. In spite of the existence of the miscibility gap and since the rate of spinodal decomposition is quite slow at room temperature, it may be possible to preserve stable, single phase $Sn_xTi_{1-x}O_2$ solid solutions for ($0\leq x \leq 0.2$) and ($0.8\leq x \leq 1.0$) by quenching (235,372,379).

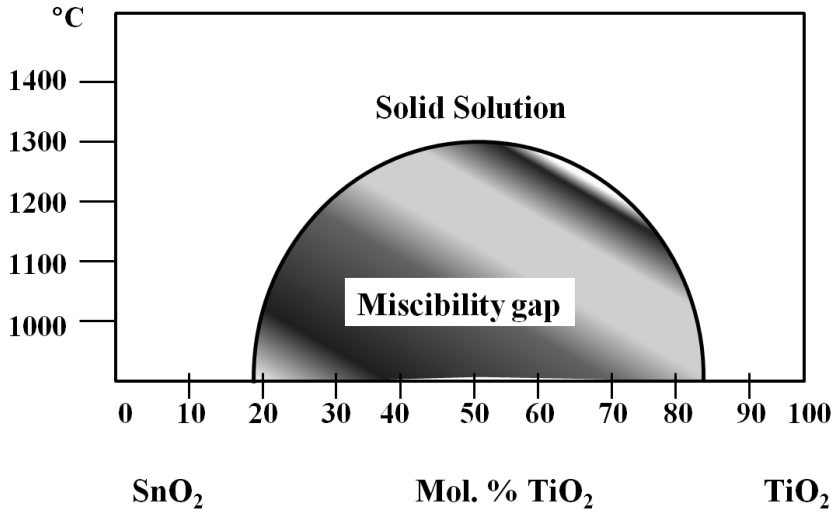

Figure 7-2: Schematic representation of the SnO_2-TiO_2 Phase diagram.

Different synthetic methods were used to prepare solid solutions of $Sn_xTi_{1-x}O_2$. Solid state reaction between a mixture of TiO_2 and SnO_2 powders at high temperature yielded highly porous micron size particles with weak mechanical strength (235,380). In addition to the traditional solid state synthetic techniques, co-precipitation from aqueous solutions which include hydrothermal, (381,382) sol−gel (173), and solvothermal (polyol-mediated)(383,384) methods have been reported. Compared with solid state reaction, these solution-based techniques require lower calcination temperatures to yield denser nanosized crystals of $Sn_xTi_{1-x}O_2$ (380–384).

The thermodynamic and kinetic properties of the SnO_2-TiO_2 system have been quite extensively studied to determine the phase diagram and to study the immiscibility and spinodal decomposition. (377) Also, extensive experimental (235,372,374,385,386) and theoretical (387–389) studies on the structural and electronic properties of $Sn_xTi_{1-x}O_2$ solid solutions have been reported. Sn-doped nanoscale or mesoporous TiO_2 have been reported (194,390,391) as anodes with excellent electrochemical performance in which Sn maintain the high capacity while TiO_2 maintain the structural stability of the electrode by accommodate the volume expansion during charge-discharge. However, apart from this, the basic electrical features and more general properties relevant to applications of the SnO_2-TiO_2 system have not yet been investigated in depth.

This chapter reports the synthesis of Sn-doped TiO_2 solid solutions through the solid state approach with characterisation by XRD and SEM. The electrical properties and the electrochemical performance of the different compositions of the solid solution are reported in this section. Due to the high electro-activity of SnO_2 and the good structural stability of TiO_2, $Sn_xTi_{1-x}O_2$ (where $0.05 \leq x \leq 0.95$) composition tested as negative electrodes for lithium-ion batteries and the results are promising.

7.2 Experimental

Single phase, Sn-doped-rutile TiO_2 solid solutions, with selected compositions given by the general formula: $Sn_xTi_{1-x}O_2$ ($0 \leq x \leq 1$), were prepared by solid-state reaction, with the exception of some intermediate compositions ($0.25 \leq x \leq 0.75$) for which phase-separation occurred on cooling by spinodal decomposition, as confirmed by x-ray-diffraction profiles (385). TiO_2 and SnO_2 were dried at 900°C for TiO_2 and 1100°C for SnO_2 and mixed in stoichiometric amounts using an agate mortar and pestle. The mixtures were pelleted, transferred to an alumina crucible and fired in air, in a muffle furnace at 1200°C for 72 hrs followed by quenching on a metal plate to reduce the possibility of spinodal decomposition. Phase analysis and determination of lattice parameters and crystal size were conducted using STOE's $WinX^{pow}$ software package.

7.3 Characterisation, structural properties and microstructure of $Sn_xTi_{1-x}O_2$ solid solutions

7.3.1 Results

The X-ray diffraction patterns of the solid solutions are shown in Figure 7-3. All samples were detected as a single phase rutile structure; significant shifts of the diffraction peak positions toward lower 2θ values were observed with increasing x. This means that the processing conditions, including cooling rate, used to synthesise these compositions did not permit spinodal decomposition; secondary phases cannot be detected at less than 1% level by X-ray powder diffraction. Table 7-1 shows the lattice parameters, cell volume, and crystal size of $Sn_xTi_{1-x}O_2$. It is clear that the lattice parameters and cell volume of the solid solutions increase with an increase in the level of Sn. A comparison of these experimental structural data

with those reported by Hirata et al. (385) , in Table 7-1, displays a good agreement. Table 7-1 also shows that the crystal size of the solid solutions prepared here decreases greatly with the substitution of 5% Sn into the TiO_2 lattice until the nominal x=0.90 when the crystal size increases gradually. The calculated values of the tetragonal lattice parameters *a* and *c* for $Sn_xTi_{1-x}O_2$ are plotted as a function of x in Figure 7-4. The axial ratio *c*/*a* and the unit cell volume *V* are also presented. It is clear that the lattice parameters and/or cell volume increase linearly with increased Sn content according to Vegard's Law.

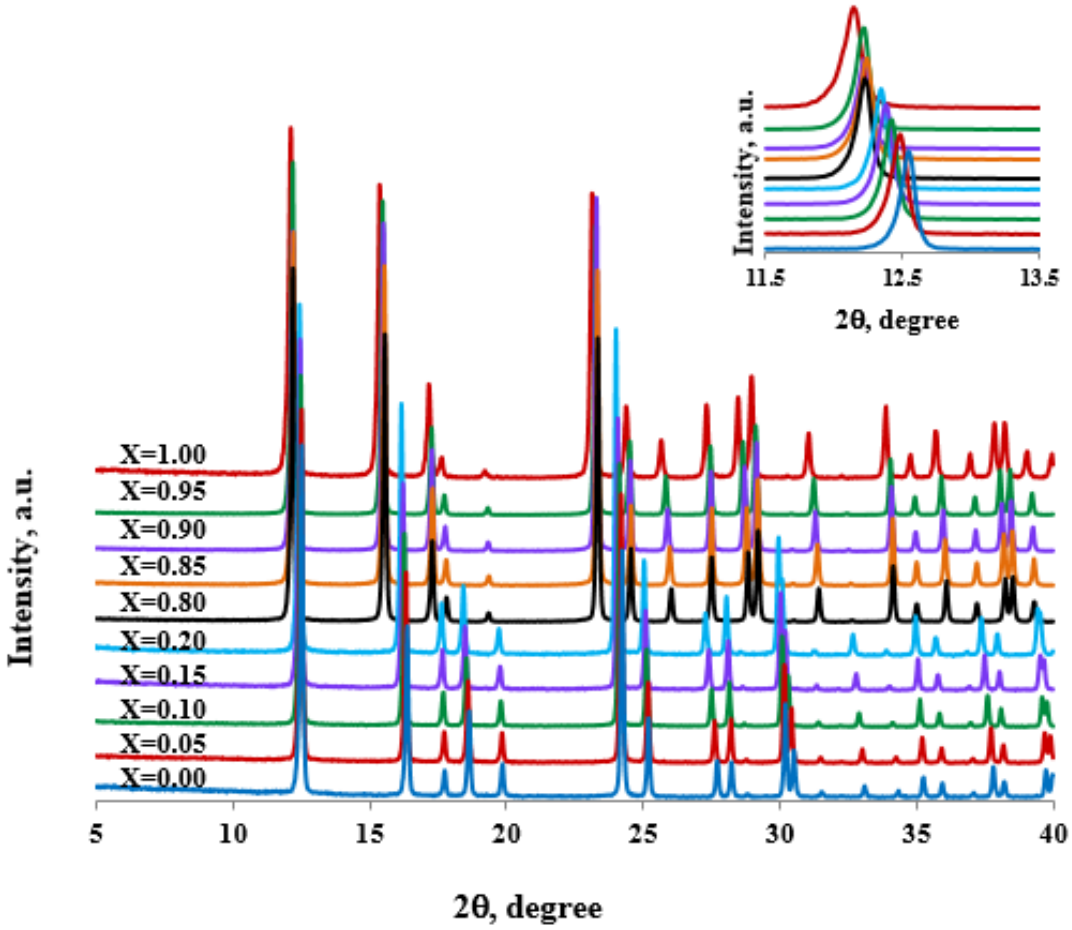

Figure 7-3: XRD patterns for $Sn_xTi_{1-x}O_2$ ($0.0 \leq x \leq 1.00$); the inset shows the shift in the peak positions around 12.5°. a.u. refers to arbitrary units of intensity as data sets have been offset vertically to show the evolution of the XRD patterns with increasing Sn content.

Table 7-1: The lattice parameters, cell volume and the particle size of $Sn_xTi_{1-x}O_2$ ($0.0 \leq x \leq 1.0$)

x (Sn level)	a (Å)			c (Å)			V (Å)3			crystal size (nm)
	A	B		A	B		A	B		
0	4.5976	4.5941	*4.5933	2.9615	2.9589	*2.9592	62.600	62.450	*62.4	36.53
0.05	4.6001	-		2.971	-		62.895	-		24.73
0.10	4.6102	4.6085		2.9831	2.9817		63.403	63.326		30.91
0.15	4.6171	-		2.9944	-		63.833	-		30.08
0.20	4.6265	4.6229		3.0074	3.0044		64.370	64.208		27.31
0.80	4.7159	4.709		3.1485	3.141		70.024	69.6		26.16
0.85	4.717	-		3.1557	-		70.213	-		22.36
0.90	4.722	4.724		3.1653	3.164		70.576	70.6		25.87
0.95	4.7253	-		3.1729	-		70.845	-		30.97
1.0	4.7454	4.7380	**4.738	3.1871	3.1911	**3.1871	71.860	71.538	**71.5	36.59

A= data from this work, B= experimental data reported by Hirata.(385,392)[*] Data from JCPDS-ICDD, No. 21, 1276, [**] Data from JCPDS-ICDD, No. 41, 1445. (Quality: *).

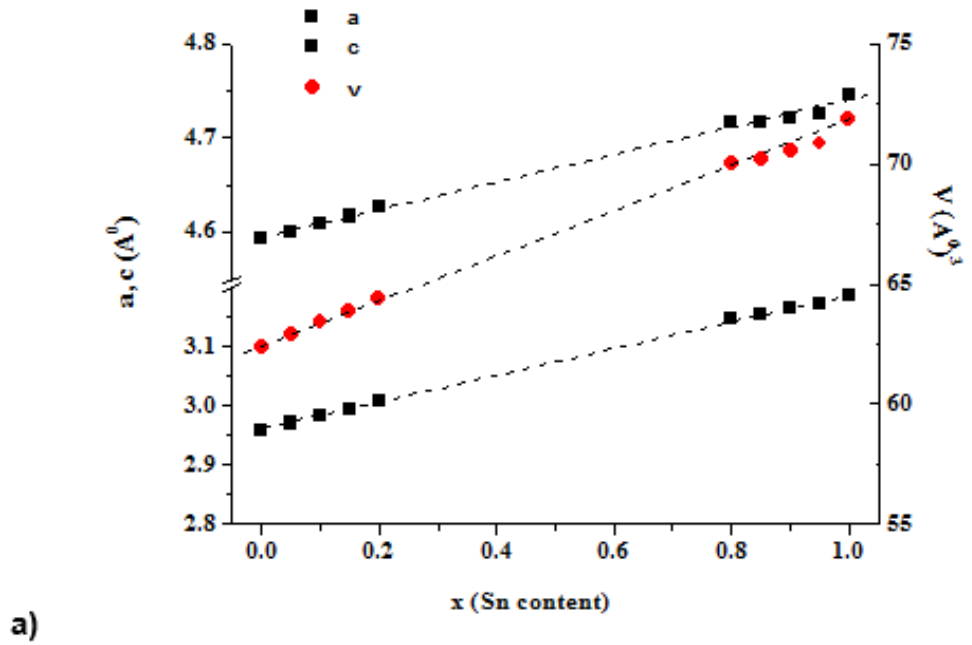

a)

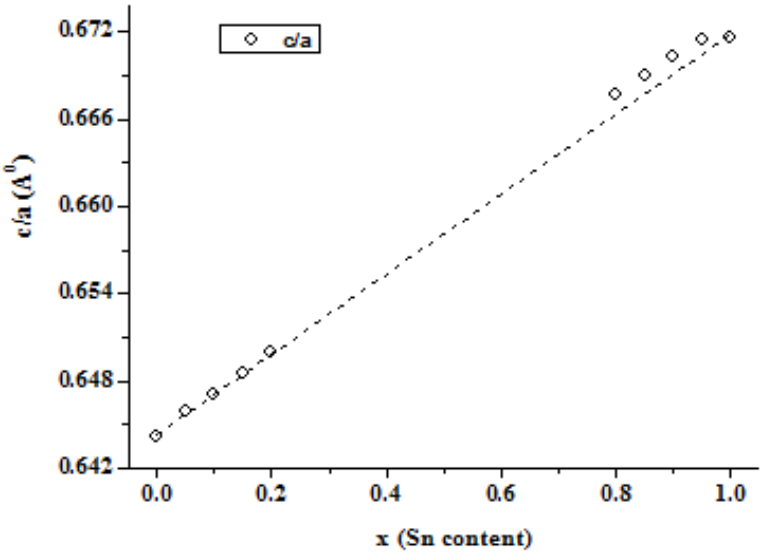

b)

Figure 7-4: Refined lattice parameters and cell volume of solid solutions $Sn_xTi_{1-x}O_2$ ($0 \leq x \leq 1.0$). Dashed lines demonstrate linearly interpolated values linking the end point binary oxides TiO_2 and SnO_2 (Vegard's Law).

The microstructure of x =0.20, sintered at 1600 °C for 6 h, is shown in Figure 7-5. SEM images show bimodal distribution of grain sizes, ~ 5– 10 μm and ~ 15- 20 μm, distributed heterogeneously with a high level of porosity. Sample homogeneity was evaluated by SEM in the backscatter mode (BSE). It shows a small fraction of a decomposed phase in the grain boundary region, which may be due to spinodal decomposition, but was not detected as a secondary phase in XRD, meaning it was lower than 1%.

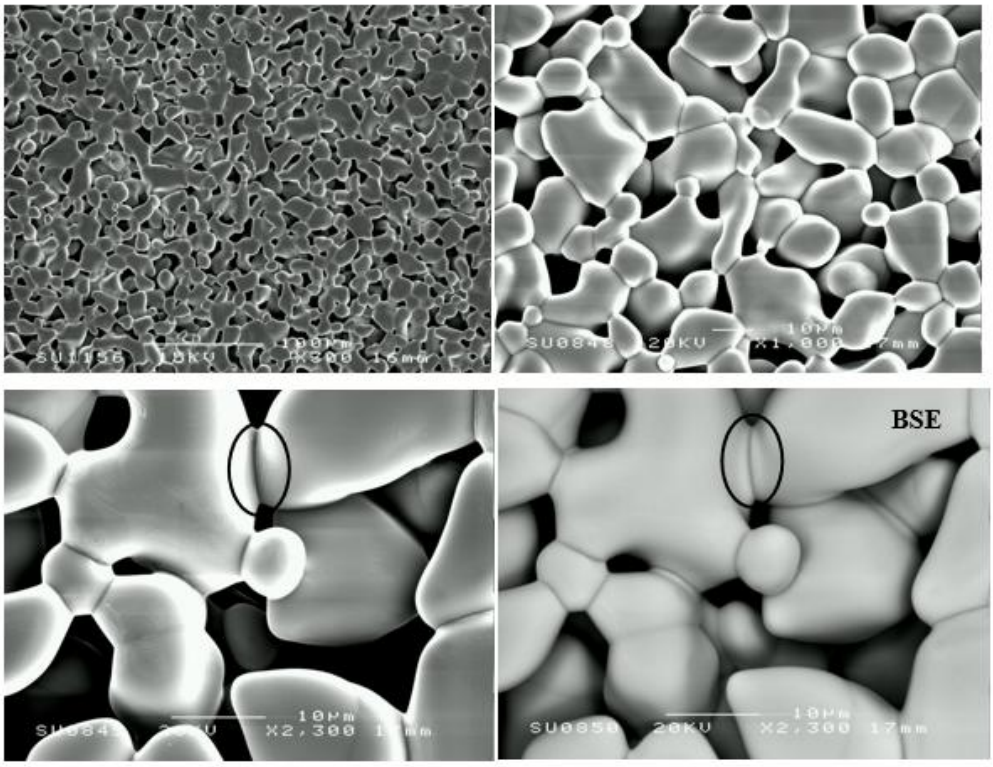

Figure 7-5: SEM micrographs of $Sn_xTi_{1-x}O_2$ (x =0.20). Sample sintered at 1600°C for 6h in an ambient atmosphere with cooling rate 5°C/min.

7.3.2 Discussion

Rutile-type solid solutions in the system TiO_2-SnO_2 were formed over the composition range, $0.00 \leq x \leq 0.20$ and $0.80 \leq x \leq 1.0$ without appearance of satellite peaks around the 101 reflection which is a normal indication of a spinodal decomposition (377,393), as confirmed by the XRD data in Figure 7-3. Mixtures of SnO_2 and TiO_2 at intermediate x, ($0.25 \leq x \leq 0.75$) were reported in other studies

(380,385,386,394) where it was concluded that spinodal decomposition cannot be avoided at some intermediate Sn concentrations.

Significant and gradual shifts of the XRD peaks of the rutile phase toward lower 2θ values were observed with changing the ratio of Ti/Sn, indicating the lattice expansion. This behaviour can be explained by the fact that the lattice of the $Sn_xTi_{1-x}O_2$ solid solutions expands as Sn^{4+} with a larger ionic radius (0.71 Å) is substituted for smaller Ti^{4+} (0.68 Å) in TiO_2. The measured lattice parameters for the end members TiO_2 and SnO_2 showed good agreement with published JCPDS data.

Based on the width of the XRD peaks, the crystal size varies from about 20 nm to 31 nm for the solid solutions while it is around 36 nm for raw materials. The decrease in crystal size has been reported previously and was attributed to the presence of Sn–O–Ti in the solid solution which inhibits the growth of crystal grains(375). The axial ratio c/a increased with x due to the relatively small change in the *a* axis as shown in Figure 7-4. This means that the displacement of ions along the *c* axis is larger than the *a* axis for TiO_2 whereas the situation is quite the reverse in SnO_2 (235); consequently, the expansion of the unit cell in the solid solutions of TiO_2-SnO_2 is anisotropic. The unit cell parameters of the rutile solid solutions, Fig. 4, followed Vegard's Law, and changed linearly with composition which is also evidence for the formation of a solid solution. This finding is consistent with those of some other studies (377,392,394) in which no deviation from Vegard's law is observed for the $Sn_xTi_{1-x}O_2$ system. In contrast, a positive deviation from Vegard's law, in which the lattice parameter is larger than that predicted by Vegard's law, has been reported in some other studies, both experimentally (235,395) and theoretically (387).

SEM images reveal various grain sizes and high porosity in a $Sn_xTi_{1-x}O_2$ (x =0.20) sample, sintered at high temperature, 1600 °C. Significant grain growth occurs during sintering at 1450 and 1550°C reported by other studies (372,393). The microstructure shows no lamellar structure meaning that it is outside the spinodal dome (363). The presence of segregation along the grain boundaries may be due to O_2 loss which leads to change in the surface layer composition resulting in segregation of impurities. Alternatively, the free energy of grain surfaces is likely to be different to that of grain interiors and phase separation may be preferred at the surface whereas it does not occur in the interior. This phenomenon was reported

by other studies which suggested that no spinodal decomposition occurs and predict that phase separation into two solid solutions of close but distinct composition is present during cooling and mainly preserved to room temperature as the kinetics of spinodal decomposition are relatively slow in $(Sn,Ti)O_2$ systems (363,372,393).

7.4 Electrical properties of $Sn_xTi_{1-x}O_2$ solid Solutions

Impedance data of $Sn_xTi_{1-x}O_2$ pellets (x= 0.10, 0.15, 0.20, 0.80 and 0.90), were measured over the range of temperature, from room temperature to 850°C; samples were too resistive to measure below 550°C.

7.4.1 Impedance data in air

7.4.1.1 $Sn_xTi_{1-x}O_2$ with x=0.90

The impedance complex plane, Z*, data Figure 7-6(a), shows two arcs with resistances at eg. 625°C of 30 and 40 kΩcm. Combined Z″/M″ spectroscopic plots are given in Figure 7-6(b). Data collected at 625°C show that the main Z″ and M″ peaks appear at different frequencies, 0.79 and 1.6 MHz respectively, and both therefore represent the bulk response of the sample. Also, another Z″ peak was observed at lower frequency, 100 Hz. Furthermore, at high temperature, 725°C, the main peaks of Z″ and M″ overlapped at similar frequencies, 1.0 MHz; another Z″ peak was observed at lower frequency, 100 Hz associated with the second component suggesting the sample is electrically inhomogeneous.

The same data presented in spectroscopic form of capacitance, C′ in Fcm^{-1} unit, Figure 7-6(c), show a plateau at high frequency with a capacitance value ~ 5.5 $pFcm^{-1}$, this magnitude of capacitance is attributed to the sample bulk response, C_1(396). The capacitance at low frequency with a value of ~ 50 and 110 $nFcm^{-1}$ respectively might be due to a surface layer or grain boundary effect, C_2.

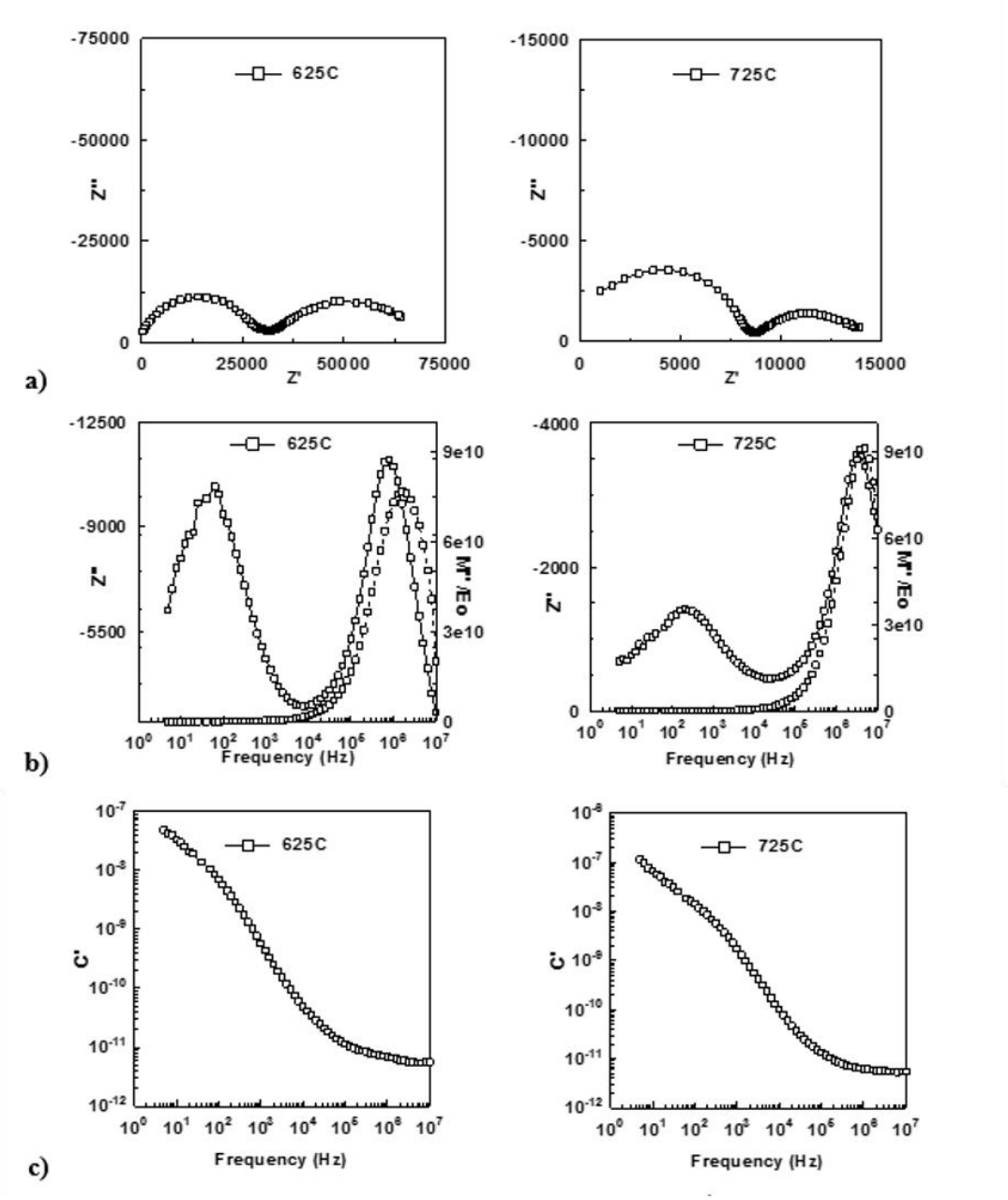

Figure 7-6: Impedance data for $Sn_xTi_{1-x}O_2$ (x = 0.90); (a) Z^* plot (b) Z″/M″ spectroscopic plot and (c) Spectroscopic plot of capacitance at 625 and 725°C.

The impedance data at 725°C upon heating and cooling is given in Figure 7-7. Samples exhibit similar behavior on heating and cooling.

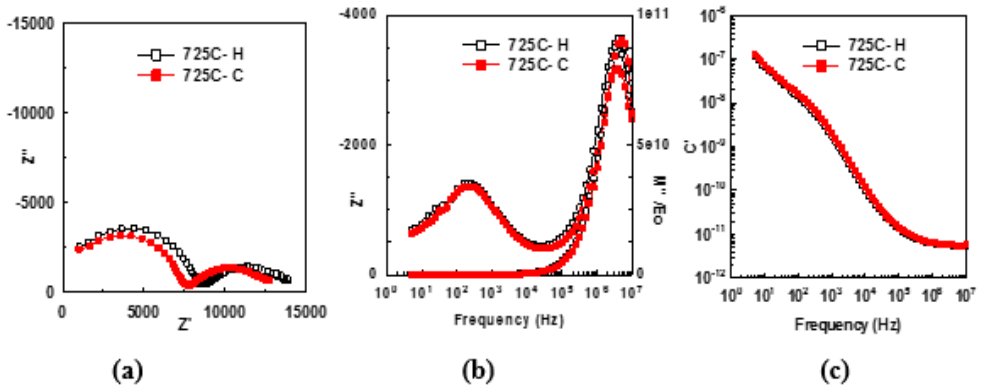

Figure 7-7: Impedance data for $Sn_xTi_{1-x}O_2$ (x =0.90) at 725°C upon heating (Black) and cooling (Red).

7.4.1.2 $Sn_xTi_{1-x}O_2$ with x=0.10

Impedance Complex plane, Z*, plots at different temperatures, Figure 7-8(a), show that the sample contains a broad arc at 630°C and a spike which became a part of another arc when temperature rises. At 850°C, the Z* plot reveals two arcs. The same data presented in spectroscopic form of capacitance, C′, in Figure 7-8(b), show a plateau at high frequency with a value of ~ 5.0pFcm^{-1}, whereas at 850°C, low frequency capacitance was ~2.9 nFcm^{-1}.

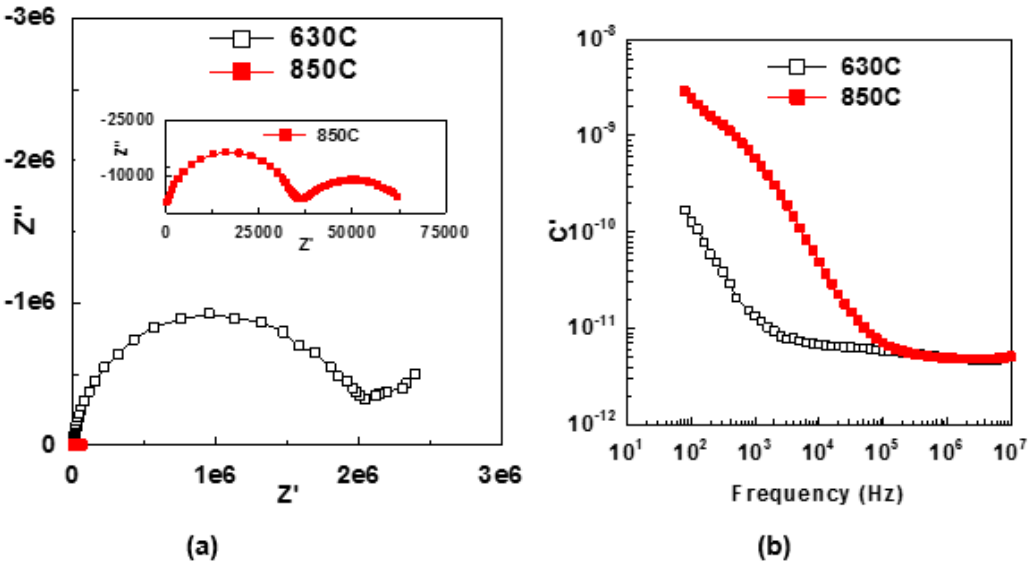

Figure 7-8: Impedance data for $Sn_xTi_{1-x}O_2$ (x =0.10) at 630 and 850°C; (a) Z* plot and (b) Spectroscopic plot of capacitance.

Figure 7-9 shows a set of impedance data for x = 0.10 taken over a wide frequency range at different temperatures. Two semicircles could be traced, Figure 7-9(a). This clearly indicates the sample contained two main resistances, the bulk resistance R_1 and the grain boundary resistance R_2. Also, it can be seen from the plots that the values of both the grain and grain boundary resistances decrease with an increase in temperature. The C' plots, Figure 7-9(b), demonstrate a frequency-independent plateau at high frequencies which is attributed to the sample bulk, C_1 with a value of $\sim$ 4.9 pFcm^{-1}. A second plateau at a lower frequency with capacitance ≈ 0.6- 2.9 nFcm^{-1} is seen at higher temperatures and is attributed to a conventional grain boundary. Combined Z″/M″ spectroscopic plots at 750°C and 850°C are given in Figure 7-9(c). At 750°C, the main Z″ and M″ peaks appear at similar frequencies and both represent the bulk response of the sample. Also, a second peak was observed at lower frequency, 100 Hz. Furthermore, at high temperature, 850°C, the main peaks of Z″ and M″ were overlapped at similar frequencies and another Z″ peak was observed at low frequency suggesting the sample is electrically inhomogeneous due to the presence of a second component.

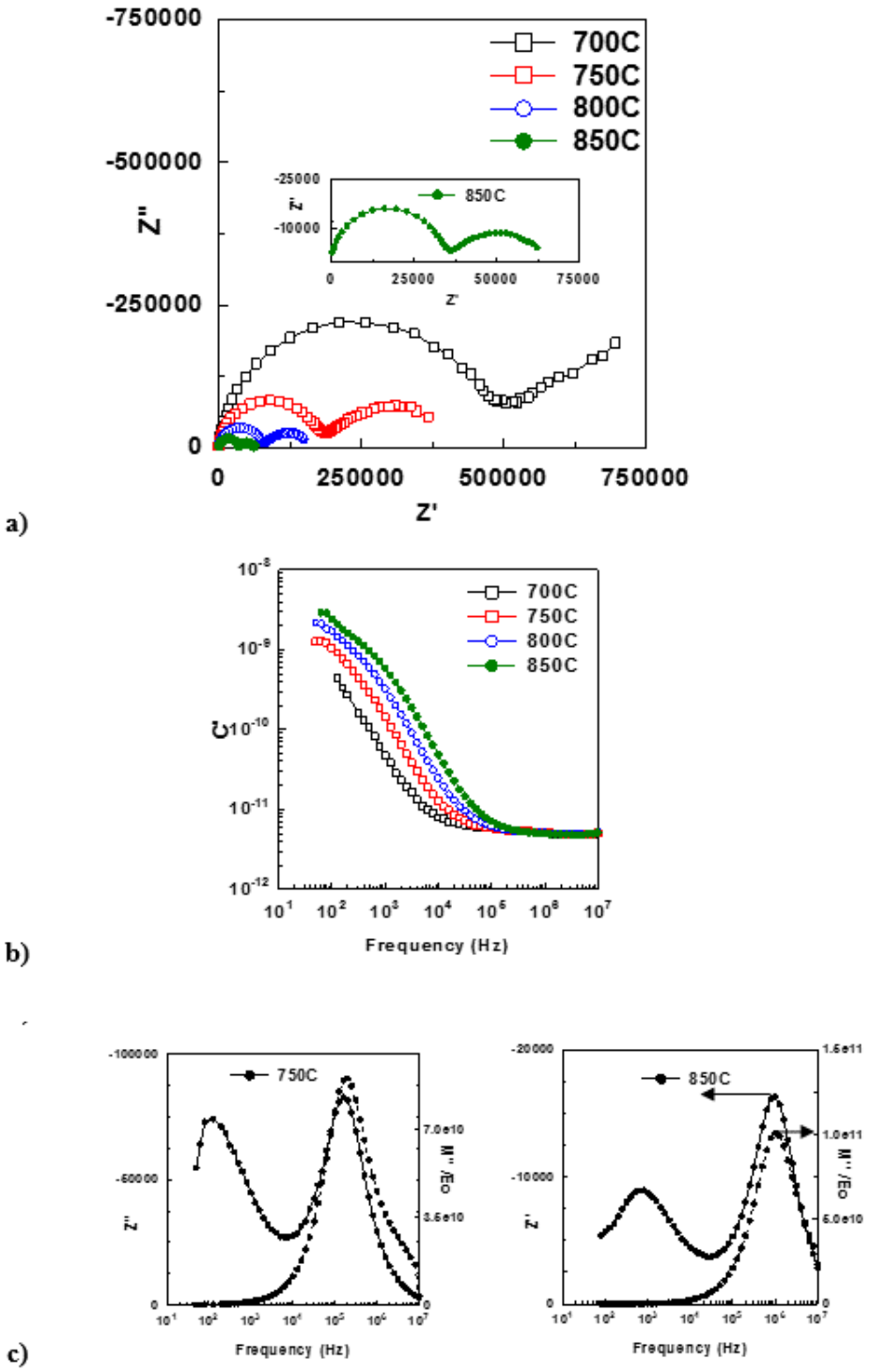

Figure 7-9: Impedance data for $Sn_xTi_{1-x}O_2$ (x = 0.10); (a) Z* plot ,(b) Spectroscopic plot of capacitance and (c) Z″/M″ spectroscopic plot at different temperatures.

The impedance data upon heating and cooling are given in Figure 7-10. At all temperatures, the sample exhibits similar behavior on heating and cooling.

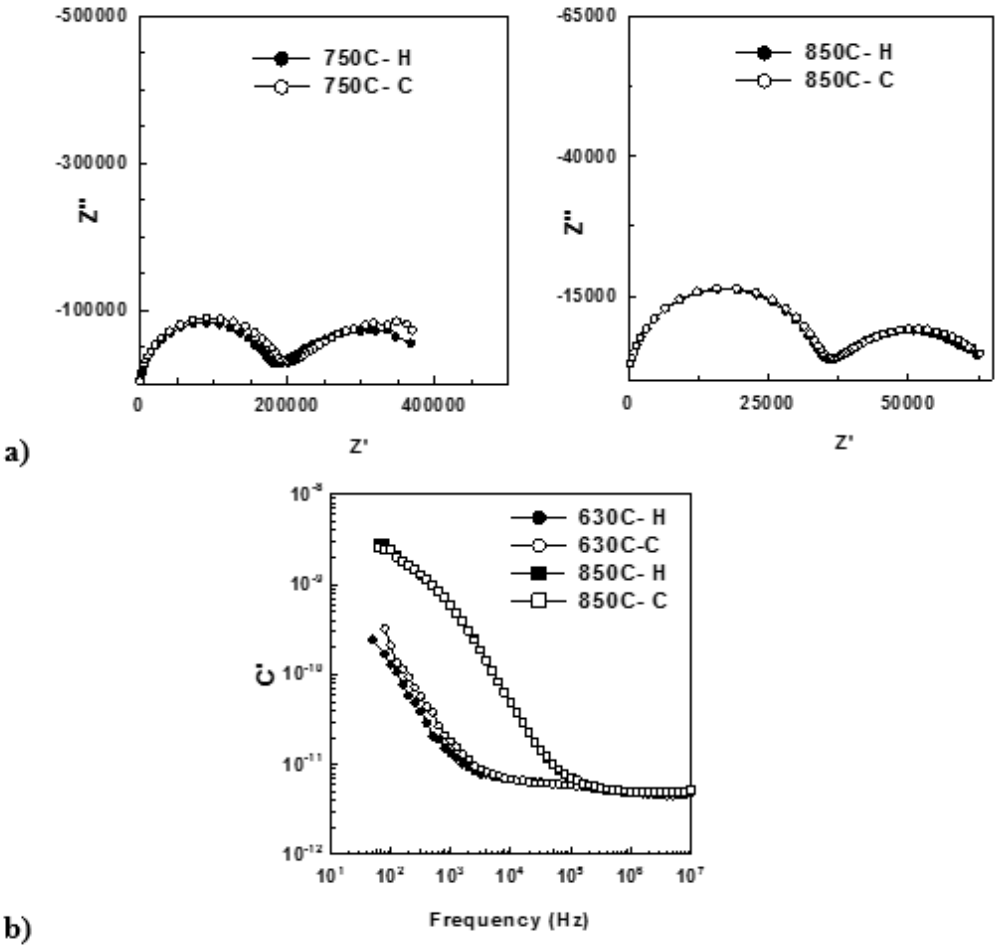

Figure 7-10: Impedance data; (a) Z* plot and (b) spectroscopic plot of capacitance for $Sn_xTi_{1-x}O_2$ (x =0.10) at different temperatures upon heating (H) and cooling (C).

7.4.1.3 $Sn_xTi_{1-x}O_2$ with x=0.20

Impedance data collected over a range of temperature (650°C -825°C) are shown in Figure 7-11(a-d). Z* plot reveals two resolved arcs as seen in Fig. 11(a). The capacitance plot, Figure 7-11 (b), shows a plateau at high frequency at all temperatures with associated capacitance of ~ 7.7 $pFcm^{-1}$, whereas, the second component at the low frequency arc has associated capacitance in the range ~ 2.0 -5.2 $nFcm^{-1}$. Combined Z″/M″ spectroscopic plots at 650°C and 800°C are given in Figure 7-11 (c). In both cases, the Z″ and M″ peaks appear at almost similar frequency of 0.13 and 2 MHz, respectively. A shoulder emerges at low frequency,

might be attributed to the grain boundary response, and became a distinct peak at 800°C.

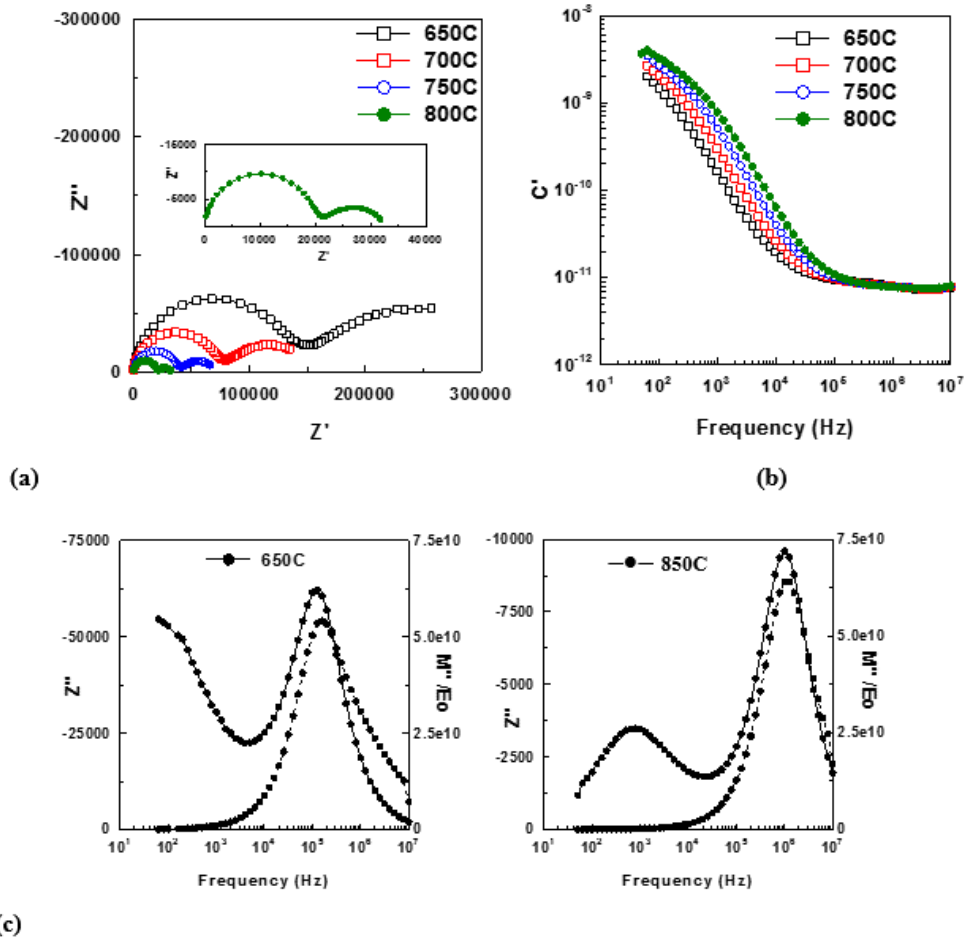

Figure 7-11: Impedance data for $Sn_xTi_{1-x}O_2$ (x =0.20); (a) Z* plot, (b) spectroscopic plot of capacitance and (c) Z″/M″ spectroscopic plot at different temperature.

Impedance data upon heating and cooling are given in Figure 7-12. At both temperatures, the sample exhibits similar behavior on heating and cooling.

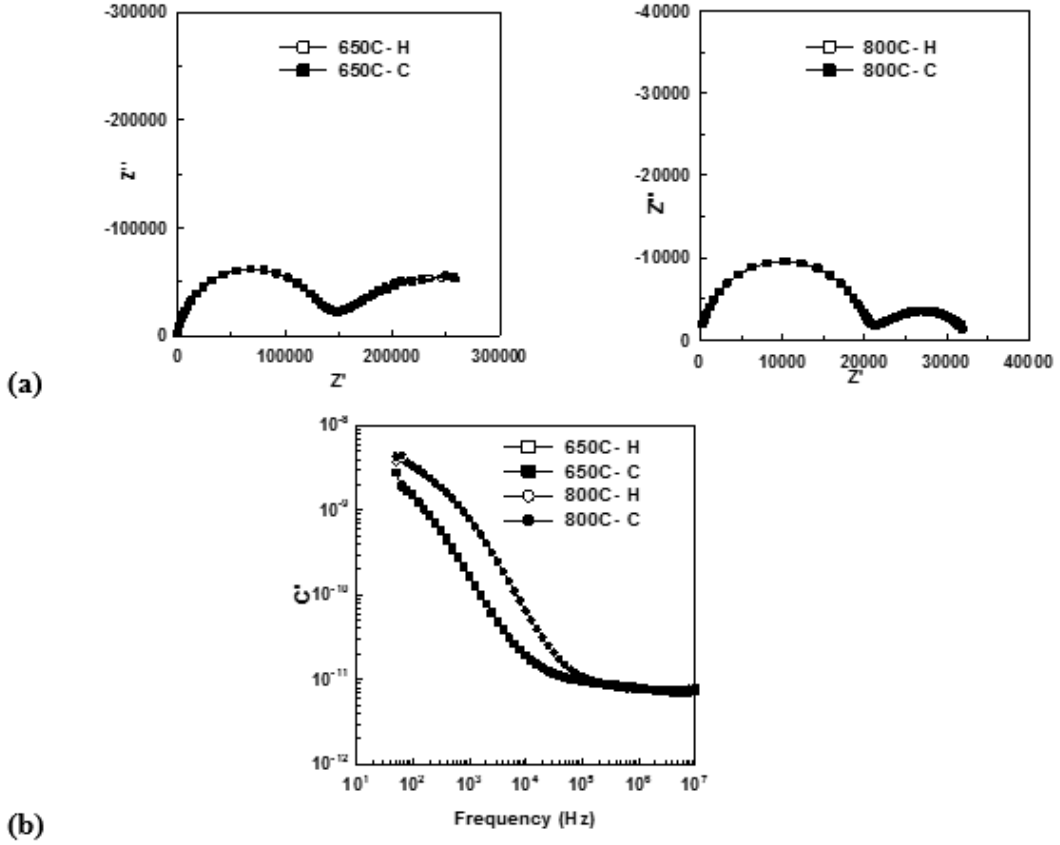

Figure 7-12: Impedance data; (a) Z* plot and (b) Spectroscopic plot of capacitance for $Sn_xTi_{1-x}O_2$ (x =0.20) at different temperatures upon heating (H) and cooling (C).

Impedance measurements were carried out for other compositions, x=0.15 and 0.80. In all samples, two components were observed with similar behaviour as previously shown.

All samples reveal a low density as shown in Table 7-2.

Table 7-2: Density values for $Sn_xTi_{1-x}O_2$ pellets.

Composition (x)	Density (%) theoretical
0.1	~67.2
0.15	~70.0
0.20	~69.8
0.80	~63.2
0.90	~64.7

7.4.1.4 Electrical conductivity

The bulk conductivity, σ_b, for (Sn, Ti) O_2 was calculated, as $\sigma_b = 1/R_b$, and plotted in Arrhenius format, $\log\sigma$ vs. 1000/T, as shown in Figure 7-12. The R values are taken from the intercept of the arc in the impedance complex plane on the Z′ axis at high frequency. The conductivity data of all samples show a linear response and follow the Arrhenius law. The sample with x= 0.10, is more resistive with an activation energy of, ~ 1.62 eV, compared to ~ 0.99 eV for higher tin content at x=0.90, although none of the samples show good semiconducting behaviour.

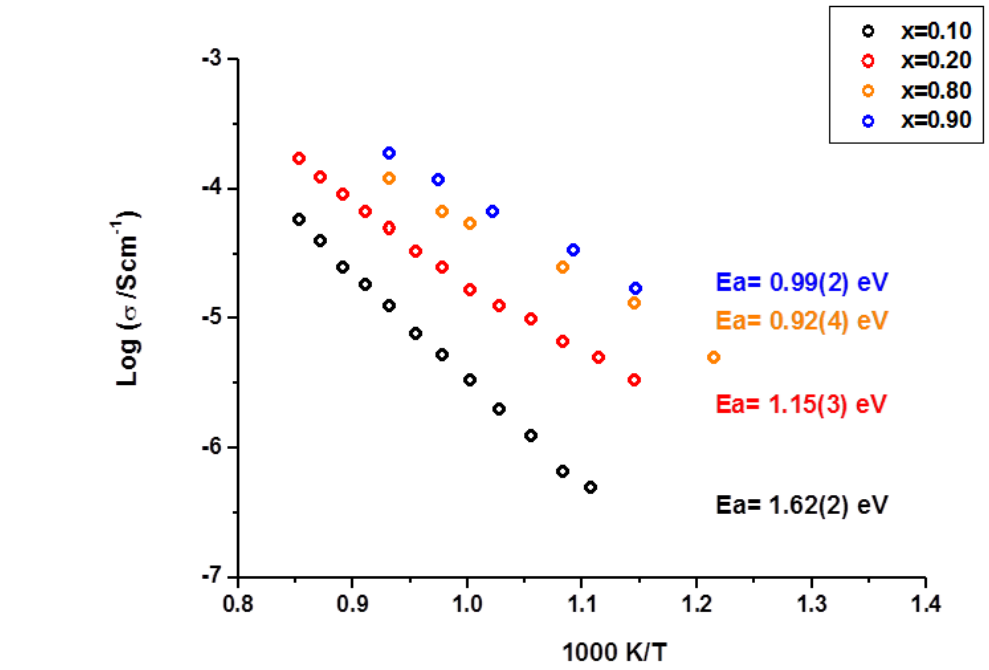

(a)

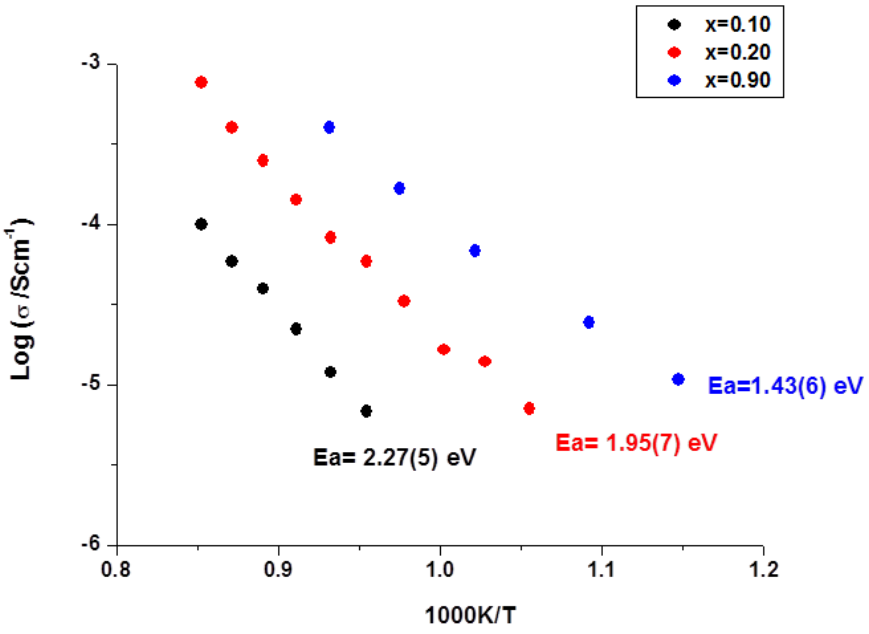

(b)

Figure 7-13: Arrhenius plot of; (a) bulk conductivity, σ_b and (b) grain boundary conductivity, $\sigma_{G.b}$, showing activation energies, E_a, for $Sn_xTi_{1-x}O_2$ (x= 0.10- 0.90).

7.4.2 Effect of atmosphere

To determine the effect of atmosphere on the electrical properties of $Sn_xTi_{1-x}O_2$, impedance measurements of samples containing 0.20 mol of SnO_2 sintered in air were taken at temperatures in the range 650°C- 850°C in an oxygen atmosphere. The same samples were then subjected to further measurements in nitrogen atmosphere, followed by measurements over the same temperature range in oxygen. Results are shown in Figure 7-14 and Figure 7-15. At 700°C, the sample under air, nitrogen and oxygen has a similar resistance which increases when the same pellet undergoes further measurements in oxygen atmosphere. At 850°C, the sample resistance increases during the measurement in oxygen atmosphere and decrease in nitrogen atmosphere compared to that in air. This cycling effect is similar to that reported in TiO_2 system showing n-type conductivity (397). The plot measured at 850°C in nitrogen reveals only one semicircle with no indication of a grain boundary component. The spectroscopic plot of capacitance, Figure 7-14(b), shows a plateau at high frequency with a capacitance value ~ 6.2 $pFcm^{-1}$ while the capacitance at low frequency has a value of ~ 2.5 and 5.5 $nFcm^{-1}$ respectively. The magnitude of the associated capacitance for the high frequency plateau is attributed to the sample bulk response, whereas the low frequency one might be due to a grain boundary effect.

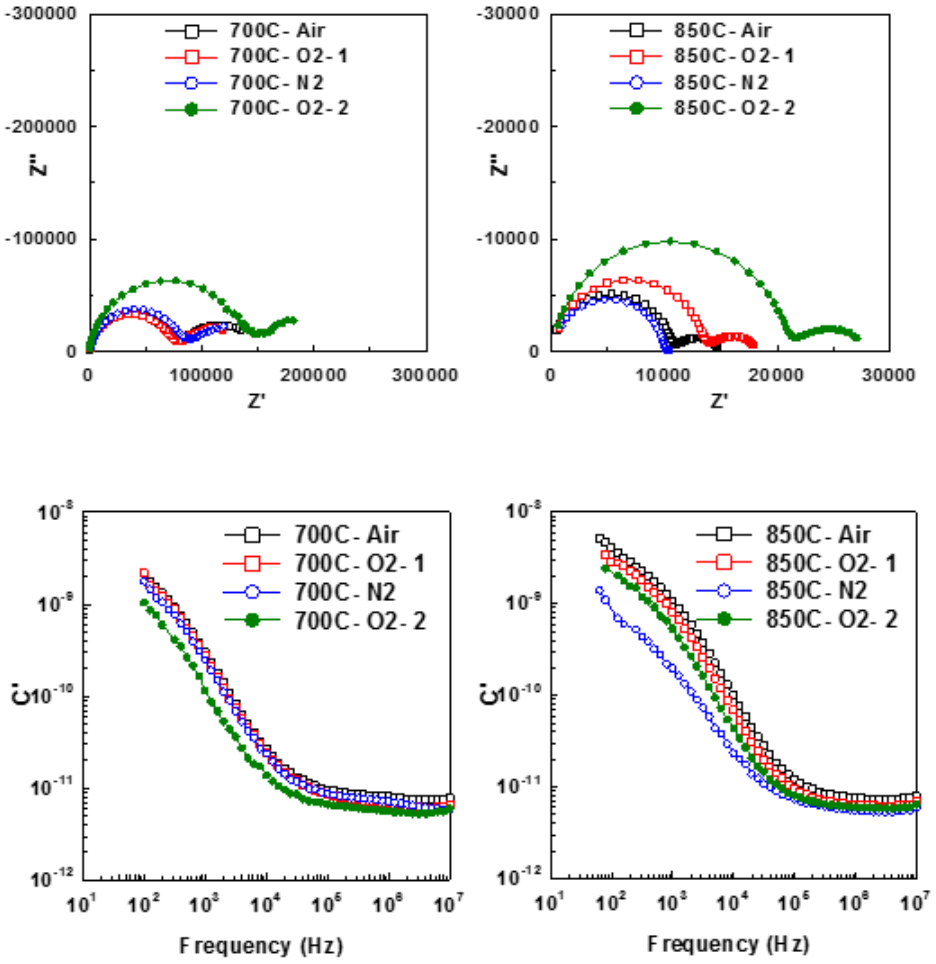

Figure 7-14: Impedance data for $Sn_xTi_{1-x}O_2$ (x = 0.20) under different atmospheres; (a) Z* plot and (b) spectroscopic plots of capacitance at 700°C and 850°C.

Combined Z″/M″ spectroscopic plots under different atmospheres at 850°C are given in Figure 7-15. The main Z″ and M″ peaks appear at similar frequencies and both characterize the bulk response of the sample. A second Z″ peak was observed at low frequency for the sample in air and oxygen, Figure 7-15(a) and (b) suggests that the sample is electrically inhomogeneous. This additional peak at low frequency disappears in nitrogen. However, it is totally recovered when the sample is subjected to further measurement at the same temperature in oxygen. Similar behaviour was observed in SnO_2-CoO-based varistor when it was subjected to thermal treatments in oxygen- and nitrogen-rich atmospheres at 900 °C (367).

Figure 7-16 shows combined Z″/M″ in N_2 at different temperature. It can be seen that the intensity of the grain boundary peak decreases by increasing the temperature. It is not clear if this due to the time required to reach equilibrium conditions, or/and the temperature increases. This gradual change happened during the measurement; thus, it is evidence of an extrinsic property not an intrinsic one.

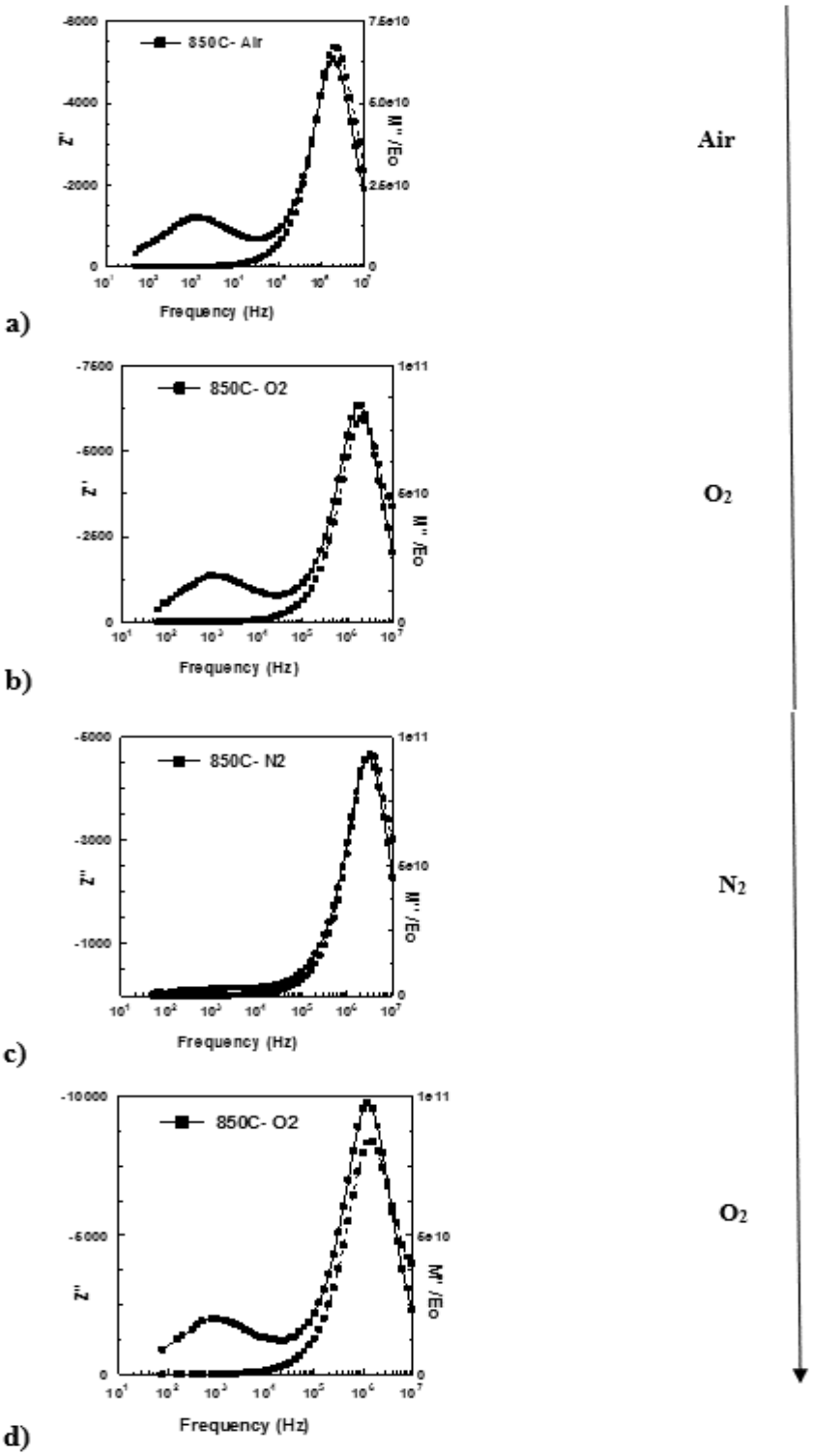

Figure 7-15: Z″/M″ spectroscopic plot for $Sn_xTi_{1-x}O_2$ (x =0.20) at 850°C under different atmosphere; (a) air, (b) O_2 after air , (c) N_2 and (d) O_2 after N_2.

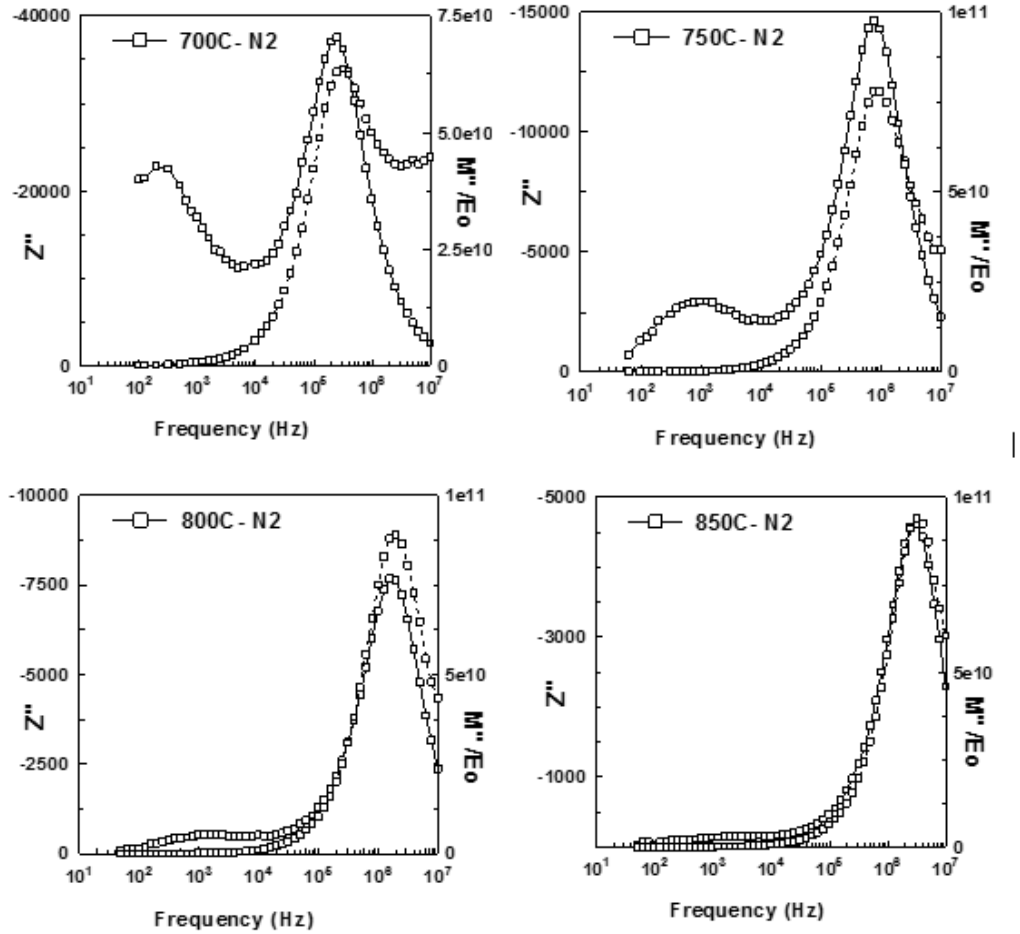

Figure 7-16: Z″/M″ spectroscopic plot for $Sn_xTi_{1-x}O_2$ (x =0.20) in N_2 at different temperatures.

Z* plots at 800°C upon heating and cooling under oxidation and reduction conditions are given in Figure 7-17(a-d). The results in air are reversible on heat-cool cycle. The sample in both nitrogen and oxygen exhibit a similar behaviour in heating and cooling, that is, two arcs can identified, however, in both case it is non-reversible on cooling.

The Arrhenius plots of σ_b, and σ_{gb} under different atmosphere (Air, O_2, N_2, O_2) is given in Figure 7-18. Conductivity data show a linear response and follow the Arrhenius law, with activation energy in the range ~ 1.00 - 1.40 eV for the bulk component. The activation energy for the grain boundary component has a value of ~ 1.30 eV in O_2 and a maximum value at ~ 3.22 eV in N_2. The conductivity of

grain boundary under air and O_2 are almost similar while in N_2, the conductivity is higher in particular at high temperature.

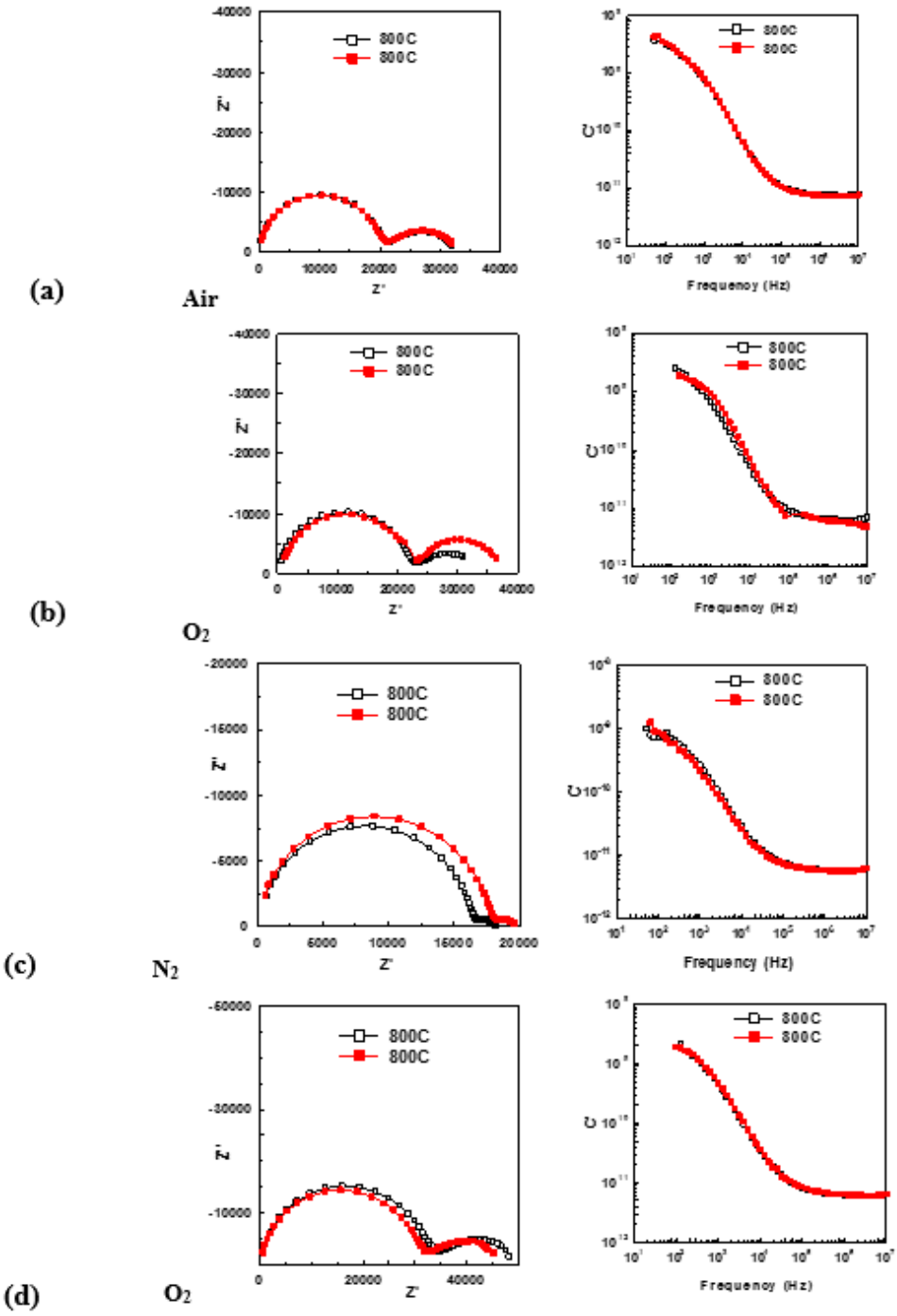

Figure 7-17: Impedance data of Z* plot for $Sn_xTi_{1-x}O_2$ (x =0.2) at 850°C upon heating (black) and cooling (red) in different atmospheres; (a) Air, (b) O_2 after air , (c) N_2 and (d) O_2 after N_2.

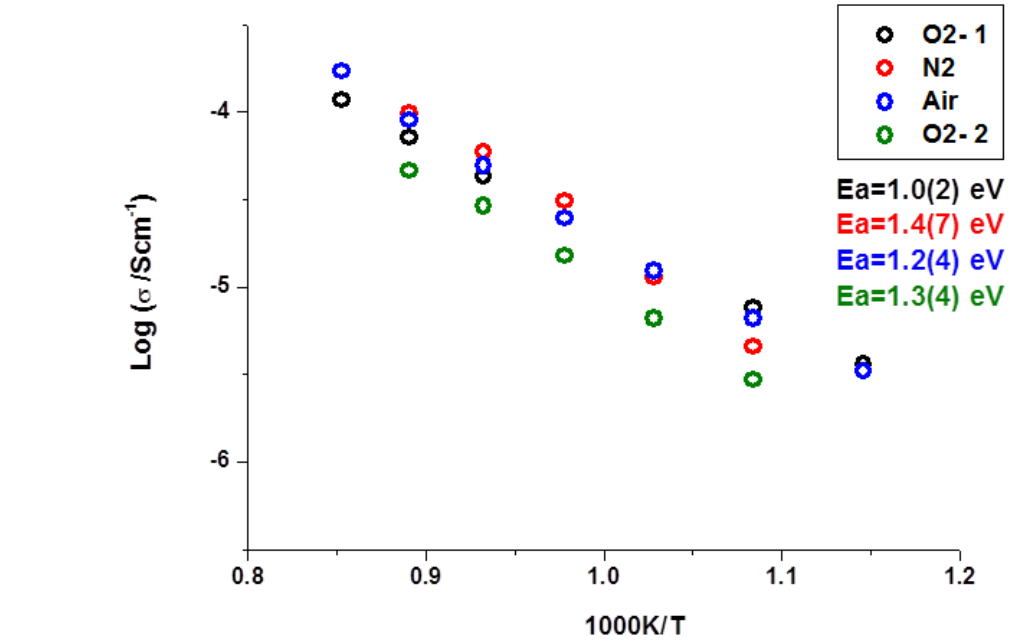

(a)

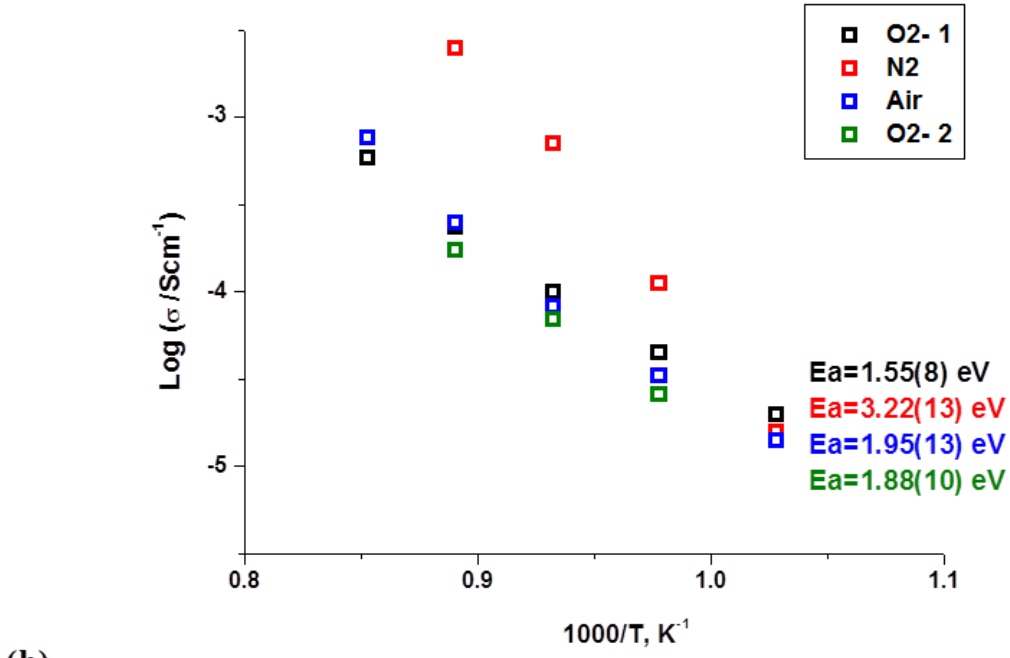

(b)

Figure 7-18: Arrhenius plot of (a) bulk conductivity, σ_g, and (b) grain boundary conductivity, σ_{gb}, for $Sn_xTi_{1-x}O_2$, (x=0.2) under different atmospheres in the following sequence; air, O_2, N_2 and O_2.

7.4.3 Effect of quenching

Oxygen vacancies have a significant effect on the physical and chemical properties of transition metal oxides (398)(399). TiO_2 is very sensitive to oxygen loss and can be reduced very easily without exposed to a reducing environment at high temperature (228).

To elucidate the role of heat treatment on electrical properties of Sn-doped TiO_2, pellets of undoped TiO_2 and $Sn_xTi_{1-x}O_2$, (x=0.2) with Pt electrodes were heated at 1300°C for one hour in N_2 atmosphere followed by quenching rapidly in air. Another pellet of undoped TiO_2 was heated at 1300°C for one hour in N_2 atmosphere then quenched rapidly in air followed by applying In-Ga electrode. The ac impedance measurements were carried out in N_2 and 5% H_2/N_2 at different temperatures. Table 7- shows the thermal treatment conditions of the pellet of TiO_2 and Sn doped TiO_2.

Table 7-3: Type of thermal treatment, electrode, quenching condition and the atmosphere during IS measurement for TiO_2 and $Sn_xTi_{1-x}O_2$.

System	Heat Treatment	Electrode	Quenching temperature/ atmosphere	Atmosphere of IS measurement
$Sn_xTi_{1-x}O_2$ (x=0.20)	NQ	Au	NA	N_2
$Sn_xTi_{1-x}O_2$ (x=0.20)	Q	Pt	1300°C/ N_2	N_2
$Sn_xTi_{1-x}O_2$ (x=0.20)	Q	Pt	1300°C/ N_2	%5 H_2/N_2
TiO_2 (R)	Q	Pt	1300°C/ N_2	%5 H_2/N_2
TiO_2 (R)	Q	In-Ga	1300°C/ N_2	%5 H_2/N_2

Impedance data for quenched TiO_2, with Pt electrode, show an approximately semicircular arc at 175°C, Figure 7-19(a), alongside a poorly resolved second arc which starts to be distinct at this temperature. Admittance data for $TiO_{2-\delta}$ show a decrease in Y′ value with decreasing frequency then became frequency-independent, Figure 7-19(b), from which the total conductivity σ_t data were obtained over the temperature range 50–250°C. The admittance versus frequency

plot for quenched TiO_2, with In-Ga electrodes, in Figure 7-19(c) reveals a frequency-independent trend over almost all the frequency range. The total conductivity σ_t data were obtained over the temperature range 26–100°C.

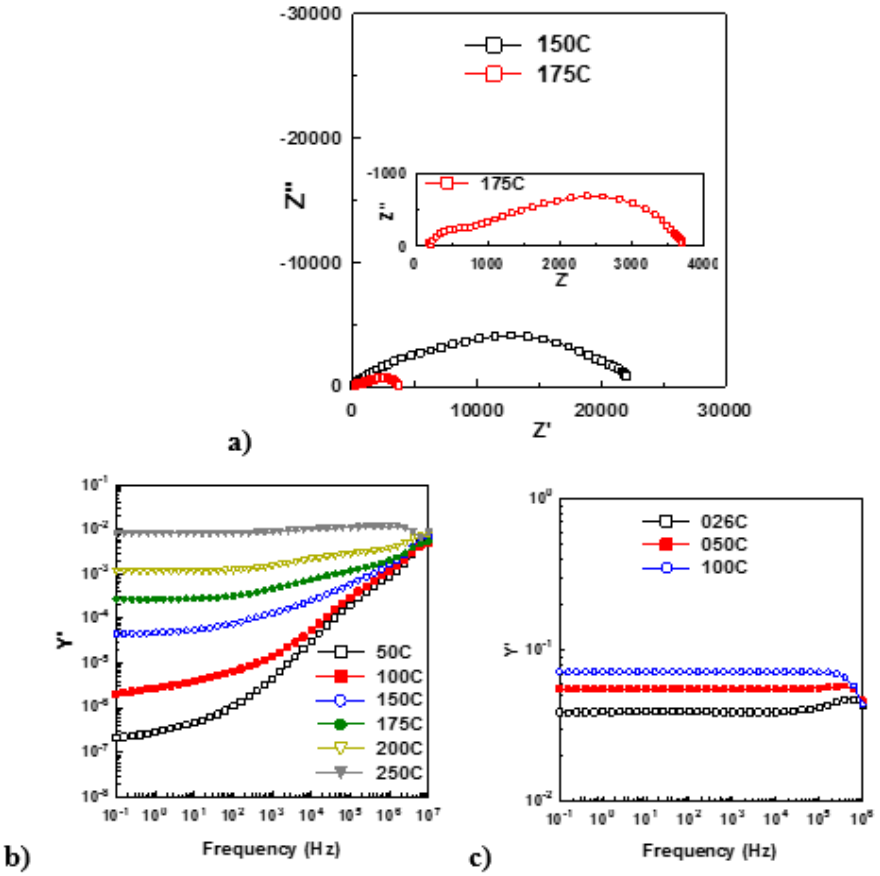

Figure 7-19: Impedance data in 5% H_2/N_2 at different temperatures for quenched TiO_2; (a) Z* plot and (b) spectroscopic plot of admittance both with Pt electrode and (c) spectroscopic plot of admittance with In-Ga electrode.

Sample resistivity of quenched $Sn_xTi_{1-x}O_2$ (x = 0.20) was determined under various reducing conditions. Electrical resistivity as a function of temperature was measured from 550°C to 750°C and from 300°C to 440°C in N_2 and 5%H_2 respectively.

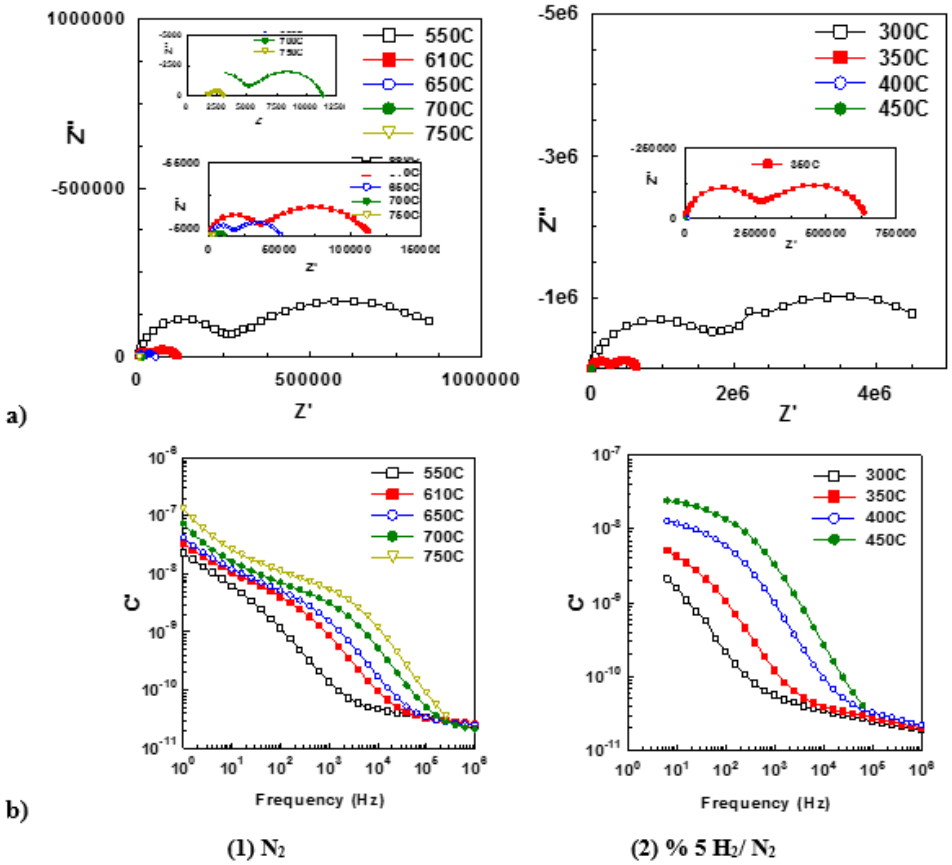

Figure 7-20: Impedance data; (a) Z* plot and (b) spectroscopic plot capacitance at different temperatures in (1) N_2 and (2) 5% H_2/ N_2 for $Sn_xTi_{1-x}O_2$ (x = 0.20) with Pt electrode quenched from 1300°C.

The bulk conductivity obtained after different heat treatments, Figure 7-21, shows a similar behaviour for non quenched sample in all different atmospheres (air, oxygen, nitrogen). Quenched sample, on the other hand, shows an increase in the conductivity in reducing gas either N_2 or 5%H_2. However, the sample exhibits more conductive behavior in 5%H_2 compared to nitrogen.

A strong dependence of the conductivity on ambient atmosphere can be seen as a drastic increase in conductivity which reaches about 3 orders of magnitude for a change from N_2 or 5% H_2/N_2. The conductivity of quenched Sn-doped TiO_2 increase in 5% H_2/N_2. A remarkable observation is the nonlinearity of the Arrhenius plots and jump in slope, around 600°C for measurement in nitrogen. Deviation from the nonlinearity of the Arrhenius plots for quenched sample measured in nitrogen may be associated with oxidation/reduction of Ti^{4+}/Ti^{3+} which lead to change in electron content in the sample.

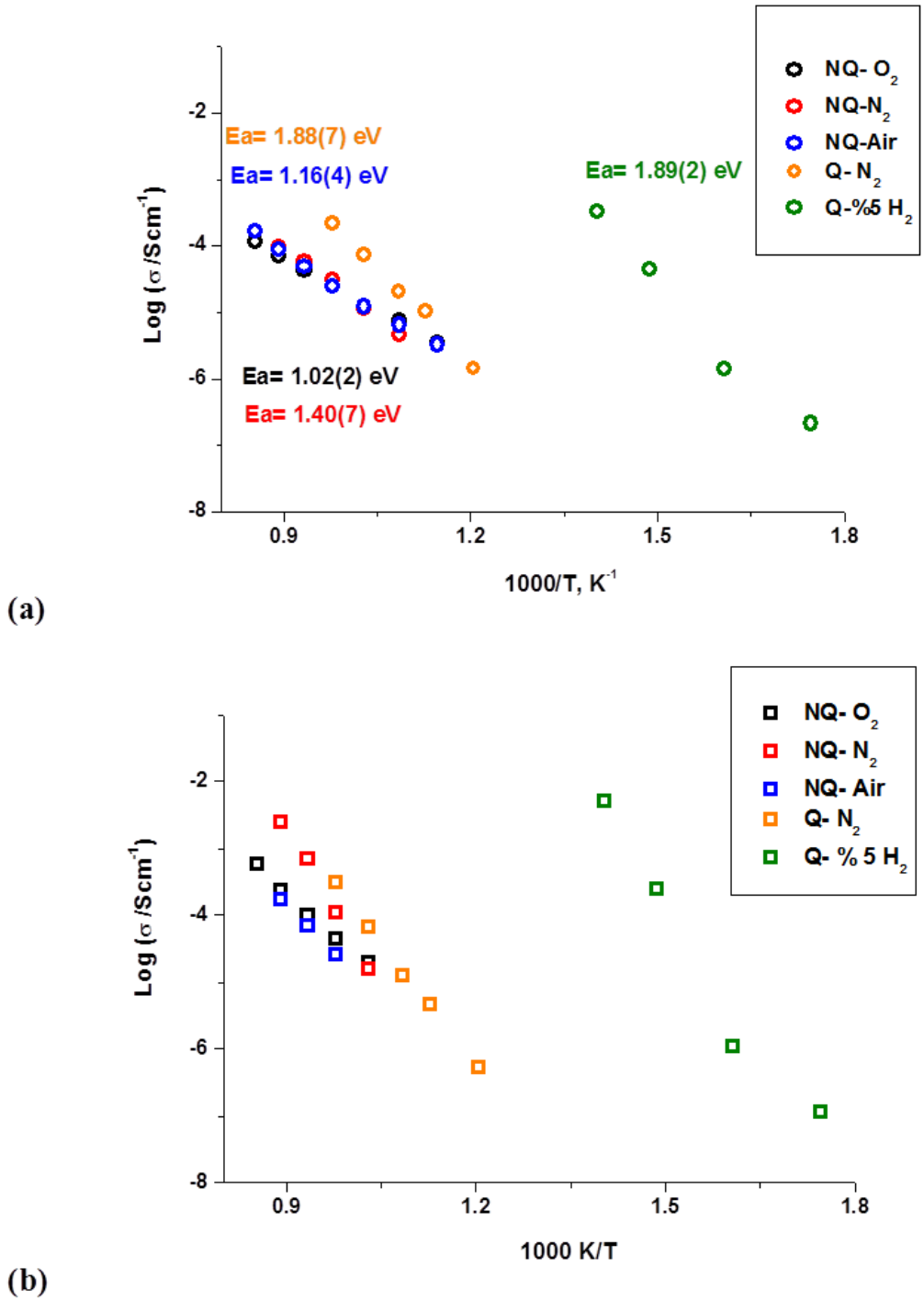

Figure 7-21: Arrhenius plot of; (a) bulk conductivity and (b) grain boundary conductivity data for $Sn_xTi_{1-x}O_2$ (x =0.20) after different heat treatments; NQ, not quenched with Au electrode; Q, quenched from 1300°C with Pt electrode, measured under different reducing conditions.

Conductivity data of quenched TiO_2 and Sn-doped TiO_2 are presented in Arrhenius format in Figure 7-22; all show linear behavior and σ_b has activation energy 1.4 eV for unquenched Sn-doped TiO_2 and ~1.88 eV for quenched sample whereas σ_t for quenched TiO_2 has activation energy 0.95 eV when quenched with Pt electrode, and 0.08 eV with In-Ga electrode. As the Pt paste electrode was applied before quenching, coating with Pt covers the surface of pellet and avoid O_2 loss which may be affected the conductivity of the material. σ_b for quenched Sn-doped TiO_2 either in N_2 or %5 H_2 atmosphere has similar activation energy. It is evident in Figure 7-22 that the impedance measurement under H_2 shows more conductive behaviour as compared to those which are carried out under N_2.

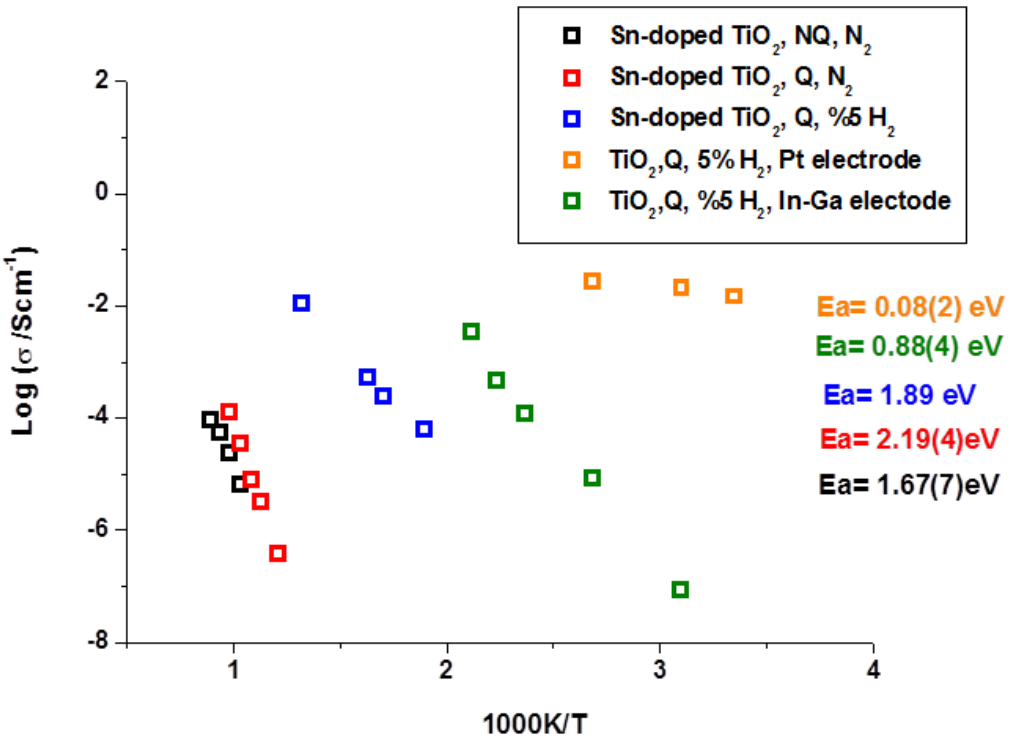

Figure 7-22: Arrhenius plot of total conductivity of undoped TiO_2 and bulk conductivity of Sn-doped TiO_2 (x=0.20) measured under different reducing conditions after different heat treatments showing activation energies, E_a; NQ, none quenching; Q, quenched from 1300°C in air.

7.4.4 Discussion

Impedance data were obtained for solid solutions of $Sn_xTi_{1-x}O_2$, (x= 0.10, 0.15, 0.20. 0.80 and 0.90). All samples are highly resistive and reliable information cannot be obtained from impedance data below 550°C. Two arcs can be clearly observed in the impedance complex plane at all temperatures ≥ 550°C, which make up the total resistance. The magnitude of the associated capacitance values indicates that the samples contain two main components; a high frequency bulk and a low frequency grain boundary which are responsible for capacity values of 10^{-12} and 10^{-9} F respectively (247). Two distinct peaks observed in Z″ versus frequency represent the bulk and a second component and indicate that the samples are inhomogeneous.

The relative permittivity (ε′) was calculated from the limiting high frequency plateau value of the capacitance to be in range of ~ 62- 87; rutile-TiO_2 has a high permittivity of about 90-170 (396). The reduction in permittivity could be due to a combination of the porosity of the pellets measured and an intrinsic reduction due to substitution of Sn^{4+} into the rutile lattice. Another reason can be attributed to poor sintering which resulting in low density of ceramics, as shown in Table 7-.

In the heating- cooling runs, the results are fully reversible for all samples.

The conductivity data of all samples show linear Arrhenius plots and the conductivity increases when Sn content in TiO_2 increases. This is consistent with the proposal that electron mobility of rutile titanium dioxide is 1/100 times smaller than that of SnO_2 mainly due to the d- type character of the conduction electrons (400). The bulk conductivity of x =0.90 is one and half order of magnitude higher than that of x =0.10, Figure 7-13, and the associated activation energy, E_a=~0.99 eV, is significantly lower than ~ 1.6 eV for x =0.10. This result are in agreement with the experimental data of (Sn, Ti)O_2 prepared via sol-gel method (401). The activation energy for x=0.10, ~1.62 eV is approximately half the band gap of TiO_2, 3.0-3.2 eV, which is as expected for intrinsic semi-conduction. The conductivity increases with increasing x, however variation of conductivity with non-stoichiometric oxygen δ, has not been investigated in this study.

Impedance data show that the $Sn_xTi_{1-x}O_2$ system exhibits resistive behavior, with high activation energy for all compositions. However, a large difference between

the activation energy of bulk and grain boundary was observed and can be an indicator for chemical difference between these regions. The segregation at the grain boundary, as shown by SEM, Figure 7-5, might induce an increase of the resistivity of the system.

Figure 7-14 illustrates the response of impedance spectroscopy of the Sn- doped TiO_2 sample treated in N_2 and O_2 atmospheres. This figure, at 850 °C, shows that the total electrical resistance of the sample in N_2 decreases to one half of its value in O_2. However, grain boundary resistance is totally recovered after treatment in an O_2 atmosphere.

In N_2, the sample loses O_2 from surface:

$$O^{2-} \rightarrow 1/2\ O_2 + 2e^- \qquad (2)$$

And conductivity increases due to extra electron.

In air/O_2, the extra peak in Z* is associated with oxidation of grain boundary or surface layer which, in some way, is different from the bulk, Figure 7-15.

For an n-type semiconductor, such as TiO_2 and SnO_2, atmospheric oxygen chemisorbs on the surface, consuming electrons:

$$½\ O_2 + 2e^- \rightarrow O^{2-}{}_{ads} \qquad (3)$$

This absorption of oxygen ion results in a decrease in conductivity which is largest at the grain boundaries. Increasing of the conductivity in N_2 can be attributed to n-type conductivity associated with an increasing in electronic carrier and lead to an increaseing in the conductivity of the material according to equation (2)

The variations in the electrical properties with increasing pO_2 are due mainly to the oxidizing effect which is reversible upon heating-cooling. This behaviour is assumed to be related to the presence of a precipitated phase between grains that is undetectable by XRD or SEM. It is assumed that the presence of this segregated phase at the grain boundary regions as shown in SEM, Figure 7-5, is caused by the beginning of spinodal decomposition which frequently observed in these $(Sn,Ti)O_2$ systems. This causes a Schottky-like barrier across grain boundaries similarly to that was reported previously for $(Sn,Ti)O_2$-based varistor system (386).

Schottky-like barrier can be explained by existence of an excess oxygen species due to O_2 adsorption at the grain boundary, and acceptor metal atoms which precipitated on the grain boundary surface, in this case *n*-type- *p*-type model is proposed in which the grain boundary region has a ‘‘*p*-type semiconductor’’ due to the precipitated phase at the grain boundary, while the bulk has an ‘‘*n*-type semiconductor’’.

Oxygen adsorption at the interfaces could be causing a Schottky barrier. The metal atoms precipitated at the grain boundaries are mainly transition metal which increases the oxygen species at the grain boundary owing to their multiple (variable) oxidation states, so O_2 absorbed on a Sn-doped TiO_2 surface undergoes ionization, with or without dissociation, by trapping electrons from the Ti 3d conduction band. These negatively charged adsorbed oxygen species cause a depletion layer in the surface and consequently Schottky-like barrier across grain boundaries and can readily act as either electron traps or electron sources (402) (228). Consequently, the transition metal becomes more oxidized when treated in O_2 atmosphere which increases the oxygen species. Alternatively, measurement under a reducing atmosphere; N_2 or H_2, eliminates excess oxygen, allowing the metal atoms to remain and, thus, decreasing the resistivity of the material. Therefore, the physical origin of the interfacial states might be extrinsic causing by the precipitating of metal atoms at the grain boundaries.

However, the Schottky-like barrier can be examined by applying a dc bias which has not been conducted for this sytem.

The electrical conductivity of undoped rutileTiO_2 was studied by West et. al.(228). It was found that the processing conditions, especially the sintering temperature, atmosphere and the cooling rate, has a major effect on the electrical conductivity of rutile. By quenching from temperatures $\geq$ 700°C without the use of a reducing atmosphere, TiO_2 becomes increasingly semiconducting (228).

For Sn-doped TiO_2, the quenched sample is no longer $Sn_xTi_{1-x}O_2$ but forms oxygen-deficient material, $Sn_xTi_{1-x}O_{2-\delta}$ and apparently forms oxygen vacancies. These oxygen vacancies are expected to generate free carriers (electrons) that affect the electrical conduction in the material and are indeed responsible for the enhancement in the electrical conductivity of the material as shown in Figure 7-21.

7.5 Electrochemical characterisation

TiO_2 as an anode for Li-ion batteries exhibits good safety, environmental friendliness, and low cost beside its negligible solubility in organic electrolyte. However, Li insertion into bulk rutile is negligible at room temperature which has been attributed to the dense close packing of the structure and poor ionic and electronic conductivities of rutile. SnO_2 has a theoretical lithium storage capacity of 781 $mAh.g^{-1}$ but experiences a large volume expansion/contraction during cycling, which leads to pulverization and poor cycle stability (89,403).

7.5.1 Cyclic voltammetry (CV)

Cyclic voltammetry (CV) was used to understand the mechanism of lithium insertion/ extraction in the $Sn_xTi_{1-x}O_2$ ($0.0 \leq x \leq 0.95$) system. The CV test was carried out at the scan rate of 0.05 mVs^{-1} between 1.0 and 3.0 V vs. Li^+/Li but the last cathodic sweep was from 3 to 0 V. The resulting voltammogram for x= 0.05 is shown in **Figure 7-23**. Two sets of peaks are observed. The first set, (1,1′), located at higher potentials corresponds to the lithium insertion/extraction in TiO_2 (89,403). The oxidation/reduction peaks of TiO_2, at ~1.90 and 1.40 V respectively, are broad and not well defined indicating sluggish lithium ion insertion/extraction kinetics. The positions of the reduction and oxidation peaks are consistent with lithium ion insertion and extraction respectively at 1.35 and 1.85 V, inset graph in **Figure 7-23**, which have been reported before for rutile-TiO_2 (263,264,404). Both oxidation and reduction peaks decreased step by step in the cycling process. This clear decrease in the intensity of this peak pair demonstrates the poor reversibility of the TiO_2 (de)intercalation reaction expressed in Eq. 4. The second set located at 1.3 and 1.0 V, (2, 2′) can be attributed to lithium insertion/ extraction in SnO_2 (255,403,405,406). Shifting of the reduction peak to higher voltages, from 0.8 V for pure SnO_2, inset graph in **Figure 7-23**, to 1.0 V in the SnO_2-TiO_2 system due to the formation of solid solutions was reported (405,407) which could be attributed to the reduction of SnO_2 to metallic Sn and Li_2O, Eq. 5 (406,408). In the anodic curve, two further peaks appear. The irreversible peak centred at about 0.8 V (no.3) is probably associated with the electrolyte decomposition and formation of a solid electrolyte interface (SEI) on the electrode surface (409). The broad peak observed at 0.6 V (no.4) can be ascribed to the formation of tin alloy phases, Li_xSn as shown in Eq. 7 (406,408,410).

$TiO_2 + xLi^+ + xe^- \leftrightarrow Li_xTiO_2$ (4)

$4Li^+ + SnO_2 + 4e^- \rightarrow Sn + 2Li_2O$ (5)

$Li+ + e^- + Electrolyte \rightarrow SEI\ (Li)$ (6)

$Sn + xLi^+ + xe^- \leftrightarrow Li_xSn \quad 0 \leq x \leq 4.4$ (7)

It is generally believed that the second and third reactions, Eq. 5 and 6, are not reversible and are responsible for the irreversible capacity loss during the first cycle (408–410). However, the oxidation peak at ~1.3 V is attributed to the reaction of Li^+ ion with SnO_2, Eq.5, as the alloying –dealloying reaction of Li-Sn occurs at voltages below 1.0 V (408,409). This indicates that the reaction expressed in Eq. 5, is partially reversible, in good agreement with the literature data (81,403,406,407,410).

The presence of Sn^{2+} and/or Sn^{4+} along with metallic Sn, previously confirmed by in situ- Mössbauer technique (405), and formation -deformation of Li_2O at voltage higher than 1.0V (406) indicates that the reaction of Li with SnO_2 is reversible to a certain degree.

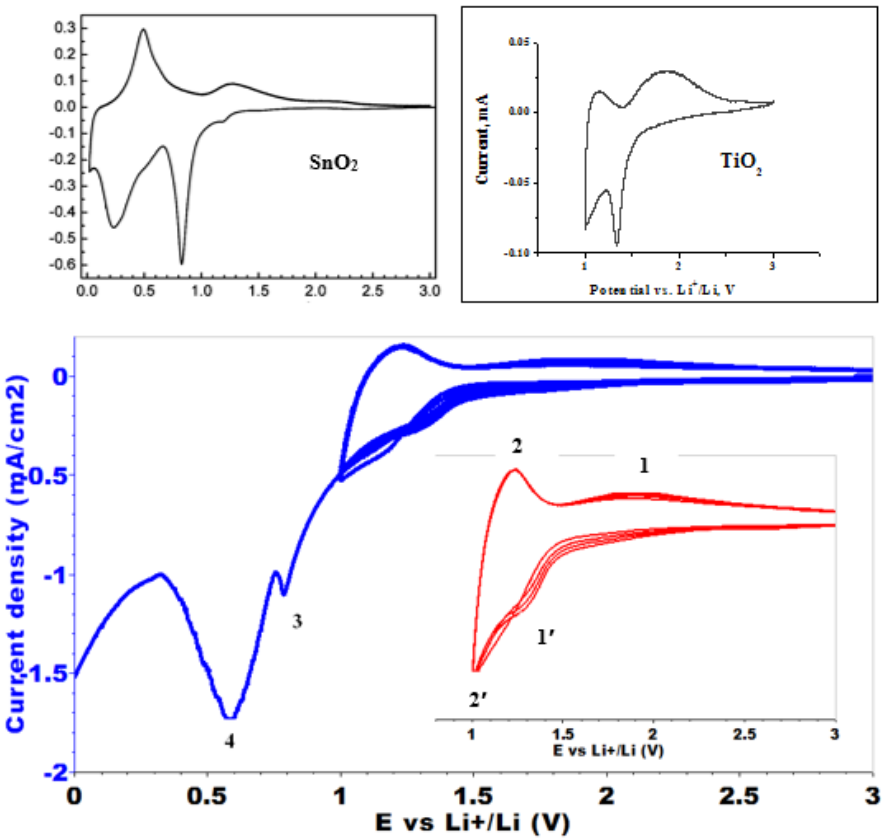

Figure 7-23: Cyclic voltammograms for $Sn_xTi_{1-x}O_2$ electrode over the potential range 0.0 -3.0 V at a scan rate of 0.05 mVs^{-1}; inset shows the CV for pure SnO_2, adopted with permission from Chem. Mater, 20/4, Demir Cakan R, Hu Y-S, Antonietti M, Maier J, Titirici M-M., Facile One-Pot Synthesis of Mesoporous SnO_2 Microspheres via Nanoparticles Assembly and Lithium Storage Properties, 1227–9. Copyright (2008) American Chemical Society (411) and TiO_2, from this work.

The peaks in the cyclic voltammograms are evidence for the number of redox active species that are present in the system. Two sets of oxidation/reduction peaks indicate that both SnO_2 and TiO_2 show activity towards insertion/extraction of lithium ion. The Li- ion insertion/ extraction in SnO_2 is more complicated than that in TiO_2 and involves the formation of lithium oxide and tin alloys in a two-step reaction (255,406,408).

The oxidation of Ti^{3+}/Ti^{4+} was reported to take place at high voltage (403) so the high intensity peaks at lower voltage suggest that the active species ,Sn^{4+}/Sn contributes to the CV of Sn-doped TiO_2.

In the initial CV cycle, the anodic- cathodic sweep was between 1 and 3 V and in this case, SnO_2 was reduced to metallic Sn and Ti^{4+} to Ti^{3+} and in subsequent cycles, the reduction of Ti^{4+} to Ti^{3+} was dominant. In the last cathodic sweep from 3V to 0V two cathodic peaks were observed below 1V, peaks 3 and 4 in the voltammogram. The strong peak at ~ 0.5 V, peak 4, is associated with Li^+/ Sn alloying and thus provides a strong evidence for metallic Sn formation in the initial cycle.

As this work aims to investigate the effect of unit cell expansion on the electrochemical property of rutile TiO_2, electrochemical reaction of SnO_2 was prevented from participating in the insertion/extraction of lithium ion by setting the cutoff voltage at 1V so that Sn could not alloy with Li^+ to form $Li_{4.4}Sn$.

7.5.2 Galvanostatic cycling with potential limitation (GCPL)

Galvanostatic charge- discharge cycling was performed after aging for 10 h at room temperature between 1.0 and 4.0 V vs. Li^+/Li. Charge-discharge profiles of the first two cycles followed by 5^{th}, 10^{th}, 15^{th} and 20^{th} and profiles of Li ion insertion-extraction into/from the $Sn_xTi_{1-x}O_2$ ($0.05 \leq x \leq 0.95$) are displayed in (Figure 7-24, Figure 7-25, Figure 7-26 and Figure 7-27) and Figure 7-28, Figure 7-29, Figure 7-30 and Figure 7-31 respectively.

The shapes of the initial charge (Li^+ extraction) and discharge (Li^+ insertion) curves of the $Sn_xTi_{1-x}O_2$ solid solutions were different. Two different regions can be seen clearly in the first charge curve: a poorly-resolved plateau as a first step of the Li ion extraction, followed by a smooth, sloped curve associated with a solid solution domain (263). In all systems, no reversible plateaus are observed during the first cycle, suggesting that the first lithium insertion results in an irreversible phase transformation. The subsequent cycles show sloped curves attributed to the insertion/extraction of lithium in a solid solution domain.

The discharge curves show distinct potential plateau at ~1.4 V, attributed to the reduction of Ti^{4+} to Ti^{3+} and a plateau at ~1.0 V attribute to the reduction of Sn^{4+} to Sn. This plateau might also correspond to the solid solution domain.

A small hump corresponding to ~0.05 Li ion was observed on first discharge for all samples which might be associated with electrolyte decomposition and formation of a solid electrolyte interface (SEI) film. During the first discharge cycle, the

voltage drops from OCV to about ~1.5 V and then attains a flat discharge plateau at ~1.0 V voltage.

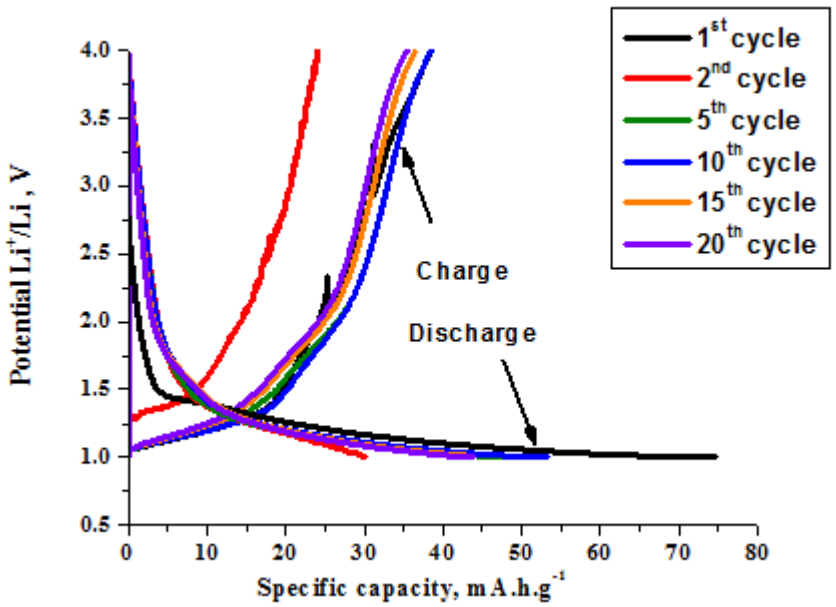

Figure 7-24: Charge-discharge profiles for $Sn_xTi_{1-x}O_2$ (x= 0.05).

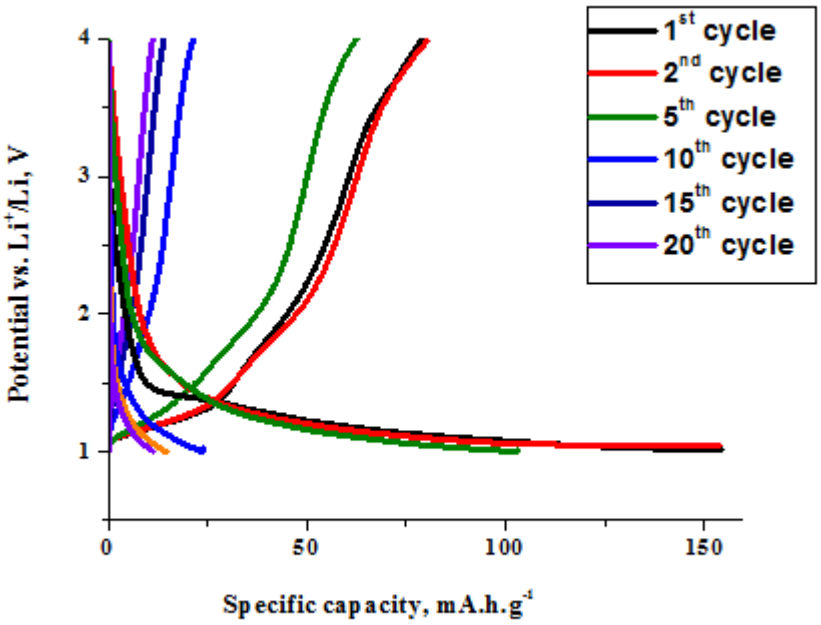

Figure 7-25: Charge-discharge profiles for $Sn_xTi_{1-x}O_2$ (x= 0.10).

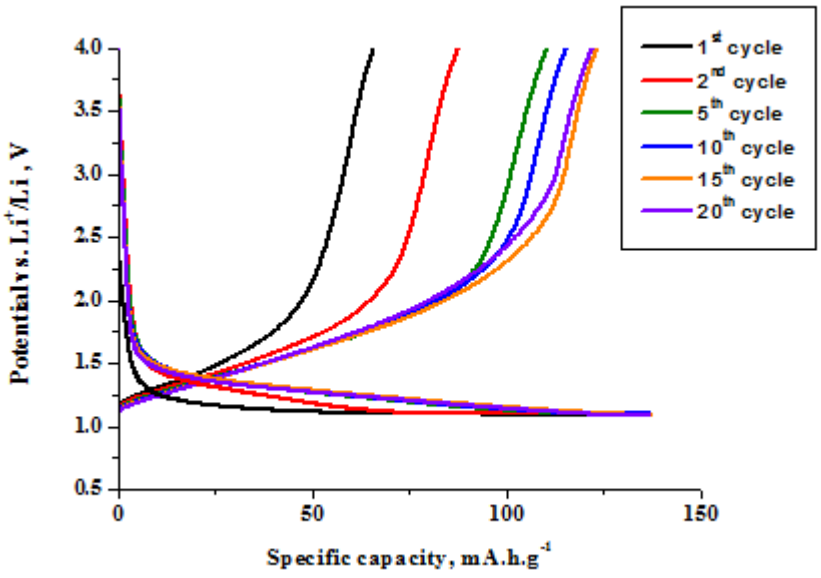

Figure 7-26: Charge-discharge profiles for $Sn_xTi_{1-x}O_2$ (x= 0.80).

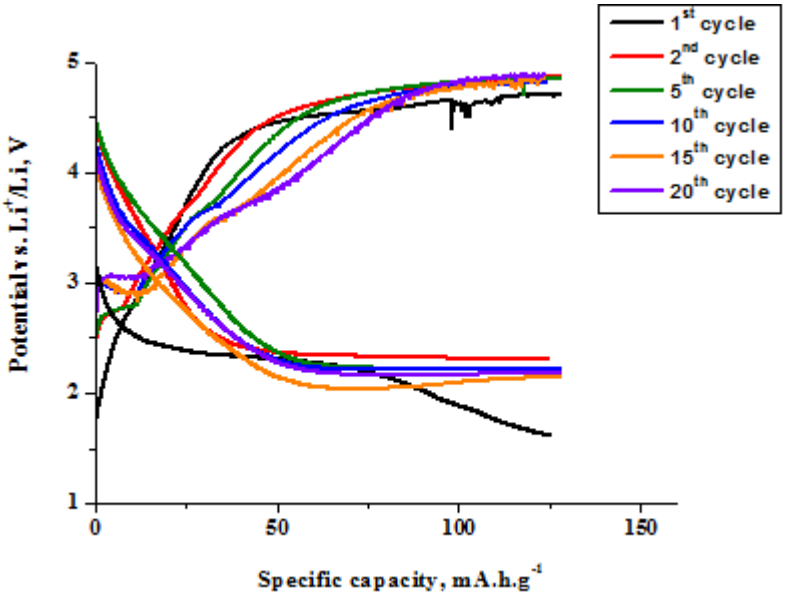

Figure 7-27: Charge-discharge profiles for $Sn_xTi_{1-x}O_2$ (x= 0.95).

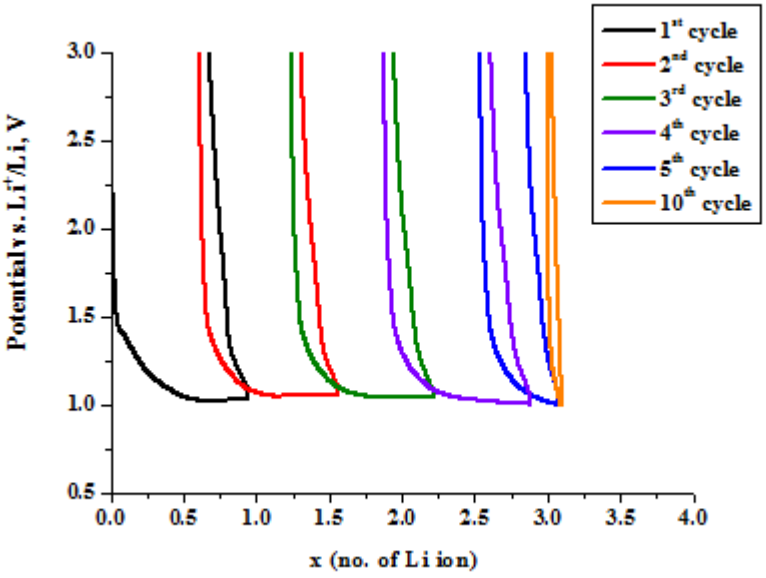

Figure 7-28: Li ion insertion–extraction profile for $Sn_xTi_{1-x}O_2$ (x= 0.05) for 10 cycles.

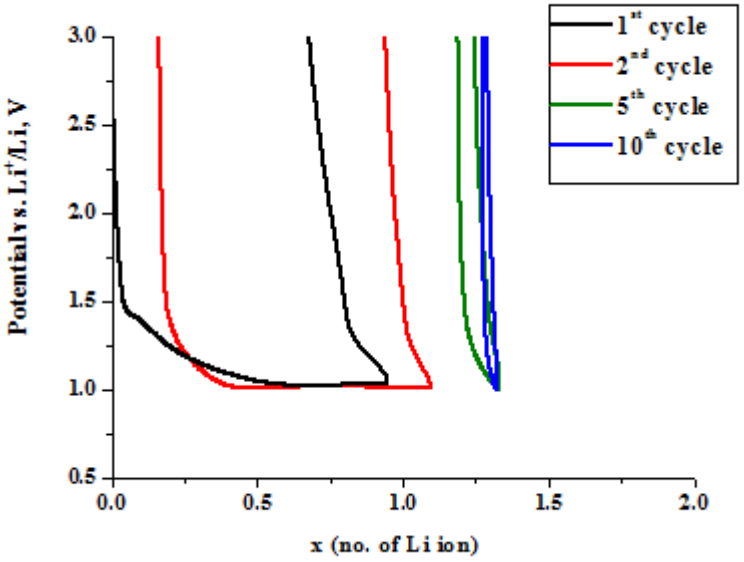

Figure 7-29: Li ion insertion–extraction profile for $Sn_xTi_{1-x}O_2$ (x= 0.10) for 10 cycles.

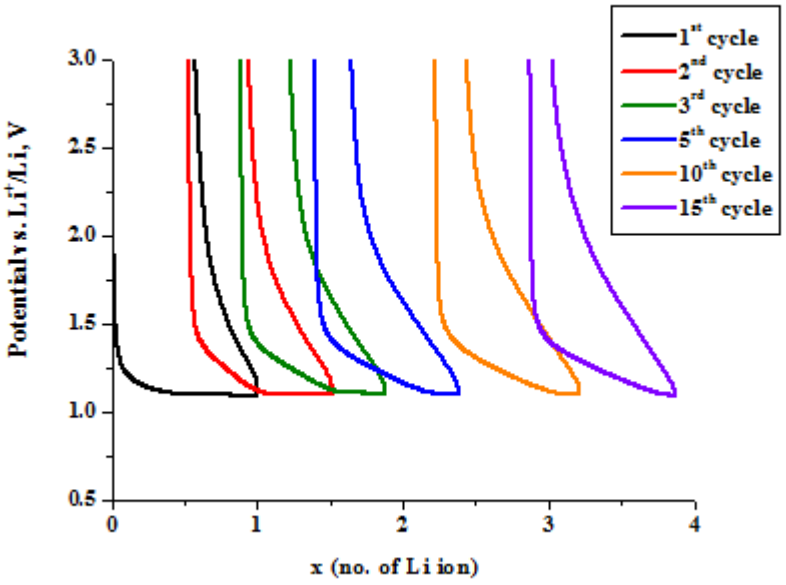

Figure 7-30: Li ion insertion–extraction profile for $Sn_xTi_{1-x}O_2$ (x= 0.80) for 10 cycles.

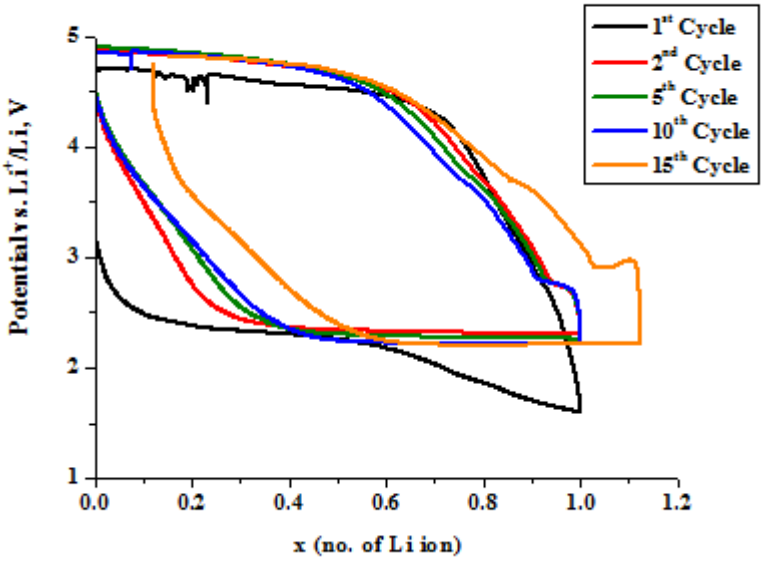

Figure 7-31: Li ion insertion–extraction profile for $Sn_xTi_{1-x}O_2$ (x= 0.95) for 10 cycles.

The specific capacities versus the number of cycles up to 20 cycles are given in Figure 7-32 and Figure 7-33 for x= 0.05 and 0.10. After first charge, a capacity loss can be observed for some samples and the irreversible lithium insertion capacity

varies from composition to composition. A significant drop in capacity was observed particularly for x=0.05, 0.15, 0.20 (not shown here) and 0.80, as ~ 50% capacity loss at first cycle. After the initial capacity loss, the capacity became quite constant for further cycles. Despite the initial cycles, good reversibility and great retention of capacity on cycling was observed for solid solutions of $Sn_xTi_{1-x}O_2$ at all compositions.

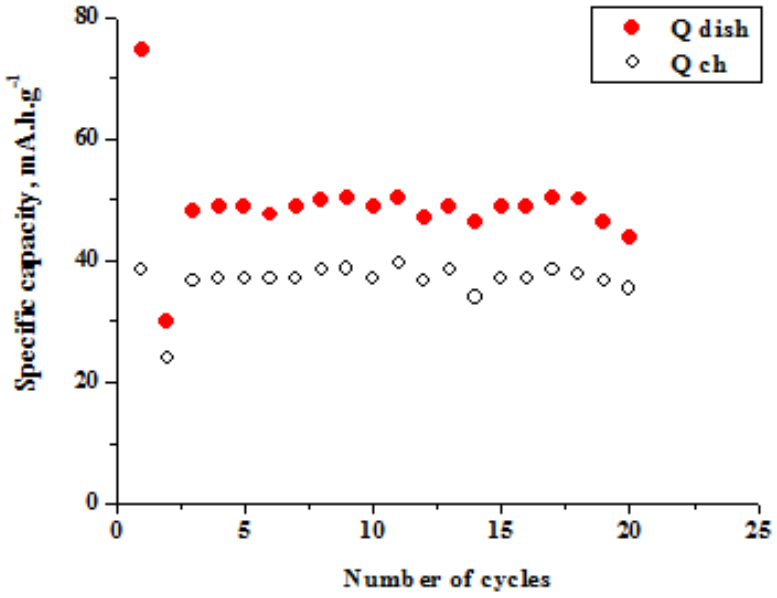

Figure 7-32: Charge-discharge capacity vs. number of cycles for $Sn_xTi_{1-x}O_2$ (x= 0.05) for 20 cycles.

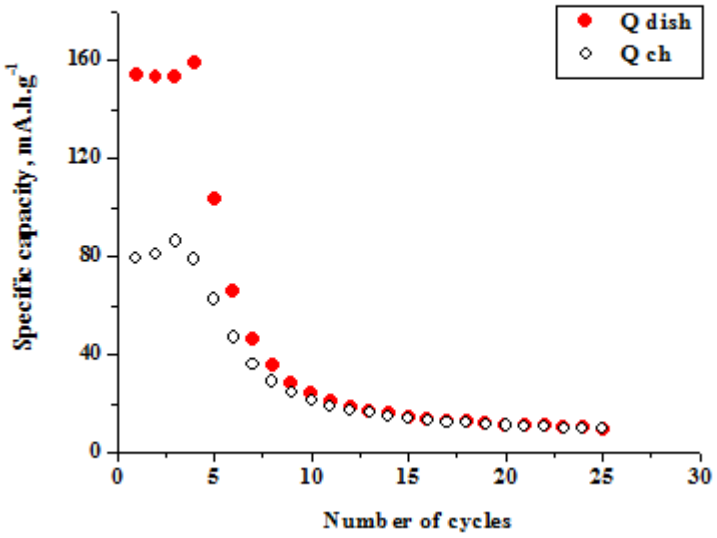

Figure 7-33: Charge-discharge capacity vs. number of cycles for $Sn_xTi_{1-x}O_2$ (x= 0.10) for 20 cycles.

On first discharge cycling, ~0.7 to 1.0 Li ions are intercalated into $Sn_xTi_{1-x}O_2$. The number of Li ions that intercalate into the rutile structure during the first cycle, and the corresponding capacities along with the percentage of Li ion extraction on first cycle and the theoretical capacity, which was calculated as one mole of Li ion intercalate, are presented in Table 7-4 and Figure 7-34. The theoretical capacity was calculated using following equation;

Q (in milliAmp.Hours per gram of active materials) = nF/ (3.6 *M)* (8)

where, Q is the theoretical specific capacity, n is the number of moles of active ion, F is the Faraday constant, 96,485 C/mol and *M* is molar mass of the active material.

About 17- 40% Li ion was extracted from the solid solutions of $Sn_xTi_{1-x}O_2$ with the composition ($0.05 \leq x \leq 0.80$). However, about 78- 90% Li ion was extracted from $Sn_xTi_{1-x}O_2$ with high tin content, $x \geq 0.85$.

Table 7-4: Insertion-extraction profile of: Li ion, experimental capacity and theoretical capacity for $Sn_xTi_{1-x}O_2$ ($0.05 \leq x \leq 0.95$) on the first cycle.

x	No. of Li^+ inserted during first cycle	% of Li^+ extracted during first cycle,	Specific capacity during first cycle		Theoretical capacity, mA.h/g (as n=1)
			Q charge, mA.h/g	Q discharge, mA.h/g	
0.05	1.0	~25	39	75	321.4
0.10	1.0	~ 30	79	154	308.3
0.15	1.0	~20	78	104	296.2
0.20	0.7	~17	77	149	285.1
0.80	1.0	~40	65.9	136.9	196.6
0.95	1.0	~90	127.5	127.5	182.1

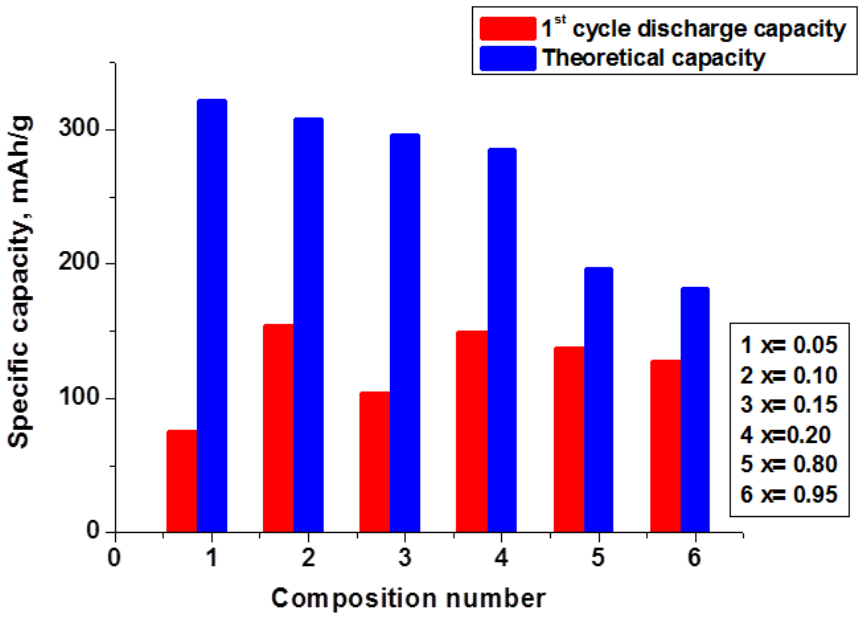

Figure 7-34: Comparison of the discharge specific capacity and theoretical capacity during first cycle for $Sn_xTi_{1-x}O_2$ ($0.05 \leq x \leq 0.95$).

7.5.3 Discussion

In this study, the cyclic performance of all samples was measured over the voltage range 1.0–3.0 V to avoid irreversible decomposition of the electrolyte. In this case, the reaction of metallic tin with lithium, as described in Eq. (7), at 0.8V is forbidden. The two plateaus at 1.5 and 1 V in charge-discharge curves of Sn-doped TiO_2 are attributed to the reversible reaction shown in Eq. (4) and partially reversible reaction in Eq. (5) which were previously reported by other authors (81,403,406,407,410). Generally, the second reaction is irreversible, thus corresponding voltage plateau at ~1.0 V should be absent from the second discharge curve leaving a large initial irreversible capacity after the first cycle. However, this plateau is still present in subsequent cycles and this supports the suggestion that the reaction described in Eq. (5) is partially reversible; this plateau might also represent the contribution of the solid solution domain.

The first discharge step for all samples reveals that up to ~1.0 of Li can intercalate into Sn-doped rutile at room temperature with a discharge capacity that reaches 154 mA.h/ g for x=0.10, while only 0.11 mol of Li, with a capacity of ~ 27 $mA.hg^{-1}$, can be inserted into undoped rutile.

During the first cycle, capacity loss is mainly due to the large irreversible Li-ion insertion capacity. Another reason for the poor initial reversibility may be the formation of metallic Sn in the initial cycle. Moreover, the electrode charging to 1.5V would cause the decomposition of the Li_2O and the reformation of SnO_2. The Li_2O matrix is assumed to hinder the aggregation of tin clusters which cause a loss in capacity due to large volume changes (411). In our case, the TiO_2 should play a key role to prevent this change and thus obtain a good cycling performance in voltage windows with a cut-off voltage between 1.0 – 3.0V. However, the capacity values can be improved by working to a cut-off voltage window below 0.5 V and in this case Sn will involve in the insertion/ extraction of Li ion.

Despite the initial cycles, Sn-doped TiO_2 system show a good reversibility, which indicates that there are no major structure change during the insertion and extraction of lithium. The most suitable compositions to use as an anode material for Li ion battery were found to be x=0.10 and 0.95 as both had a good capacity value with excellent capacity retention.

The electrochemical behaviour has been reported for nanosized Sn-doped TiO_2 mainly as anatase phase. Samples of $Ti_{2/3}Sn_{1/3}O_2$ nanocrystals (412) and Sn-doped TiO_2 nanotube (413–415) exhibit improved electronic conductivity with good rate capability and especially excellent cycling stability. A specific capacity of 257-386 mAh/ g after 50 cycles at 0.1 C has been reported for Sn-dopedTiO_2 nanotube, with coulombic efficiency of 99.2 %. However, it is difficult to apply them in large scale manufacturing due to the complexity of the process and thus the high cost of as-prepared material.

8. GENERAL CONCLUSIONS AND SUGGESTIONS FOR FUTURE STUDY

8.1 Review of the study

Investigations of rutile TiO_2 as an anodic material for lithium ion batteries have been presented. These studies include the following aspects:

- Studies of the influence of quenching and doping on the electrochemical performance of rutile;
- Studies of the influence of rutile as starting materials on the electrochemical performance of LTO;
- Synthesis of solid solutions of Cu, M co-doped rutile, (M= Nb^{5+} and Ta^{5+}) by using *a* conventional solid state approach and their characterization as anodes for lithium ion batteries;
- Electrochemical performance improvement of rutile anode materials by doping routes with aliovalent ions, such as Sn^{4+} and Cu^{2+}, M co-doped, (M= Nb^{5+} and Ta^{5+});
- Detailed studies on electrical behaviour of Sn-doped and Cu, M co-doped rutile systems , (M= Nb^{5+} and Ta^{5+}).
- Characterisation of the nature of the potential barrier in Sn-doped and Cu, Ta co-doped rutile based varistor systems by impedance spectroscopy and demonstration that the potential barrier is a Schottky-like barrier.

Based on the results that emerge from the studies of the above aspects, general conclusions are presented below:

- The desired properties of TiO_2 may be obtained by the modification of defect disorder through the imposition of controlled oxygen activity and/or the incorporation of aliovalent ions that lead to the formation of donor and acceptor levels. Both were applied in this work through: increasing the oxygen vacancies by quenching from high temperature and doping with metal ions, such as Sn^{4+} and Cu^{2+}, M co-doped, (M= Nb^{5+} and Ta^{5+}).

- Investigation of electrochemical behaviour of bulk rutile shows that only 0.11 mol of Li ion can be inserted into rutile structure along with a specific capacity of ~ 26 mA.h/ g, this is consistent with Li insertion into bulk rutile being negligible at room temperature.
- Oxygen-deficient rutile $TiO_{2-\delta}$ has been obtained by quenching the rutile sample from high temperature: 1400°C in liquid N_2. In comparison to fully oxidized rutile, reduced rutile shows a small improvement in electrochemical performance on the first cycle as 0.21 mole of Li ion was intercalated with a specific capacity of ~ 49 mA.h/ g; however after the first cycle, the electro-activity toward Li intercalation is similar, suggesting that increasing the electronic conductivity does not have a significant effect on the electrochemical performance of bulk rutile .
- LTO was synthesized by a solid-state reaction using two different TiO_2 phases; anatase and rutile. The effect of rutile on the LTO electrochemical performance was examined. Rutile was more efficient in terms of preparing phase pure LTO than anatase while anatase was more effective in achieving high specific capacity of LTO than rutile.
- Homogeneous solid solutions of doped and co-doped rutile have been prepared in the range: $0.05 \leq x \leq 0.15$ for $Cu_xTa_{2x}Ti_{1-3x}O_2$; $0.05 \leq x \leq 0.20$ for $Cu_xNb_{2x}Ti_{1-3x}O_2$;and $0.05 \leq x \leq 0.20$ and $0.80 \leq x \leq 0.95$ for $Sn_xTi_{1-x}O_2$, through solid state route where Ti^{4+} is partially replaced by Sn^{4+} and a combination of divalent (Cu^{2+})- pentavalent ions (Nb^{5+}, Ta^{5+}), their characterization reveal an increase in their lattice parameters, *a* and *c*, and unit cell volume with an increase in dopant level. Unit cell dimensions expand linearly according to Vegard's law.
- SEM images point to phase precipitation at grain boundary in Sn-doped rutile as a bulk surrounded by a thin grain boundary layer which displays different properties to those of the bulk probably because of the non-stoichiometry at the surface. Further study is needed to identify the composition of this phase.
- The electrical properties of the doped rutile are investigated by impedance spectroscopy (IS) measurements. The electrode effect: sputtered, paste, Au and Pt, is readily observed in terms of type of metal electrode and the processing of the electrode. The variations in the electrical properties with atmosphere are suggested to be related to the

presence of a precipitated (residual) phase/s (TiO_2, CuO, SnO_2) between grains that is undetectable by XRD.

- Cyclic voltammetry was used to understand the mechanism of lithium insertion/ extraction into/from doped rutile. Cathodic and anodic peaks are assigned to the Ti^{4+}/Ti^{3+} redox couple, however, an electrochemically-active Sn^{4+}/Sn contribution to the CV of Sn-doped TiO_2 is observed.
- No major structural change has been detected in ex-situ XRD patterns; however, the appearance of a flat plateau in charge-discharge profile suggests that the compound undergoes distinct phase changes during insertion of Li. Further studies are required to study the phase changes occurring during Li insertion.
- Improved electrochemical performance of rutile TiO_2 is noted. Cu, M co-doped rutile delivered capacity in the range 56- 78 mA.h/ g. Sn-doped system has much higher capacity (154 corresponding to one mole of Li^+ with x=0.10), the high capacity in this system would be because of the presence of Sn^{4+}/Sn redox couple in the CV.
- Irreversible capacity loss on the first cycle is noted, possibly due to the structural rearrangement of the rutile TiO_2 crystal lattice or irreversible trapping of lithium ions in the host rutile structure. However, in the subsequent cycles, both undoped and doped rutile TiO_2 show excellent retention of capacity.
- The overall performance of the battery could be improved by controlling various factors such as electrode preparation, cell construction, electrode thickness and operating conductions.
- Improved electronic conductivity of reduced rutile does not improve its reactivity towards lithium intercalation. Limitation of the lithium insertion into rutile structure has been improved by doping which leads to expanding the unit cell dimensions of rutile and hence facilitating Li ion diffusion. Doped rutile shows a much higher electro-activity towards Li insertion than undoped rutile. However, a major drawback in the electrochemical behaviour of doped rutile is a significant loss of capacity on cycling.

8.2 Future study

Although a series of studies on the structural, electrical and electrochemical properties of $Cu_xTa_{2x}Ti_{1-3x}O_2$, $Cu_xNb_{2x}Ti_{1-3x}O_2$ and SnO_2 has been carried out in the present work, it is of note that the characterisation of the electrode performance has focused on the specific capacity and cycle life. Other parameters and properties of the electrode such as capacity loss and rate capability have not been considered. It is therefore suggested that efforts should be made to study these parameters in order to further understand and improve the performance of the electrodes.

- The reason for the varistor behaviour of all doped rutile systems can be further investigated by using scanning electron microscopy (SEM), energy dispersive spectroscopy (EDS) and transmission electron microscopy (TEM) to identify the microstructure of the precipitate phase/s between grain boundaries.
- The reason for the improved specific capacity of the Sn-doped rutile can be further investigated by using *in-situ* neutron diffraction. This will give direct evidence of intermediate compounds (Li_2O and Sn) and provide clearly understanding of the mechanism behind the oxidation-reduction reactions during charge-discharge processes. For other systems prepared in this project, more detailed insight into the lithiated $Cu_xM_{2x}Ti_{1-3x}O_2$ structure is also needed.
- In Chapter 7, Sn substitution into rutile TiO_2 using the solid state reaction is very promising in terms of improving its electrochemical performance. Further research using element doping such as Sn, Nb co-doped, should lead to higher performance anodes for lithium ion batteries.

9. REFERENCES

1. Bruce PG. Energy storage beyond the horizon: Rechargeable lithium batteries. Solid State Ionics. 2008;179(21-26):752–60.

2. Shao-Horn Y. Understanding phase transformations in lithium battery materials by transmission electron microscopy" Science and Technology of Lithium Batteries. Nazri, G. Kluwer Academic; 2003.

3. Pralong V. Lithium intercalation into transition metal oxides: A route to generate new ordered rock salt type structure. Prog Solid State Chem. 2009;37:262–77.

4. Huggins RA. Advanced of batteries: Materials Science Aspects. US: Springer; 2009.

5. Delmas C, Menetrier M, Croguennec L, Levasseur S, Peres JP, Pouillerie C, et al. Lithium batteries: a new tool in solid state chemistry. Int J Inorg Mater. 1999;1:11–9.

6. Whittingham MS. Electrical Energy Storage and Intercalation Chemistry. Science (80-). 1976;192(4244):1226.

7. Poizot P, Laruelle S, Grugeon S, Dupont L, Tarascon J-M. Nano-sized transition-metal oxides as negative-electrode materials for lithium-ion batteries. Nature. 2000;407(September).

8. Godshall NA, Raistrick ID, Huggins RA. Thermodynamic investigations of ternary lithium-transition metal-oxygen cathode materials. Mater Res Bull. 1980;15:561.

9. Thackeray MM, Coetzer J. A preliminary investigation of the electrochemical performance of α-Fe_2O_3 and Fe_3O_4 cathodes in high-temperature cells. Mater Res Bull. 1981;16(5):591.

10. Gabano J-P. Lithium Batteries. New York: Academic Press; 1983.

11. Kaun TD, Nelson PA, Redey L, Vissers DR, Henriksen GL. High temperature lithium/sulfide batteries. Electrochim Acta. 1993;38(9):1269.

12. Badway F, Plitz I, Grugeon S, Laruelle S, Dollé M, Gozdz AS, et al. Metal Oxides as Negative Electrode Materials in Li-Ion Cells. Electrochem Solid-State Lett. 2002;5(6):A115. Available from: http://www.scopus.com/inward/record.url?eid=2-s2.0-0036000916&partnerID=tZOtx3y1

13. Larcher D, Sudant G, Leriche JB, Chabre Y, Tarascon JM. D. Larcher, G. Sudant, J.B. Leriche, Y. Chabre, J.M. Tarascon,. J Electrochem Soc. 2002;149:A234—A241.

14. Li H, Balaya P, Maier J. Li-Storage via Heterogeneous Reaction in Selected Binary Metal Fluorides and Oxides. J Electrochem Soc. 2004;151(11):A1878—A1885.

15. Grugeon S, Laruelle S, Dupont L, Tarascon JM. An update on the reactivity of nanoparticles Co-based compounds towards Li. Solid State Sci. 2003;5(6):895.

16. Bruce P. G., A. R. Armstrong RG. New intercalation compounds for lithium batteries: layered $LiMnO_2$. J Mater Chem. 1999;9:193.

17. Mizushima K, Jones PC, Wiseman PJ, Goodenough JB. Li_xCoO_2 (0<x<-1): A new cathode material for batteries of high energy density. Mater Res Bull. 1980;15(6):783–9.

18. Morales J, Pérez-Vicente C, Tirado JL. Cation distribution and chemical deintercalation of $Li_{1-x}Ni_{1+x}O_2$. Mater Res Bull. 1990;25(5):623–30.

19. Dahn JNR and JR. Electrochemical and In Situ X-Ray Diffraction Studies of Lithium Intercalation in Li_xCoO_2. J Electrochem Soc. 1992;139(8):2091–7.

20. Ueda, A., Ohzuku T. Solid- State Redox Reactions of $LiCoO_2$ ($R\bar{3}m$) for 4 Volt Secondary Lithium Cells. J Electrochem Soc. 1994;141(11):2972–7.

21. Dahn JR, Sacken U Von, Juzkow MW, Al-Janaby H. Rechargeable $LiNiO_2$ / Carbon Cells. J Electrochem Soc. 1991;138(8):2207–11.

22. Broussely M, Perton F, Biensan P, Bodet JM, Labat J, Lecerf A, et al. Li_xNiO_2, a promising cathode for rechargeable lithium batteries. J Power Sources. 1995 Mar;54(1):109–14. Available from: http://www.sciencedirect.com/science/article/pii/0378775394020499

23. Armstrong AR, Bruce PG., Synthesis of layered $LiMnO_2$ as an electrode for rechargeable lithium batteries. Nature. 1996;381:499–500.

24. Bruce PG, Armstrong AR, Huang H. New and optimised lithium manganese oxide cathodes for rechargeable lithium batteries. J Power Sources. 1997;68(1):19–23.

25. Capitaine F, Gravereau P, Delmas C. A new variety of $LiMnO_2$ with a layered structure. Solid State Ionics. 1996;89(3-4):197.

26. Thackeray MM, Johnson PJ, Picciotto LA De, Bruce PG, Goodenough JB. Electrochemical extraction of lithium from $LiMn_2O_4$. Mater Res Bull. 1984;19(2):179.

27. David WIF, Thackeray MM, Picciotto LA De, Goodenough JB. Structure refinement of the spinel-related phases $Li_2Mn_2O_4$ and $Li_{0.2}Mn_2O_4$. Solid State Chem. 1987;67(2):316–23.

28. Thackeray MM, David WIF, Bruce PG, Goodenough JB. Lithium insertion into manganese spinels. Mater Res Bull. 1983;18(4):461.

29. Padhi AK, Nanjundaswamy KS, Goodenough JB. Phospho-olivines as Positive-Electrode Materials for Rechargeable Lithium Batteries. J Electrochem Soc. 1997;144:1188.

30. Wakihara M. Recent developments in lithium ion batteries. Mater Sci Eng R Reports. 2001;33(4):109–34.

31. Konno R. structure, phase relationship and electrochemical properties of cathode materials- nickel, manganese and iron systems. international open seminar- high energy density lithium batteries for the coming generation. Tokyo: Italian Institute of Culture; 1998.

32. Guo Z. Investigation On Cathode Materials for Lithium-Ion Batteries. University of Wollongong; 2003.

33. Broussely M, Biensan P, Simon B. Lithium insertion into host materials: the key to success for Li ion batteries. Electrochim Acta. 1999;45(1-2):3–22.

34. Tabuchi M, Masquelierb C, Takeuchi T, Ado K, Matsubaraa I, Shirane T, Using Hydrothermal Reaction. Solid state ionics. 1996;90:129–32.

35. Jang Y Il, Moorehead WD, Chiang YM. Synthesis of the monoclinic and orthorhombic phases of $LiMnO_2$ in oxidizing atmosphere. Solid State Ionics. 2002;149(3-4):201–7.

36. Chung Sung-Yoon, Blocking Jason T. CY-M. Electronically conductive phospho-olivines as lithium storage electrodes. Nat Mater. 2002;1(2):123.

37. Huang H., Yin S.C. NLF. Approaching Theoretical Capacity of $LiFePO_4$ at Room Temperature at High Rates. Electrochem Solid-State Lett. 2001;4(10):A170.

38. Goodenough JB. Design considerations. Solid State Ion. 1994;69(3-4):184–98.

39. Julien CM, Mauger A, Zaghib K, Groult H. Comparative Issues of Cathode Materials for Li-Ion Batteries. 2014;132–54.

40. Idris MS. synthesis and characteration of lithium nickel manganese cobalt oxide as cathode material. university of Sheffield; 2011.

41. Xu K. Nonaqueous Liquid Electrolytes for Lithium-Based Rechargeable Batteries. Chem Rev. 2004;104(10):4303–417.

42. Tarascon, J.M., Guyomard D. New Electrolyte Compositions Stable Over the 0 to 5 V Voltage Range and Compatible with the $Li_{1+x}Mn_2O_4$/Carbon Li-Ion Cells. Solid State Ionics. 1994;69:293–305.

43. Aurbach, D., Ein-Eli, Y., Markovsky, B., Zaban, A., Luski, S., Carmeli Y, Yamin H. The Study of Electrolyte Solutions Based on Ethylene and Diethyl

Carbonates for Rechargeable Li Batteries. II:Graphite Electrodes. J Electrochem Soc. 1995;142:2882–9.

44. Newman, G.H., Francis, R. W., Gaines, L. H., Rao BM. Hazard Investigations of $LiClO_4$ / Dioxolane Electrolyte. J Electrochem Soc. 1980;127(9):2025.

45. Takata, K., Morita, M., Matsuda, Y., Matsui K. Cycling Characteristics of Secondary Li Electrode in $LiBF_4$/Mixed Ether Electrolytes. J Electrochem Soc. 1985;132:126–8.

46. Linden, D., Reddy TB. Handbook of Batteries. 3rd ed. New York: McGraw-Hill; 2001.

47. Yang, H., Zhuang, G. V., Ross Jr. PN. Yang, H., Zhuang, G. V., Ross Jr., P. N. J Power Sources. 2006;161:573.

48. Hofmann A, Schulz M, Hanemann T. Effect of Conducting Salts in Ionic Liquid based Electrolytes: Viscosity, Conductivity, and Li-Ion Cell Studies. Int J Electrochem Sci. 2013;8:10170–89.

49. Xu W, Angell CA. A Fusible Orthoborate Lithium Salt with High Conductivity in Solutions. Electrochem Solid-State Lett. 2000;3(8):366.

50. Xu W, Angell CA. Weakly Coordinating Anions, and the Exceptional Conductivity of Their Nonaqueous Solutions. Electrochem Solid-State Lett. 2001;4(1):E1–4.

51. Larush-Asraf L, Biton M, Teller H, Zinigrad E, Aurbach D. On the electrochemical and thermal behavior of lithium bis(oxalato)borate (LiBOB) solutions. J Power Sources. 2007;174(2):400.

52. Balsara DTH and NP. Polymer Electrolytes. Annu Rev Mater Res. 2013;43:503–25.

53. Cao C, Li Z-B, Wang X-L ZX-B and HW-Q. Recent advances in inorganic solid electrolytes for lithium batteries. Front Energy Res. 2014;2:25.

54. Hong HY-P. Crystalstructureandionicconductivityof$Li_{14}Zn(GeO_4)_4$ and othernewLi^+ superionicconductors. MaterResBull. 1978;13:117–24.

55. Dumon, A., Huang, M., Shen, Y., andNan CW. High Li ionconductivityinstrontiumdoped$Li_7La_3Zr_2O_{12}$ garnet. SolidStateIonics. 2013;243:36–41.

56. Aono, H., Sugimoto, E., Sadaoka, Y., Imanaka, N., andAdachi G. Ionic conductivity of solid electrolytes based on lithium titanium phosphate. J Electrochem Soc. 1990;137:1023–7.

57. Yamauchi, A., Sakuda, A., Hayashi, A., andTatsumisago M. Preparation and ionic conductivities of (100-x)(0.75Li2S•0.25P2S5)•xLiBH4 glasselectrolytes. J PowerSources. 2013;244:707–10.

58. Seino, Y., Ota, T., Takada, K., Hayashi, A., andTatsumisago M. Asulphide lithium superion conductor is superior to liquid ion conductors for use in rechargeable batteries. EnergyEnvironSci. 2014;7:627–31.

59. Tarascon JM, Armand M. Issues and challenges facing rechargeable lithium batteries. Nature. 2001;414(6861):359–67.

60. Xu K. Nonaqueous Liquid Electrolytes for Lithium-Based Rechargeable Batteries. Chem Rev. 2004;104(10):4303.

61. Xu K. Secondary batteries - Lithium rechargeable systems | Electrolytes: Overview, in Encyclopedia of Electrochemical Power Sources. Amsterdam.: Elsevier; 2009. 51-70.

62. Nazri GPGA. Batteries: Science and Technology. Springer; 2003.

63. Park T-H, Yeo J-S, Seo M-H, Miyawaki J, Mochida I, Yoon S-H. Enhancing the rate performance of graphite anodes through addition of natural graphite/carbon nanofibers in lithium-ion batteries. Electrochim Acta. 2013, 93:236–40. Available from: http://www.sciencedirect.com/science/article/pii/S0013468613000042

64. Goriparti S, Miele E, De Angelis F, Di Fabrizio E, Proietti Zaccaria R, Capiglia C. Review on recent progress of nanostructured anode materials for Li-ion batteries. Journal of Power Sources. Elsevier; 2014. p. 421–43.

65. PAULING L. The structure and properties of graphite and boron nitride. Proc natn Acad Sci USA,. 1966;56:1646.

66. Nelson RF. Power requirements for batteries in hybrid electric vehicles. J Power Sources. 2000;91(1):2.

67. John W. F. To, Zheng Chen, Hongbin Yao, Jiajun He, Kwanpyo Kim, Ho-Hsiu Chou, Lijia Pan, Jennifer Wilcox YC and ZB. Ultrahigh Surface Area Three-Dimensional Porous Graphitic Carbon from Conjugated Polymeric Molecular Framework. ACS Cent Sci. 2015;1:68−76.

68. Castro Neto AH, Guinea F, R. PM. Drawing conclusions from graphene. Phys World. 2006;19(11):33.

69. Liang M, Zhi L. Graphene-based electrode materials for rechargeable lithium batteries. J Mater Chem. 2009;19:5871–8.

70. Brownson DAC, Kampouris DK, Banks CE. An overview of graphene in energy production and storage applications. J Power Sources. 2011 Jun ;196(11):4873–85. Available from: http://www.sciencedirect.com/science/article/pii/S0378775311003764

71. Pan D, Wang S, Zhao B, Wu M, Zhang H, Wang Y, et al. Li Storage Properties of Disordered Graphene Nanosheets. Chem Mater. 2009;21(14):3136–42.

72. Lian P, Zhu X, Liang S, Li Z, Yang W, Wang H. Large reversible capacity of high quality graphene sheets as an anode material for lithium-ion batteries. Electrochim Acta. 2010;55(12):3909–14.

73. Wang Z-L, Xu D, Wang H-G, Wu Z, Zhang X-B. In Situ Fabrication of Porous Graphene Electrodes for High-Performance Energy Storage. ACS Nano. 2013;7(3):2422–30.

74. Bhardwaj T, Antic A, Pavan B, Barone V, Fahlman BD. Enhanced electrochemical lithium storage by graphene nanoribbons. J Am Chem Soc. 2010;132:12556–8.

75. Xia H, Zhu D, Fu Y, Wang X. $CoFe_2O_4$-graphene nanocomposite as a high-capacity anode material for lithium-ion batteries. Electrochim Acta. 2012;83:166–74.

76. Pham VH, Kim K-H, Jung D-W, Singh K, Oh E-S, Chung JS. Liquid phase co-exfoliated MoS_2–graphene composites as anode materials for lithium ion batteries. J Power Sources. 2013;244:280–6.

77. Wu Y, Wei Y, Wang J, Jiang K, Fan S. Conformal Fe_3O_4 Sheath on Aligned Carbon Nanotube Scaffolds as High-Performance Anodes for Lithium Ion Batteries. Nano Lett. 2013;13(2):818–23.

78. Hu A, Chen X, Tang Y, Tang Q, Yang L, Zhang S. Self-assembly of Fe_3O_4 nanorods on graphene for lithium ion batteries with high rate capacity and cycle stability. Electrochem Commun. 2013;28:139–42.

79. Rao, B. M. L., Francis, R. W. , Christopher HA. Lithium-aluminium electrodes. J Electrochem Soc. 1977;124:1490–2.

80. Bruce PG., Bruno Scrosati J-MT. Nanomaterials for Rechargeable Lithium Batteries. Angew Chem Int Ed. 2008;47(16):2930–46.

81. Winter M, Besenhard JO. Electrochemical lithiation of tin and tin-based intermetallics and composites. Electrochim Acta. Elsevier Science Ltd; 1999;45(1):31–50.

82. Huggins R. Lithium batteries. Boston: Kuwer Academic; 2004.

83. Aricò AS, Bruce P, Scrosati B, Tarascon J-M, van Schalkwijk W. Nanostructured materials for advanced energy conversion and storage devices. Nat Mater. 2005;4(5):366–77.

84. Derrien G, Hassoun J, Panero S, Scrosati B. Nanostructured Sn–C Composite as an Advanced Anode Material in High-Performance Lithium-Ion Batteries. Adv Mater. 2007;19(17):2336–40.

85. Kim H, Han B, Choo J, Cho J. Three-Dimensional Porous Silicon Particles for Use in High-Performance Lithium Secondary Batteries. Angew Chem Int Ed. 2008;47(52):10151–4.

86. Kepler, K. D., Vaughey, J. T. , Thackeray MM. $Li_xCu_6Sn_5$ (0<x<13): an intermetallic insertion electrode for rechargeable lithium batteries. Electrochem Solid State Lett. 1999;2:307.

87. Idota Y. Tin-Based Amorphous Oxide: A High-Capacity Lithium-Ion-Storage Material. Science. 1997. p. 1395–7.

88. Winter, M. Besenhard JO. Electrochemical lithiation of tin and tin-based intermetallics and composites. Electrochim Acta. 1999;45(1-2):31–50.

89. Kulova TL. New electrode materials for lithium-ion batteries (Review). Russ J Electrochem. 2013;49(1):1–25. Available from: http://link.springer.com/10.1134/S1023193513010102

90. Morales J. Improving the Electrochemical Performance of SnO_2 Cathodes in Lithium Secondary Batteries by Doping with Mo. J Electrochem Soc. 1999;146(5):1640.

91. Chou SL, Wang JZ, Liu HK, Dou SX., SnO_2 meso-scale tubes: One-step, room temperature electrodeposition synthesis and kinetic investigation for lithium storage. Electrochem commun. Elsevier B.V.; 2009;11(2):242–6. Available from: http://dx.doi.org/10.1016/j.elecom.2008.11.017

92. Zeng ZY, Tu JP, Huang XH, Wang XL, Zhao XB, Li KF. Electrochemical Properties of a Mesoporous Si/TiO_2 Nanocomposite Film Anode for Lithium-Ion Batteries. Electrochem Solid-State Lett. 2008 [cited 2015 Jun 24];11(6):A105. Available from: http://www.scopus.com/inward/record.url?eid=2-s2.0-42349096076&partnerID=tZOtx3y1

93. Liang Y, Fan J, Xia XH, Luo YS, Jia ZJ. Modified hydrothermal synthesis of SnO_y-SiO_2 for lithium-ion battery anodes. Electrochim Acta. 2007;52(19):5891–5.

94. Wang G, Gao XP, Shen PW. Hydrothermal synthesis of Co_2SnO_4 nanocrystals as anode materials for Li-ion batteries. J Power Sources. 2009;192(2):719–23.

95. Zhang T, Fu LJ, Gao J, Wu YP, Holze R, Wu HQ. Nanosized tin anode prepared by laser-induced vapor deposition for lithium ion battery. J Power Sources. 2007;174(2):770–3.

96. Arbizzani C, Beninati S, Lazzari M, Mastragostino M. Carbon paper as three-dimensional conducting substrate for tin anodes in lithium-ion batteries. J Power Sources. 2005;141(1):149–55.

97. Poizot P, Laruelle S, Grugeon S, Dupont L, Tarascon JM. Searching for new anode materials for the Li-ion technology: Time to deviate from the usual path. J Power Sources. 2001;97-98:235–9.

98. Grugeon S, Laruelle S, Herrera-Urbina R, Dupont L, Poizot P, Tarascon J-M. Particle Size Effects on the Electrochemical Performance of Copper Oxides toward Lithium. J Electrochem Soc. 2001;148(4):A285.

99. Débart a., Dupont L, Poizot P, Leriche J-B, Tarascon JM. A Transmission Electron Microscopy Study of the Reactivity Mechanism of Tailor-Made CuO Particles toward Lithium. J Electrochem Soc. 2001;148(11):A1266.

100. Goriparti S, Miele E, De Angelis F, Di Fabrizio E, Proietti Zaccaria R, Capiglia C. Review on recent progress of nanostructured anode materials for Li-ion batteries. J Power Sources [Internet]. Elsevier B.V; 2014;257:421–43. Available from: http://dx.doi.org/10.1016/j.jpowsour.2013.11.103

101. Zhang L, Hu P, Zhao X, Tian R, Zou R, Xia D. Controllable synthesis of core–shell Co@CoO nanocomposites with a superior performance as an anode material for lithium-ion batteries. J Mater Chem. 2011;21(45):18279–83.

102. Xu J-S, Zhu Y-J. Monodisperse Fe3O4 and γ-Fe2O3 magnetic mesoporous microspheres as anode materials for lithium-ion batteries. ACS Appl Mater Interfaces [Internet]. 2012;4(9):4752–7. Available from: http://www.ncbi.nlm.nih.gov/pubmed/22934532

103. Zhu X, Wu W, Liu Z, Li L, Hu J, Dai H, et al. A reduced graphene oxide-nanoporous magnetic oxide iron hybrid as an improved anode material for lithium ion batteries. Electrochim Acta [Internet]. Elsevier Ltd; 2013;95:24–8. Available from: http://dx.doi.org/10.1016/j.electacta.2013.02.029

104. Hwang JK, Lim HS, Sun YK, Suh K Do. Monodispersed hollow carbon/Fe_3O_4 composite microspheres for high performance anode materials in lithium-ion batteries. J Power Sources [Internet]. Elsevier B.V; 2013;244:538–43. Available from: http://dx.doi.org/10.1016/j.jpowsour.2013.02.017

105. Kim IT, Magasinski A, Jacob K, Yushin G, Tannenbaum R. Synthesis and electrochemical performance of reduced graphene oxide/maghemite composite anode for lithium ion batteries. Carbon N Y [Internet]. Elsevier Ltd; 2013;52:56–64. Available from: http://dx.doi.org/10.1016/j.carbon.2012.09.004

106. Winter M, Besenhard JO. Handbook of Battery Materials. Besenhard JO, editor. New York: Wiley; 1999. 383 p.

107. Inaba M, Oba Y, Niina F, Murota Y, Ogino Y, Tasaka A, et al. TiO_2(B) as a promising high potential negative electrode for large-size lithium-ion batteries. J Power Sources. 2009;189(1):580–4.

108. Kavan L, Grätzel M, Gilbert SE, Klemenz C, Scheel HJ. Electrochemical and photoelectrochemical investigation of single-crystal anatase. J Am Chem Soc. 1996;118(28):6716–23.

109. Exnar I, Kavan L, Huang SY, Grätzel M. Novel 2 V rocking-chair lithium battery based on nano-crystalline titanium dioxide. Journal of Power Sources. 1997. p. 720–2.

110. Wagemaker M, Kearley GJ, Van Well AA, Mutka H, Mulder FM. Multiple Li positions inside oxygen octahedra in lithiated TiO2 anatase. J Am Chem Soc. 2003;125(3):840–8.

111. Sudant G, Baudrin E, Larcher D, Tarascon J-M. Electrochemical lithium reactivity with nanotextured anatase-type TiO_2. Journal of Materials Chemistry. 2005.

112. Armstrong AR, Armstrong G, Canales J, García R, Bruce PG. Lithium-ion intercalation into TiO_2-B nanowires. Adv Mater. 2005;17(7):862–5.

113. Global Lithium Ion Battery Market (Cathode, Anode, and Electrolytic solution) - Industry Analysis, Size, Share, Growth, Trends, and Forecast, 2013 – 2019 [Internet]. Available from: http://www.transparencymarketresearch.com/lithium-ion-battery-market.html

114. Liu B, Luo T, Mu G, Wang X, Chen D, Shen G. Rechargeable Mg-Ion Batteries Based on WSe2 Nanowire Cathodes. ACS Nano. 2013;7(9):8051–8.

115. Palomares V, Serras P, Villaluenga I, Hueso KB, Carretero-Gonzalez J, Rojo T. Na-ion batteries, recent advances and present challenges to become low cost energy storage systems. Energy Environ Sci. 2012;5:5884–901.

116. Mark J. Armstrong, Colm O'Dwyer, William J. Macklin JDH. Evaluating the performance of nanostructured materials as lithium-ion battery electrodes. Nano Res. 2014;7(1):1–62.

117. https://www.sisinternational.com/lithium-ion-battery/.

118. http://www.iflscience.com/technology/new-metal-air-battery-drives-car-1800km-without-recharge.

119. Lee S-K, Oh S-M, Park E, Scrosati B, Hassoun J, Park M-S, et al. Highly Cyclable Lithium–Sulfur Batteries with a Dual-Type Sulfur Cathode and a Lithiated Si/SiO_x Nanosphere Anode. Nano Lett [Internet]. 2015;150409105927001. Available from: http://pubs.acs.org/doi/abs/10.1021/nl504460s

120. Osiak M, Geaney H, Armstrong E, O'Dwyer C. Structuring materials for lithium-ion batteries: advancements in nanomaterial structure, composition,

and defined assembly on cell performance. J Mater Chem A [Internet]. 2014;2(25):9433. Available from: http://xlink.rsc.org/?DOI=c4ta00534a

121. Scrosati B, Garche J. Lithium batteries: Status, prospects and future. J Power Sources. 2010;195(9):2419–30.

122. Chiodo L, Salazar M, Romero A, Laricchia, Sala S, Della F, et al. Structure, Electronic, and Optical Properties of TiO_2 Atomic Clusters: An Ab Initio Study. J Chem Phys. 2011;135:244704.

123. Roy P, Berger S, Schmuki P. TiO_2 Nanotubes: Synthesis and Applications. Angew Chem Int Ed. 2011;50:2904–39.

124. Zhang H, Zou Y, Sun Y, Sun L, Xu F, Zhang J, et al. A novel thermal-insulating film incorporating microencapsulated phase-change materials for temperature regulation and nano-TiO_2 for UV-blocking. Sol Energy Mater Sol Cells [Internet]. Elsevier; 2015;137:210–8. Available from: http://linkinghub.elsevier.com/retrieve/pii/S0927024815000793

125. Choi W. Pure and Modified TiO_2 Photocatalysts and Their Environmental. Appl Catal Surv Asia. 2006;10:16–28.

126. Park Y, Lee S-H, Kang SO, Choi W. Organic dye-sensitized TiO_2 for the redox conversion of water pollutants under visible light. Chem Commun (Camb). 2010;46(14):2477–9.

127. Orlov a, Chan MS, Jefferson D a, Zhou D, Lynch RJ, Lambert RM. Photocatalytic degradation of water-soluble organic pollutants on TiO_2 modified with gold nanoparticles. Environ Technol. 2006;27(7):747–52.

128. Zhu G-N, Wang Y-G, Xia Y-Y. Ti-based compounds as anode materials for Li-ion batteries. Energy & Environmental Science. 2012. p. 6652.

129. Jackson, Mark J., Ahmed W, editor. Surface Engineered Surgical Tools and Medical Devices. Springer; 2006. 49-63 p.

130. Wang L, Xu HW, Chen PC, Zhang DW, Ding CX, Chen CH. Electrostatic spray deposition of porous Fe_2O_3 thin films as anode material with improved electrochemical performance for lithium–ion batteries. J Power Sources

[Internet]. 2009 Sep;193(2):846–50. Available from: http://www.sciencedirect.com/science/article/pii/S0378775309005722

131. Liu, H., Wang, G., Park, J., Wang, J., Liu, H., Zhang C. Electrochemical performance of α-Fe_2O_3 nanorods as anode material for lithium-ion cells. Electrochim Acta. 2009;54(6):1733.

132. Yang Z, Choi D, Kerisit S, Rosso KM, Wang D, Zhang J, et al. Nanostructures and lithium electrochemical reactivity of lithium titanites and titanium oxides: A review. Journal of Power Sources. 2009. p. 588–98.

133. Reddy MA, Kishore MS, Pralong V, Caignaert V, Varadaraju U V., Raveau B. Room temperature synthesis and Li insertion into nanocrystalline rutile TiO_2. Electrochem commun. 2006;8(8):1299–303.

134. Armstrong AR, Armstrong G, Canales J, Bruce PG. TiO_2-B nanowires. Angew Chemie - Int Ed. 2004;43(17):2286–8.

135. Ren H, Yu R, Wang J, Jin Q, Yang M, Mao D, et al. Multishelled TiO_2 Hollow Microspheres as Anodes with Superior Reversible Capacity for Lithium Ion Batteries. 2014;

136. Ohzuku T, Ueda A, Yamamota N. Zero-Strain Insertion Material of $Li[L_{i1/3}Ti_{5/3}]O_4$ for Rechargeable Lithium Cells. J Electrochem Soc. 1995;142(5):1431–5.

137. Zaghib K, Simoneau M, Armand M, Gauthier M. Electrochemical study of $Li_4Ti_5O_{12}$ as negative electrode for Li-ion polymer rechargeable batteries. Journal of Power Sources. 1999. p. 300–5.

138. Nakahara K, Nakajima R, Matsushima T, Majima H. Preparation of particulate $Li_4Ti_5O_{12}$ having excellent characteristics as an electrode active material for power storage cells. J Power Sources. 2003;117(1-2):131–6.

139. Yi T-F, Jiang L-J, Shu J, Yue C-B, Zhu R-S, Qiao H-B. Recent development and application of $Li_4Ti_5O_{12}$ as anode material of lithium ion battery. J Phys Chem Solids. 2010;71(9):1236.

140. Xiangcheng Sun, Pavle V. Radovanovicb BC. Advances in spinel $Li_4Ti_5O_{12}$ anode materials for lithium-ion batteries. NewJChem, 2015, 39, 38. 2015;39:38.

141. Naoi K, Ishimoto S, Isobe Y, Aoyagi S. High-rate nano-crystalline $Li_4Ti_5O_{12}$ attached on carbon nano-fibers for hybrid supercapacitors. J Power Sources. 2010;195(18):6250.

142. Shu J. Electrochemical behavior and stability of $Li_4Ti_5O_{12}$ in a broad voltage window. J Solid State Electrochem. 2009;13(10):1535.

143. Yao X, Xie S, Chen C, Wang Q, Sun J, Li Y, et al. Comparisons of graphite and spinel $Li_{1.33}Ti_{1.67}O_4$ as anode materials for rechargeable lithium-ion batteries. Electrochim Acta. 2005;50(20):4076.

144. Yi T-F, Yang S-Y, Xie Y. Recent advances of $Li_4Ti_5O_{12}$ as a promising next generation anode material for high power lithium-ion batteries. J Mater Chem A [Internet]. Royal Society of Chemistry; 2015;3:5750–77. Available from: http://xlink.rsc.org/?DOI=C4TA06882C

145. Sun X, Radovanovic P V., Cui B. Advances in spinel $Li_4Ti_5O_{12}$ anode materials for lithium-ion batteries. New J Chem [Internet]. Royal Society of Chemistry; 2015;39(1):38–63. Available from: http://xlink.rsc.org/?DOI=C4NJ01390E

146. Gao J, Jiang C-Y, Ying J-R, Wan C-R. Preparation and characterization of high-density spherical $Li_4Ti_5O_{12}$ anode material for lithium secondary batteries. J Power Sources. 2006;155(2):364–7.

147. Chen CH, Vaughey JT, Jansen AN, Dees DW, Kahaian AJ, Goacher T, et al. Studies of Mg-substituted $Li_{4-x}Mg_xTi_5O_{12}$ spinel electrodes (0 <= x <= 1) for lithium batteries. J Electrochem Soc [Internet]. 2001;148(1):A102–4. Available from: <Go to ISI>://WOS:000166129600015\nhttp://scitation.aip.org/getabs/servlet/GetabsServlet?prog=normal&id=JESOAN00014800000100A102000001&idtype=cvips&gifs=yes&ref=no

148. Ouyang C-Y, Zhong Z-Y, Lei M-S. Ab initio studies of structural and electronic properties of $Li_4Ti_5O_{12}$ spinel. Electrochem Commun. 2007;9(5):1107–12.

149. Amatucci GG, Badway F, Pasquier A Du, Zheng T. An Asymmetric Hybrid Nonaqueous Energy Storage Cell. Electrochem Soc. 2001;148(8):A930.

150. Huang S, Wen Z, Zhu X, Lin Z. Effects of dopant on the electrochemical performance of $Li_4Ti_5O_{12}$ as electrode material for lithium ion batteries. J Power Sources [Internet]. 2007; 165(1):408–12. Available from: http://www.scopus.com/inward/record.url?eid=2-s2.0-33846796259&partnerID=tZOtx3y1

151. Cheng L, Yan J, Zhu G-N, Luo J-Y, Wang C-X, Xia Y-Y. General synthesis of carbon-coated nanostructure $Li_4Ti_5O_{12}$ as a high rate electrode material for Li-ion intercalation. J Mater Chem. 2010;20:595.

152. Aravindan V, Lee Y-S, Yazami R, Madhavi S. TiO2 polymorphs in “rocking-chair” Li-ion batteries. Mater Today [Internet]. 2015;18(6):345–51. Available from: http://linkinghub.elsevier.com/retrieve/pii/S1369702115000796

153. Koudriachova M V., Harrison NM, Leeuw SW. Diffusion of Li-ions in rutile. An ab initio study. Solid State Ionics. 2003;157:35.

154. Kubiak P, Pfanzelt M, Geserick J, Hörmann U, Hüsing N, Kaiser U, et al. Electrochemical evaluation of rutile TiO_2 nanoparticles as negative electrode for Li-ion batteries. J Power Sources. 2009;194(2):1099–104.

155. Payne C, Teter MP, Allan DC, Arias TA, Joannapulos JD. Iterative minimization techniques for ab initio total-energy calculations: molecular dynamics and conjugate gradients. Rev Mod Phys. 1992;64:1045.

156. Koudriachova M V., Harrison NM, Leeuw SW. Density-functional simulations of lithium intercalation in rutile. Phys Rev B Condens Matter Mater Phys. 2002;65:235423.

157. Dylla AG, Henkelman G, Stevenson KJ. Lithium Insertion in Nanostructured TiO_2 (B) Architectures. Acc Chem Res. 2013;46:1104.

158. Li J, Tang Z, Zhang Z. Preparation and Novel Lithium Intercalation Properties of Titanium Oxide Nanotubes. Electrochem Solid-State Lett [Internet]. 2005; 8(6):A316. Available from: http://www.scopus.com/inward/record.url?eid=2-s2.0-20844446853&partnerID=tZOtx3y1

159. Cava RJ, Murphy DW, Zahurak S, Santoro A, Roth RS. The crystal structures of the lithium-inserted metal oxides $Li_{0.5}TiO_2$ anatase, $LiT_{i2}O_4$ spinel, and $Li_2Ti_2O_4$. J Solid State Chem. 1984;53(1):64.

160. Zachau-Christiansen B, West K, Jacosen T AS. Lithium insertion in different TiO_2 modifications. Solid State Ionics. 1988;28:1176.

161. Kavan L, Kalbáč M, Zukalová M, Exnar I, Lorenzen V, Nesper R, et al. Lithium Storage in Nanostructured TiO 2 Made by Hydrothermal Growth. Chem Mater [Internet]. 2004;16(3):477–85. Available from: http://apps.webofknowledge.com/full_record.do?product=UA&search_mode=MarkedList&qid=28&SID=P15BdKtLnsBhHZeECeL&page=1&doc=4&colName=WOS&cacheurlFromRightClick=no

162. Wagemaker M, Borghols WJH, Mulder FM. Large Impact of Particle Size on Insertion Reactions . A Case for Anatase LiTiO Large Impact of Particle Size on Insertion Reactions . A Case. JAmChemSoc. 2007;129(March):4323–7.

163. Qiu YC, Yan KY, Yang SH, Jin LM, Deng H, Li WS. Synthesis of Size-Tunable Anatase TiO_2 Nanospindles and Their Assembly into Anatase@Titanium Oxynitride/Titanium Nitride Graphene Nanocomposites for Rechargeable Lithium Ion Batteries with High Cycling Performance. ACS Nano. 2010;4(11):6515.

164. Das K, Patel M, Bhattacharyya AJ. Effect of Nanostructuring and Ex situ Amorphous Carbon Coverage on the Lithium Storage and Insertion Kinetics in Anatase Titania. ACS Appl Mater Interfaces. 2010;2(7):2091.

165. Cao FF, Wu XL, Xin S, Guo G, Wan LJ. Facile Synthesis of Mesoporous TiO_2−C Nanosphere as an Improved Anode Material for Superior High Rate 1.5 V Rechargeable Li Ion Batteries Containing $LiFePO_4$−C Cathode. Phys Chem C. 2010;114(22):10308.

166. Nam SH, Shim HS, Kim YS, Dar MA, Kim JG, Kim WB. Ag or Au Nanoparticle-Embedded One-Dimensional Composite TiO_2 Nanofibers Prepared via Electrospinning for Use in Lithium-Ion Batteries. ACS Appl Mater Interfaces. 2010;2(7):2046.

167. Kim H, Kim MG, Shin TJ, Shin HJ, Cho J. TiO_2@Sn core-shell nanotubes for fast and high density Li-ion storage material. Electrochem commun [Internet]. Elsevier B.V.; 2008;10(11):1669–72. Available from: http://dx.doi.org/10.1016/j.elecom.2008.08.035

168. Guo YG, Hu YS, Sigle W, Maier J. Superior Electrode Performance of Nanostructured Mesoporous TiO_2 (Anatase) through Efficient Hierarchical Mixed Conducting Networks. Adv Mater. 2007;19(16):2087.

169. Bao SJ, Bao QL, Li CM, Zhi-Li Dong. Novel porous anatase TiO_2 nanorods and their high lithium electroactivity. Electrochem commun. 2007;9(5):1233–8.

170. Liu, Z. L., Hong, L., Guo B. Physicochemical and electrochemical characterization of anatase titanium dioxide nanoparticles. J Power Sources. 2005;143(1-2):231.

171. Jiang C, Wei M, Qi Z, Kudo T, Honma I, Zhou H. Particle size dependence of the lithium storage capability and high rate performance of nanocrystalline anatase TiO_2 electrode. J Power Sources. 2007;166(1):239–43.

172. Maier J. Nanoionics: ion transport and electrochemical storage in confined systems. Nat Mater. 2005;4:805.

173. Cao Y, He T, Zhao L, Wang E, Yang W, Cao Y. Structure and Phase Transition Behavior of Sn^{4+} -Doped TiO_2 Nanoparticles. 2009;18121–4.

174. Wang, Y. Cao GZ. Synthesis and Enhanced Intercalation Properties of Nanostructured Vanadium Oxides. Chem Mater. 2006;18:2787.

175. Armstrong G, Armstrong a. R, Bruce PG, Reale P, Scrosati B. TiO_2B) nanowires as an improved anode material for lithium-ion batteries containing

$LiFePO_4$ or $LiNi_{0.5}Mn_{1.5}O_4$ cathodes and a polymer electrolyte. Adv Mater. 2006;18(19):2597–600.

176. Xiang GL, Li TY, Zhuang J, Wang X. Large-scale synthesis of metastable TiO_2(B) nanosheets with atomic thickness and their photocatalytic properties. Chem Commun. 2010;46:6801.

177. Armstrong AR, Armstrong G, Canales J, Bruce PG. TiO_2-B nanowires as negative electrodes for rechargeable lithium batteries. Journal of Power Sources. 2005. p. 501–6.

178. Feist TP, Davies PK. he soft chemical synthesis of TiO_2(B) from layered titanates. J Solid State Chem. 1992;101(2):275.

179. Panduwinata, D., Gale JD. A first principles investigation of lithium intercalation in TiO_2-B. Mater Chem. 2009;19:3931.

180. Arrouvel C, Parker SC, Islam MS. Lithium Insertion and Transport in the TiO_2-B Anode Material: A Computational Study. Chem Mater. 2009;21:4778–83.

181. Armstrong AR, Arrouvel C, Gentili V, Parker SC, Islam MS, Bruce PG. Lithium Coordination Sites in Li_xTiO_2(B): A Structural and Computational Study. Chem Mater. 2010;22:6426–32.

182. Andreev YG, Panchmatia PM, Liu Z, Parker SC, Islam MS, Bruce PG. The shape of TiO_2-B nanoparticles. J Am Chem Soc [Internet]. 2014;136(17):6306–12. Available from: http://www.ncbi.nlm.nih.gov/pubmed/25005683

183. Guo Z, Dong X, Zhou D, Du Y, Wang Y, Xia Y. TiO_2(B) nanofiber bundles as a high performance anode for a Li-ion battery. RSC Adv [Internet]. 2013;3(10):3352. Available from: http://xlink.rsc.org/?DOI=c2ra23336c

184. Lee DH, Kim DW, Park JG. Enhanced Rate Capabilities of Nanobrookite with Electronically Conducting MWCNT Networks. Cryst Growth Des. 2008;8(12):4506.

185. Yang Z, Du G, Guo Z, Yu X, Chen Z, Guo T, et al. TiO_2(B)@carbon composite nanowires as anode for lithium ion batteries with enhanced reversible capacity and cyclic performance. J Mater Chem. 2011;21(24):8591–6.

186. Zhou WJ, Liu H, Boughton RI, Du GJ, Lin JJ, Wang JY, et al. One-dimensional single-crystalline Ti–O based nanostructures: properties, synthesis, modifications and applications. J Mater Chem. 2010;20:5993.

187. Liu H, Bi Z, Sun X-G, Unocic RR, Paranthaman MP, Dai S, et al. Mesoporous TiO_2–B Microspheres with Superior Rate Performance for Lithium Ion Batteries. Adv Mater. 2011;23(30):3450–4.

188. Murphy DW, Di Salvo FJ, Carides JN, Waszczak JV. Topochemical reactions of rutile related structures with lithium. Materials Research Bulletin. 1978. p. 1395–402.

189. Ohzuku T, Takehara Z, Yoshizawa S. Nonaqueous lithium/titanium dioxide cell. Electrochim Acta. 1979;24(2):219–22.

190. MACKLIN W. Performance of titanium dioxide-based cathodes in a lithium polymer electrolyte cell. Solid State Ionics. 1992. p. 694–700.

191. Hu YS, Kienle L, Guo YG, Maier J. High lithium electroactivity of nanometer-sized rutile TiO_2. Adv Mater. 2006;18(11):1421–6.

192. Koudriachova M, Harrison N, de Leeuw S. Effect of Diffusion on Lithium Intercalation in Titanium Dioxide. Physical Review Letters. 2001. p. 1275–8.

193. Gligor F, de Leeuw SW. Lithium diffusion in rutile structured titania. Solid State Ionics. 2006;177(26-32 SPEC. ISS.):2741–6.

194. Deng D, Kim MG, Lee JY, Cho J. Green energy storage materials: Nanostructured TiO_2 and Sn-based anodes for lithium-ion batteries. Energy Environ Sci. 2009;2(8):818.

195. Kofstad P. Nonstoichiometry, diffusion, and electrical conductivity in binary metal oxides. New York: Wiley Interscience; 1972.

196. Kang JW, Kim DH, Mathew V, Lim JS, Gim JH, Kim J. Particle Size Effect of Anatase TiO_2 Nanocrystals for Lithium-Ion Batteries. J Electrochem Soc. 2011;158(2):A59.

197. Bresser D, Paillard E, Binetti E, Krueger S, Striccoli M, Winter M, et al. Percolating networks of TiO_2 nanorods and carbon for high power lithium insertion electrodes. J Power Sources [Internet]. Elsevier B.V.; 2012;206:301–9. Available from: http://dx.doi.org/10.1016/j.jpowsour.2011.12.051

198. Hwang H, Kim H, Cho J. MoS2 nanoplates consisting of disordered graphene-like layers for high rate lithium battery anode materials. Nano Lett. 2011;11(11):4826–30.

199. Moretti A, Kim GT, Bresser D, Renger K, Paillard E, Marassi R, et al. Investigation of different binding agents for nanocrystalline anatase TiO_2 anodes and its application in a novel, green lithium-ion battery. J Power Sources [Internet]. Elsevier B.V; 2013;221:419–26. Available from: http://dx.doi.org/10.1016/j.jpowsour.2012.07.142

200. Ren Y, Liu Z, Pourpoint F, Armstrong a. R, Grey CP, Bruce PG. Nanoparticulate TiO_2(B): An Anode for Lithium-Ion Batteries. Angew Chemie Int Ed [Internet]. 2012;51(9):2164–7. Available from: http://doi.wiley.com/10.1002/anie.201108300

201. Maier J. Nanoionics: ion transport and electrochemical storage in confined systems. Nat Mater. 2005;4(11):805–15.

202. Sides CR, Li N, Patrissi CJ, Scrosati B, Martin CR. Nanoscale Materials for Lithium-Ion Batteries. MRS Bull. 2002;27(08):604–7.

203. Fang F, Futter J, Markwitz a, Kennedy J. UV and humidity sensing properties of ZnO nanorods prepared by the arc discharge method. Nanotechnology. 2009;20(24):245502.

204. Park SJ, Kim YJ, Lee H. Synthesis of carbon-coated TiO_2 nanotubes for high-power lithium-ion batteries. J Power Sources [Internet]. Elsevier B.V.;

2011;196(11):5133–7. Available from: http://dx.doi.org/10.1016/j.jpowsour.2011.01.105

205. Han H, Song T, Bae J-Y, Nazar LF, Kim H, Paik U. Nitridated TiO_2 hollow nanofibers as an anode material for high power lithium ion batteries. Energy Environ Sci. 2011;4(11):4532.

206. Qiao H, Wang Y, Xiao L, Zhang L. High lithium electroactivity of hierarchical porous rutile TiO_2 nanorod microspheres. Electrochem commun. 2008;10(9):1280–3.

207. Song B, Liu S, Jian J, Lei M, Wang X, Li H, et al. Electrochemical properties of TiO_2hollow microspheres from a template-free and green wet-chemical route. J Power Sources. 2008;180(2):869–74.

208. Wang J, Bai Y, Wu M, Yin J, Zhang WF. Preparation and electrochemical properties of TiO_2 hollow spheres as an anode material for lithium-ion batteries. J Power Sources. 2009;191(2):614–8.

209. Xu J, Wang Y, Li Z, Zhang WF. Preparation and electrochemical properties of carbon-doped TiO_2 nanotubes as an anode material for lithium-ion batteries. Journal of Power Sources. 2008. p. 903–8.

210. Lafont U, Simonin L, Gaberscek M, Kelder EM. Carbon coating via an alkyl phosphonic acid grafting route: Application on TiO_2. J Power Sources. 2007;174(2):1104–8.

211. Park, C. M., Chang, W. S., Jung, H., Kim, J. H., Sohn H. Nanostructured Sn/TiO_2/C composite as a high-performance anode for Li-ion batteries. J Electrochem Commun. 2009;11(1):2165.

212. Lindsay MJ, Skyllas-Kazacos M, Luca V. Anodically synthesized titania films for lithium batteries: Effect of titanium substrate and surface treatment. Electrochim Acta. 2009;54(13):3501–9.

213. Lindsay MJ, Blackford MG, Attard DJ, Luca V, Skyllas-Kazacos M, Griffith CS. Anodic titania films as anode materials for lithium ion batteries. Electrochim Acta. 2007;52(23):6401–11.

214. Baudrin E, Cassaignon S, Koelsch M, Jolivet JP, Dupont L, Tarascon JM. Structural evolution during the reaction of Li with nano-sized rutile type TiO_2 at room temperature. Electrochem commun. 2007;9(2):337–42.

215. Jiang C, Honma I, Kudo T, Zhou H. Nanocrystalline Rutile TiO_2 Electrode for High-Capacity and High-Rate Lithium Storage. Electrochem Solid-State Lett [Internet]. 2007 ;10(5):A127. Available from: http://www.scopus.com/inward/record.url?eid=2-s2.0-33947311517&partnerID=tZOtx3y1

216. Borghols WJH, Wagemaker M, Lafont U, Kelder EM, Mulder FM. Impact of nanosizing on lithiated rutile TiO_2. Chem Mater. 2008;20(9):2949–55.

217. Kim SJ, Noh S-Y, Kargar A, Wang D, Graham GW, Pan X. In situ TEM observation of the structural transformation of rutile TiO_2 nanowire during electrochemical lithiation. Chem Commun [Internet]. Royal Society of Chemistry; 2014;50(69):9932. Available from: http://xlink.rsc.org/?DOI=C4CC04161E

218. Pfanzelt M, Kubiak P, Wohlfahrt-Mehrens M. Nanosized TiO_2 Rutile with High Capacity and Excellent Rate Capability. Electrochem Solid-State Lett. 2010;13(7):A91–4.

219. Hassoun J, Pfanzelt M, Kubiak P, Wohlfahrt-Mehrens M, Scrosati B. An advanced configuration TiO_2/$LiFePO_4$ polymer lithium ion battery. J Power Sources. 2012;217:459–63.

220. Jin Y, Liu Y, Wang Y, Li X, Hu S, Li W. Synthesis of dandelion-like TiO_2 microspheres as anode materials for lithium ion batteries with enhanced rate capacity and cyclic performances. Int J Miner, Met Mater. 2012;19(11):1058.

221. Min KM, Park KS, Kim JC, Lee DH, Kim DW. Synthesis and Li electroactivity of dandelion-like nanorutile. Ceram Int. 2013;39(3):3459–62.

222. Bai Y, Liu Z, Zhang N, Sun K. One-pot synthesis of 3-D dandelion-like architectures constructed by rutile TiO_2 nanorods grown along [001] axis for high-rate lithium ion batteries. RSC Adv [Internet]. Royal Society of

Chemistry; 2015;5(27):21285–9. Available from: http://xlink.rsc.org/?DOI=C5RA00006H

223. Hu T, Sun X, Sun H, Yu M, Lu F, Liu C, et al. Flexible free-standing graphene-TiO_2 hybrid paper for use as lithium ion battery anode materials. Carbon N Y. 2013;51(1):322–6.

224. Qiu J, Zhang P, Ling M, Li S, Liu P, Zhao H, et al. Photocatalytic synthesis of TiO_2 and reduced graphene oxide nanocomposite for lithium ion battery. ACS Appl Mater Interfaces [Internet]. 2012;4(7):3636–42. Available from: http://www.ncbi.nlm.nih.gov/pubmed/22738305

225. Zhen meng meng, guo XJ, Gao G, Liu L, Zhou Z. Rutile TiO_2 Nanobundles on Reduced Graphene Oxides as Anode Materials for Li Ion Batteries. Chem Commun [Internet]. The Royal Society of Chemistry; 2014; Available from: http://pubs.rsc.org/en/Content/ArticleLanding/2014/CC/C4CC05480F\nhttp://pubs.rsc.org/en/content/articlehtml/2014/cc/c4cc05480f

226. Lan T, Qiu H, Xie F, Yang J, Wei M. Rutile TiO_2 Mesocrystals/Reduced Graphene Oxide with High-Rate and Long-Term Performance for Lithium-Ion Batteries. Sci Rep [Internet]. 2015;5:8498. Available from: http://www.nature.com/doifinder/10.1038/srep08498

227. Cherian CT. Studies on nanostructured metal oxides as prospective anodes for lithium ion batteries. National University of Singapore; 2013.

228. Liu Y, West AR. Semiconductor-insulator transition in undoped rutile, TiO_2, ceramics. J Am Ceram Soc. 2013;96(1):218–22.

229. Ghicov, A., Yamamoto, M., Schmuki P. Lattice widening in niobium-doped TiO_2 nanotubes: efficient ion intercalation and swift electrochromic contrast. Angew Chem, Int Ed. 2008;47(41):7934–7.

230. Pan H, Chen N, Shen S, Huang J. Preparation and Characteristics of Nb5+, Ta^{5+}/TiO_2 Nanoscale Powders by Sol–Gel Process Using $TiCl_3$. J sol-gel Sci Technol [Internet]. 2005;34(1):63–9. Available from: http://www.springerlink.com/index/k6m667q18h080921.pdf

231. Wu, X. W., Wu, D. J., Liu XJ. Silver-doping induced lattice distortion in TiO_2 nanoparticles. Chin Phys Lett 2009, 26 (7), 077809. 2009;26(7):077809.

232. Wang Y, Smarsly BM, Djerdj I. Niobium doped TiO_2 with mesoporosity and its application for lithium insertion. Chem Mater. 2010;22(24):6624–31.

233. Huajun Tian Fengxia Xin XT and WH. High lithium electroactivity of boron-doped hierarchical rutile submicrosphere. J Mater Chem A. 2014;2:10599–606.

234. Hiroyuki Usui, Sho Yoshioka, Kuniaki Wasada, Masahiro Shimizu and HS. Nb-Doped Rutile TiO_2: a Potential Anode Material for Na-Ion Battery. ACS Appl Mater Interfaces. 2015;7:6567−6573.

235. Harunsani MH, Oropeza FE, Palgrave RG, Egdell RG. Electronic and Structural Properties of $Sn_xTi_{1-x}O_2$ ($0.0 \leq x \leq 0.1$) Solid Solutions. Chem Mater. 2010;22:1551–8.

236. Reeves-McLaren N, Ferrarelli MC, Tung Y-W, Sinclair DC, West AR. Synthesis, structure and electrical properties of $Cu_{3.21}Ti_{1.16}Nb_{2.63}O_{12}$ and the CuO_x–TiO_2–Nb_2O_5 pseudoternary phase diagram. J Solid State Chem. 2011;184(7):1813–9.

237. West AR. Basic Solid State Chemistry. 2nd ed. Wiley, New York; 1999.

238. Hubbard SBCR. Accuracy in Powder Diffraction. Washington : National Bureau of Standards; 1980.

239. WinXPOW S. STOE WinXPOW. Darmstadt, Germany: STOE and Cie GmbH; 2004.

240. Reeves N. Basic instructions for WinXPOW software. 2011.

241. West AR. Solid State Chemistry and Its Applications. 2nd ed. John Wiley & Sons, Ltd; 2014.

242. Langford, J.I. and Wilson a. JC. Seherrer after Sixty Years: A Survey and Some New Results in the Determination of Crystallite Size. J Appl Cryst. 1978;11:102–13.

243. Sterianou I. Bismuth-based perovskites for high temperature piezoelectric applications,unpublished thesis. University of Sheffield; 2008.

244. EC-Lab software user's manual. EC-Lab software user's manual. Bio-Logic science instruments; 2009.

245. Wang J. Analytical Electrochemistry. 3rd ed. Wiley-VCH Verlag; 2006.

246. Levi MD. Solid-State Electrochemical Kinetics of Li-Ion Intercalation into $Li_{1-x}CoO_2$: Simultaneous Application of Electroanalytical Techniques SSCV, PITT, and EIS. Journal of The Electrochemical Society. 1999. p. 1279.

247. Irvine JTS, Sinclair DC, West AR. Electroceramics: characterisation by impedance spectroscopy. Adv Mater. 1990;2:132–8.

248. Barsoukov E, Macdonald JR. Impedance Spectroscopy: Theory, Experiment, and Applications. Impedance Spectroscopy: Theory, Experiment, and Applications. John Wiley & Sons, Inc.; 2005. 1-595 p.

249. Hodge IM, Ingram MD, West AR. Impedance and modulus spectroscopy of polycrystalline solid electrolytes. Journal of Electroanalytical Chemistry and Interfacial Electrochemistry. 1976. p. 125–43.

250. Sinclair DC. Characterization of Electro-materials using ac Impedance Spectroscopy. Bol la Soc Esp Ceram y Vidr. 1995;65:55–66.

251. Sinclair DC, West AR. Impedance and modulus spectroscopy of semiconducting $BaTiO_3$ showing positive temperature coefficient of resistance. J Appl Phys. 1989;66(8):3850–6.

252. Sinclair DC, Morrison FD, West AR. Applications of combined impedance and electric modulus spectroscopy to characterise electroceramics. Intern Ceram. 2000;2:33–8.

253. Bauerle JE. Study of solid electrolyte polarization by a complex admittance method. J Phys Chem Solids [Internet]. 1969; 30(12):2657–70. Available from: http://www.sciencedirect.com/science/article/pii/0022369769900390

254. Kim J, Cho J. Rate Characteristics of Anatase TiO_2 Nanotubes and Nanorods for Lithium Battery Anode Materials at Room Temperature. Journal of The Electrochemical Society. 2007. p. A542.

255. Kavan L. Lithium Insertion into Mesoscopic and Single-Crystal TiO_2 (Rutile) Electrodes. J Electrochem Soc [Internet]. Electrochemical Soc Inc; 1999 [cited 2015 Jun 24];146(4):1375. Available from: http://www.scopus.com/inward/record.url?eid=2-s2.0-0032679784&partnerID=tZOtx3y1

256. Kofstad P. Nonstoichiometry, Diffusion and Electrical Conductivity of Binary Metal Oxides. Wiley-International, New York; 1972. 81-109 p.

257. Metadise. Lesson 1 [Internet]. Available from: http://metadise.org/

258. Hu YS, Kienle L, Guo YG, Maier J. High lithium electroactivity of nanometer-sized rutile TiO_2. Adv Mater. 2006;18(11):1421–6.

259. Tilley RJD. Defects in Solids. Defects in Solids. 2008. 1-529 p.

260. Matzke H. Nonstoichiometric Oxides. Sorensen OT, editor. Academic Press, New York; 1981.

261. Zhao B, Cai R, Jiang S, Sha Y, Shao Z. Highly flexible self-standing film electrode composed of mesoporous rutile TiO_2/C nanofibers for lithium-ion batteries. Electrochim Acta [Internet]. Elsevier Ltd; 2012;85:636–43. Available from: http://dx.doi.org/10.1016/j.electacta.2012.08.126

262. Wang W, Sa Q, Chen J, Wang Y, Jung H, Yin Y. Porous TiO2/C nanocomposite shells as a high-performance anode material for lithium-ion batteries. ACS Appl Mater Interfaces. 2013;5(14):6478–83.

263. Hong Z, Wei M, Lan T, Jiang L, Cao G. Additive-free synthesis of unique TiO_2 mesocrystals with enhanced lithium-ion intercalation properties. Energy & Environmental Science. 2012. p. 5408.

264. Milne NA, Skyllas-Kazacos M, Luca V. Crystallite size dependence of lithium intercalation in nanocrystalline rutile. J Phys Chem C. 2009;113(30):12983–95.

265. DeFord JW, Johnson OW. Electron transport properties in rutile from 6 to 40 K. J Appl Phys [Internet]. 1983; 54(2):889. Available from: http://scitation.aip.org/content/aip/journal/jap/54/2/10.1063/1.332051

266. Batteries HOF, Library DE, Companies TM. Source : Handbook of batteries. Cell. 2004. 1200 p.

267. Mukai K, Kato Y, Nakano H., Understanding the zero-strain lithium insertion scheme of $Li[Li_{1/3}Ti_{5/3}]O_4$:strucctural changes at atomic scale clarified by raman spectroscopy, J. Phys. Chem. C, 2014;118(6), 2992-2999.

268. Colbow KM, Dahn JR, Haering RR. Structure and electrochemistry of the spinel oxides $LiTi_2O_4$ and $Li_{4/3}Ti_{5/3}O_4$. J Power Sources. 1989;26(3 -4 pt2):397–402.

269. Zaghib K. Electrochemistry of Anodes in Solid-State Li-Ion Polymer Batteries. Journal of The Electrochemical Society. 1998. p. 3135.

270. Takai S, Kamata M, Fujine S, Yoneda K, Kanda K, Esaka T. Diffusion coefficient measurement of lithium ion in sintered $Li_{1.33}Ti_{1.67}O_4$ by means of neutron radiography. Solid State Ionics. Elsevier Science Publishers B.V.; 1999;123(1):165–72.

271. ROSSEN E, REIMERS J, DAHN J. Synthesis and electrochemistry of spinel LT-$LiCoO_2$. Solid State Ionics. 1993. p. 53–60.

272. Allen JL, Jow TR, Wolfenstine J. Low temperature performance of nanophase $Li_4Ti_5O_{12}$. J Power Sources. 2006;159(2):1340–5.

273. Choi Z, Kramer D, Mönig R. Correlation of stress and structural evolution in $Li_4Ti_5O_{12}$.-based electrodes for lithium ion batteries. J Power Sources [Internet]. Elsevier B.V; 2013;240:245–51. Available from: http://linkinghub.elsevier.com/retrieve/pii/S0378775313005971

274. Ge H, Li N, Li D, Dai C, Wang D. Study on the theoretical capacity of spinel lithium titanate induced by low-potential intercalation. J Phys Chem C. 2009;113(16):6324–6.

275. Scharner S, Weppner W, Schmid-Beurmann P. Cation Distribution in Ordered Spinels of the Li_2O-TiO_2-Fe_2O_3System. J Solid State Chem [Internet]. 1997;134(1):170–81. Available from: http://www.sciencedirect.com/science/article/B6WM2-45K14SH-W/2/f11314c32fe3bea9b9e69860fe60052d

276. Robertson AD, Tukamoto H, Irvine JTS. $Li_{1+x}Fe_{1-3x}Ti_{1+2x}O_4$ (0 . 0<x<0.33) Based Spinels : Possible Negative Electrode Materials for Future Li-Ion Batteries. J Electrochem Soc. 1999;146(11):3958–62.

277. Qiu C, Yuan Z, Liu L, Ye N, Liu J. Sol–gel preparation and electrochemical properties of La-doped $Li_4Ti_5O_{12}$. anode material for lithium-ion battery. J Solid State Electrochem [Internet]. 2012;17(3):841–7. Available from: http://www.scopus.com/inward/record.url?eid=2-s2.0-84878489746&partnerID=tZOtx3y1

278. Ohzuku T, Tatsumi K, Matoba N, Sawai K. Electrochemistry and Structural Chemistry of Li[CrTi]O_4 (Fd3m) in Nonaqueous Lithium Cells. J Electrochem Soc [Internet]. Electrochemical Soc Inc; 2000:3592. Available from: http://www.scopus.com/inward/record.url?eid=2-s2.0-0034292774&partnerID=tZOtx3y1

279. Zhang Y, Zhang C, Lin Y, Xiong DB, Wang D, Wu X, et al. Influence of Sc^{3+} doping in B-site on electrochemical performance of $Li_4Ti_5O_{12}$. anode materials for lithium-ion battery. J Power Sources. 2014;250:50–7.

280. Kubiak P, Garcia A, Womes M, Aldon L, Olivier-Fourcade J, Lippens PE, et al. Phase transition in the spinel $Li_4Ti_5O_{12}$. induced by lithium insertion - Influence of the substitutions Ti/V, Ti/Mn, Ti/Fe. Journal of Power Sources. 2003. p. 626–30.

281. Huang S, Wen Z, Zhu X, Lin Z. Preparation and Electrochemical Performance of Spinel-Type Compounds $Li_4Ti_5O_{12}$. (y=0, 0.10, 0.15, 0.25). J Electrochem Soc [Internet]. 2005 ;152(1):A186. Available from: http://www.scopus.com/inward/record.url?eid=2-s2.0-12844261205&partnerID=tZOtx3y1

282. Lin JY, Hsu CC, Ho HP, Wu SH. Sol-gel synthesis of aluminum doped lithium titanate anode material for lithium ion batteries. Electrochim Acta. 2013;87:126–32.

283. Wolfenstine J, Allen JL. Electrical conductivity and charge compensation in Ta doped $Li_4Ti_5O_{12}$.. J Power Sources. 2008;180(1):582–5.

284. Hao Y-J, Lai Q-Y, Lu J-Z, Ji X-Y. Effects of dopant on the electrochemical properties of $Li_4Ti_5O_{12}$. anode materials. Ionics (Kiel). 2007;13(5):369–73.

285. Zhao H, Li Y, Zhu Z, Lin J, Tian Z, Wang R. Structural and electrochemical characteristics of $Li_{4-x}Al_xTi_5O_{12}$ as anode material for lithium-ion batteries. Electrochim Acta. 2008;53(24):7079–83.

286. Tian B, Xiang H, Zhang L, Li Z, Wang H. Niobium doped lithium titanate as a high rate anode material for Li-ion batteries. Electrochim Acta. 2010;55(19):5453–8.

287. Aldon L, Kubiak P, Womes M. Chemical and electrochemical Li-insertion into the $Li_4Ti_5O_{12}$. spinel. Chem … [Internet]. 2004;(11):5721–5. Available from: http://pubs.acs.org/doi/abs/10.1021/cm0488837

288. Yuan T, Wang K, Cai R, Ran R, Shao Z. Cellulose-assisted combustion synthesis of $Li_4Ti_5O_{12}$. adopting anatase TiO_2 solid as raw material with high electrochemical performance. J Alloys Compd. 2009;477(1-2):665–72.

289. Yuan T, Cai R, Gu P, Shao Z. Synthesis of lithium insertion material Li4Ti5O12 from rutile TiO2 via surface activation. J Power Sources. 2010;195(9):2883–7.

290. Snyder MQ, Trebukhova SA, Ravdel B, Wheeler MC, DiCarlo J, Tripp CP, et al. Synthesis and characterization of atomic layer deposited titanium nitride thin films on lithium titanate spinel powder as a lithium-ion battery anode. J Power Sources. 2007;165(1):379–85.

291. Nakajima T, Ueno A, Achiha T, Ohzawa Y, Endo M. Effect of surface fluorination and conductive additives on the electrochemical behavior of

lithium titanate ($Li_{4/3}Ti_{5/3}O_4$) for lithium ion battery. J Fluor Chem. 2009;130:810–5.

292. Bach S, Pereira-ramos JP, Baffier N. Electrochemical behavior of a lithium titanium spinel compound synthesized via a sol–gel process. Journal of Materials Chemistry. 1998. p. 251–3.

293. Kavan L, Procházka J, Spitler TM, Kalbáč M, Zukalová M, Drezen T, et al. Li Insertion into $Li_4Ti_5O_{12}$. (Spinel) Charge Capability vs. Particle Size in Thin-Film Electrodes. J Electrochem Soc [Internet]. 2003;150(7):A1000–7. Available from: http://jes.ecsdl.org/content/150/7/A1000\nhttp://jes.ecsdl.org/content/150/7/A1000.full.pdf

294. Sun X, Hegde M, Zhang Y, He M, Gu L, Wang Y, et al. Structure and Electrochemical Properties of Spinel $Li_4Ti_5O_{12}$.Nanocomposites as Anode for Lithium-Ion Battery. 2014;9:1583–96.

295. Gao J, Ying J, Jiang C, Wan C. High-density spherical $Li_4Ti_5O_{12}$./C anode material with good rate capability for lithium ion batteries. J Power Sources. 2007;166(1):255–9.

296. Li J, Tang Z, Zhang Z. Controllable formation and electrochemical properties of one-dimensional nanostructured spinel $Li_4Ti_5O_{12}$. Electrochem commun. 2005;7(9):894–9.

297. Prakash AS, Manikandan P, Ramesha K, Sathiya M, Tarascon JM, Shukla AK. Solution-combustion synthesized nanocrystalline $Li_4Ti_5O_{12}$. as high-rate performance li-ion battery anode. Chem Mater. 2010;22(9):2857–63.

298. Wolfenstine J, Lee U, Allen JL. Electrical conductivity and rate-capability of $Li_4Ti_5O_{12}$. as a function of heat-treatment atmosphere. J Power Sources. 2006;154(1):287–9.

299. Guerfi A, Sévigny S, Lagacé M, Hovington P, Kinoshita K, Zaghib K. Nano-particle $Li_4Ti_5O_{12}$. spinel as electrode for electrochemical generators. Journal of Power Sources. 2003. p. 88–94.

300. Wen L, Lu Q, Xu G. Molten salt synthesis of spherical $LiNi_{0.5}Mn_{1.5}O_4$ cathode materials. Electrochim Acta. 2006;51(21):4388–92.

301. Kavan L, Gratzel M. Facile Synthesis of Nanocrystalline $Li_4Ti_5O_{12}$. (Spinel) Exhibiting Fast Li Insertion. Electrochem Solid-State Lett [Internet]. ECS; 2002;5(2):A39–42. Available from: http://link.aip.org/link/?ESL/5/A39/1

302. Shen C, Zhang X, Zhou Y, Li H. Preparation and characterization of nanocrystalline $Li_4Ti_5O_{12}$.by sol – gel method. Mater Chem Phys. 2002;78:437–41.

303. Hao YJ, Lai QY, Lu JZ, Wang HL, Chen YD, Ji XY. Synthesis and characterization of spinel $Li_4Ti_5O_{12}$. anode material by oxalic acid-assisted sol-gel method. J Power Sources. 2006;158(2 SPEC. ISS.):1358–64.

304. Kalbáč M, Zukalová M, Kavan L. Phase-pure nanocrystalline $Li_4Ti_5O_{12}$. for a lithium-ion battery. Journal of Solid State Electrochemistry. 2003. p. 2–6.

305. Vujković M, Stojković I, Mitrić M, Mentus S, Cvjetićanin N. Hydrothermal synthesis of $Li_4Ti_5O_{12}$./C nanostructured composites: Morphology and electrochemical performance. Mater Res Bull. 2013;48(2):218–23.

306. Fattakhova D, Petrykin V, Brus J, Kostlánová T, Dědeček J, Krtil P. Solvothermal synthesis and electrochemical behavior of nanocrystalline cubic Li-Ti-O oxides with cationic disorder. Solid State Ionics. 2005;176(23-24):1877–85.

307. Cheng L, Liu H-J, Zhang J-J, Xiong H-M, Xia Y-Y. Nanosized Li[sub 4]Ti[sub 5]O[sub 12] Prepared by Molten Salt Method as an Electrode Material for Hybrid Electrochemical Supercapacitors. Journal of The Electrochemical Society. 2006. p. A1472.

308. Bai Y, Wang F, Wu F, Wu C, Bao L ying. Influence of composite LiCl-KCl molten salt on microstructure and electrochemical performance of spinel $Li_4Ti_5O_{12}$.. Electrochim Acta. 2008;54(2):322–7.

309. Ju SH, Kang YC. Effects of drying control chemical additive on properties of $Li_4Ti_5O_{12}$. negative powders prepared by spray pyrolysis. J Power Sources. 2010;195(13):4327–31.

310. Kiliç Dokan F, Şahan H, Özdemır N, Özdemır B, Patat Ş. Effects of TiO_2 Source on the Electrochemical Performance of $Li_4Ti_5O_{12}$. Acta Phys Pol A [Internet]. 2014;125(2):650–1. Available from: http://przyrbwn.icm.edu.pl/APP/PDF/125/a125z2p156.pdf

311. Hong CH, Noviyanto A, Ryu JH, Kim J, Yoon DH. Effects of the starting materials and mechanochemical activation on the properties of solid-state reacted $Li_4Ti_5O_{12}$. for lithium ion batteries. Ceram Int. 2012;38(1):301–10.

312. Ganesan M. $Li_4Ti_{2.5}Cr_{2.5}O_{12}$ as anode material for lithium battery. Ionics (Kiel). 2008;14(5):395–401.

313. Wang GJ, Gao J, Fu LJ, Zhao NH, Wu YP, Takamura T. Preparation and characteristic of carbon-coated $Li_4Ti_5O_{12}$. anode material. J Power Sources. 2007;174(2):1109–12.

314. Kerisit S, Rosso KM, Yang Z, Liu J. Dynamics of Coupled Lithium / Electron Diffusion in TiO_2 Polymorphs. Work. 2009;113(49):20998–1007.

315. Li L, Tsung CK, Yang Z, Stucky GD, Sun L, Wang J, et al. Rare-earth-doped nanocrystalline titania microspheres emitting luminescence via energy transfer. Adv Mater. 2008;20(5):903–8.

316. Bussian D a, Crooker S a, Yin M, Brynda M, Efros AL, Klimov VI. Tunable magnetic exchange interactions in manganese-doped inverted core-shell ZnSe-CdSe nanocrystals. Nat Mater [Internet]. Nature Publishing Group; 2009;8(1):35–40. Available from: http://dx.doi.org/10.1038/nmat2342

317. Morgan BJ, Scanlon DO, Watson GW. Small polarons in Nb- and Ta-doped rutile and anatase TiO_2. J Mater Chem. 2009;19(29):5175.

318. Sakata K. Study of the Phase Transition in $Nb_xTi_{1-x}O_2$. J Phys Soc Jpn. 1969;26(4):1067.

319. Sakata K, Nishida I, Matsushima M, Sakata T. Electrical and magnetic properties of $Nb_xTi_{1-x}O_2$. J Phys Soc Jpn. 1969;27(2):506.

320. Mei B, Sánchez MD, Reinecke T, Kaluza S, Xia W, Muhler M. The synthesis of Nb-doped TiO_2 nanoparticles by spray drying: an efficient and scalable method. J Mater Chem. 2011;21(32):11781.

321. Sheppard LR, Bak T, Nowotny J. Electrical properties of niobium-doped titanium dioxide. 1. Defect disorder. J Phys Chem B. 2006;110(45):22447–54.

322. Navale SC, Vadivel Murugan A, Ravi V. Varistors based on Ta-doped TiO_2. Ceram Int. 2007;33(2):301–3.

323. Gao Y, Liang Y, Chambers S a. Synthesis and characterization of Nb-doped TiO_2 (110) surfaces by molecular beam epitaxy. Surf Sci. 1996;348(1-2):17–27.

324. Fehse M, Cavaliere S, Lippens PE, Savych I, Iadecola A, Monconduit L, et al. Nb-doped TiO_2 nanofibers for lithium ion batteries. J Phys Chem C. 2013;117(27):13827–35.

325. Niishiro R, Kato H, Kudo A. Nickel and either tantalum or niobium-codoped TiO_2 and $SrTiO_3$ photocatalysts with visible-light response for H_2 or O_2 evolution from aqueous solutions. Phys Chem Chem Phys. 2005;7(10):2241–5.

326. Teleki A, Bjelobrk N, Pratsinis SE. Flame-made Nb- and Cu-doped TiO_2 sensors for CO and ethanol. Sensors Actuators, B Chem. 2008;130(1):449–57.

327. Shannon RD. Handbook of Chemistry and Physics. 74th ed. CRC Press, Boca Raton, FL; 1974. A32751-767 p.

328. Shannon RD, Pask JA. Kinetics of the Anatase-Rutile Transformation. J Am Ceram Soc [Internet]. Blackwell Publishing Ltd; 1965;48(8):391–8. Available from: http://dx.doi.org/10.1111/j.1151-2916.1965.tb14774.x

329. Ould-Chikh S, Proux O, Afanasiev P, Khrouz L, Hedhili MN, Anjum DH, et al. Photocatalysis with chromium-doped TiO_2: Bulk and surface doping. ChemSusChem. Wiley-VCH Verlag; 2014;7(5):1361–71.

330. Araña J, Doña-Rodríguez JM, Melián JAH, Rendón ET, Díaz OG. Role of Pd and Cu in gas-phase alcohols photocatalytic degradation with doped TiO_2. J Photochem Photobiol A Chem. 2005;174(1):7–14.

331. Manivel A, Naveenraj S, Sathish Kumar PS, Anandan S. CuO-TiO_2 Nanocatalyst for Photodegradation of Acid Red 88 in Aqueous Solution. Sci Adv Mater [Internet]. 2010;2(1):51–7. Available from: http://openurl.ingenta.com/content/xref?genre=article&issn=1947-2935&volume=2&issue=1&spage=51

332. Cao F-F, Xin S, Guo Y-G, Wan L-J. Wet chemical synthesis of Cu/TiO_2 nanocomposites with integrated nano-current-collectors as high-rate anode materials in lithium-ion batteries. Phys Chem Chem Phys. 2011;13(6):2014–20.

333. Wang B, Zhao Y, Hu L, Cao J, Gao F, Liu Y, et al. Improved and excellent CO sensing properties of Cu-doped TiO_2 nanofibers. Chinese Sci Bull. 2010;55(3):228–32.

334. Slamet, Nasution HW, Purnama E, Kosela S, Gunlazuardi J. Photocatalytic reduction of CO_2 on copper-doped Titania catalysts prepared by improved-impregnation method. Catal Commun. 2005;6(5):313–9.

335. Nian JN, Chen SA, Tsai CC, Teng H. Structural feature and catalytic performance of Cu species distributed over TiO_2 nanotubes. J Phys Chem B. 2006;110(51):25817–24.

336. Li W, Shah SI, Huang C, Jung O, Ni C. Metallorganic chemical v apor deposition and characterization of TiO_2 nanoparticles. 2002;96:247–53.

337. Yan MF, Rhodes WW. Preparation and properties of TiO_2 varistors. Appl Phys Lett. 1982;40(6):536–7.

338. Wu JM, Chen CJ. Dielectric properties of (Ba, Nb) doped TiO2 ceramics: Migration mechanism and roles of (Ba, Nb). J Mater Sci. Kluwer Academic Publishers; 1988;23(11):4157–64.

339. Sousa VC de, Ca´ssia-Santos, Barrado CM, Bomio MRD, Leite ER, Varela JA, et al. Effect of atmosphere on the electrical properties of TiO_2 –SnO_2 varistor systems. J Mater Sci Mater Electron. 2004;15(10):665.

340. Follador Neto RG, De Souza ECF, De Andrade AVC, Antunes SRM, Antunes AC. Influence of Nb_2O_5 on the varistor behavior of TiO_2-Cr_2O_3 system. J Mater Sci Mater Electron. 2013;24(3):938–44.

341. Wang WY, Zhang DF, Chen XL. Nonlinear electrical characteristics and dielectric properties of (Ca,Ta)-doped TiO_2 ceramics. J Mater Sci [Internet]. 2003;38(9):2049–54. Available from: <Go to ISI>://000182581500030

342. Gaikwad AB, Navale SC, Ravi V. TiO_2 ceramic varistor modified with tantalum and barium. Mater Sci Eng B Solid-State Mater Adv Technol. 2005;123(1):50–2.

343. Dy E, Hui R, Zhang J, Liu ZS, Shi Z. Electronic conductivity and stability of doped titania ($Ti_{1-x}M_xO_2$, M = Nb, Ru, and Ta)- A density functional Theory-Based comparison. J Phys Chem C. 2010;114(31):13162–7.

344. Traversa, E., Di Vona, M. L. , Licoccia, S., Sacerdoti, M., Carotta, M. C., Gallana, M. Martinelli G. Sol-gel nanosized semiconducting titania based powders for thick-film gas sensors. J. Sol-Gel Sci. Technol. 2000;19(1):193–6.

345. Wang CM, Wang JF, Chen HC, Su W Bin, Zang GZ, Qi P, et al. Effects of CuO on the grain size and electrical properties of SnO_2-based varistors. Mater Sci Eng B Solid-State Mater Adv Technol. 2005;116(1):54–8.

346. Grandin A, Borel MM, Michel C, Raveau B. Ternary copper oxides with the rutile structure: The compounds $Ti_{1-x}Cu_x/3Nb_{2x}/3O_2$. Mater Res Bull. 1983;18:239–46.

347. Pang L-X, Wang H, Zhou D, Yao X. Sintering behavior, structures and microwave dielectric properties of a rutile solid solution system: $(A_xNb_{2x})Ti_{1-3x}O_2$ (A=Cu, Ni). J Electroceramics [Internet]. 2008; 23(1):13–8. Available from: http://www.scopus.com/inward/record.url?eid=2-s2.0-71449126741&partnerID=tZOtx3y1

348. García JA, Villafuerte-Castrejón ME, Andrade J, Valenzuela R, West AR. New rutile solid solutions, $Ti_{1-4x}Li_xM_{3x}O_2$: M = Nb, Ta, Sb. Mater Res Bull. 1984;19(5):649–54.

349. Attia A, Wang Q, Huang X, Yang Y. Titanium phosphates as positive electrode in lithium-ion batteries: composition, phase purity and electrochemical performance. J Solid State Electrochem [Internet]. 2011; 16(4):1461–71. Available from: http://www.scopus.com/inward/record.url?eid=2-s2.0-84862697744&partnerID=tZOtx3y1

350. Huang H, Zhang WK, Gan XP, Wang C, Zhang L. Electrochemical investigation of TiO_2/carbon nanotubes nanocomposite as anode materials for lithium-ion batteries. Mater Lett. 2007;61(1):296–9.

351. Irvine JTS, Sinclair DC, West AR. Electroceramics: characterization by impedance spectroscopy. Adv Mater [Internet]. 1990;2(3):132–8. Available from: http://doi.wiley.com/10.1002/adma.19900020304\n<Go to ISI>://3714684

352. Parker RA, Wasilik JH. Dielectric Constant and Dielectric Loss of TiO_2 (Rutile) at Low Frequencies. Phys Rev [Internet]. 1960;120(5):1631–7. Available from: http://www.scopus.com/inward/record.url?eid=2-s2.0-33646218926&partnerID=tZOtx3y1

353. Sinclair D. Use of blocking In/Ga electrodes for conductivity measurements. Solid State Ionics. 1990;37(4):295–8.

354. Wypych A, Bobowska I, Tracz M, Opasinska A, Kadlubowski S, Krzywania-Kaliszewska A, et al. Dielectric properties and characterisation of titanium dioxide obtained by different chemistry methods. J Nanomater. 2014;2014.

355. Marinel S, Choi DH, Heuguet R, Agrawal D, Lanagan M. Broadband dielectric characterization of TiO_2 ceramics sintered through microwave and conventional processes. Ceram Int [Internet]. Elsevier; 2013;39(1):299–306. Available from: http://dx.doi.org/10.1016/j.ceramint.2012.06.025

356. Blanchin MG, Bursill LA, Lafage C. Deformation and microstructure of rutile [Internet]. Proceedings - Royal Society of London, A. 1990. p. 175–202. Available from: http://www.scopus.com/inward/record.url?eid=2-s2.0-0025587182&partnerID=tZOtx3y1

357. Cho E, Han S, Ahn H-S, Lee K-R, Kim S, Hwang C. First-principles study of point defects in rutile $TiO_{2-x.}$ Phys Rev B. 2006;73(19):2–5.

358. Eder D, Kramer R. Stoichiometry of “titanium suboxide.” Phys Chem Chem Phys. 2003;5(6):1314–9.

359. Chen J, Lin LB, Jing FQ. Theoretical study of F-type color center in rutile TiO2. J Phys Chem Solids. 2001;62(7):1257–62.

360. Regonini D, Adamaki V, Bowen CR, Pennock SR, Taylor J, Dent a. CE. AC electrical properties of TiO_2 and Magnéli phases, Ti_nO_{2n-1}. Solid State Ionics [Internet]. 2012;229:38–44. Available from: http://www.sciencedirect.com/science/article/pii/S0167273812005619

361. Pike GE, Seager CH. The dc voltage dependence of semiconductor grain-boundary resistance. J Appl Phys. 1979;50(5):3414–22.

362. Peng Z, Gao R, Jiang F, He J, Fu X. Microstructure and nonohmic properties of SnO_2–Ta_2O_5–TiO_2 varistor system doped with CuO. Int J Mod Phys B [Internet]. World Scientific Publishing Co. Pte Ltd; 2014; 28(15):1450085. Available from: http://www.scopus.com/inward/record.url?eid=2-s2.0-84900329987&partnerID=tZOtx3y1

363. Bueno PR, Varela JA. Electronic Ceramics Based on Polycrystalline SnO_2, TiO_2 and $(Sn_xTi_{1-x})O_2$ Solid Solution. Mater Res. 2006;9(3):293–300.

364. Pennewiss J., Hoffman B., Varistor made from TiO2- Practicability and limits, Materials Letters, 1990;9(5):219–26.

365. Yang S, Wu J. Effects of Nb 2 O 5 in (Ba, Bi, Nb)-added TiC>2 ceramic varistors. 1995;(September 1994).

366. Bueno PR, Camargo E, Longo E, Leite E, Pianaro SA, Varela JA. Effect of Cr_2O_3 in the varistor behaviour of TiO_2. J Mater Sci Lett [Internet]. 1996;15(23):2048–50. Available from: http://www.scopus.com/inward/record.url?eid=2-s2.0-0030414481&partnerID=tZOtx3y1

367. Bueno PR, Leite ER, Oliveira MM, Orlandi MO, Longo E. Role of oxygen at the grain boundary of metal oxide varistors: A potential barrier formation mechanism. Appl Phys Lett. 2001;79(1):48–50.

368. Pike J, Chan SW, Zhang F, Wang X, Hanson J. Formation of stable Cu_2O from reduction of CuO nanoparticles. Appl Catal A Gen. 2006;303(2):273–7.

369. Adams TB, Sinclair DC, West AR. Characterization of grain boundary impedances in fine- and coarse-grained $CaCu_3Ti_4O_{12}$ ceramics. Phys Rev B. 2006;73:094124.

370. Li, W., Schwartz R. Maxwell-Wagner relaxations and their contributions to the high permittivity of calcium copper titanate ceramics. Phys Rev B. 2007;75:012104.

371. Kim I-D, Rothschild A, Tuller HL. Direct current bias effects on grain boundary Schottky barriers in $CaCu_3Ti_4O_{12}$. Sect Title Electr Phenom. 2006;88(7):072902/1–072902/3.

372. Bueno PR, Leite ER, Bulhoes LOS, Longo E, Paiva-Santos CO. Sintering and mass transport features of $(Sn,Ti)O_2$ polycrystalline ceramics. J Eur Ceram Soc. 2003;23(6):887–96.

373. Akurati KK, Vital A, Hany R, Bommer B, Graule T, Winterer M. One-step flame synthesis of SnO_2/TiO_2 composite nanoparticles for photocatalytic applications. International Journal of Photoenergy. 2005. p. 153–61.

374. Zakrzewska K, Radecka M, Rekas M. Effect of Nb, Cr, Sn additions on gas sensing properies of TiO_2 thin films. Thin Solid Films. 1997;310:161.

375. Lin J, Yu JC, Lo D, Lam SK. Photocatalytic Active of Rutile $Ti_{1-x}Sn_xO_2$ Solid Solutions. J Catal. 1999;183:368.

376. Harunsani MH, Oropeza FE, Palgrave RG, Egdell RG. Electronic and Structural Properties of $Sn_xTi_{1-x}O_2$ ($0.0 \leq x \leq 0.1$) Solid Solutions. Chem Mater. 2010;22:1551-1558.

377. Takahashi J, Kuwayama M, Kamiya H, Takatsu M, Oota T, Yamai I. Decomposition behaviours of dopant-free and doped solid solutions in the TiO_2-SnO_2 system. J Mater Sci [Internet]. Kluwer Academic Publishers; 1988;23(1):337–42. Available from: http://www.scopus.com/inward/record.url?eid=2-s2.0-0023849932&partnerID=tZOtx3y1

378. THomas C. Yuan AVV. Kinetics of Spinodal Decomposition in the TiO_2-SnO_2 System: The Effect of Aliovalent Dopants. J Am Ceram Soc. 1988;71(1):12–21.

379. Tennakone K, Bandara J. Photocatalytic activity of dye-sensitized tin(IV) oxidenanocrystalline particles attached to zinc oxide particles:long distance electron transfer via ballistic transport ofelectrons across nanocrystallites. Appl Catal A Gen. 2001;208:335.

380. Hochepied J f., Berger MH, Dynys F, Dessombz A, Sayir A. Aqueous Co.precipitated $Ti_{0.5}Sn_{0.5}O_2$ Nanopowders as Precusors for Dense Spinodally Decomposed Ceramics. J Am Ceram Soc. 2011;94(12):4226.

381. Zhao Y, Liu J, Shi L, Yuan S, Fang J, Wang Z, et al. Surfactant-free synthesis uniform $Ti_{1-x}Sn_xO_2$ nanocrystal colloids and their photocatalytic performance. Appl Catal B Environ [Internet]. Elsevier B.V.; 2010;100(1-2):68–76. Available from: http://dx.doi.org/10.1016/j.apcatb.2010.07.013

382. Yu J, Liu S, Zhou M. Enhanced photocalytic activity of hollow anatase microspheres by Sn^{4+} incorporation. J Phys Chem C. 2008;112(6):2050–7.

383. Sasikala R, Shirole a., Sudarsan V, Sakuntala T, Sudakar C, Naik R, Highly dispersed phase of SnO_2 on TiO_2 nanoparticles synthesized by polyol-mediated route: Photocatalytic activity for hydrogen generation. Int J Hydrogen Energy [Internet]. Elsevier Ltd; 2009;34(9):3621–30. Available from: http://dx.doi.org/10.1016/j.ijhydene.2009.02.085

384. Trotochaud L, Boettcher SW. Synthesis of rutile-phase $Sn_xTi_{1-x}O_2$ solid-solution and $(SnO_2)_x/(TiO2)_{1-x}$ core/shell nanoparticles with tunable lattice constants and controlled morphologies. Chem Mater. 2011;23(22):4920–30.

385. Hirata T, Ishioka K, Kitajima M, Doi H. Concentration Dependence of Optical Phonons in the TiO_2-SnO_2 System. Phys Rev B - Condens Matter. 1996;53(13):8442–8.

386. Bueno PR, Cassia-Santos MR, Simo?es LGP, Gomes JW, Longo E, Varela JA. Low-voltage varistor based on (Sn,Ti)O2 ceramics. J Am Ceram Soc [Internet]. 2002;85(1):282–4. Available from: http://www.scopus.com/scopus/inward/record.url?eid=2-s2.0-0036346818&partnerID=40&rel=R7.0.0

387. Sensato FR, Custodio R, Longo E, Beltrán A, Andrés J. Electronic and structural properties of $Sn_xTi_{1-x}O_2$ solid solutions: a periodic DFT study. Catalysis Today. 2003. p. 145–52.

388. Yu X, Li C, Tang H, Ling Y, Tang TA, Wu Q, et al. First principles study on electronic structures and properties of Sn-doped rutile TiO_2. Comput Mater Sci. 2010;49(2):430–4.

389. Long R, Dai Y, Huang B. Geometric and electronic properties of Sn-doped TiO_2 from first-principles calculations. J Phys Chem C. 2009;113(2):650–3.

390. Peng Z, Shi Z, Liu M. Mesoporous Sn-TiO_2 composite electrodes for lithium batteries. Chem Commun [Internet]. 2000;(21):2125–6. Available from: http://www.scopus.com/inward/record.url?eid=2-s2.0-0034619625&partnerID=tZOtx3y1

391. Wang H, Huang H, Niu C, Rogach AL. Ternary Sn-Ti-O based nanostructures as anodes for lithium ion batteries. Small [Internet]. Wiley-

VCH Verlag; 2015;11(12):1364–83. Available from: http://www.scopus.com/inward/record.url?eid=2-s2.0-84925115361&partnerID=tZOtx3y1

392. Hirata T. Oxygen Position, Octahedaral Distortion, and Bond-Valence Parameter from Bond Lengths in $Ti_{1-x}Sn_xO_2$ ($0 \leq x \leq 1$). j Am Ceram Soc. 2000;83(12):3205.

393. Dynys FW, Berger M, Sehirlioglu A. Thermoelectric Properties of Undoped and Doped $(Ti_{0.75}Sn_{0.25})O_2$. Tan X, editor. J Am Ceram Soc [Internet]. 2012;95(2):619–26. Available from: http://doi.wiley.com/10.1111/j.1551-2916.2011.04794.x

394. Ma Y, Navrotsky A. Calorimetric Study of Heats of Mixing in $Sn_xTi_{1-x}O_2$ Rutile Solid Solutions. J Am Ceram Soc [Internet]. 2010;93(10):3432–6. Available from: http://doi.wiley.com/10.1111/j.1551-2916.2010.03896.x

395. Cassia-Santos MR, Souza AG, Soledade LEB, Varela JA, Longo E. Thermal And Structural Investigation Of $(Sn_{1-X}Ti_{x)}O_2$ Obtained By The Polymeric Precursor Method. J Therm Anal Cal. 2005;79.

396. Parker RA. Static dielectric constant of Rutile (TiO_2), 1.6-1060° K. Phys Rev. 1961;124(6):1719–22.

397. Adepalli KK, Kelsch M, Merkle R, Maier J. Enhanced ionic conductivity in polycrystalline TiO_2 by “one-dimensional doping”. Phys Chem Chem Phys [Internet]. 2014;16(10):4942–51. Available from: http://www.ncbi.nlm.nih.gov/pubmed/24477488

398. Goodenough JB. Influence of atomic vacancies on the properties of transition-metal oxides. I. TiO_x and VO_x. Phys Rev B. 1972;5(8):2764–74.

399. Ganduglia-Pirovano MV, Hofmann A, Sauer J. Oxygen vacancies in transition metal and rare earth oxides: Current state of understanding and remaining challenges. Surf Sci Rep. 2007;62(6):219–70.

400. Nasu NTK, Siratori AFK. Electronic Conduction in Oxides. 2nd ed. Fulde E by P, editor. Springer; 1991.

401. Radecka M, Pasierb P, Zakrzewska K, Rekas M. Transport properties of (Sn,Ti)O_2 polycrystalline ceramics and thin films. Solid State Ionics. Elsevier Science Publishers B.V.; 1999;119(1):43–8.

402. Prades M, Alonso PJ, West AR, Pablo J, Non-ohmic AR. Non-Ohmic Phenomena in Mn-doped $BaTiO_3$. 2012;(11).

403. Bhatt MD, O'Dwyer C. Recent progress in theoretical and computational investigations of Li-ion battery materials and electrolytes. Phys Chem Chem Phys [Internet]. Royal Society of Chemistry; 2015;17(7):4799–844. Available from: http://xlink.rsc.org/?DOI=C4CP05552G

404. Yi J, Li X, Hu S, Li W, Zeng R, Fu Z, et al. TiO2-coated SnO_2 hollow spheres as anode materials for lithium ion batteries. Rare Met. 2011;30(6):589–94.

405. Sandu I, Brousse T, Schleich DM, Danot M. The chemical changes occurring upon cycling of a SnO_2 negative electrode for lithium ion cell: In situ Mossbauer investigation. J Solid State Chem. 2006;179(2):476–85.

406. Kim MH, Kang YC. Electrochemical Properties of Spherical Hollow SnO 2 - TiO_2 -C Composite Powders Prepared by Spray Pyrolysis. 2013;c:3676–86.

407. Liu H, Long D, Liu X, Qiao W, Zhan L, Ling L. Facile synthesis and superior anodic performance of ultrafine SnO_2-containing nanocomposites. Electrochim Acta. 2009;54(24):5782–8.

408. Lupo F Di, Gerbaldi C, Meligrana G, Bodoardo S. Novel SnO_2 / Mesoporous Carbon Spheres Composite Anode for Li-ion Batteries. Int J Electrochem Sci. 2011;6:3580–93.

409. Zhao ZW, Guo ZP, Yao P, Liu HK. Mesoporous Carbon-Tin Nanocomposites as Anode Materials for Li-ion Battery. J Mater Sci Technol. 2008;24(4):657.

410. Besenhard JO, Winter M, Yang J, Biberacher W. Filming mechanism of lithium-carbon anodes in organic and inorganic electrolytes. J Power Sources. 1995;54(2):228–31.

411. Demir-Cakan R, Hu Y-S, Antonietti M, Maier J, Titirici M-M. Facile One-Pot Synthesis of Mesoporous SnO_2 Microspheres via Nanoparticles Assembly and Lithium Storage Properties. Chem Mater. American Chemical Society; 2008;20(4):1227–9.

412. Issac I, Scheuermann M, Becker SM, Bardají EG, Adelhelm C, Wang D, et al. Nanocrystalline $Ti_{2/3}Sn_{1/3}O_2$ as anode material for Li-ion batteries. J Power Sources [Internet]. Elsevier B.V.; 2011;196(22):9689–95. Available from: http://dx.doi.org/10.1016/j.jpowsour.2011.07.046

413. Kyerematen NA, Hornebecq V, Knauth P, Djenizian T. Properties of Sn-doped TiO_2 nanotubes fabricated by anodization of co-sputtered Ti-Sn thin films. Electrochim Acta [Internet]. Elsevier Ltd; 2012;62:192–8. Available from: http://dx.doi.org/10.1016/j.electacta.2011.12.021

414. Yu C, Bai Y, Yan D, Li X, Zhang W. Improved electrochemical properties of Sn-doped TiO_2 nanotube as an anode material for lithium ion battery. J Solid State Electrochem [Internet]. 2014;18(7):1933–40. Available from: http://link.springer.com/10.1007/s10008-014-2436-9

415. Yan D, Yu C, Bai Y, Zhang W, Chen T, Hu B, et al. Sn-doped TiO_2 nanotubes as superior anode materials for sodium ion batteries. Chem Commun [Internet]. Royal Society of Chemistry; 2015;51(39):8261–4. Available from: http://xlink.rsc.org/?DOI=C4CC10020D

Appendices

Appendix A

Impedance data for $Cu_xTa_{2x}Ti_{1-3x}O_2$ (x =0.10) with different metal electrodes upon heating and cooling at different temperatures in air.

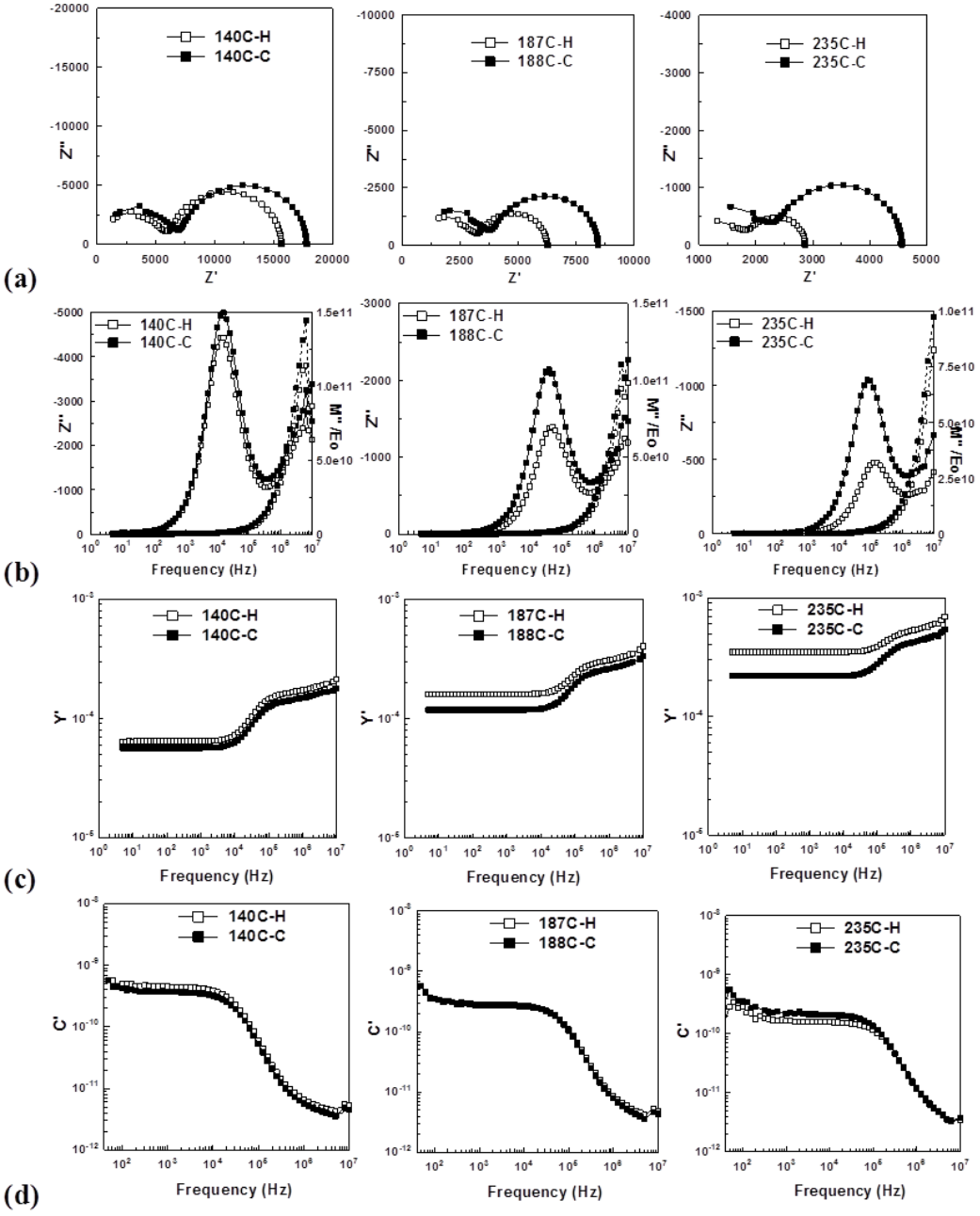

Figure A-1: Impedance data for $Cu_xTa_{2x}Ti_{1-3x}O_2$ (x =0.10) with sputtered Au electrode at different temperature upon heating (H) and cooling (C) in air: (a) Z* plot (b) Z″/M″, (c) admittance and (d) capacitance

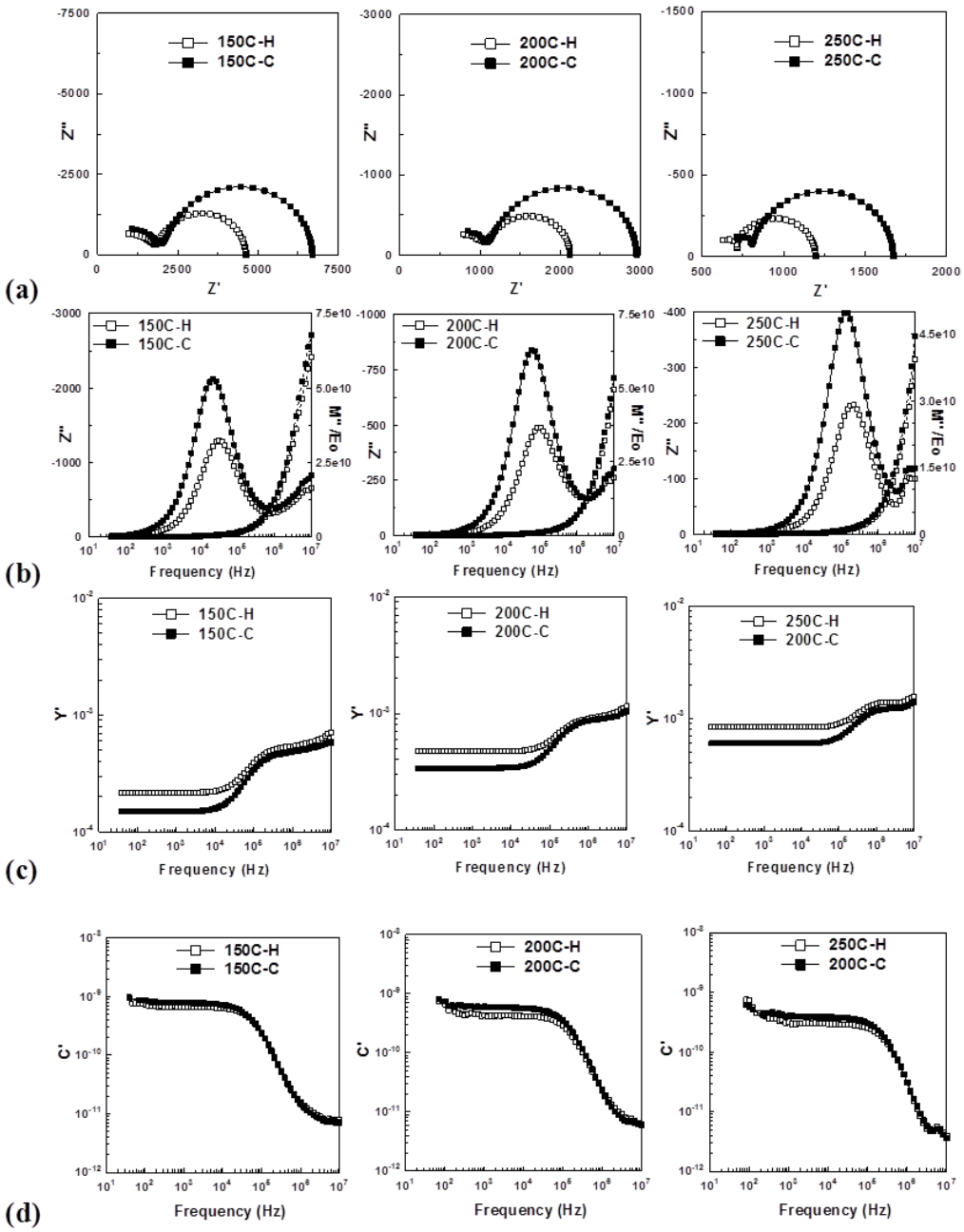

Figure A-2: Impedance data for $Cu_xTa_{2x}Ti_{1-3x}O_2$ (x =0.10) with sputtered Pt electrode: (a) Z* plot, (b) Z″/M″ spectroscopic plot, (c) spectroscopic plot of admittance and (d) spectroscopic plot of capacitance upon heating (H) and cooling (C) at different temperatures in air.

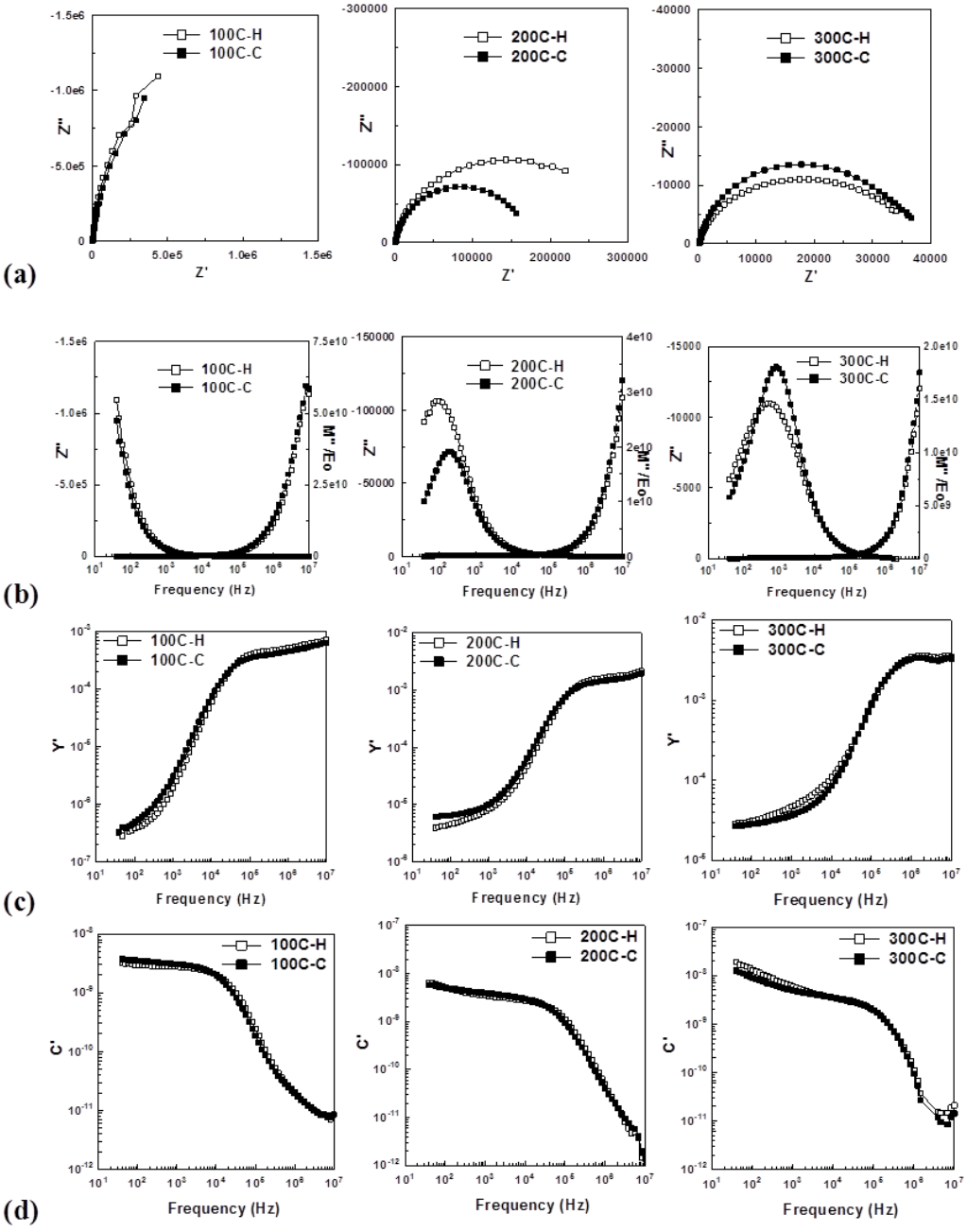

Figure A-3: Impedance data of: (a) Z* plot, (b) Z″/M″, (c) admittance plot and (d) capacitance plot for $Cu_xTa_{2x}Ti_{1-3x}O_2$ (x =0.10) with Au paste electrode upon heating (H) and cooling (C) at different temperature in air.

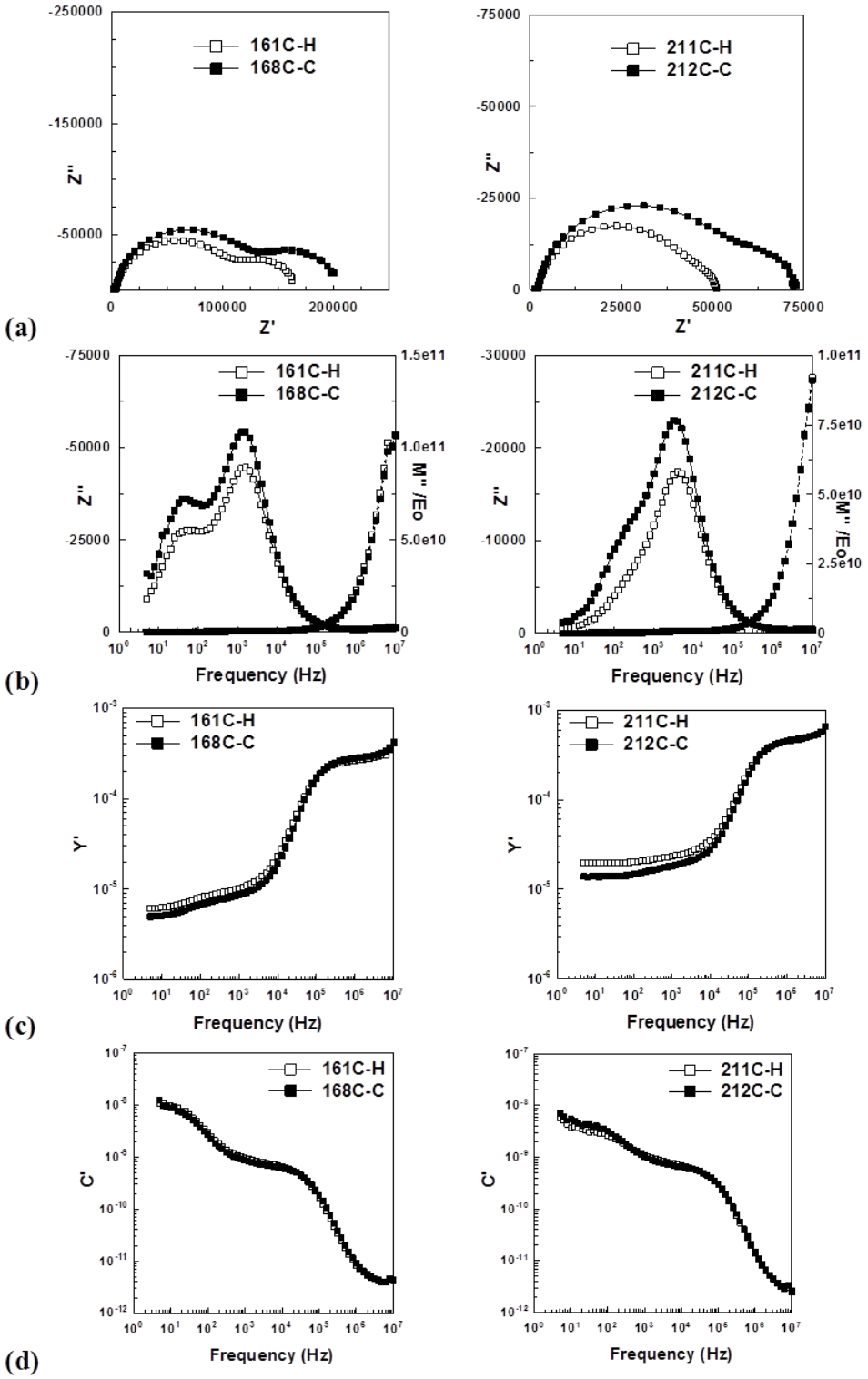

Figure A-4: Impedance data of: (a) Z^* plot, (b) Z″/M″ (c) admittance and (d) capacitance, for $Cu_xTa_{2x}Ti_{1-3x}O_2$ (x =0.10) with Pt paste electrode at different temperature upon heating and cooling in air.

Appendix B

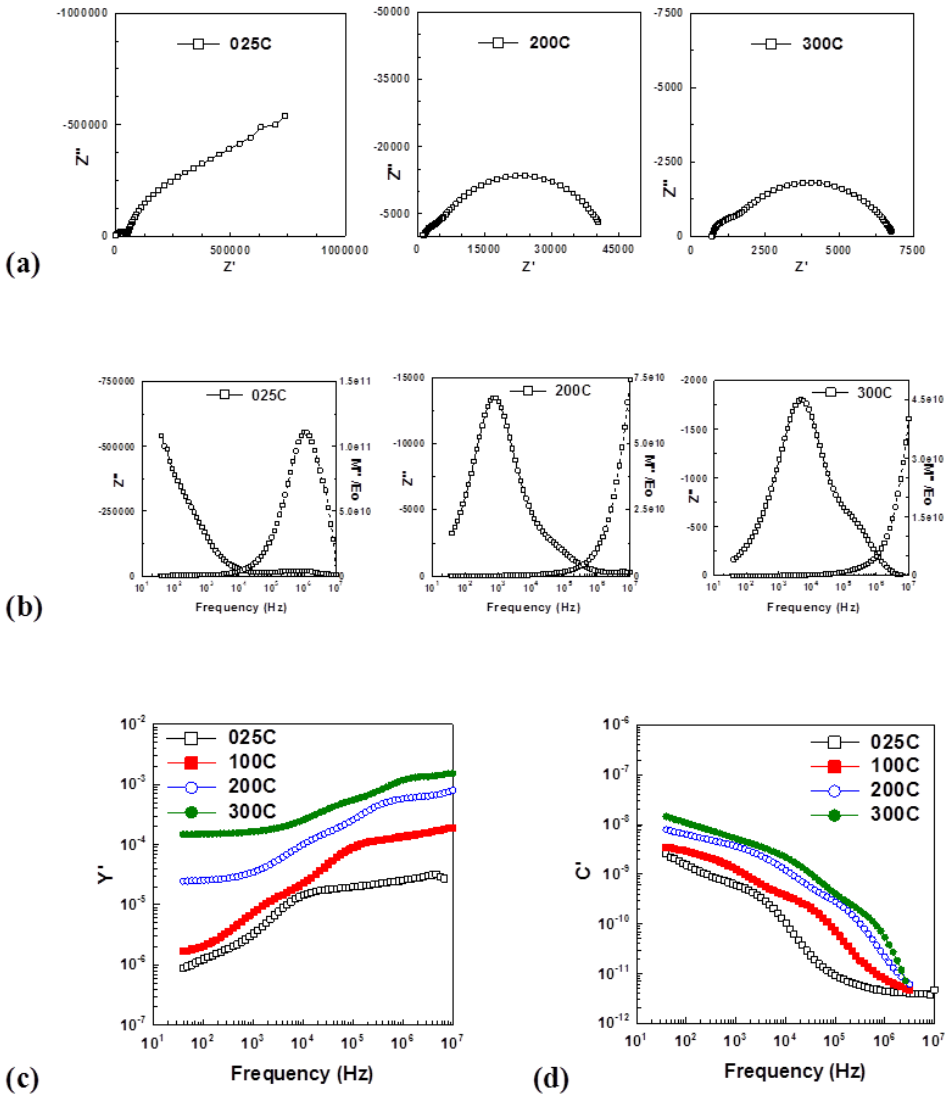

Figure B-1: Impedance data of: (a) Z^* plot and (b) Z''/M'', (c) admittance and (d) capacitance spectroscopic plots for $Cu_xTa_{2x}Ti_{1-3x}O_2$ (x = 0.12) with Au paste electrode at different temperatures; room temperature, 200 and 300°C in air.

Appendix c

Impedance data for $Cu_xTa_{2x}Ti_{1-3x}O_2$ (x =0.10) with different metal electrodes upon heating and cooling at different temperatures in different atmospheres.

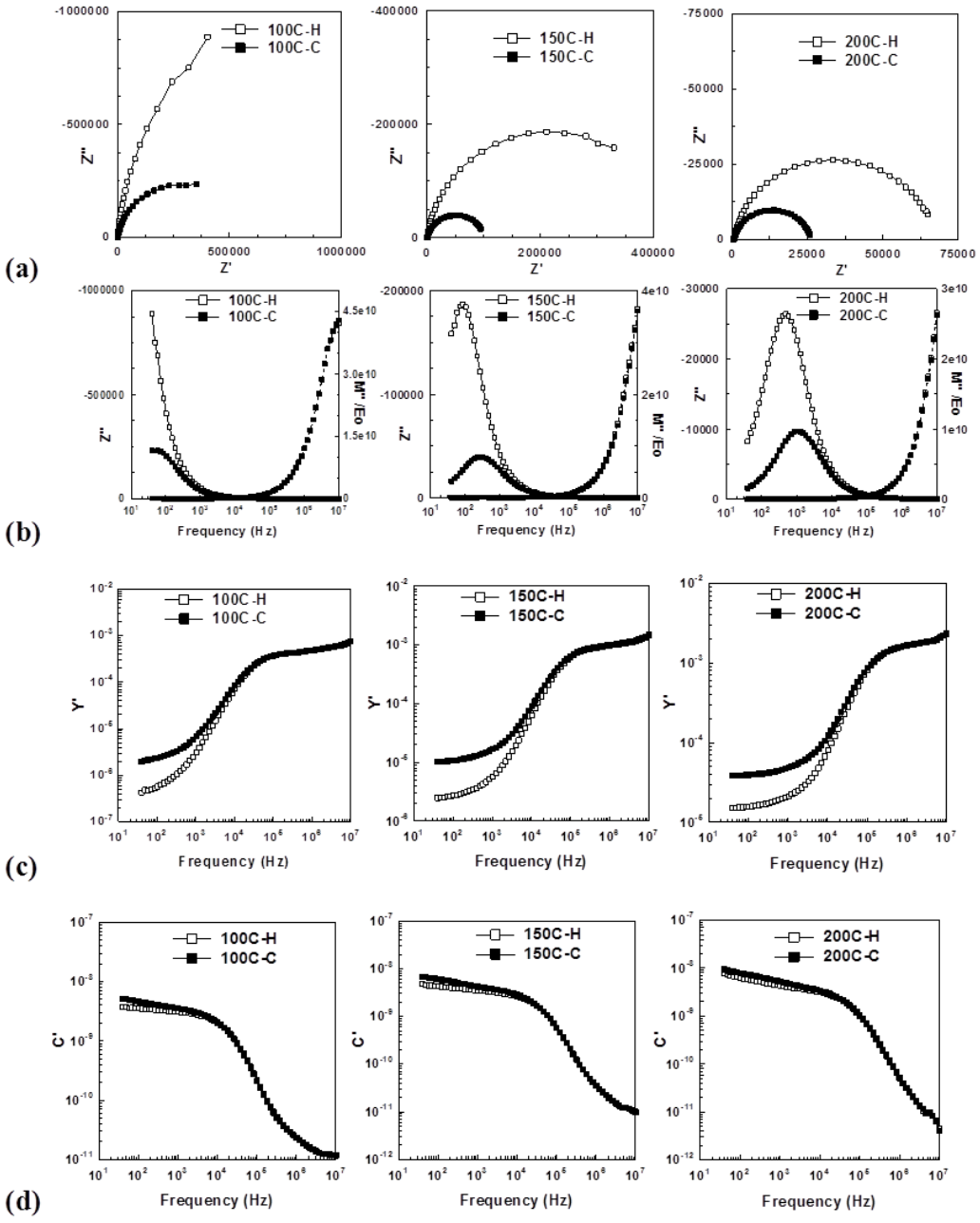

Figure C-1: Spectroscopic plot of: (a) Z* plot, (b) Z″/M″, (c) admittance and (d) capacitance at different temperatures for $Cu_xTa_{2x}Ti_{1-3x}O_2$ (x = 0.10) with Au paste electrode upon heating (H) and cooling (C) in N_2 atmosphere.

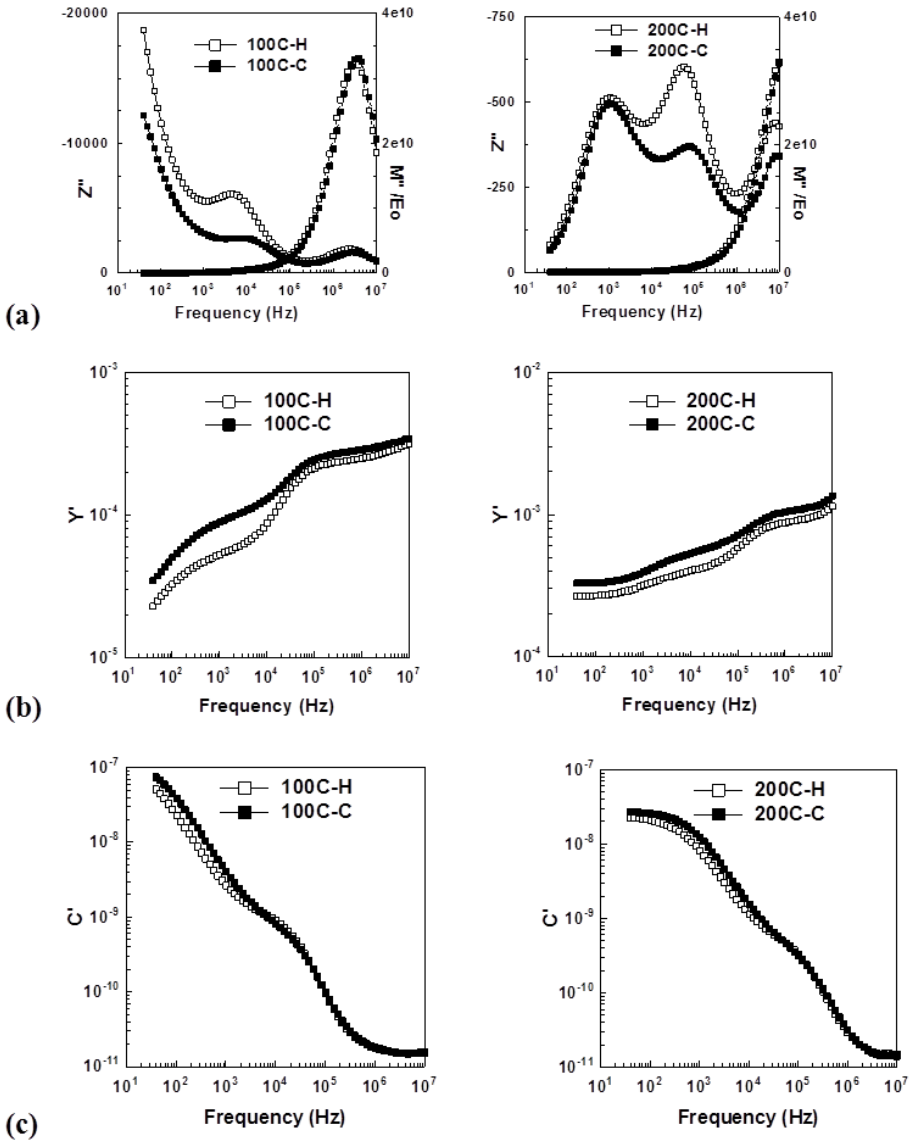

Figure C-2: Impedance data of: (a) Z* plot, (b) Z″/M″ , (c) admittance and (d) capacitance for $Cu_xTa_{2x}Ti_{1-3x}O_2$ (x =0.10) with Pt paste electrode during heating (H) and cooling (c) at 100 and 200°C in N_2 atmosphere.

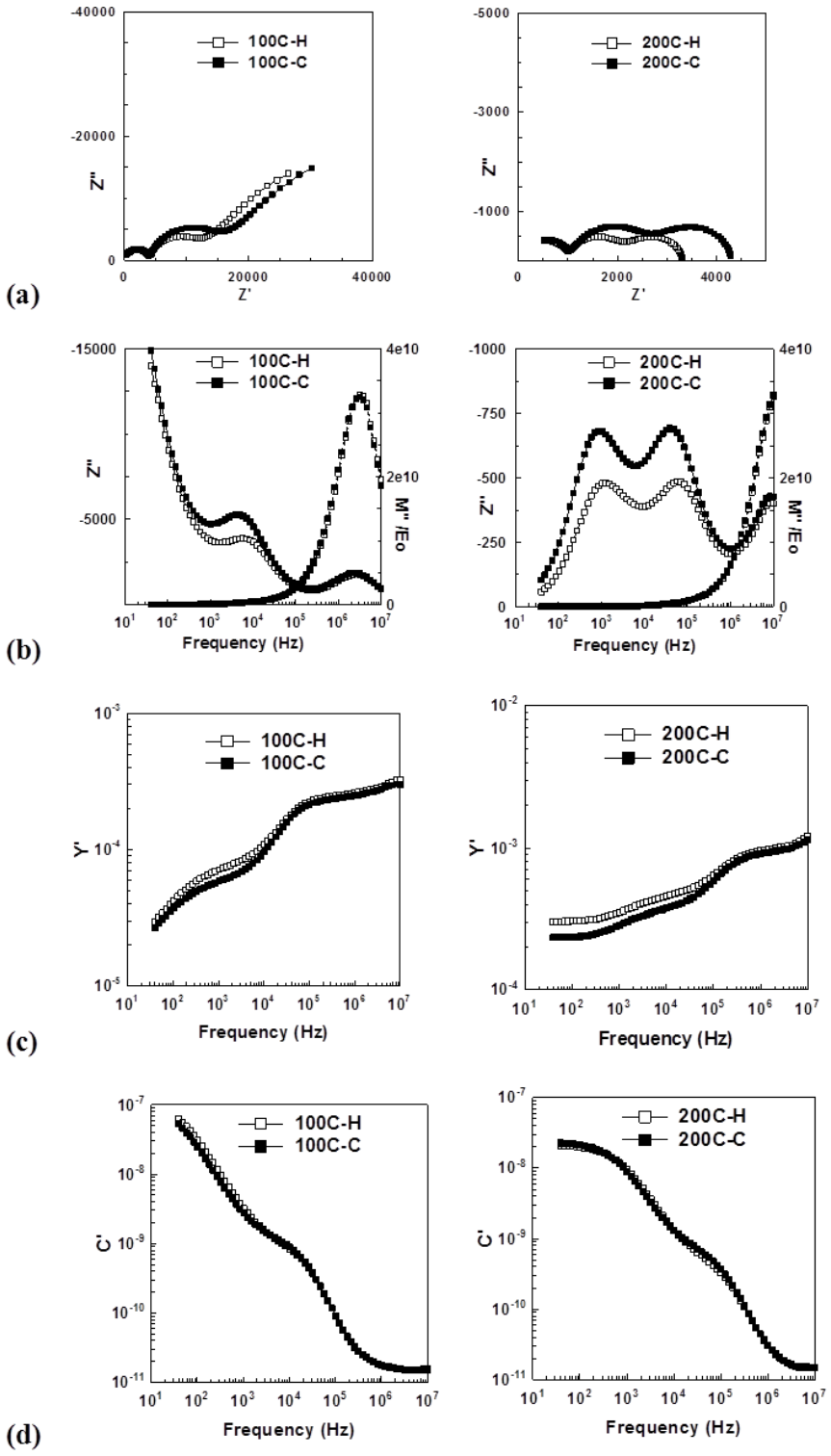

Figure C-3: Impedance data of; (a) Z* plot, (b) Z″/M″ , (c) admittance and (d) capacitance for $Cu_xTa_{2x}Ti_{1-3x}O_2$ (x =0.10) with Pt paste electrode during heating (H) and cooling (C) at 100 and 200°C in O_2 atmosphere.

Appendix D

Impedance data for $Cu_xTa_{2x}Ti_{1-3x}O_2$ (x = 0.10) with Au and Pt paste electrodes before and after applying DC bias with 1, 5 and 10V after different times at 200°C in Air.

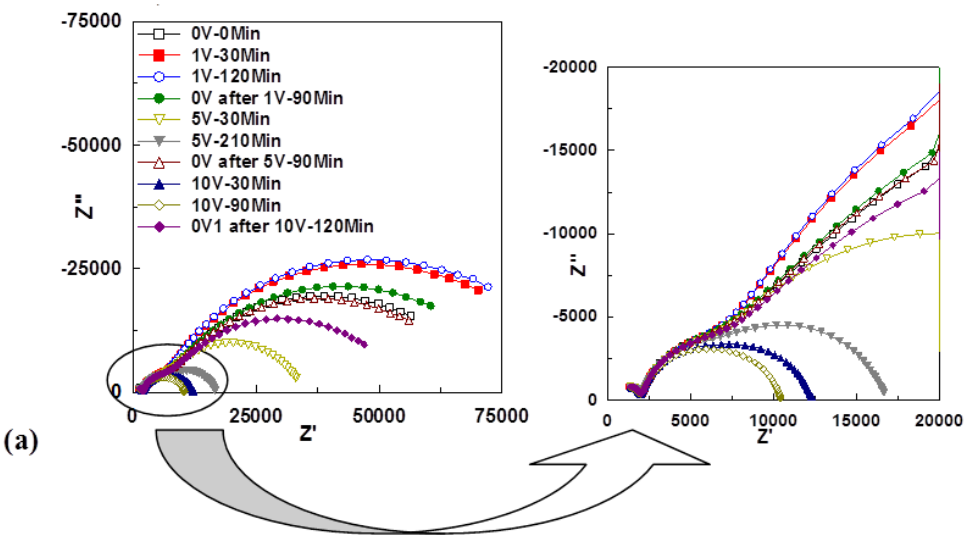

(a)

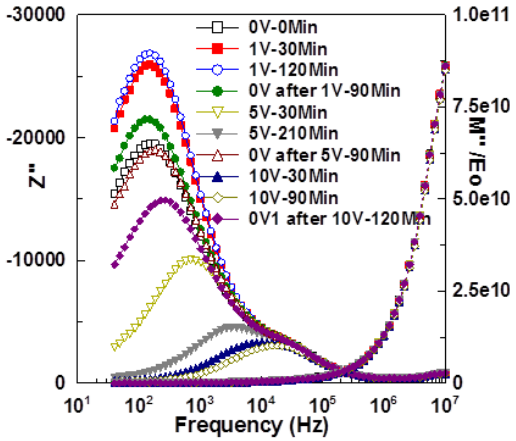

(b)

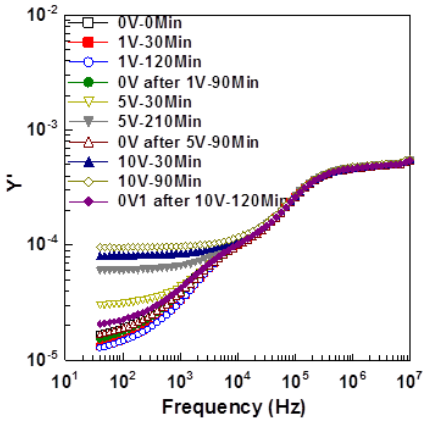

(c)

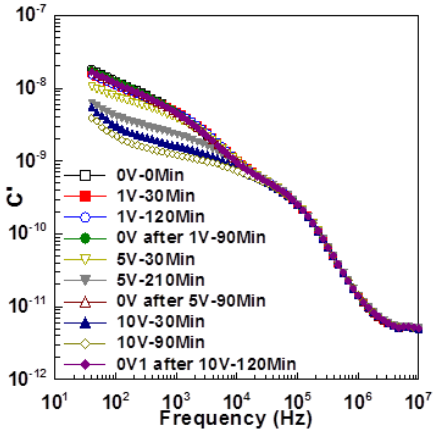

(d)

Figure D-1: Impedance data for $Cu_xTa_{2x}Ti_{1-3x}O_2$ (x = 0.10) with Au paste electrode before and after applying DC bias with 1, 5 and 10V after different times: (a) Z^* plot, (b) Z″/M″ (c) admittance and (d) capacitance, at 200°C in Air.

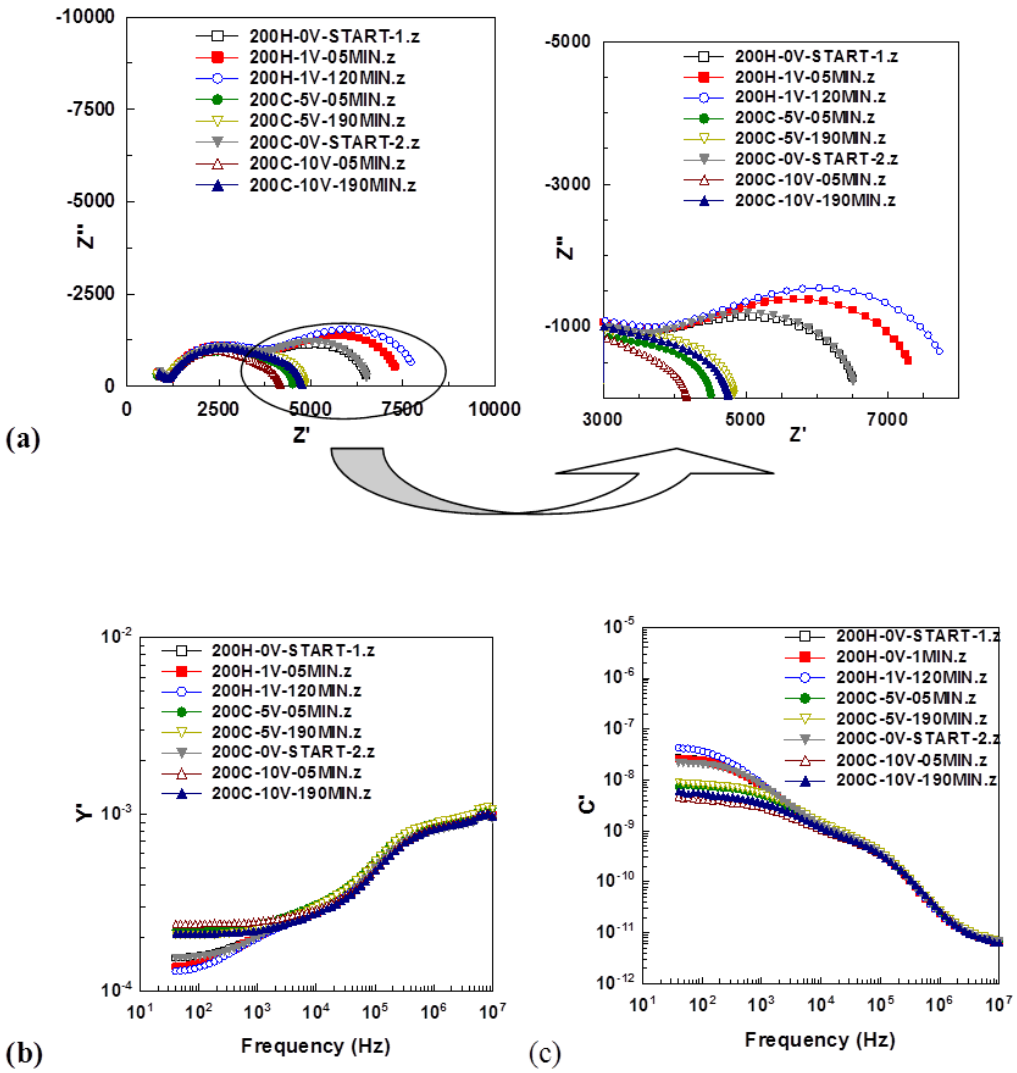

Figure D-2: Impedance data for $Cu_xTa_{2x}Ti_{1-3x}O_2$ (x = 0.10) with Pt paste electrode applying DC bias with 1, 5 and 10 V after different times: (a) Z^* plot, (b) admittance and (c) capacitance, at 200°C in Air.